COMPACT SILICON DIFFRACTIVE SENSOR:

DESIGN, FABRICATION, AND FUNCTIONAL DEMONSTRATION

A Thesis
Presented to
The Academic Faculty

by

Jonathan Stephen Maikisch

In Partial Fulfillment
of the Requirements for the Degree
Doctor of Philosophy in the
School of Electrical and Computer Engineering

Georgia Institute of Technology
December 2012

COMPACT SILICON DIFFRACTIVE SENSOR:

DESIGN, FABRICATION, AND FUNCTIONAL DEMONSTRATION

Approved by:

Professor Thomas K. Gaylord, Advisor
School of Electrical and Computer Engineering
Georgia Institute of Technology

Professor Abhijit Chatterjee
School of Electrical and Computer Engineering
Georgia Institute of Technology

Professor Muhannad S. Bakir
School of Electrical and Computer Engineering
Georgia Institute of Technology

Professor Phillip N. First
School of Physics
Georgia Institute of Technology

Professor Donald D. Davis
School of Electrical and Computer Engineering
Georgia Institute of Technology

Date Approved: November 1, 2012

ACKNOWLEDGEMENTS

During my time at Georgia Tech, numerous people have made a positive impact on both my life and my research. Words are insufficient to express the depths of my gratitude, but written here is my best effort to acknowledge those that have enriched both my life and my work.

It has been an honor and a privilege to have Professor Thomas K. Gaylord as my advisor. When one discusses the virtues of an outstanding individual, it is appropriate to draw comparisons with other outstanding individuals. This can prove difficult when the individual in question is in a class all their own. Prof. Gaylord is such an individual. It is truly rare to find someone so accomplished and yet so dedicated to his students and their work. Prof. Gaylord has served as my role model in both the research lab and the classroom, and he will continue to be a role model in my future career.

I would also like to thank the members of my thesis committee: Prof. Muhannad S. Bakir, Prof. Donald D. Davis, Prof. Abhijit Chatterjee, and Prof. Philip N. First. Their input and comments have been invaluable throughout this process. I must also express gratitude for making the time within their busy schedules to participate. It is sincerely appreciated.

I also must thank other members of the Georgia Tech Optics Laboratory, both past and present: Dr. Brent Bachim, Lieutenant Colonel Matt Burrow, Prof. Yin-Jung Chang, Dr. Michael Hutsel, Micah Jenkins, Prof. Gregory Kilby, Joe Kummer, Matthieu Leibovici, Dr. Chien-I Lin, Dr. Carole Montarou, Donald Sedivy, Dr. Justin Stay, Dr. Ricardo Villalaz, and Dr. Shun-Der Wu. Whether it was assembling components in the

lab, working out a tough problem in our offices, discussing research at our Friday lunch meetings, or simply enjoying time at one of our barbeque/chili cookouts, my interactions with you will be remembered and cherished.

From the Georgia Tech Nanotechnology Research Center, I would like to thank Devin Brown, Gary Spinner, Mikkel Thomas, Eric Woods, and the rest of the clean room staff. Without your help, fabrication would still be giving me nightmares.

From the Georgia Tech Research Institute, I would like to thank Dr. Daniel Campbell for your expertise and the use of your equipment and chemicals. With your help, the proof-of-concept sensor was successfully realized.

I would also like to thank my family whom have supported me through the trials and tribulations of life as a graduate student: my father Stephen, my mother Mary, and my sister Nicole. There is no substitute for your love and encouragement which has lifted me when I was down and driven me to succeed. I sincerely appreciate all you have done for me and only hope I can return your love and support in kind.

Finally, I must thank Emily Smithpeters for all of your love and support. Thank you for putting up with my late nights in the clean room or the lab and my long weekends spent doing work. Thank you for being there to lift me up when the problems I faced seemed insurmountable and giving me the encouragement I needed to overcome them. Thank you for your smile when I walk through the door, which has always succeeded in bringing about a smile of my own.

Jonathan Stephen Maikisch

Georgia Institute of Technology

November 2012

TABLE OF CONTENTS

Page

LIST OF TABLES

Page

LIST OF FIGURES

Page

LIST OF ACRONYMS AND ABBREVIATIONS

1-D One Dimensional

2-D Two Dimensional

3-D Three Dimensional

AMI Acetone, Methanol, and Isopropyl Alcohol

AR Anti-Reflection

ATR Attenuated Total Reflection

BCB Benzocyclobutene

BOX Buried Oxide

CAMFR Cavity Modeling Framework

CCD Charge-Coupled Device

CSDS Compact Silicon Diffractive Sensor

CCW Counterclockwise

CW Clockwise

EBL Electron-Beam Lithography

EMI Electromagnetic Interference

FEP Fluorinated Ethylene Propylene

FDTD Finite-Difference Time-Domain

Ga Gaussian

HSQ Hydrogen Silsesquioxane

ICP Inductively-Coupled Plasma

IEN Institute for Electronics and Nanotechnology

LOAC Lab-on-a-Chip

MZI Mach-Zehnder Interferometer

μ-TAS Micro-Total Analysis System

NA Numerical Aperture

PBIBMA poly n-butyl-isobutyl methacrylate

PDMS polydimethylsiloxane

PEEK Polyether Ether Ketone

PFA Perfluoroalkoxy

PML Perfectly-Matched Layer

PTFE Polytetrafluoroethylene

PW Plane Wave

RCWA Rigorous Coupled-Wave Analysis

SEM Scanning Electron Microscope

SOI Silicon-On-Insulator

SPR Surface Plasmon Resonance

STS Surface Technology Systems Plc.

TE Transverse Electric

TM Transverse Magnetic

TNT 2,4,6-Trinitrotoluene

TWCW Two-Wave Coupled-Wave

UV Ultraviolet

LIST OF SYMBOLS

A	Cross-sectional area (μm^2)
α	Grating boundary angle (incident side) (degrees) (+ CW)
α	Microscope objective half angular aperture (degrees)
α_m	Grating boundary angle (diffracted side) (degrees) (+ CCW)
β	Guided-mode propagation constant (μm^{-1})
β_0	Out-coupling grating incident propagation constant (μm^{-1})
β_m	Out-coupling grating diffracted propagation constant (μm^{-1})
β_{SP}	Surface plasmon propagation constant (μm^{-1})
C	Toluene concentration (ppm)
C_{sat}	Saturated toluene concentration (ppm)
D	EBL exposure dose ($\mu C / cm^2$)
d_G	Groove depth (nm)
D_H	Hydraulic diameter (μm)
DE	Diffraction efficiency
$DE_{i,j}$	Diffraction efficiency in region i and of order j
$DE_{i,j}^T$	Target diffraction efficiency in region i and of order j
DE_B	Diffraction efficiency with Bragg incidence
DE_D	Fraction of light diffracted by sensor
DE_N	Fraction of light passed by sensor to next element

DE_R	Fraction of light reflected by sensor
d	Grating thickness (μm)
ε_d	Dielectric relative permittivity
ε_m	Metal relative permittivity
F	Grating fill factor
FOM_1	Figure of merit for RCWA grating design points
FOM_2	Figure of merit for secondary grating design candidates
γ	Incident angle within grating boundary (degrees) (+ CCW)
γ	Grating strength parameter
γ_B	Incident Bragg angle within grating boundary (degrees) (+ CCW)
γ_m	Diffracted angle within grating boundary (degrees) (+ CW)
$I_{i,j}$	Measured diffracted order intensity
$I_{1,0}$	Reflected intensity
$I_{3,0}$	Transmitted intensity
$I_{3,1}$	Diffracted intensity
k_0	Free-space wavenumber ($rad / \mu m$)
L	Interaction length (mm)
L	Microring resonator circumference (μm)
L	Laminar flow channel length (mm)
L_{DOWN}	Input waveguide taper-down region length (μm)
L_P	Wetted perimeter (μm)

L_{SM}	Input waveguide single-mode region length (μm)
L_{UP}	Input waveguide taper-up region length (μm)
Λ	Grating period (μm)
λ	Free-space wavelength (μm)
λ_{res}	Microring resonator resonant wavelength (μm)
$\Delta\lambda_{3dB}$	Microring resonator full-width half-maximum of spectral peak (μm)
μ	Dynamic viscosity (*cP*)
NA	Numerical aperture
N_{eff}	Guided mode effective index
n	Refractive index
n_0	Refractive index within primary grating boundary
n_{0c}	Refractive index within primary grating boundary with no immobilization
n_{0x}	Refractive index within primary grating boundary with immobilization
n_1	Refractive index outside primary grating boundary
n_G	Grating average refractive index
n_g	Grating groove refractive index
n_F	Fundamental Fourier component of the grating refractive index
n_r	Grating ridge refractive index
ΔP	Laminar flow pressure drop (*psi*)
ΔP_C	Microchannel pressure drop (*psi*)
P_F	Maximum microchannel flow pressure (*psig*)

P_{in} Mach-Zehnder interferometer input power (W)

P_N Normalized output power

ΔP_O Microchannel outlet pressure drop (psi)

P_{out} Mach-Zehnder interferometer output power (W)

p_{bg} Background pixel level

$p_{x,y}$ Pixel level

ϕ Grating groove sidewall angle (degrees)

φ_0 Mach-Zehnder interferometer phase bias (degrees)

φ_m Mach-Zehnder interferometer phase shift (degrees)

Ψ Bragg dephasing rate (degrees/RIU)

Q Microring resonator quality factor

Q Combined flow rate (μL / min)

$Q_{toluene}$ Toluene syringe flow rate (μL / min)

Q_{water} Water syringe flow rate (μL / min)

ρ Etch selectivity

θ Incident angle (degrees) (+ CCW)

θ_{-1} Out-coupling grating output angle (degrees)

θ_{bias} Secondary grating designed bias angle (degrees)

$\theta_{i,j}$ Diffracted angle in region i and of order j (degrees)

θ_m Diffracted angle (degrees) (+ CW)

θ_{mx} Diffracted angle with effective index variation (degrees)

w	Grating groove width (*nm*)
w_{bias}	Grating groove etch bias (*nm*)
w_c	Corrected EBL grating groove width (*nm*)
w_{CO}	Input waveguide single-mode cutoff width (*nm*)
w_{in}	Input waveguide input region width (μm)
w_{out}	Input waveguide taper-up output width (μm)
w_{SM}	Input waveguide single-mode region width (*nm*)
ξ	Bragg dephasing parameter (degrees)

SUMMARY

Lab-on-a-chip (LOAC) devices integrate laboratory functions onto a single chip. These chips can be centimeters or even millimeters in size. One or several functions can be integrated, including fluid handling (separation and mixing) and delivery (microfluidic valves and pumps), analyte detection, and data processing. Integrated LOAC functions provide multiple advantages over their benchtop equivalents. Integrated fluid handling and delivery significantly improves times for processes such as separation and mixing [1-4]. Integrated detection improves analyte selectivity [1] and enables multiplexed analyte detection [2]. Integration of data processing enables miniaturization of the final device for increased portability. The field has rapidly expanded since the introduction of micro-total analysis systems (μTAS) by Manz in 1990 [1, 3, 4].

Application areas for LOAC devices are numerous and include medicine, food safety, environmental monitoring, homeland security, and military operations. It is commercially desirable to move towards field-deployable LOAC devices. Increased portability is crucial. Reduction of device size and elimination of external supporting equipment is necessary to increase device portability. This requires integration of multiple functions. Simultaneously, critical parameters including selectivity, robustness, and sensitivity must not be diminished, but enhanced. Optical sensors offer a robust detection platform that is inherently immune to electro-magnetic interference (EMI). These sensors are also capable of excellent sensitivities based on resonances or interference effects. Sensitivities up to 1.0×10^{-7} refractive index units (RIU) have been predicted [5]. There are several methods of optical detection, including fluorescence,

chemiluminescence, and evanescent field interaction. Fluorescence sensors detect light emitted by fluorescent label molecules when optically excited. Chemiluminescence sensors detect light emitted as the result of a chemical reaction with a chemiluminescent label molecule. Evanescent field sensors detect changes in refractive index initiated by analyte immobilization. This is achieved by detecting shifts in optical resonances, interference patterns, or other optical properties. Waveguide-based sensors with evanescent field interaction are best suited to integration, and have the advantage of not requiring chemical labels. The most promising and relevant optical platforms for integration include surface plasmon resonance (SPR), Mach-Zehnder interferometric (MZI), and microring resonator sensors.

Considering the current state-of-the-art, there is a clear need for a robust integrated optical sensing platform with micron-scale device sizes, intensity-based (as opposed to spectral-based) detection, and 2-D sensor array capability. Micron-scale device sizes enable dense sensor population. SPR and MZI sensors are limited to devices sizes of millimeters [6-10]. Microring resonator sensors meet this requirement with device sizes of tens of microns [11, 12]. Intensity-based detection enables use of integrated photodetectors to reduce device size and cost. SPR, MZI, and microring resonator sensors operate in intensity-based mode with measurement of optical attenuation [6, 8-11, 13-17]. However, attenuation measurements are susceptible to degradation of the optical signal. A robust intensity-based detection scheme should be independent of source fluctuations. A 2-D sensor array configuration enables multiplexed and redundant sensing. Such an array requires linear sequences of sensors to share source power. Ideally, sensors should split power intrinsically. This removes the need for

complex geometries and additional optical splitters. SPR and MZI sensors have not been demonstrated with this capability. Microring resonator sensors have been shown in a 2-D array configuration [18]. However, this configuration is only possible with spectral-based detection. To meet the commercial demand for field-deployable LOAC devices, the sensing platform must also exhibit high sensitivity and robust operation while minimizing cost and fabrication difficulty.

The primary objective of the research presented in this thesis is to develop a class of integrated compact silicon diffractive sensors (CSDS) based on in-plane diffraction gratings [19-24]. This class of sensors uses a silicon-on-insulator (SOI) substrate to limit costs, exploit established fabrication processes, enable integration of supporting electronics, and use the well-understood telecommunications wavelength of $\lambda = 1.55 \mu m$. Sensing is achieved by combining constant-diffraction-efficiency and highly-angularly-selective in-plane resonance-domain diffraction gratings. Detection is based on the diffraction efficiency of the highly angularly selective grating. In-plane diffraction gratings offer many advantages for integrated optical sensing. Device sizes are small with grating thicknesses of typically only a few microns. Detection of diffraction efficiencies is intensity-based. Since diffraction efficiency is a ratio, the measurement is attenuation independent. Careful design of the in-plane gratings allows intrinsic splitting of source light. Light is used by multiple sensors in a linear sequence without the addition of optical splitters. Linear sensor arrays fabricated in parallel enable compact 2-D sensor arrays for multiplexed and redundant sensing.

In this research, the design processes for the constant-diffraction-efficiency and the highly angularly selective gratings are detailed [19-24]. Gratings are simulated with

rigorous coupled-wave analysis (RCWA) for plane-wave incidence and finite-difference time-domain (FDTD) analysis for plane-wave and Gaussian incidence. Simulation results show that RCWA is a simple and efficient tool to design accurately CSDS gratings. Fabrication results are presented for the CSDS gratings [21-23]. An inductively coupled plasma (ICP) Bosch etch process enables grating fabrication to within one percent of designed values with nearly vertical sidewalls. Experimental results are presented for CSDS grating diffraction efficiencies [22, 23]. The diffraction efficiencies agree with simulation, and simulations show that further refinements can be made to achieve better agreement and remove unwanted reflections. The prototype sensor response was characterized with refractive index oils for a single sensor [23] and a sensor individually addressed in a linear sensor array [24]. The results agree well with simulation. The linear sensor array prototype demonstrates the intrinsic splitting mechanism and forms the basis of a 2-D sensor array. Finally, a toluene sensor was functionally demonstrated [24]. Toluene is chosen as an analyte because it is well-understood and relatively easy to handle. The proof-of-concept device includes a polymer immobilization layer and microfluidic delivery of toluene. Toluene concentrations as low as 100ppm are measured, corresponding to a refractive index change of $3\times10^{-4}\,RIU$.

The CSDS platform offers features that are highly desirable in developing a field-deployable LOAC device. The presented research successfully demonstrates the platform's functionality. Planned efforts to improve sensitivity, refine analyte delivery, and develop high-throughput fabrication will position the CSDS platform to meet commercial demand for portable, robust, low-cost devices with high sensitivity.

CHAPTER 1

INTRODUCTION

The first lab-on-a-chip (LOAC) was developed in 1975 at Stanford University by Terry [25]. It was a gas chromatographic sensor fabricated on a single silicon wafer by a combination of photolithography and chemical etching. Included on the silicon wafer was an injection valve and a separation column. A separate silicon wafer included a thermal conductivity detector and was clamped to the original wafer. The device was capable of separating gases on a time scale of seconds. In the words of Terry, it reduced "the size of the sensor from that of a bulky laboratory instrument to a pocket-sized package, while closely retaining the performance of a larger device." While this work represented a major breakthrough, it was largely ignored. In 1990, Manz *et al.* proposed the concept of a micro-total analysis system (μ-TAS) [3]. This paper highlighted the advantages of integrating fluid transport and handling. By decreasing the relevant geometries, hydrodynamic and diffusion theory predicted faster and more efficient separation processes and faster transport times. The μ-TAS concept was envisioned as encompassing multiple fluid-delivery components and detection schemes. This approach generated a great deal of interest, initially in increasing sensor selectivity and lifetime. In the 1990's, a significant amount of work was published on enabling technologies including integrated pumps, valves, and detection systems [1]. In 1994, Verpoorte et al. extended the concept to include both electrochemical and optical detection [2]. This approach highlighted the advantages of integration for multiplexed detection. Academic and industry involvement in the LOAC field has grown exponentially since the mid-

1990's [4]. New research is published every year exploring evolving microfluidic technologies, new application areas, and enhanced measurement techniques and detection schemes. An entire journal, *Lab-on-a-Chip* [26], is dedicated to technologies relevant to the LOAC field. New commercial devices by companies including Biacore [27], Agilent [28], Epoch Biosciences [29], and Caliper [30] enter the marketplace every year. Recent work has focused on LOAC devices for chemical and biological sensing applications.

Application areas for LOAC chemical and biological sensors include medical diagnostics, food safety, environmental quality, homeland security, and military operations. LOAC sensors have medical applications in delivering patient care and providing laboratory screening. LOAC sensors provide advantages for medical applications in minimizing device size, the amount of biological material required, and data acquisition time. Medical sensors have been developed for analytes including nucleotides [31-34], pathogens [35, 36], antibodies [37, 38], hormones [39], and cancer markers [40, 41]. Applications in food safety are important from a public health perspective. In food safety, sensors have been developed for toxins [42, 43], allergens [44, 45], and chemical contaminants [15, 46, 47]. Environmental quality applications are important for protecting public health and monitoring ecosystems at risk of contamination. Sensors for heavy metals [48, 49], pesticides [50-52], and 2,4,6-trinitrotoluene (TNT) [53, 54] have been reported. For food safety and environmental quality applications, LOAC sensors provide advantages in minimizing measurement time and enabling smaller devices for field deployment. Homeland security and military applications focus on detection of harmful weapon-based substances, including chemical and biological warfare agents [55-59]. These applications have strict requirements on

selectivity, measurement time, and device size. LOAC devices provide the advantages needed to meet these requirements. Sensors for anthrax and various chemical agents have been reported. New applications for LOAC chemical and biological sensors are continuously being discovered and investigated. The field is expanding rapidly, and it is increasingly difficult to keep track of developments and advancements in LOAC applications. Recent work has been devoted to developing robust integrated detection platforms with high sensitivity for multiplexed and redundant sensing [18, 34, 38, 60]. Fully integrated detection reduces device size and cost. This enables commercially desirable field-deployable devices.

Optical measurements are inherently immune to electromagnetic interference (EMI) and resonant optical measurements offer high sensitivity. The primary methods of optical detection include fluorescence, chemiluminescence, and evanescent-wave interaction [61, 62]. Fluorescence requires an analyte to be labeled with a fluorophore. This fluorophore emits light for detection when optically excited. Chemiluminescence requires an analyte to be labeled with a molecule which emits light as the result of a binding reaction. Both approaches require labels and are not integrated easily. Evanescent-wave sensors detect changes in refractive index initiated by analyte immobilization. Refractive index changes can be measured by detecting shifts in optical properties including resonance or interference. This class of sensors lends itself well to integration. Various integrated evanescent-wave sensors for LOAC integration have been investigated in the literature. The most promising and relevant of these technologies include surface plasmon resonance (SPR), Mach-Zehnder interferometric (MZI), and microring resonator sensors.

1.1 Surface Plasmon Resonance Sensors

Coupling to surface plasmons was first observed in 1902 by Wood [63]. Wood illuminated a metallic diffraction grating and reported narrow dark bands in the spectrum of diffracted light. He referred to these narrow bands as "anomalies." In 1941, Fano reported that these "anomalies" were due to excitation of electromagnetic surface waves [64]. Otto linked this effect to the excitation of surface plasmons in 1968 with the attenuated total reflection (ATR) method [65]. Also in 1968, Kretschmann and Raether reported an alternative ATR configuration for exciting surface plasmon modes [66]. The methods of coupling to surface plasmon modes developed by Otto, Kretschmann, and Raether initiated investigation into surface plasmons and their applications. It also enabled future work into sensing applications. In 1978, surface plasmons were first applied as a sensor in the characterization of thin films by Pockrand at International Business Machines (IBM) [67-69].

The three most common configurations for SPR sensors are illustrated in Fig. 1.1.

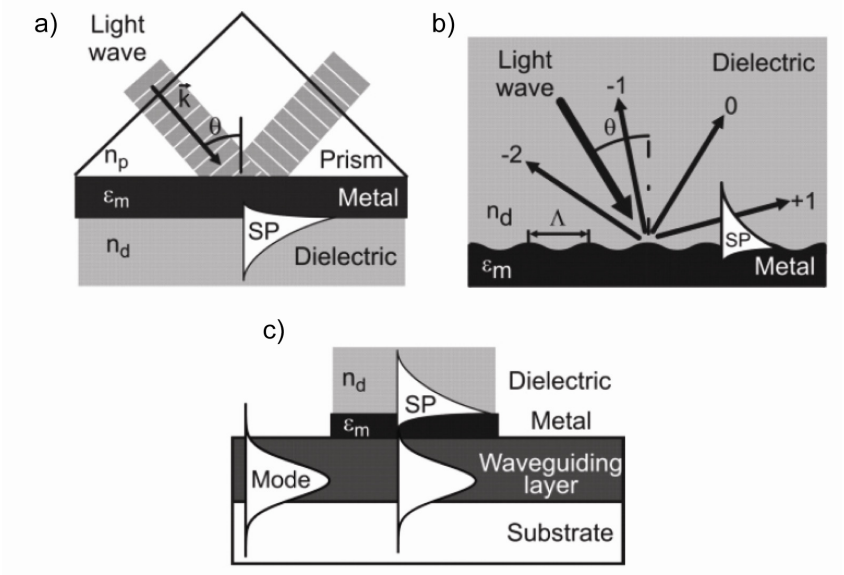

Figure 1.1: Common SPR configurations including a) prism coupler, b) grating coupler, and c) waveguide coupler. [70]

In the Kretschmann prism coupler configuration depicted in Fig. 1.1 a), light enters a high-refractive-index prism and is totally reflected at the prism-metal interface. An evanescent wave penetrates the thin metal layer to the metal-dielectric interface. Coupling to the surface plasmon mode at this interface requires matching the propagation constant. This is done by changing the incident angle at the prism. The propagation constant of the plasmonic mode at the metal-dielectric interface depends on the dielectric refractive index [66]. Sensing is achieved by functionalizing the dielectric surface and immobilizing analyte to alter the refractive index. In the grating coupler configuration shown in Fig. 1.1 b), incident light is backward-diffracted from the metal surface at various angles. It is possible for a backward-diffracted beam to couple to a plasmonic mode if the horizontal component of the propagation constant matches [71]. Functionalizing the dielectric for analyte immobilization changes the coupling condition and enables sensing. Prism couplers and grating couplers find wide use in SPR sensor applications [43, 45, 70, 72-75]. However, these configurations are not compatible with integrated sources and photodetection. The waveguide coupler configuration is the most suitable for a fully integrated sensor.

The waveguide coupler configuration, as depicted in Fig. 1.1 c), consists a planar waveguide with a section clad by a metal-dielectric interface. As light passes through the metal-dielectric clad region, it evanescently interacts with the interface. If the guided mode and the plasmonic mode have matching propagation constants, coupling can occur [13, 70, 76]. This is expressed by the condition that

$$\beta = \mathrm{Re}\{\beta_{SP}\}, \tag{1.1}$$

where β is the guided-mode propagation constant and β_{SP} is the propagation constant of the plasmonic mode. The propagation constant of a plasmonic mode at a metal-dielectric interface is expressed as

$$\beta_{SP} = \frac{2\pi}{\lambda}\sqrt{\frac{\varepsilon_d \varepsilon_m}{\varepsilon_d + \varepsilon_m}}, \tag{1.2}$$

where $\varepsilon_d = \varepsilon_{dr} + i\varepsilon_{di}$ and $\varepsilon_m = \varepsilon_{mr} + i\varepsilon_{mi}$ are the permittivities of the dielectric and metal respectively. Here, ε_{dr} and ε_{mr} are the real parts of the permittivity while ε_{di} and ε_{mi} are the imaginary parts. From the solution of Maxwell's equations for lossless metal and dielectric ($\varepsilon_{mi} = \varepsilon_{di} = 0$), plasmonic modes only occur for $\varepsilon_{mr} < -\varepsilon_{dr}$ [13]. Metals with highly negative permittivities, such as gold, silver, and aluminum, are commonly used in SPR sensors for this reason. Realistically, metals have loss and ε_{mi} is non-zero. In this case, guided modes exists for $\varepsilon_{mr} > -\varepsilon_{dr}$. These modes have extremely high attenuation and are normally not of interest. This propagation constant is only for transverse magnetic (TM) polarization. There are no solutions to Maxwell's equations for transverse electric (TE) modes [13]. Plasmonic modes are enabled by the discontinuity of the electric field at the metal-dielectric interface. From Eq. (1.2), it is observed that the coupling condition will vary with the refractive index of the dielectric layer.

Sensing in waveguide-coupled SPR sensors is achieved by modulation of the dielectric refractive index with the presence of immobilized analyte. The configuration used by Debackere fabricated in silicon-on-insulator (SOI) [14] is depicted in Fig. 1.2. As the refractive index in the sample medium region varies, the coupling condition shifts. This shift in resonant wavelength can be detected spectrally or by the attenuation of a monochromatic source (intensity-based). Waveguide-coupled SPR sensors have been

implemented with spectral-based [14, 15, 77] and intensity-based [6, 7, 14] detection. Typical sensitivities of $10^{-4}\,RIU$ are reported for interaction lengths on the order of a millimeter [6, 7]. Smaller interaction lengths on the order of tens of microns are reported as capable of producing comparable sensitivities, but this has yet to be demonstrated [14].

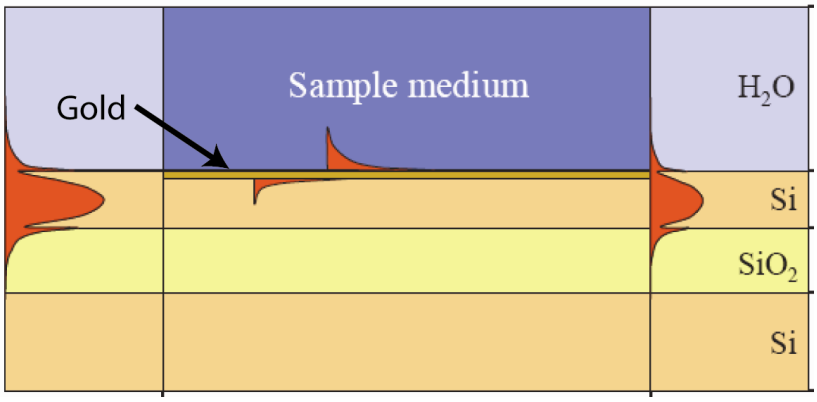

Figure 1.2: A waveguide-coupled SPR sensor fabricated in SOI. The refractive index of the sample medium region is detected by device. [14]

Linear arrays of waveguide-coupled SPR sensors for multiplexed sensing have been developed by Pang [78, 79]. Microfluidic delivery and photodetection are integrated into the reported device. Linear arrays of sensors are relatively straightforward, but development of a 2-D sensor has yet to be demonstrated. Accomplishing a 2-D array with intensity-based detection would be difficult. It would require the addition of integrated optical splitters and a complex geometry.

1.2 Mach-Zehnder Interferometric Sensors

Waveguide sensors based on Mach-Zehnder interferometry were patented in 1990 by Hartman [80]. The configuration of a typical integrated MZI sensor is illustrated in Fig. 1.3.

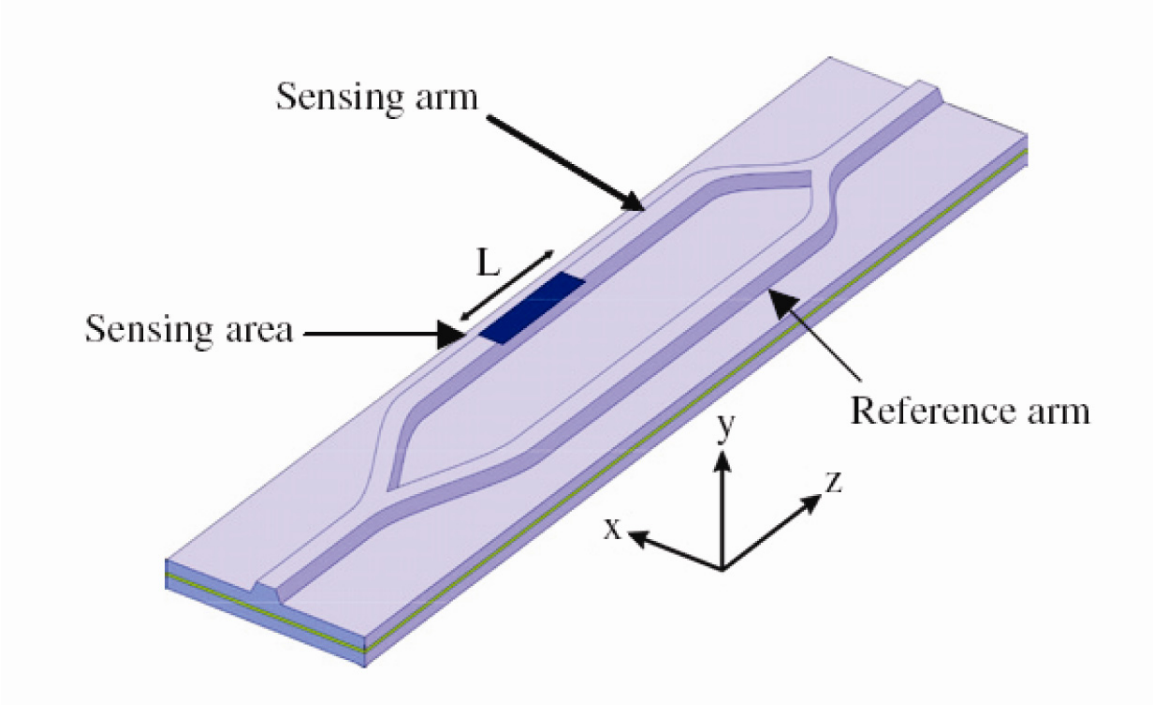

Figure 1.3: MZI sensor configuration. Analyte immobilization takes place in the sensing area of the sensing arm. [10]

Incident light is split into two beams of equal intensity. One beam enters the reference arm and the other enters the sensing arm. The beams are then recombined to produce an interference pattern. When the effective index of the sensing area changes, light traversing the sensing arm experiences an accumulated phase shift,

$$\Delta\varphi_m = \frac{2\pi}{\lambda}\Delta N_{eff} L\,, \tag{1.3}$$

where ΔN_{eff} is the change in effective index and L is the length of the sensing area [61]. Immobilized analyte in the sensing area changes the effective index. This alters the accumulated phase shift and produces a measurable change in the interference. The response can be enhanced by increasing the change in effective index or the interaction length. MZI sensors can be designed with single-mode [8-10, 16, 17, 81] or multi-mode waveguides [35, 36, 82-84].

Interference in single-mode MZI sensors produces a sinusoidal variation in output power. The normalized output power is expressed as

$$\frac{P_{out}}{P_{in}} = \frac{1}{2}\left[1 + \cos(\Delta\varphi_m + \Delta\varphi_0)\right], \tag{1.4}$$

where $\Delta\varphi_0$ is the biased phase shift when no analyte is present [61]. In 2003, Prieto reported a single-mode MZI sensor fabricated in silicon nitride with rib waveguides [8]. The paper demonstrated a refractive index sensitivity of $2\times10^{-4}\,RIU$. The predicted lower limit of index sensitivity was $7\times10^{-6}\,RIU$ with an interaction length of $L = 15mm$. Later work by Sepulveda demonstrated a sensitivity of $6\times10^{-4}\,RIU$ [10]. Sepulveda predicted a similar lower limit of index sensitivity with the same interaction length. Sepulveda also predicted that with integration of the light source and photodetection, this lower limit could be improved to $10^{-7}\,RIU$. In 2009, Lechuga extended this lower refractive index sensitivity limit to $10^{-7}\,RIU$ with $L = 15mm$ [9]. This work fabricated a linear array of MZI sensors with integrated microfluidic delivery. Bernini proposed an alternative configuration for linear arrays of MZI sensors in 2004 [81]. This work introduced a generalized MZI device with one reference arm and multiple sensing arms. These arms are attached to multi-mode interference devices at each end for light delivery and recombination. The predicted sensitivity for the proposed device is $5.5\times10^{-5}\,RIU$.

The Hartman interferometer is a multiplexable multi-mode MZI sensor patented in 1990 [80, 84]. The platform has been used to detect numerous chemical and biological species [35, 83, 85, 86]. Light is coupled by an input grating coupler to the sensing and reference arms. The light is then combined in an integrated beamsplitter/combiner and coupled out-of-plane by an output grating coupler. The interference pattern is imaged on

a charge-coupled device (CCD) for detection. The Hartman interferometer has been integrated into a linear sensor array as depicted in Fig. 1.4. One issue with this configuration is that it requires imaging a large portion of the interference pattern. Interference in multi-mode MZI devices produces a pattern of bright and dark fringes.

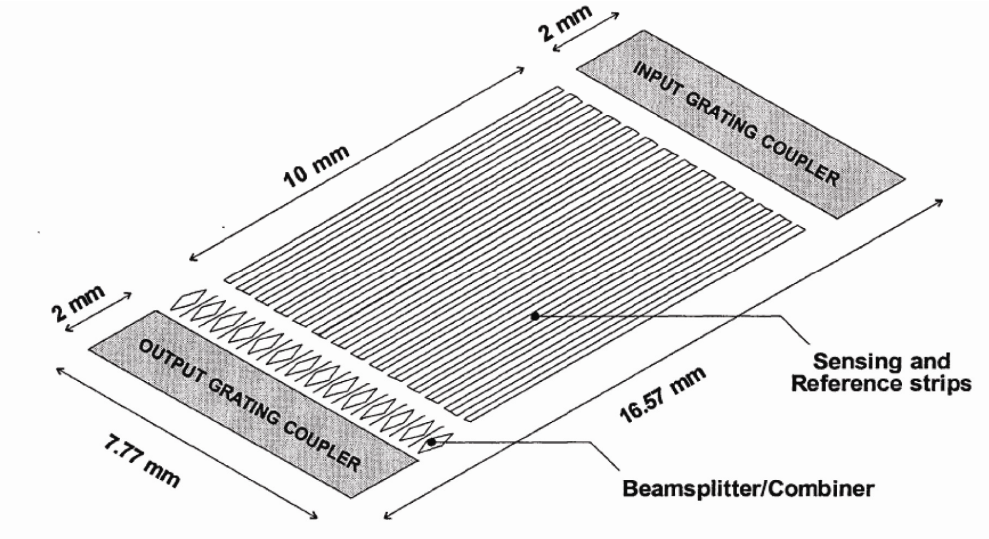

Figure 1.4: Linear array of Hartman interferometers. [86]

Detection of this interference pattern is difficult to accomplish with integrated photodetectors. For this reason, a single-mode device is better suited to integrated detection.

Integration of MZI sensors into a 2-D array would be difficult due to the large device lengths ($L > 10mm$). Such a configuration would require additional integrated optical splitters and complex geometries.

1.3 Microring Resonator Sensors

The microring resonator is an attractive platform for LOAC sensors. Microring resonator sensors typically have device sizes on the order of microns [12, 14, 38, 60, 87] or tens of microns [5, 11, 88, 89]. This is significantly smaller than the typical millimeter sizes of

SPR or MZI sensors. These devices can be designed with high quality factors for high sensitivity [11]. There are two common configurations of microring resonators shown in Fig. 1.5.

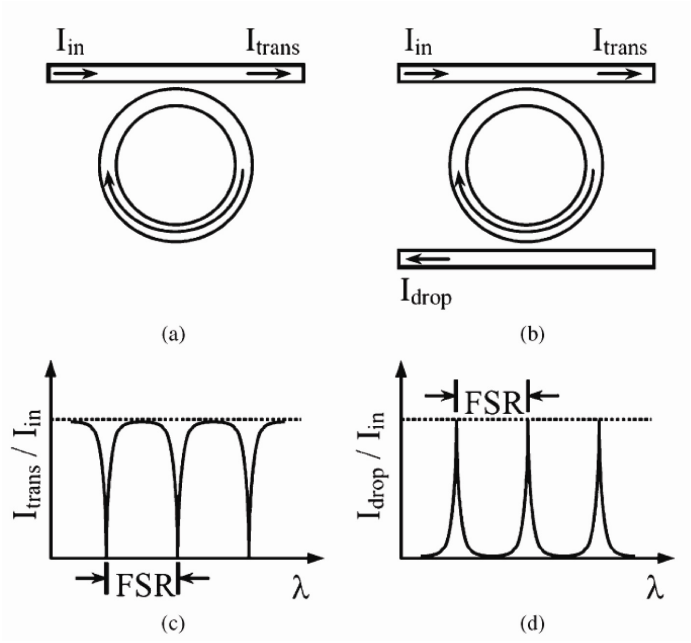

Figure 1.5: Common microring resonator sensor configurations: (a) single port and (b) double port. The transmission port output for both types has a notched response as in (c) and the drop port of the double-port configuration has the complementary response as in (d). [11]

In both configurations, broadband light from a waveguide is evanescently coupled into the ring resonator. Resonant coupling occurs when the optical path length through the microring is a multiple of 2π. This coupling occurs for resonant wavelengths

$$\lambda_{res} = \frac{L}{m} N_{eff}, \tag{1.5}$$

where L is the circumference of the microring, N_{eff} is the effective index of the guided mode, and m is an integer [12]. In the single-port configuration from Fig. 1.5 (a), the resonant wavelengths are detected as minimums in the transmission port spectrum as in Fig. 1.5 (c). In the double-port configuration from Fig. 1.5 (b), light coupled to the

microring is then evanescently coupled to another waveguide, called the drop port. Resonant wavelengths are detected as maximums in the drop port spectrum. The quality factor of a microring resonator is

$$Q = \frac{\lambda_{res}}{\Delta\lambda_{3dB}}, \tag{1.6}$$

where $\Delta\lambda_{3dB}$ is the full-width half-maximum or full-width half-minimum of the resonant spectral peak or dip, respectively [12, 14].

Microring resonator sensors achieve sensing by immobilizing analyte on the ring waveguide surface. The presence of analyte modifies the effective index of the waveguide and shifts the resonant wavelength. The spectral resolution is enhanced by narrower spectral peaks or dips. The spectral resolution is proportional to the refractive index sensitivity. Higher quality factors enable better spectral resolutions and refractive index sensitivities [11]. Theoretical microring devices can achieve extremely high quality factors. Realization of these devices is often limited by fabrication capabilities. Increasing the achievable quality factor has been the subject of recent work [11, 90, 91]. In 2006, Chao reported a microring resonator sensor with a quality factor of $Q = 5,000$ and a demonstrated refractive index sensitivity of $5\times10^{-5}\,RIU$ [11]. The device was fabricated by molding polymer on a silicon substrate. Chao predicted that with an improved quality factor of $Q = 20,000$, the device would be capable of sensing refractive index changes of $10^{-7}\,RIU$. De Vos developed a microring resonator sensor with a double-port configuration on an SOI platform [12, 14, 38, 60]. Moving to an SOI platform allowed for decreased device sizes on the order of microns as depicted in Fig. 1.6.

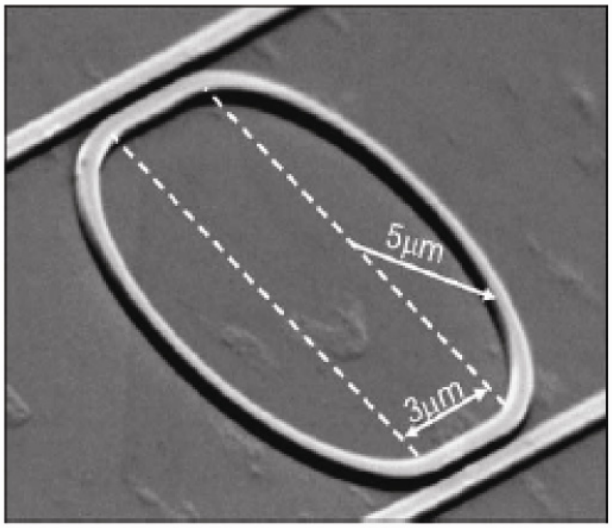

Figure 1.6: Double-port microring resonator fabricated in SOI. [12]

The SOI platform also enabled use of telecommunications wavelengths around $1.55\mu m$. The demonstrated refractive index sensitivity was $10^{-5}\,RIU$.

Arrayed configurations of microring resonator sensors have been proposed for multiplexed detection. Iqbal reported a configuration with 32 individually addressable microring resonators [5]. In the reported device, 24 microrings are exposed to analyte for detection and the remaining 8 are used for monitor purposes. Iqbal stated the system is capable of sensing refractive index changes on the order of $10^{-7}\,RIU$. Multiplexed sensing of oligonucleotides was demonstrated. Flueckiger developed a 2-D array of microring resonator sensors [18]. The platform is integrated onto a SOI substrate and uses telecommunications wavelengths near $1.55\mu m$. Analyte is delivered to columns of sensors. Waveguides deliver light to rows of sensors in sequence. This configuration is shown in Fig. 1.7.

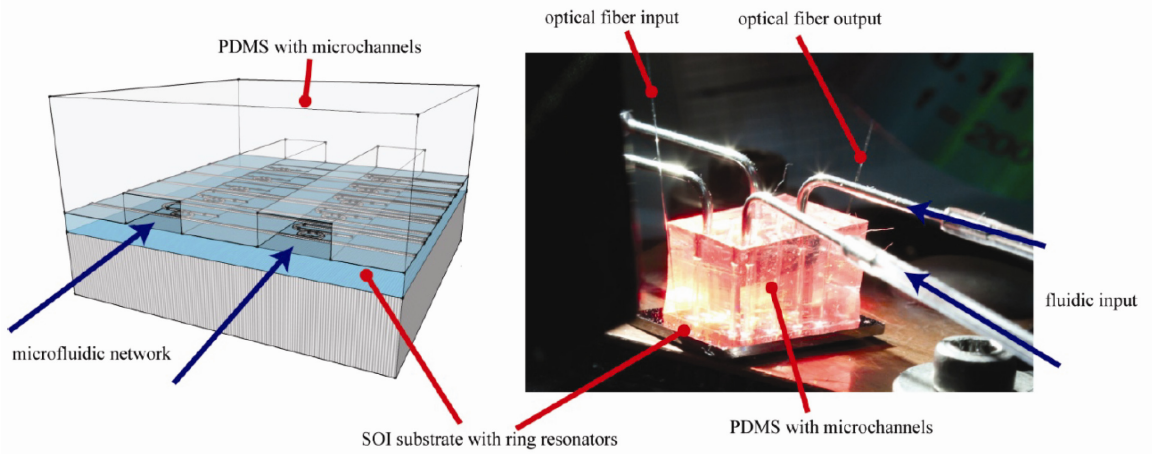

Figure 1.7: Configuration of 2-D microring resonator array for multiplexed sensing. [18]

Each waveguide couples to multiple microring resonators in sequence. Resonators in sequence are tuned to different resonant wavelengths. This enables multiple sensors to be represented in the same measurement. The refractive index sensitivity of each sensor was approximately $10^{-4}\,RIU$.

Microring resonator sensors are strong candidates for LOAC applications. Advantages include small device size, high sensitivity, silicon integrability, and 2-D array capability. The major drawback for this class of sensors is reliance on spectral-based detection. Spectral-based detection is difficult to achieve with integrated photodiodes. A method of integrated spectroscopy has been demonstrated by Xia [92]. This method uses a photonic crystal spectrometer to image the spectrum to an integrated photodiode array. Multiple sensors tuned to different wavelengths can be interrogated. This method allows for integrated photodetection and 2-D arrays, but increases device size and complexity. It is not yet clear if this technique can achieve competitive refractive index sensitivities.

Alternatively, microring resonator devices can be operated with a monochromic source and the attenuation can be measured [12, 14]. This is similar to intensity-based

operation of an SPR sensor. Linear arrays of microring resonators with individual waveguides and detectors can be implemented with intensity-based detection. Development of 2-D sensor arrays would require the addition of optical splitters and complex geometries.

1.4 Integrated Optical Platform for Field-deployable LOAC Applications

Field-deployable LOAC devices are highly commercially desirable. Field-deployable devices require small device sizes, integrated functionality (fluid delivery, detection, and data acquisition), and multiplex capability. There is a need for a robust integrated optical sensing platform with micron-scale device sizes, intensity-based detection (as opposed to spectral-based), and 2-D sensor array capability. Table 1.1 compares the ability of SPR, MZI, and microring resonator sensors to meet these requirements.

Table 1.1: Integrated optical sensing platform features with intensity-based detection for LOAC applications.

Integrated Optical Sensor Platforms				
Optical Sensor Platform	**Intensity-Based Detection**	**Micron-Scale Device Size**	**Attenuation Independence**	**Intrinsic Splitting for 2-D Sensor Arrays**
Surface Plasmon Resonance	Yes	No	No	No
Mach-Zehnder Interferometers	Yes	No	No	No
Microring Resonators	Yes	Yes	No	No

Micron-scale device sizes enable dense sensor population. SPR and MZI sensors are limited to devices sizes of millimeters. Microring resonator sensors meet this requirement with device sizes of microns or tens of microns. Intensity-based detection reduces cost and enables use of integrated sources and photodetectors. SPR, MZI, and microring resonator sensors are capable of intensity-based detection with measurement of optical attenuation. However, attenuation measurements are susceptible to degradation of the optical signal. A robust platform requires intensity-based measurement that is unaffected by source fluctuations. A 2-D sensor array configuration enables multiplexed and redundant sensing. Integration in a 2-D sensor array requires multiple sensors in a linear sequence to share source power. Ideally, this should be accomplished without the addition of optical splitters or complex geometries. SPR and MZI sensors have not been demonstrated with this capability. Microring resonator sensors have been shown in a 2-D array configuration [18]. However, this configuration is only possible with spectral-based detection. None of SPR, MZI, or microring resonators sensor meet all of these requirements. Additionally, the platform must demonstrate a high sensitivity. Microring resonator and MZI sensors have predicted sensitivities of $10^{-7}\,RIU$. Potential platforms must meet or exceed this sensitivity.

1.5 Research Objectives and Contributions

The primary objective of the presented research is to develop an integrated compact silicon diffractive sensor (CSDS) platform based on in-plane diffraction gratings for field-deployable LOAC applications. A silicon-on-insulator (SOI) substrate is used to limit costs, exploit established fabrication processes, enable integration of supporting electronics, and use the well-understood telecommunications wavelength of $1.55\mu m$.

Sensing is achieved by combining constant-diffraction-efficiency and highly angularly selective in-plane resonance-domain diffraction gratings. Detection is based on the diffraction efficiency of the highly-angularly-selective grating. In-plane diffraction gratings offer many advantages for integrated optical sensing. Device sizes are small with grating thicknesses typically only a few microns. Detection of diffraction efficiencies is intensity-based (as opposed to spectral-based). Further, the relative values of transmitted and diffracted intensity are independent of attenuation in the system. This enables robust operation. Also, the use of in-plane diffraction gratings allows for source light to be shared by linear arrays of sensors without additional optical splitters. This intrinsic splitting mechanism enables compact 2-D arrays of sensors for multiplexed and redundant sensing.

The CSDS design, optimization, fabrication, characterization, and functional demonstration presented in this thesis resulted in the following accomplishments and contributions:

1. Development of the CSDS platform by combining an in-plane constant-efficiency variable-diffraction-angle grating and an in-plane high-angular-selectivity grating [19-23].

2. Determination of grating orientation and boundary conditions to maximize response and minimize Bragg dephasing that may negatively impact measurement [19-23].

3. Development of a streamlined grating design and optimization process with rigorous coupled-wave analysis (RCWA) and validation of the process with finite-difference time-domain (FDTD) analysis with Gaussian beam incidence [19-23].

4. Optimization and sensitivity analysis of gratings designed to detect toluene [19-23].

5. Development of the grating fabrication process which yields features within 1% of target values with electron-beam lithography (EBL) and nanoscale Bosch etching [21-23].

6. Development of the experimental apparatus and methodology to characterize grating designs, characterize sensor response, and functionally demonstrate toluene detection [22-24].

7. Characterization of toluene sensor grating designs with refractive index oils to demonstrate agreement with simulation [22, 23].

8. Characterization of sensor response with refractive index oils to validate design and demonstrate agreement with simulation [23].

9. Characterization of a linear sensor array prototype to demonstrate individual addressability and 2-D array capability [24].

10. Functional demonstration of a CSDS toluene sensor with microfluidic delivery [24].

The research in this field includes efforts to refine grating designs for improved performance, increase sensitivity with integrated photodetectors and sources, develop integrated microfluidic delivery, and enable high-throughput fabrication with nano-imprint lithography (NIL). These efforts will position the class of CSDS sensors to meet the requirements for field-deployable LOAC devices.

1.6 Thesis Overview

The previously described research contributions and accomplishments are presented in detail in the following chapters.

First, the development of the CSDS platform is presented in Chapter 2. The combination of in-plane grating characteristics of diffracted angle and angular selectivity offers a sensing mechanism to realize the advantages of micron-scale device size, intensity-based detection, attenuation independence, and intrinsic splitting for linear sensor arrays. Grating orientation and boundary conditions are determined to maximize response and minimize the effects of Bragg dephasing which may negatively impact measurement. Material selections are established for toluene detection. Grating design requirements are detailed for the optimization process.

The grating design and optimization process is detailed in Chapter 3. This process uses RCWA with plane-wave incidence. Validation with FDTD analysis with Gaussian beam incidence shows that RCWA is an efficient design tool. Grating designs for a toluene sensor are optimized and sensitivity analysis is performed. FDTD sensor simulations indicate a lower detection limit of $10^{-8} RIU$ to meet the demands of commercial LOAC applications.

Sensor fabrication is presented in Chapter 4. Gratings are patterned with EBL and etched with a nano-scale Bosch process. This produces grating features that are within 1% of target values. Grating boundaries are defined with optical lithography. Microfluidic channels are fabricated for analyte delivery for a functional demonstration of toluene detection.

The experimental apparatus and measurement methodology are presented in Chapter 5. A vertical detection scheme removes the limitations of multiple external

photodetectors. Designs for input waveguides and out-coupling gratings are presented. The Labview program to record measurements in real time and the measurement methodology are detailed. Fluid delivery is achieved with syringe pumps to control the flow rate and toluene concentration.

In Chapter 6, the toluene sensor grating designs are experimentally characterized. Refractive index oils are used to establish that the grating response agrees with simulation. Undesired reflections are observed but do not impact the quality of measurement. These reflections are reproduced with 3-D FDTD simulation and refinements are presented to minimize them.

In Chapter 7, the toluene sensor response is experimentally characterized with refractive index oils. The response agrees well with simulation. A linear sensor array prototype is presented. Sensors are individually addressed with refractive index oils. This demonstrates 2-D array capability. Toluene detection is functionally demonstrated with microfluidic delivery. Concentrations as low as 100ppm are detected, corresponding to a refractive index change of $3\times10^{-4}\,RIU$.

Research results and contributions are summarized in Chapter 8. Future work to enable field-deployable LOAC sensors is described.

Appendix A provides a detailed analysis of the primary grating boundary orientation determination.

Appendix B provides simulated grating sensitivity data.

Appendix C details the grating fabrication process.

Appendix D provides concise step-by-step grating fabrication instructions.

CHAPTER 2

IN-PLANE DIFFRACTION GRATING SENSOR DESIGN

In-plane diffraction gratings offer significant advantages over conventional integrated optical sensing platforms. The requirement of millimeter-scale device size, as discussed for surface plasmon resonance [6, 7] and Mach-Zehnder interferometric [8-10] sensors in Chapter 1, is inherently satisfied. The only spatial parameters affecting grating operation and influencing overall device size are the grating thickness and period. Grating thickness is a factor in determining the device response, however increased thickness does not necessarily correlate with improved response. In-plane surface-relief gratings with constant diffraction efficiency and high angular selectivity can be designed with thicknesses of only a few microns [23]. The diffracted angle is completely independent of the grating thickness. Operating in the resonance domain, the grating period is on the order of a wavelength of light. At near-infrared telecommunications wavelengths, the grating period is not a significant contributing factor to the overall device size. Micron-scale grating thicknesses enable dense sensor population. This is critical in meeting the commercial demand for field-deployable devices capable of multiplexed and redundant sensing.

In-plane diffraction gratings also enable intensity-based detection as opposed to spectral-based detection. Measurements based on diffracted angle and angular selectivity are obtained with detection of diffraction efficiency. Incident light can be produced with a monochromatic source such as a heterogeneously integrated III-V laser [93, 94]. Detection can be achieved with integrated silicon p-i-n photodiodes [95] or germanium-

based photodiodes [96]. Spectral detection, as is typically used in surface plasmon resonance [14, 15, 77] and microring resonator sensors [11, 12, 14, 60], is more costly and difficult to integrate. Integration of the source and detectors reduces the device footprint, reduces cost, enhances device robustness, and simplifies integration with supporting electronics. These features are highly desirable in developing a field-deployable device.

Intensity-based detection with in-plane diffraction gratings is also attenuation-independent. The advantages of intensity-based detection in cost and integrability are typically balanced by the effects of optical signal degradation. External factors that can affect the optical attenuation include drift of the source amplitude, fabrication defects between the source, device, and photodiodes, degradation of materials over time, and temperature variations. The diffraction efficiency of a grating is the ratio between the optical power in the diffracted order of interest to the incident optical power. By extension, the diffraction efficiency can be measured as the ratio between the power in the order of interest to the sum of the powers in all existing orders, assuming the amount of scattered power is small. Careful design of the grating device can make the power in backward-diffracted orders negligible and minimize the number of required photodiodes. Since the measured diffraction efficiency is a ratio, it is inherently independent of source attenuation. Furthermore, the effects of variation in photodiode response are minimized by measurement of the diffraction efficiency. Such variations are likely to affect simultaneously all photodiodes and be balanced in the calculation of the measured ratio. Single-mode Mach-Zehnder interferometric sensors operate with intensity-based detection and surface plasmon resonance [6, 7, 14] and microring resonator sensors [11,

14] can be designed to operate with intensity-based detection at a specific wavelength. However, none of these sensor types inherently feature attenuation independence. An attenuation-independent measurement enabled by in-plane diffraction gratings alleviates the effects of optical signal degradation and provides the robust operation demanded in field-deployable LOAC applications.

In-plane diffraction gratings also enable compact 2-D sensor arrays. As the surrounding refractive index varies, the transmitted angle remains equal to the incident angle. Careful design leads to constant diffraction efficiencies. The transmitted order with constant angle and diffraction efficiency is a suitable incident source for subsequent grating sensors in a linear sequence. This splitting mechanism is intrinsic to the sensor and relieves the requirement for external splitting. Desired splitting ratios can be achieved via design. With several linear sensor arrays fabricated in parallel, a compact 2-D sensor array can be realized. Microring resonator sensors [5, 18] can be designed with linear sensor arrays sharing source power. However, each device in the linear array is tuned to a different wavelength, requiring broadband sources and spectral detection. Simultaneously achieving intensity-based detection and compact 2-D sensor arrays requires the addition of optical splitters and increased complexity of the device geometry. The intrinsic splitting mechanism of in-plane diffraction gratings relieves these requirements. Compact 2-D arrays of in-plane diffraction grating sensors enables multiplexed and redundant sensing for field deployable LOAC devices.

2.1 Compact Silicon Diffractive Sensor Concept

The compact silicon diffractive sensor (CSDS) platform consists of two separate in-plane diffraction gratings as depicted in Fig. 2.1. The primary grating is bounded by an

immobilization layer. Target analyte is delivered by the fluid input microchannel and immobilized. This alters the refractive index surrounding the grating. The secondary grating is designed to be highly angularly selective. It is oriented to accept light diffracted by the primary grating.

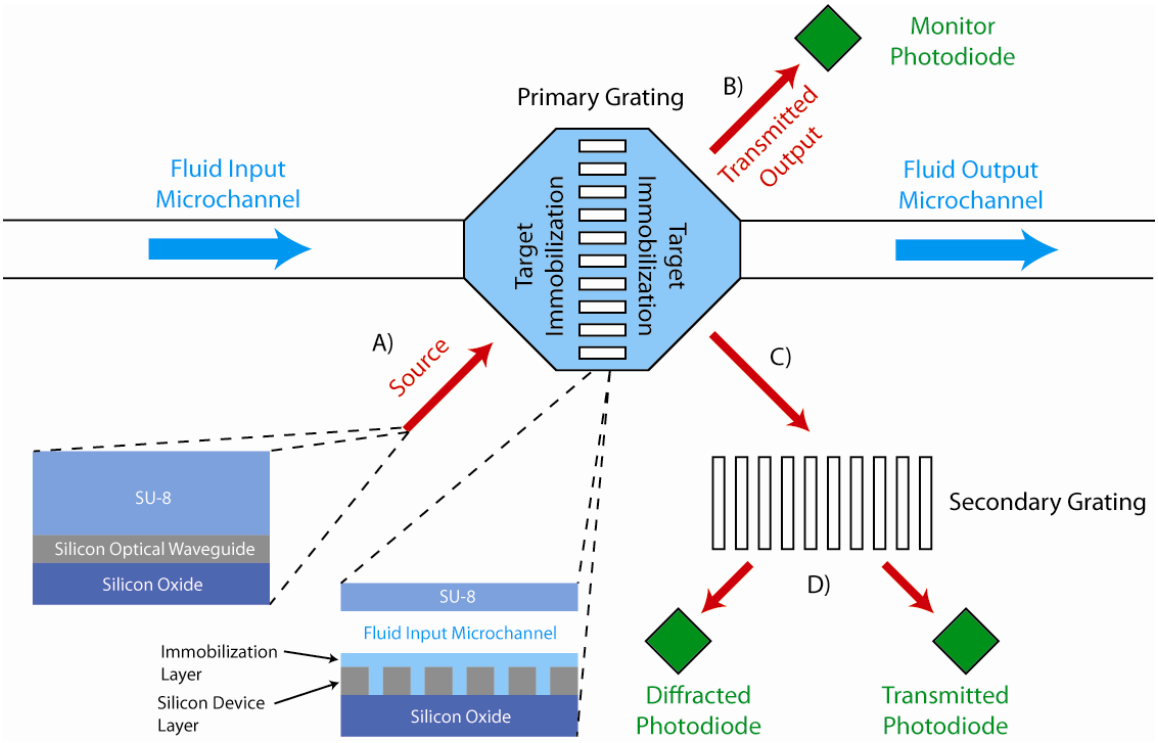

Figure 2.1: CSDS platform operation and structure. Sensor operation is as follows: A) Source light is incident upon the primary grating. B) A fixed portion of the incident light is transmitted to a monitor photodiode or an additional sensor element. C) The remaining light is diffracted toward the secondary grating at an angle dependent on the amount of immobilized analyte. D) Light incident upon the secondary grating is diffracted and transmitted in a measured ratio.

Operation of the CSDS platform proceeds as shown in Fig. 2.1:

A) Source light passes under the immobilization layer boundary and is incident upon primary grating.

B) A fixed portion of the incident light is transmitted through the primary grating toward a monitor photodiode or another CSDS sensor in a linear sensor array.

The portion of light transmitted is a constant value determined by the grating design process.

C) The remaining portion of light is diffracted by the primary grating toward the secondary grating. The diffracted angle is sensitively dependent on the refractive index surrounding the primary grating. This refractive index is determined by the amount of analyte immobilized.

D) Light incident upon the highly angularly selective secondary grating is both diffracted and transmitted. The diffraction efficiencies are determined by the incident angle and the corresponding amount of analyte immobilized. This light is detected by the appropriate photodiodes and related back to the analyte concentration.

The layer structure of the CSDS sensor is illustrated in Fig. 2.1. Source light at the telecommunications wavelength of $\lambda = 1.55 \mu m$ is confined to the fundamental slab mode of the silicon device layer on the silicon-on-insulator (SOI) wafer. The light is linearly polarized with the electric field orientation perpendicular to the layer interfaces. This is normally referred to as the TM mode for waveguides and the TE mode for gratings. This polarization is necessary to maximize forward diffraction efficiencies and minimize backward diffraction efficiencies. Gratings and photodiodes are fabricated in the silicon device layer of the SOI wafer, enabling use of mature silicon processing technologies. The microfluidic channel is fabricated in the polymer cladding layer for analyte delivery. A thin immobilization layer is deposited on the region bounding and covering the primary grating within the microfluidic channel.

Realization of a compact 2-D sensor array for LOAC applications is depicted in Fig. 2.2. Source light is incident upon several 1-D linear arrays of CSDS sensors. In each linear array, the primary grating diffraction efficiencies are 20%, 25%, 33%, and 50% for this case of four sensors for each source. An even distribution of the incident source power (20%) is provided to each secondary grating. Microfluidic channels deliver the fluid under test to each row of bounded primary gratings. Monitor photodiodes at the end of each linear CSDS array monitor the intended 20% of incident source power. This provides for a full accounting of the light in the 2-D CSDS array. This configuration enables delivery of various test fluids to multiple sensors for multiplexed and redundant sensing. Multiplexed sensing enables devices to detect multiple analytes in parallel. Redundant sensing is a safeguard to compensate for failures in individual sensors, microfluidic channels, and lines of incident source power. These features are highly commercially desirable for field-deployable devices.

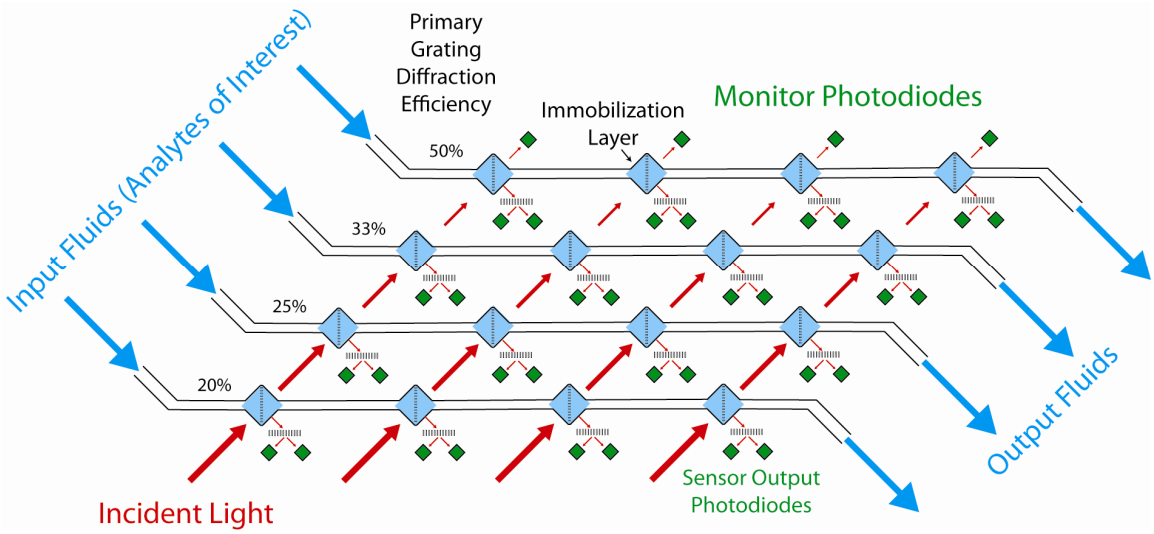

Figure 2.2: Compact 2-D CSDS sensor array. In each linear array of sensors, the primary grating diffraction efficiencies are 20%, 25%, 33%, and 50%. This provides 20% of the source power in each linear sequence to the secondary gratings. Monitor photodiodes are included at the end of each sensor sequence to increase device robustness.

2.2 CSDS Toluene Sensor Materials

For a functional demonstration, materials are chosen to establish critical properties including refractive indices and layer thicknesses. Toluene is chosen as the test analyte for the CSDS platform proof-of-concept. Toluene is well-understood and relatively easy to handle. Immobilization of toluene is achieved via free-volume filling with a $70nm$ layer of poly n-butyl-isobutyl methacrylate (PBIBMA). High-glass-transition-temperature polymers such as PBIBMA and Teflon AF have been shown to work well for toluene with this mechanism [83]. As depicted in Fig. 2.3, the analyte of interest is trapped in interstitial spaces within the immobilization layer, modifying the refractive index.

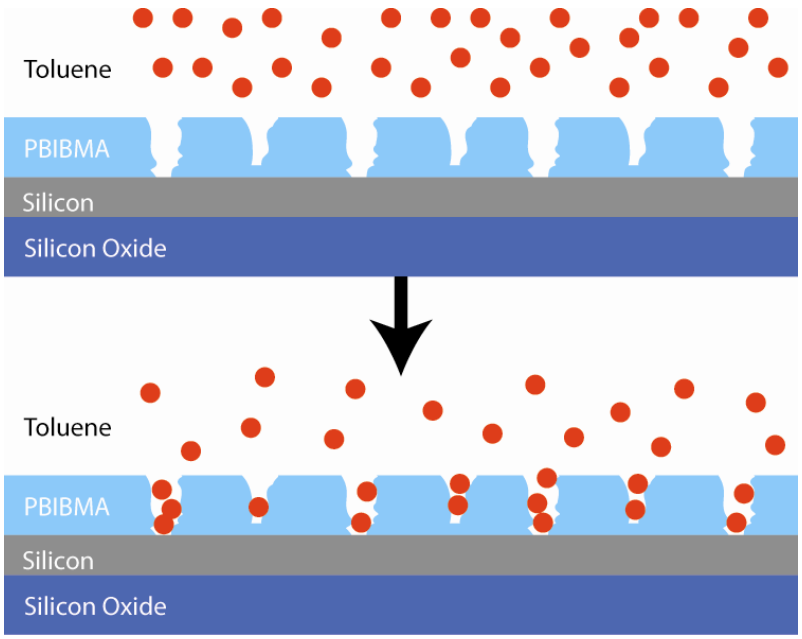

Figure 2.3: Immobilization of toluene in PBIBMA via free-volume filling. As toluene (n=1.497) is trapped in interstitial spaces within the PBIBMA (n=1.471) layer, the refractive index increases.

This immobilization technique is more efficient when the analyte being trapped is also used to dilute the polymer. For this reason, the PBIBMA used is diluted in toluene.

SU-8 from MicroChem [97] in the 2002 formulation is chosen as the polymer cladding for its mechanical and thermal stability. The 2002 formulation is specifically chosen since it is the thickest formulation filtered down to a maximum particle size of $0.2\,\mu m$. Because the CSDS gratings operate in the resonance domain, the grating grooves will be much smaller than a wavelength. This choice is necessary to ensure that the SU-8 will properly fill the grating grooves.

The indices of refraction of SU-8 and PBIBMA after deposition have been determined to be 1.581 and 1.471 respectively at $\lambda = 1.55\mu m$ using a J. A. Woolam [98] Variable Angle Spectroscopic Ellipsometer. Taking the refractive indices of silicon (3.475) and silicon oxide (1.455) [99], the single-mode cutoff thicknesses for the silicon waveguiding layer are $275nm$ and $318nm$ for regions clad by PBIBMA and SU-8 respectively. With these constraints, SOI wafers from SOITEC [100] were obtained with a $250nm$ silicon device layer and a $3\mu m$ buried oxide layer. The calculated effective indices for the slab waveguide modes [101] are 2.305 and 2.341 for PBIBMA and SU-8 cladding respectively.

For the proof-of-concept device, microchannels are patterned in sheets of DuPont [102] Teflon perfluoroalkoxy (PFA). These optically clear sheets have a thickness of $254\mu m$ and offer excellent solvent resistance. Loctite [103] 401 cyanoacrylate is used to bond the microchannel assembly. It is capable of bonding to a variety of thermoplastics, including Teflon PFA, with the 770 surface primer. It also features resistance to moisture and non-polar solvents such as toluene.

2.3 Bounded In-plane Primary Grating

The function of the primary grating is to accept light at a known incident angle and to diffract it at a given diffracted angle with a specified diffraction efficiency. As shown in Fig. 2.1, the primary grating is in a region bounded by the extent of the microchannel. The effective index of the silicon waveguiding layer under and outside the microchannel will differ. As the interior effective index varies with the presence of immobilized analyte the diffracted output angle also changes. It is desirable to maximize this variation in diffracted output angle. The diffraction efficiency should remain constant, even in the presence of immobilized analyte. This allows for a constant ratio of diffracted light and transmitted light. This is important if the transmitted light is to be used in another sensor or detected for monitoring purposes.

The primary grating configuration with boundaries is depicted in Fig. 2.4. The incident and diffracted angles, θ and θ_m respectively, are both chosen to be $45°$. This orientates sensor elements at right angles, and simplifies fabrication and layout of a 2-dimensional array as in Fig. 2.2. A critical question is the orientation of the boundaries. To fulfill the Bragg condition and enable high diffraction efficiencies in the forward-diffracted orders, the boundary orientation angles, α and α_m, should be equal. Three specific cases are examined: parallel surfaces that are parallel to the grating fringes ($\alpha = \alpha_m = 0$), parallel surfaces that are normal to the grating fringes ($\alpha = \alpha_m = 90°$), and normal surfaces that are oriented $45°$ to the grating fringes ($\alpha = \alpha_m = 45°$).

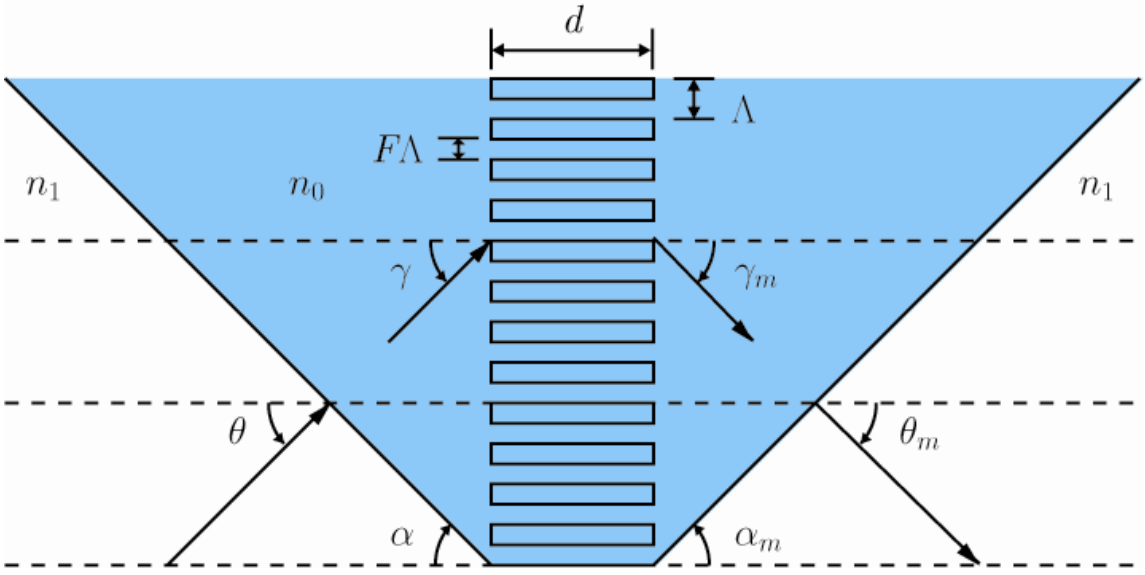

Figure 2.4: Bounded primary grating configuration. Grating parameters represented include the thickness, d, period, Λ, and fill factor, F. The incident and diffracted angles within the bounded area are γ and γ_m respectively. Outside the bounded area, these angles are θ and θ_m. The boundary orientation angles on the incident and diffracted sides are α and α_m. The refractive index within the boundary is n_0 and the surrounding refractive index is n_1.

The grating period, Λ, necessary for the desired incident and diffracted angles is determined to be

$$\Lambda = \frac{\lambda}{n_0}\left(\sin\left\{\cos^{-1}\left[\frac{n_1}{n_0}\cos(\theta+\alpha)\right]-\alpha\right\}+\sin\left\{\cos^{-1}\left[\frac{n_1}{n_0}\cos(\theta_m+\alpha_m)\right]-\alpha_m\right\}\right)^{-1} \quad (2.1)$$

The output angle variation, $\Delta\theta_m = \theta_{mx} - \theta_m$, is determined for refractive index changes within the bounded region. The new refractive index is defined as $n_{0x} = n_0 + \Delta n_0$ to reflect analyte immobilization. The new diffracted angle is determined to be

$$\theta_{mx} = \cos^{-1}\left\{\frac{n_{0x}}{n_1}\cos\left[\sin^{-1}\left(\frac{n_0}{n_{0x}}\Gamma-\sin\left\{\cos^{-1}\left[\frac{n_1}{n_{0x}}\cos(\theta+\alpha)\right]-\alpha\right\}\right)+\alpha_m\right]\right\}-\alpha_m, \quad (2.2)$$

where Γ is

$$\Gamma = \sin\left\{\cos^{-1}\left[\frac{n_1}{n_0}\cos\left(\theta+\alpha\right)\right]-\alpha\right\}+\sin\left\{\cos^{-1}\left[\frac{n_1}{n_0}\cos\left(\theta_m+\alpha_m\right)\right]-\alpha_m\right\}. \qquad (2.3)$$

The derivation of these relationships is detailed in Appendix A.

The output angle variation, $\Delta\theta_m$, is plotted against the effective index within the immobilization region, n_{0x}, in Fig. 2.5 for the three cases of boundary orientation with $\theta = \theta_m = 45°$, $n_0 = 2.305$ (PBIBMA), and $n_1 = 2.341$ (SU-8).

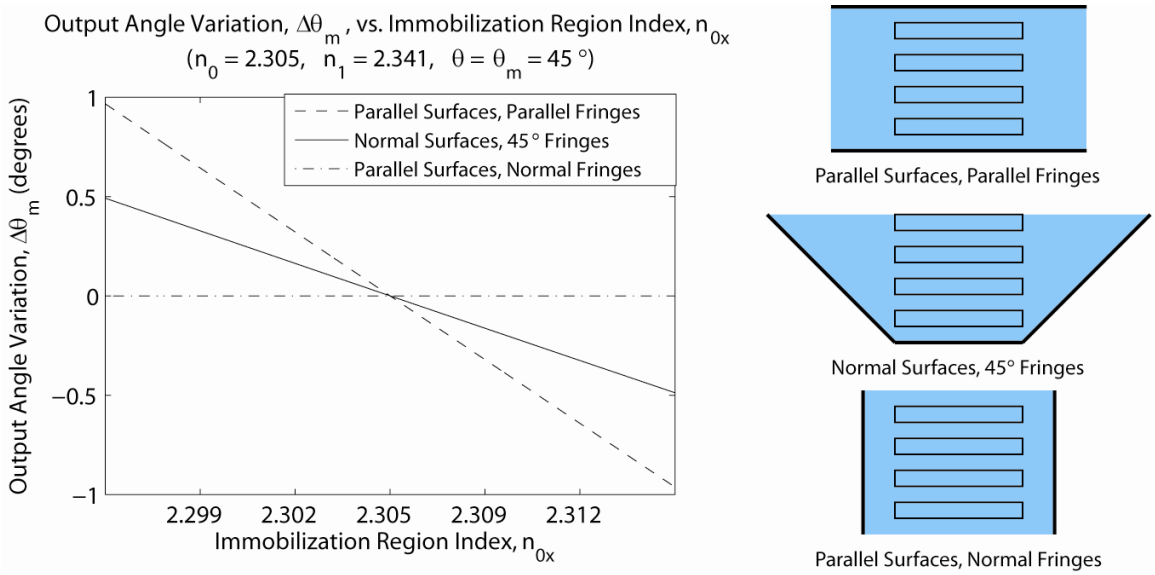

Figure 2.5: Output angle variation, $\Delta\theta_m$, plotted against the effective index within the immobilization region, n_{0x}, for the three cases of boundary orientation with $\theta = \theta_m = 45°$, $n_0 = 2.305$ (PBIBMA), and $n_1 = 2.341$ (SU-8).

For the case of parallel surfaces that are normal to the grating fringes ($\alpha = \alpha_m = 90°$), the output angle remains constant. Refraction at the boundaries opposes changes in the output angle within the immobilization region. With normal surfaces that are orientated $45°$ to the grating fringes ($\alpha = \alpha_m = 45°$), the output angle varies at a rate of

$0.049°/mRIU$. The case with parallel surfaces that are parallel to the grating fringes, ($\alpha = \alpha_m = 0°$), produces the greatest output angle variation of $0.096°/mRIU$. As the boundary angles decrease, refractive effects at the boundaries increase the output angle variation.

The effects of boundary orientation on diffraction efficiency are also examined. As the internal effective index, n_0, varies, the internal incident angle, γ, can also vary and deviate from the Bragg condition. To determine how boundary orientation affects diffraction efficiency, the Bragg dephasing parameter is examined. When the design is such that $\alpha = \alpha_m$, $\theta = \theta_m$, $\gamma = \gamma_m$, and the grating period, Λ, initially is given by the Bragg condition, then the Bragg dephasing parameter is $\xi = (\gamma - \gamma_B)(\pi d / \Lambda)$. Here, γ_B is the interior incident angle that fulfills the Bragg condition for a given n_0 and d is the grating thickness. Ideally, the rate of Bragg dephasing should be minimized. The rate of Bragg dephasing is determined to be

$$\Psi = \frac{\pi d}{\Lambda}\frac{\partial}{\partial n_0}(\gamma) + \frac{\pi d}{\Lambda}\frac{\frac{n_{0c}}{n_0^2}\sin(\gamma_c - \alpha)}{\left\{1 - \left[\frac{n_{0c}}{n_0}\sin(\gamma_c - \alpha)\right]^2\right\}^{1/2}}, \tag{2.4}$$

where

$$\gamma_c = \cos^{-1}\left[\frac{n_1}{n_{0c}}\cos(\theta + \alpha)\right] - \alpha \tag{2.5}$$

and

$$\frac{\partial}{\partial n_0}(\gamma) = \frac{-\frac{n_1}{n_0^2}\cos(\theta+\alpha)}{\left\{1-\left[\frac{n_1}{n_0}\cos(\theta+\alpha)\right]^2\right\}^{1/2}}. \tag{2.6}$$

In these relationships, γ is the actual interior incident angle and n_{0c} is the refractive index of the immobilization layer with no analyte present. For the PBIBMA cladding unperturbed by analyte presence, $n_{0c} = 2.305$. The derivation of these relationships is included in Appendix A.

The rate of Bragg dephasing, Ψ, is plotted against the effective index within the immobilization region, n_{0x}, in Fig. 2.6 for the three cases of boundary orientation with $\theta = \theta_m = 45°$, $n_0 = 2.305$ (PBIBMA), and $n_1 = 2.341$ (SU-8).

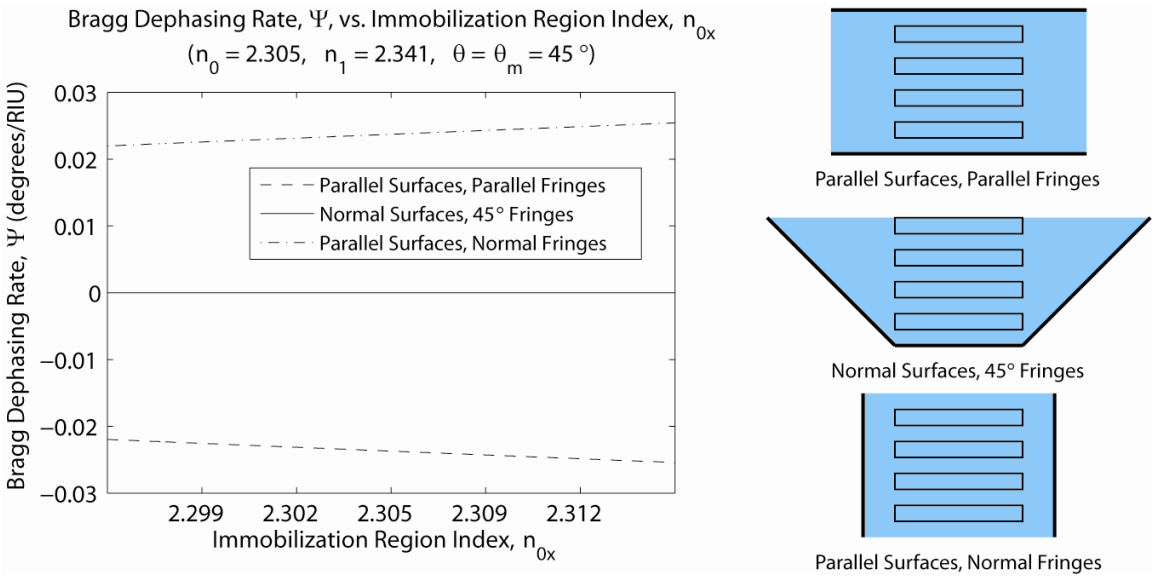

Figure 2.6: Rate of Bragg dephasing, Ψ, plotted against the effective index within the immobilization region, n_{0x}, for the three cases of boundary orientation with $\theta = \theta_m = 45°$, $n_0 = 2.305$ (PBIBMA), and $n_1 = 2.341$ (SU-8).

In both cases with parallel surfaces that are parallel and normal to the grating fringes, the magnitude of the Bragg dephasing rate is between $0.02°/RIU$ and $0.03°/RIU$. There is zero dephasing for the case with normal surfaces that are oriented $45°$ to the grating fringes. This occurs since incident light is normal to the boundaries and there is no refraction. It is for this reason that the case with normal surfaces that are oriented $45°$ to the grating fringes is chosen for the primary grating. The output angle variation is less than that for the case with parallel surfaces that are parallel to the grating fringes, but the loss in response can compensated with careful design of the secondary grating. Deterioration of diffraction efficiency with effective index variation cannot be easily compensated.

Selection of normal surfaces with $\alpha = \alpha_m = 45°$ yields simplified expressions for the grating period from Eq. (2.1),

$$\Lambda = \frac{\lambda}{n_0\sqrt{2}}, \tag{2.7}$$

and output angle variation from Eq.(2.2),

$$\theta_{mx} = \cos^{-1}\left(\frac{n_{0x}}{n_1}\cos\left\{\sin^{-1}\left[\sqrt{2}\left(\frac{n_0}{n_{0x}} - \frac{1}{2}\right)\right] + \frac{\pi}{4}\right\}\right) - \frac{\pi}{4}. \tag{2.8}$$

To determine grating thickness and fill factor, Kogelnik two-wave coupled-wave (TWCW) analysis [104] is employed. TCWC is not useful for explicitly determining grating thicknesses and fill factors due to lack of backward-diffracted orders in the analysis. Backward-diffracted orders can be significant due to the high index contrast between the grating grooves and ridges. This analysis can provide an overview of where

to begin searching with a more accurate simulation. In two-wave first-order coupled-wave analysis, the diffraction efficiency is expressed as

$$DE = \sin^2\left(\frac{\pi n_F d}{\lambda \cos\theta}\right), \tag{2.9}$$

where d is the grating thickness and θ is the incident angle within the grating region. As the grating thickness increases, this diffraction will vary more quickly with changes in the effective index. To minimize variations in diffraction efficiency, the grating thickness should be as small as possible. The fundamental Fourier component of the grating refractive index, n_F, is defined as

$$n_F = \frac{2}{\pi}\left(n_r - n_g\right)\sin\left(\pi F\right), \tag{2.10}$$

where F is the grating fill factor, the grating ridge refractive index is $n_r = 2.305$, and the grating groove refractive index is $n_g = 1.471$ (PBIBMA). To determine the incident angle within the grating region, θ, the effective index within the grating region, n_G, must first be obtained. This is done by solving the transcendental equation given by Rytov [105],

$$\sqrt{n_G^2 - n_g^2}\,\tanh\left[\left(\frac{\Lambda}{\lambda}\right)\pi\left(1-F\right)\sqrt{n_G^2 - n_g^2}\right] = \sqrt{n_r^2 - n_G^2}\,\tan\left[\left(\frac{\Lambda}{\lambda}\right)\pi F\sqrt{n_r^2 - n_G^2}\right]. \tag{2.11}$$

The incident angle within the grating region is then determined with Snell's law and the exterior incident angle of $45°$. The calculated diffraction efficiencies agree reasonably well with exact solutions calculated with rigorous coupled-wave analysis (RCWA) as depicted in Fig. 2.7. From TWCW analysis it is observed that suitable grating thicknesses less than $2\mu m$ can be found for a full range of desired diffraction efficiencies. Also, some insight is gained into appropriate fill factors by comparing the effective index within the grating region to that of the surrounding region. Higher reflection is expected

with a greater difference in effective index. This indicates that fill factor values greater than 0.5 would be appropriate (however, in this research a broader range of fill factor values are considered for thoroughness). With these insights, the grating thicknesses and fill factors are explicitly determined via simulation to obtain the desired diffraction efficiencies and fabrication and alignment tolerances.

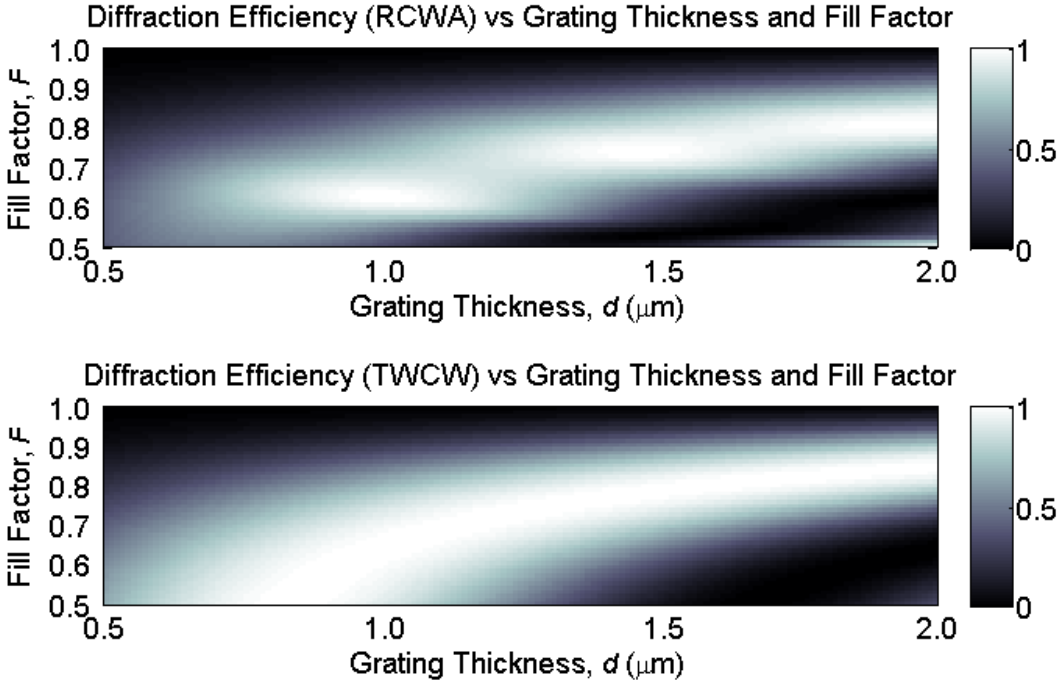

Figure 2.7: Plot of diffraction efficiency vs. grating thickness and fill factor for the exact formulation with rigorous coupled-wave analysis and the Kogelnik two-wave coupled-wave analysis.

2.4 Angularly Selective In-plane Secondary Grating

The function of the secondary grating is to accept light output from the primary grating and diffract it for detection. As the incident angle at the secondary grating varies, the diffraction efficiency should significantly change. The detected diffraction efficiency is related to an immobilized analyte concentration. Overall sensor sensitivity depends on the

angular selectivity of the secondary grating. Operation should be in a region of linear, monotonic change in diffraction efficiency. This allows for differentiation between positive and negative changes in incident angle and thus positive and negative changes in the effective index surrounding the primary grating. The diffraction efficiency response when operating near a Bragg condition is typically broad and symmetric with respect to incident angle. To meet these criteria, the secondary grating needs to operate at a controlled angular shift from the Bragg condition.

The secondary grating configuration is shown in Fig. 2.8. For layout considerations similar to those for the primary grating, the incident and diffracted angles are chosen as $\theta = \theta_m = 45°$. Unlike the primary grating, there are no boundaries as the entire area is clad by the same material (SU-8 in this case). Determination of the grating period must be done via numerical simulation since the Bragg condition is not fulfilled. This process is detailed in Chapter 3.2.

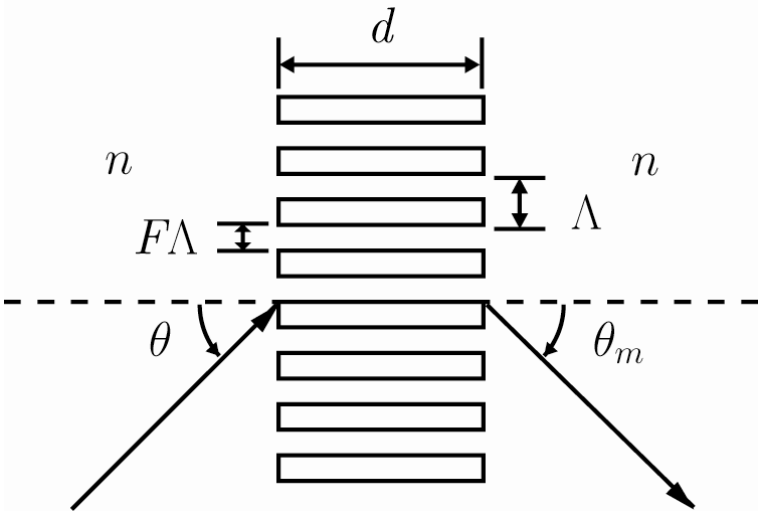

Figure 2.8: Secondary grating configuration. Grating parameters represented include the thickness, d, period, Λ, and fill factor, F. The incident and diffracted angles are θ and θ_m respectively, and the surrounding refractive index is n.

The forward diffraction equation for the secondary grating takes the form

$$n\sin\theta - n\sin(-\theta_m) = \lambda/\Lambda\,. \tag{2.12}$$

As the incident angle varies, so do the transmitted and diffracted angles. The transmitted angle will be the same as the incident angle, but an expression is needed for variation of output angle to ensure photodetector alignment. Replacing θ with $\theta+\Delta\theta$ and θ_m with $\theta_m+\Delta\theta_m$ in the forward diffraction equation, the variation in diffracted angle is found to be

$$\Delta\theta_m = \sin^{-1}\left[\frac{\lambda}{n\Lambda} - \sin\left(\theta+\Delta\theta\right)\right] - \theta_m\,. \tag{2.13}$$

Determination of the grating thickness and fill factor is also relegated to numerical simulation. This is necessary to develop the desired behavior (operation at a controlled angular shift from a Bragg condition giving high sensitivity with a linear, monotonic response) with readily achievable fabrication and alignment tolerances. The Bragg dephasing parameter, $\xi = \left|\theta-\theta_b\right|\pi d/\Lambda$, is examined to gain insight into the angular selectivity. As with the primary grating in Eq. (2.4), the rate of dephasing is proportional to the grating thickness. For high angular sensitivity, the rate of dephasing should be maximized. Consequently, designs should have large grating thicknesses. The ratio of off-Bragg-angle to on-Bragg-angle diffraction efficiency is

$$\frac{DE}{DE_B} = \frac{\gamma^2}{\sin^2\gamma}\frac{\sin^2\left[\left(\gamma^2+\xi^2\right)^{1/2}\right]}{\left(\gamma^2+\xi^2\right)}, \tag{2.14}$$

where $\gamma = \left(\pi n_F d\right)/\left(\lambda\cos\theta\right)$ is the grating strength parameter. The grating thickness is also proportional to the grating strength parameter. Caution must be exercised in opting for larger thicknesses. Sensitivities to fabrication tolerances will generally increase with

the grating strength parameter. Additionally, scattering can become an issue. A balance must be struck in the design process to attain the desired angular selectivity while maintaining readily achievable fabrication tolerances and avoiding scattering. As the fill factor approaches high values near unity and low values near zero, the fundamental Fourier component of the grating refractive index, n_F, in Eq. (2.10) will approach zero. Subsequently, the grating strength parameter, γ, will also approach zero. In this limit, the ratio from Eq. (2.14) becomes

$$\lim_{\gamma \to 0} \frac{DE}{DE_B} = \frac{\sin^2 \xi}{\xi^2}, \tag{2.15}$$

which decreases rapidly as the Bragg dephasing increases, indicating a strong angular selectivity. As discussed for the primary grating, higher fill factor values would be preferable to decrease the index contrast between the grating and the surrounding region to avoid unwanted reflection. This suggests that in addition to increasing the thickness to enhance angular selectivity, higher fill factor values should be considered.

CHAPTER 3

DEVICE DESIGN AND OPTIMIZATION

Application areas for integrated optical sensors may require distinct designs to account for differences in material properties or sensor geometries. For a sensing platform to be suitable for multiple field-deployable LOAC applications, its design process must be efficient and accurate. Rigorous coupled-wave analysis (RCWA) has been used extensively in grating design for this purpose [19-23, 106-115]. Since RCWA is an exact analysis, the accuracy of results is limited primarily to the numerical precision, number of refractive index harmonics, and number of diffracted orders used in calculation. RCWA is also simple to implement in any modern programming language and does not require large amounts of processing time to complete. This is particularly valuable in evaluating fabrication and alignment tolerances for multiple design candidates. Evaluation of one million data points takes approximately four hours with a typical personal computer. However, RCWA is only applicable to plane wave incidence unless simulations with multiple incident wavevectors are performed to simulate Gaussian incidence [116]. In most cases, plane-wave analysis proves sufficiently accurate and its simpler implementation proves advantageous to efficient grating design. The RCWA calculations in this research are performed with the FORTRAN programming language to maximize computational efficiency.

Realistically, the designed gratings will have Gaussian beams incident upon them. The suitability of a plane-wave analysis in the design process must be quantified.

Validation of plane-wave analysis with RCWA is performed with 2-D finite-difference time-domain (FDTD) simulations [21-23]. Both plane-wave and Gaussian beam incidence are simulated to make a definitive comparison. The FDTD simulations completed here used the MEEP engine [117-119] under the Ubuntu operating system. All FDTD simulations are performed with a resolution of approximately $\lambda/21$ for acceptable precision and manageable computation time. FDTD simulations with Gaussian beam incidence have a beam waist of $2\mu m$. The simulation space boundaries parallel to the grating fringes are periodic for plane-wave incidence and all remaining boundaries are perfectly matched layers (PML) implemented within the MEEP engine. Here, the design process with RCWA is outlined and results are presented for optimized grating profiles and grating sensitivities. Comparisons of RCWA to FDTD for plane-wave and Gaussian beams are presented.

3.1 Primary Grating

Optimization of the primary grating begins with determination of the necessary grating period to satisfy the Bragg condition. Solving Eq. (2.7) with $n_0 = 2.305$ and $\lambda = 1.55\mu m$ gives a grating period of $\Lambda = 0.475\mu m$. With a typical change in effective index of 0.01 in the cladding [83, 120], a corresponding variation in output angle of $\Delta\theta_m = 0.4971°$ is determined from Eq. (2.8). Next, a series of RCWA simulations are performed for a broad range of grating thicknesses and fill factors. Since grating sensitivity generally increases with thickness, only thickness values similar in magnitude to the wavelength of interest are simulated. This is to obtain a constant diffraction efficiency and wide fabrication tolerances as discussed in Chapter 2.3. Thickness values between $0.5\mu m$ and

$2.0\mu m$ with a step size of $1nm$ and fill factor values between 0.001 and 0.999 with a step size of 0.001 are simulated. The efficiency of RCWA allows for a computation time of only about six hours. By starting with a small step size reflecting available fabrication capabilities, steps are saved in performing more focused simulations for individual grating candidates. For a more general design, a larger initial step size can be used and subsequent simulations can have smaller step sizes within specific regions of interest. The results of this simulation are applicable for all target diffraction efficiencies. Primary gratings are designed here with diffraction efficiencies of 20%, 25%, 33%, and 50% for inclusion in a compact 2-D CSDS array.

To determine the best candidates for specific target diffraction efficiencies, a figure-of-merit is evaluated for each data point. This figure-of-merit is defined as

$$FOM_1 = \log\left[\left(\left|\frac{DE_{1,0}^T - DE_{1,0}}{DE_{1,0}^T + 1}\right| + \left|\frac{DE_{1,1}^T - DE_{1,1}}{DE_{1,1}^T + 1}\right| + \left|\frac{DE_{3,0}^T - DE_{3,0}}{DE_{3,0}^T + 1}\right| + \left|\frac{DE_{3,1}^T - DE_{3,1}}{DE_{3,1}^T + 1}\right|\right)^{-1}\right], \quad (3.1)$$

where the DE terms correspond to the diffraction efficiencies illustrated in Fig. 3.1 and the superscript T denotes a target diffraction efficiency.

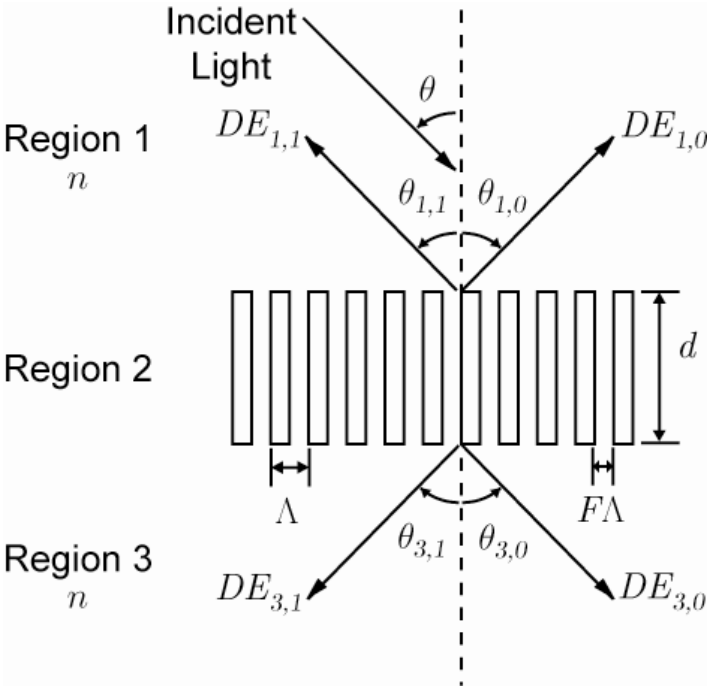

Figure 3.1: Configuration for RCWA simulation. The diffracted and transmitted orders are $DE_{3,1}$ and $DE_{3,0}$, while the backward-diffracted and reflected orders are $DE_{1,1}$ and $DE_{1,0}$.

Generally, the backward-diffracted orders are minimized with target values of zero. For example, a grating designed to diffract 25% of the incident light will have target parameters $DE_{1,0}^{T} = 0$, $DE_{1,1}^{T} = 0$, $DE_{3,0}^{T} = 0.75$, and $DE_{3,1}^{T} = 0.25$. Potential design candidates can be identified by pinpointing maxima of the figure-of-merit. A color map highlighting regions with potential candidates for a target diffraction efficiency of 25% is presented in Fig. 3.2.

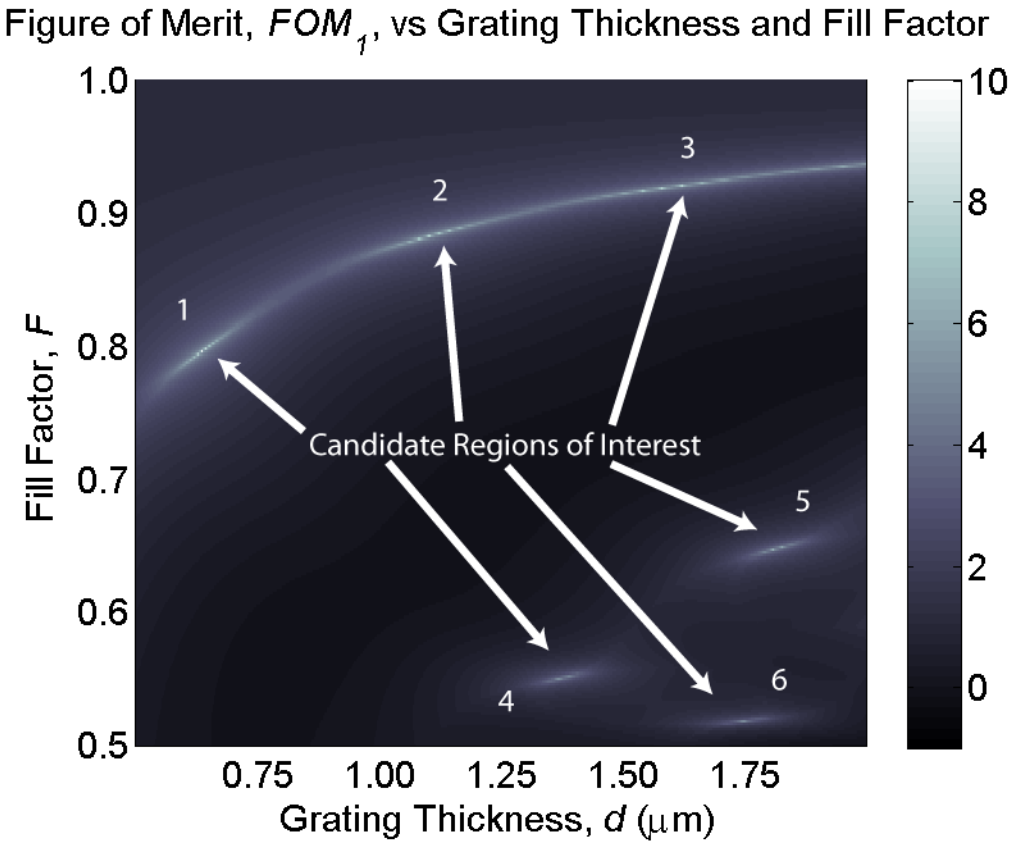

Figure 3.2: A plot of figure-of-merit vs. grating thickness and fill factor for a primary grating target diffraction efficiency of 25%. Regions with potential design candidates are highlighted.

Color maps for the other target diffraction efficiencies exhibit similar behaviors with the same number of highlighted regions of interest. These can be found in Appendix B. The identified candidates listed in Table 3.1 must be evaluated to determine which will be chosen. Candidate sensitivities to variations in thickness and fill factor are examined for minimal values. Since the initial simulations were run with a sufficiently small step size, these data are readily available. These sensitivities are shown in Figs. 3.3 and 3.4 for the candidates with a 25% target diffraction efficiency.

Table 3.1: Primary grating design candidates identified with RCWA. Chosen candidates are in bold face.

Primary Grating Preliminary Candidates ($\lambda = 1.55\mu m,\ \Lambda = 0.475\mu m,\ n = n_r = 2.305,\ n_g = 1.471$)				
Diffraction Efficiency	**Candidate**	**Thickness** $d\ (\mu m)$	**Fill Factor** F	**Figure of Merit** FOM_1
20%	**1**	**0.615**	**0.811**	**8.318**
	2	1.084	0.892	9.390
	3	1.565	0.925	8.901
	4	1.393	0.548	5.687
	5	1.831	0.643	6.837
	6	1.716	0.519	4.966
25%	**1**	**0.636**	**0.794**	**9.461**
	2	1.101	0.880	9.750
	3	1.577	0.916	9.186
	4	1.376	0.551	5.514
	5	1.813	0.647	6.966
	6	1.745	0.518	5.122
33%	**1**	**0.668**	**0.770**	**8.679**
	2	1.142	0.864	10.538
	3	1.604	0.903	8.761
	4	1.342	0.555	5.434
	5	1.774	0.652	6.656
	6	1.778	0.516	6.656
50%	**1**	**0.725**	**0.731**	**8.170**
	2	1.191	0.834	9.236
	3	1.668	0.881	8.394
	4	1.278	0.563	5.407
	5	1.721	0.664	6.910
	6	1.847	0.513	4.662
Simulation Space		$0.5 - 2.0\mu m$	$0.001 - 0.999$	

In these sensitivity plots, the diffraction efficiencies are plotted for thickness variations of $\pm 50nm$ and fill factor variations of $\pm 5\%$. For all candidates, sensitivity to grating thickness is small, but is slightly superior in candidates one, two, and three.

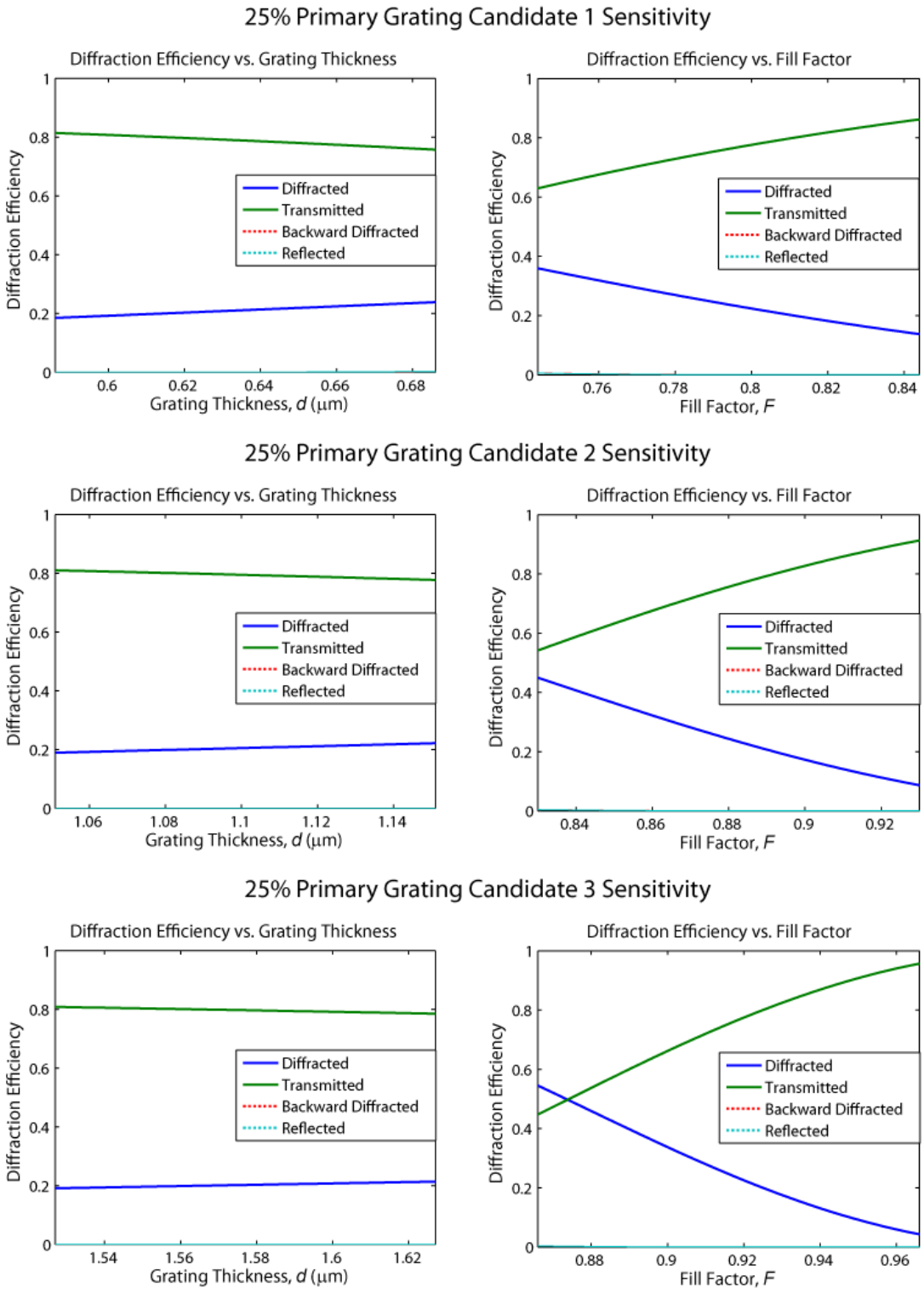

Figure 3.3: RCWA thickness and fill factor sensitivities for primary grating candidates 1, 2, and 3 with target diffraction efficiencies of 25%.

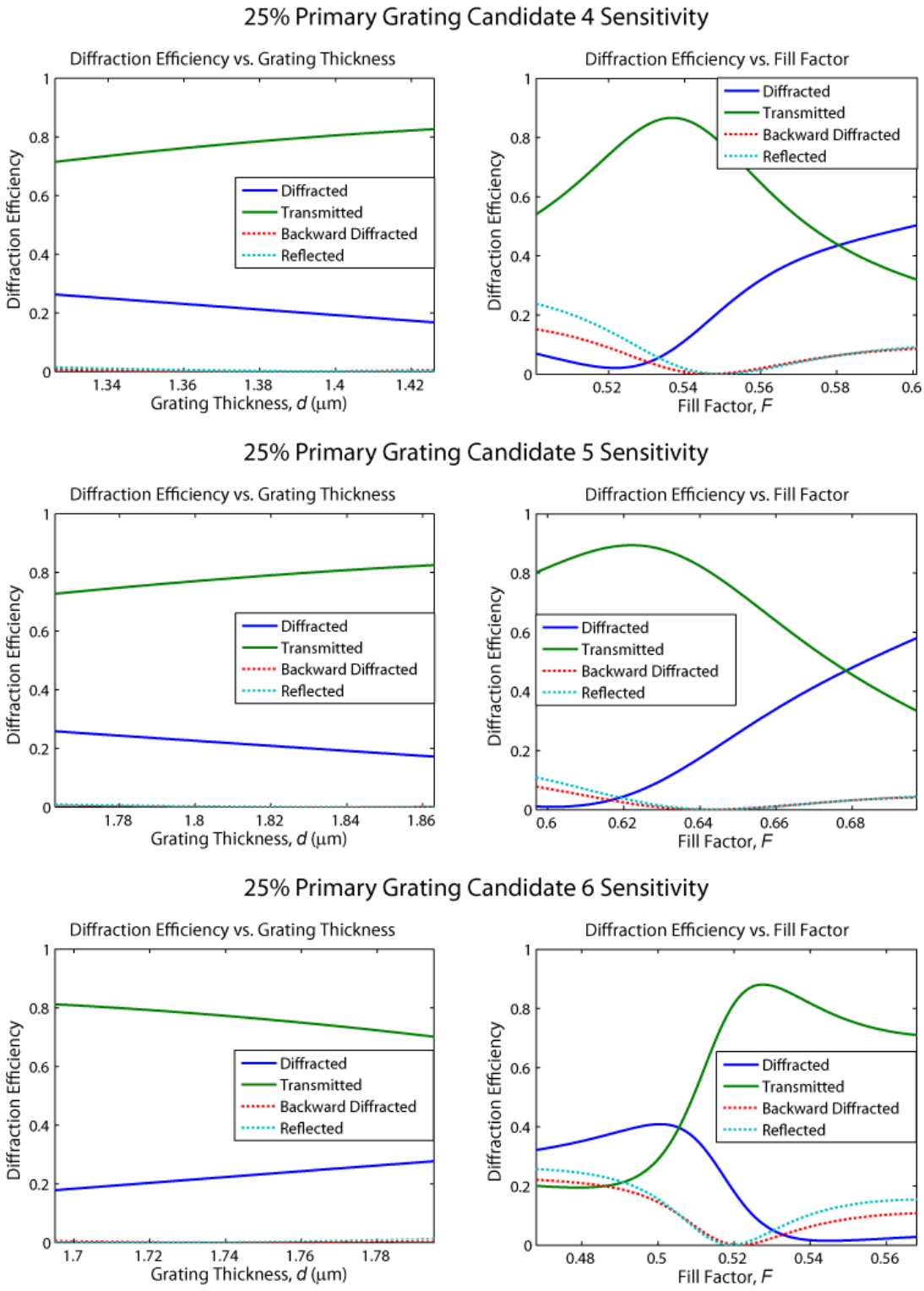

Figure 3.4: RCWA thickness and fill factor sensitivities for primary grating candidates 4, 5, and 6 with target diffraction efficiencies of 25%.

A much greater difference is apparent in the sensitivity to fill factor. Candidates four, five, and six exhibit large variations in diffraction efficiency within the 5% fill factor range. In addition, the significant presence of the backward-diffracted and reflected orders is highly undesirable. These behaviors immediately eliminate candidates four, five, and six from contention. Candidate three with a fill factor 0.916 is also eliminated because of fabrication concerns. In general, candidates with a fill factor greater than 0.90 and corresponding groove widths less than $48nm$ are removed from contention due to issues with fabrication of small grooves and filling those grooves with the PBIBMA cladding material. Of the remaining candidates, candidate one has a slightly inferior thickness sensitivity to candidate two, but the fill factor sensitivity is significantly improved. Candidate one is chosen over candidate two for its superior sensitivity to fill factor. Controlling groove width in fabrication can be difficult for small grooves, particularly in terms of variables and fluctuations during the etch process. This candidate selection process is similar for the other target diffraction efficiency cases. In each case, candidates with smaller grating thicknesses and higher fill factors generally have superior fabrication tolerances. The grating profiles with the smallest thicknesses are chosen when the fill factors are similar in order to minimize fill factor sensitivity. Optimized grating designs for target diffraction efficiencies of 20%, 25%, 33%, and 50% are presented in Table 3.2. Alignment tolerance and sensitivity to the surrounding refractive index are found to be minimal as depicted for the 25% target diffraction efficiency profile in Fig. 3.5. Sensitivity data for thickness, fill factor, incident angle, and surrounding refractive index of the remaining optimized designs can be found in Appendix B.

Table 3.2: Designs for primary and secondary gratings simulated with RCWA, FDTD Plane-Wave (FDTD-PW), and FDTD Gaussian (FDTD-Ga) analyses.

Primary Grating ($\lambda = 1.55\mu m$, $\Lambda = 0.475\mu m$, $n = n_r = 2.305$, $n_g = 1.471$)						
Grating Parameters			**Diffraction Efficiencies**			
Target Diffraction Efficiency $DE_{3,1}^{T}$ (%)	Thickness d (μm)	Fill Factor F	Diffracted $DE_{3,1}$ (%)	Transmitted $DE_{3,0}$ (%)	Backward Diffracted $DE_{1,1}$ (%)	Reflected $DE_{1,0}$ (%)
20% RCWA			20.02	79.98	0.00	0.00
20% FDTD-PW	0.615	0.811	20.55	79.42	0.01	0.02
20% FDTD-Ga			19.85	80.10	0.01	0.04
25% RCWA			25.00	75.00	0.00	0.00
25% FDTD-PW	0.636	0.794	25.43	74.53	0.01	0.03
25% FDTD-Ga			24.75	75.20	0.00	0.05
33% RCWA			33.33	66.67	0.00	0.00
33% FDTD-PW	0.668	0.770	33.57	66.38	0.02	0.03
33% FDTD-Ga			32.90	67.03	0.00	0.07
50% RCWA			50.00	50.00	0.00	0.00
50% FDTD-PW	0.725	0.731	49.86	50.08	0.02	0.04
50% FDTD-Ga			49.10	50.77	0.01	0.12
Secondary Grating ($\lambda = 1.55\mu m$, $\Lambda = 0.498\mu m$, $n = n_r = 2.341$, $n_g = 1.581$)						
RCWA			52.50	47.03	0.20	0.27
FDTD-PW	3.105	0.852	50.24	49.28	0.17	0.31
FDTD-Ga			48.00	51.39	0.22	0.39

Analysis of these designs with Gaussian beam incidence is performed with FDTD simulation. Plane-wave incidence with periodic boundary conditions is simulated to ensure that the grating devices are accurately represented in the simulation space. This mode of simulation is depicted in Fig. 3.6 for the primary grating design with a 25% diffraction efficiency. A comparison between RCWA and FDTD plane-wave analysis is presented in Table 3.2. The results are within 1%, showing excellent agreement.

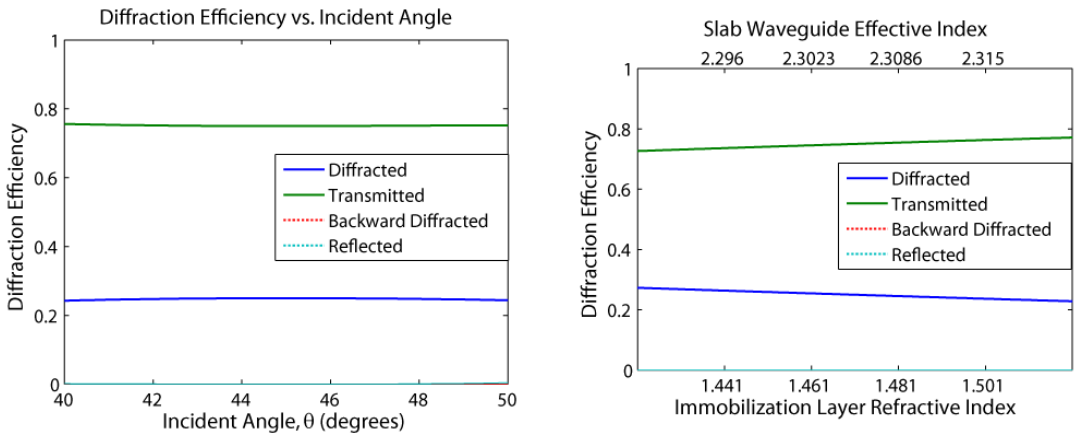

Figure 3.5: RCWA alignment (left) and surrounding refractive index (right) sensitivities for the primary grating design with target diffraction efficiency of 25%.

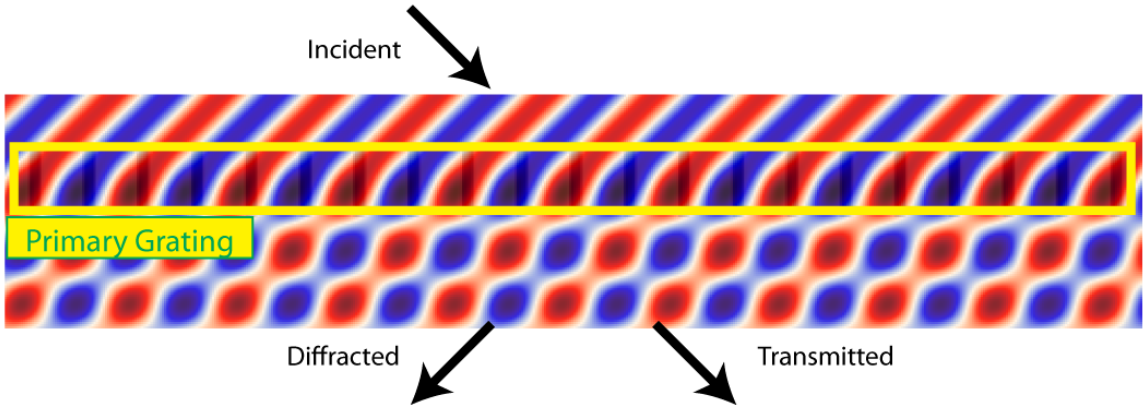

Figure 3.6: FDTD simulation with plane-wave incidence for the primary grating design with 25% diffraction efficiency.

FDTD plane-wave simulations are also performed for varying grating thickness, fill factor, incident angle, and surrounding refractive index to compare sensitivities. These results are compared to those from RCWA analysis in Fig. 3.7 for the 25% primary grating. Results for the remaining primary grating designs can be found in Appendix B. Again, the results for all primary grating designs are within 2%, showing excellent agreement. This establishes that the FDTD simulation space accurately models the primary grating designs.

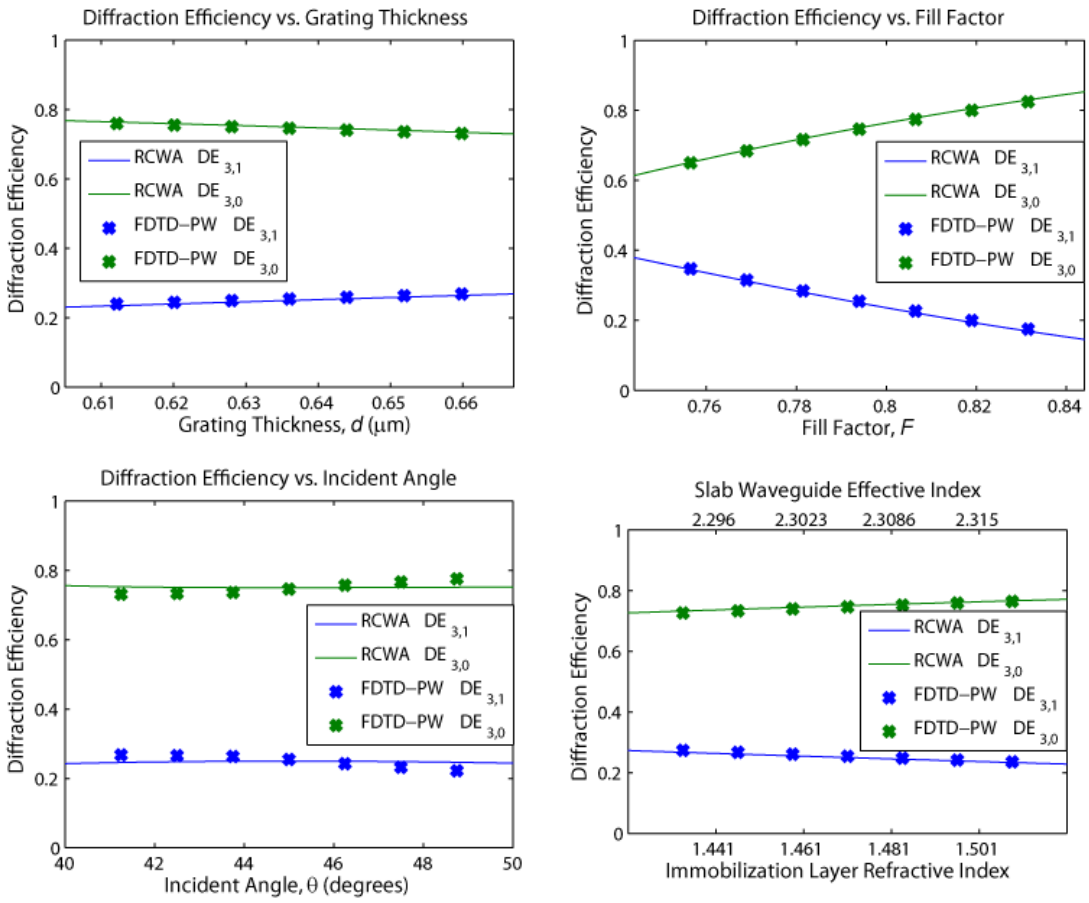

Figure 3.7: FDTD plane-wave incidence sensitivity data for the primary grating design with 25% diffraction efficiency. Plots include sensitivities for thickness (top left), fill factor (top right), incident angle (bottom left), and surrounding refractive index (bottom right).

Simulation with Gaussian beam incidence requires the addition of PML's at all boundaries and expansion of the simulation space to accommodate adequately the beam size. Consequently, the number of time steps required increases along with the total simulation time. Each FDTD simulation with Gaussian beam incidence requires approximately two hours for completion with a typical personal computer. This emphasizes the need for an efficient CSDS design tool such as RCWA. An example of FDTD simulation with Gaussian beam incidence for the primary grating design with a 25% diffraction efficiency is shown in Fig. 3.8.

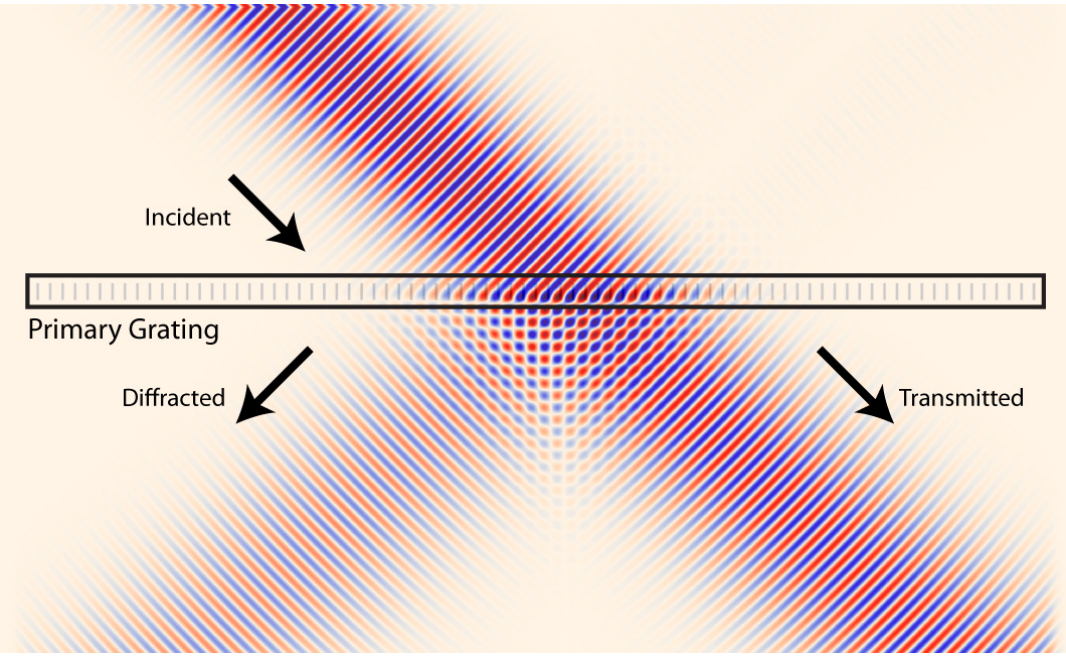

Figure 3.8: FDTD simulation with Gaussian beam incidence for the primary grating design with 25% diffraction efficiency.

Results comparing FDTD Gaussian beam analysis with RCWA and FDTD plane-wave analysis are presented in Table 3.2. Similar to the case of plane-wave incidence, the results are within 1%, showing excellent agreement. Sensitivity analysis compared to RCWA for the 25% primary grating is shown in Fig. 3.9. Plots for the remaining primary grating sensitivity comparisons are found in Appendix B. The data show that FDTD simulation with Gaussian beam incidence is in excellent agreement with RCWA for all primary grating designs. The discrepancies between analyses are less than 2%. Optimized primary gratings exhibit the desired fabrication tolerances, even with Gaussian beam incidence. This indicates that even though RCWA is a plane-wave analysis, it is an efficient and accurate tool for designing CSDS primary gratings.

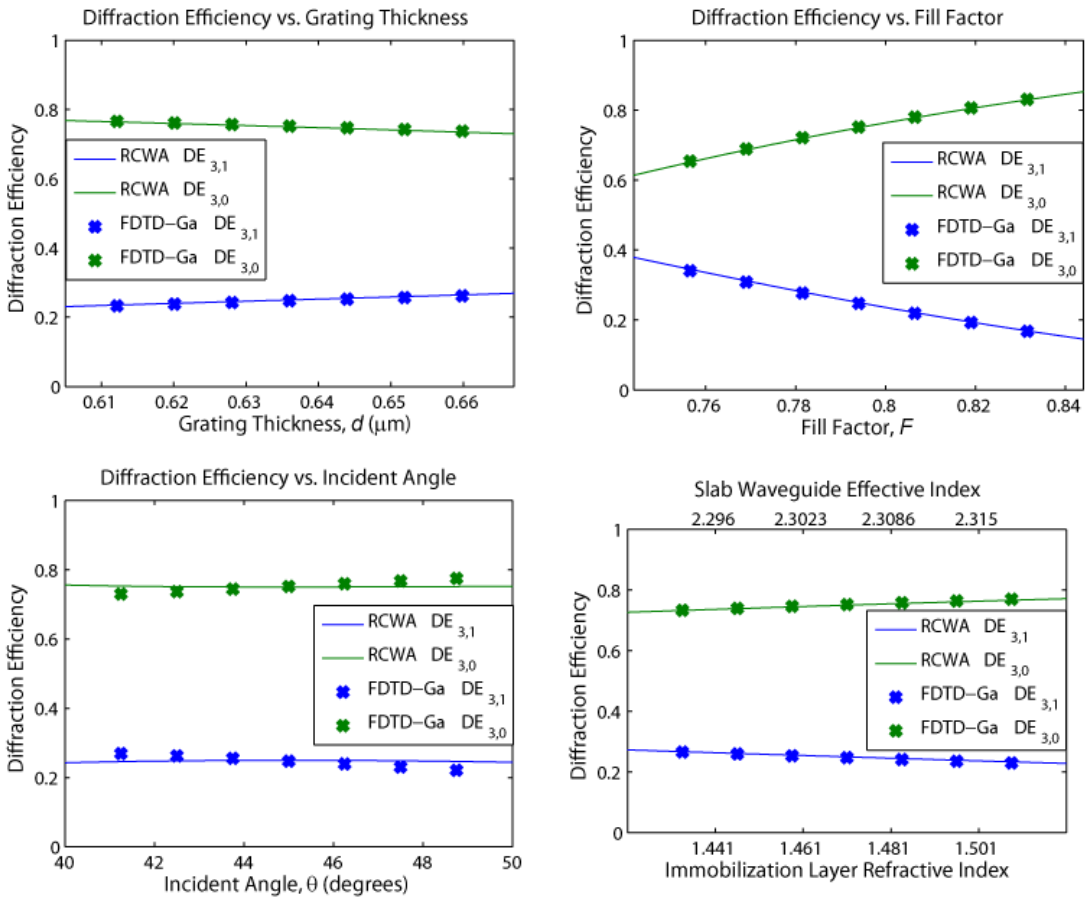

Figure 3.9: FDTD Gaussian beam incidence sensitivity data for the primary grating design with 25% diffraction efficiency. Plots include sensitivities for thickness (top left), fill factor (top right), incident angle (bottom left), and surrounding refractive index (bottom right).

3.2 Secondary Grating

The secondary grating must operate away from the Bragg condition for a linear, monotonic response to changes in incident angle. The secondary grating design process is presented in the flowchart in Fig. 3.10. Initially, the process is similar to that for primary grating design. The initial search is for candidate gratings with nearly 100% diffraction efficiency that fulfill the Bragg condition with $\Lambda = 0.468 \mu m$, $\theta = \theta_m = 45°$, and $n_0 = 2.341$.

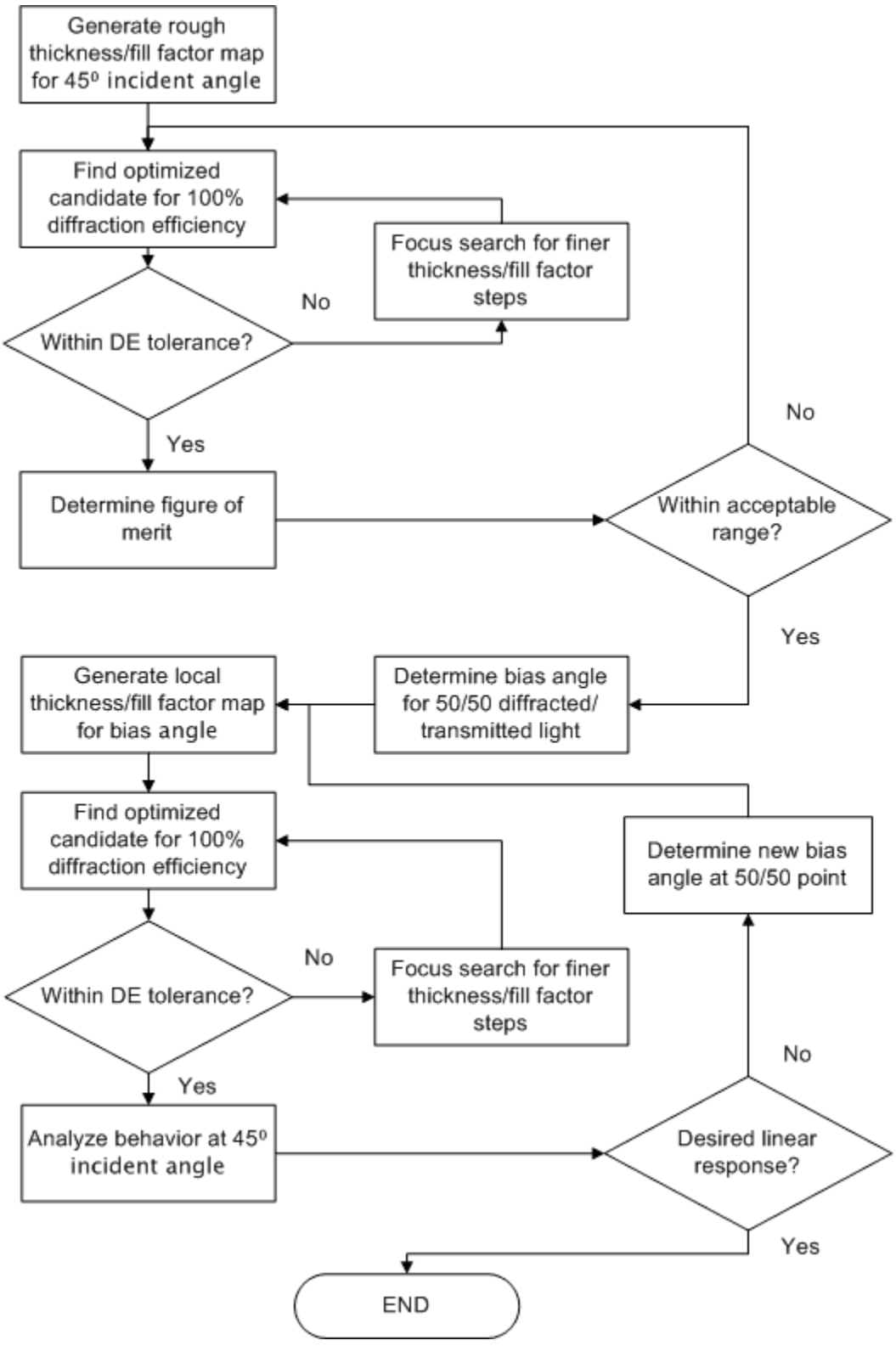

Figure 3.10: Design flowchart for the secondary grating operating away from the Bragg condition.

RCWA simulations are performed for grating thicknesses between $1-4\mu m$ with a step size of $1nm$. The range of larger thicknesses is chosen to obtain greater angular selectivity as predicted by the Kogelnik TWCW analysis. The upper limit of $4\mu m$ is chosen to avoid increased scattering and unreasonable fabrication tolerances. Simulated fill factors range from 0.001 to 0.999 with a step size of 0.001 as done for the primary gratings. Each point is evaluated with the figure of merit from Eq. (3.1) with $DE_{1,0}^{T}=0$, $DE_{1,1}^{T}=0$, $DE_{3,0}^{T}=0.0$, and $DE_{3,1}^{T}=1.0$. The figure of merit plot in Fig. 3.11 reveals 11 candidates.

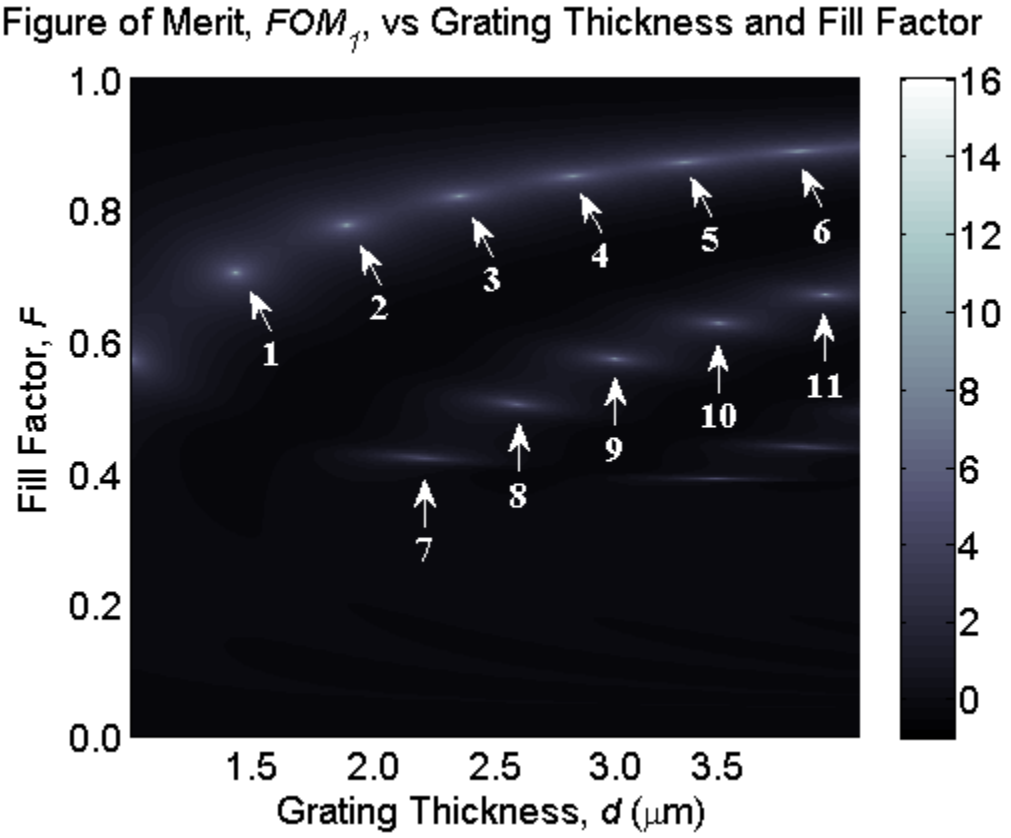

Figure 3.11: Plot of figure-of-merit, FOM_1, for secondary grating preliminary candidates vs. grating thickness and fill factor with a target diffraction efficiency of 100%. Numbered regions with potential candidates for the secondary grating design starting point are highlighted.

These candidates are listed in Table 3.3. If the candidate points are not acceptably close to 100% diffraction efficiency, the step size can be decreased for a focused search. The chosen step size of $1nm$ is indicative of the available fabrication capabilities and provides candidates with diffraction efficiencies greater than 99%. These results are sufficient to preclude more focused simulation.

Table 3.3: Secondary grating preliminary candidates designed for $DE_{3,1} = 100\%$**.** The chosen candidate is in bold face.

Secondary Grating Preliminary Candidates ($\lambda = 1.55\mu m,\ \Lambda = 0.468\mu m,\ n = n_r = 2.341,\ n_g = 1.581$)			
Candidate	**Thickness** $d\ (\mu m)$	**Fill Factor** F	**Figure of Merit** FOM_2
1	1.433	0.703	0.229
2	1.888	0.774	0.280
3	2.350	0.818	0.299
4	**2.814**	**0.848**	**0.304**
5	3.283	0.870	0.294
6	3.748	0.886	0.265
7	2.188	0.423	-0.577
8	2.583	0.504	-0.483
9	2.992	0.572	-0.359
10	3.418	0.626	-0.276
11	3.856	0.669	-0.277
Simulation Space	$1-4\mu m$	$0.001-0.999$	

Evaluation of each candidate must weigh angular sensitivity vs. fabrication tolerances. The angular sensitivity of each candidate is simulated for a range of incident angles from $40°$ to $50°$. Thickness and fill factor sensitivities are taken from the original simulation data since the step size is sufficiently small. The sensitivity plots for each candidate are presented in Appendix B. To choose the most appropriate candidate as a starting point of the secondary grating design, the figure of merit,

$$FOM_2 = \Omega - \Phi, \tag{3.2}$$

is defined. Here, Ω is the sum of the slopes for the diffracted and transmitted efficiencies at the incident angles where $DE_{3,1} = 50\%$ on both the left and right side of the angular selectivity peak (as in Fig. 3.12) with $DE_{3,1} = 100\%$,

$$\Omega = \left|\frac{\Delta DE_{3,0}^{50\%}}{\Delta\theta}\right|_{\theta<45^\circ} + \left|\frac{\Delta DE_{3,1}^{50\%}}{\Delta\theta}\right|_{\theta<45^\circ} + \left|\frac{\Delta DE_{3,0}^{50\%}}{\Delta\theta}\right|_{\theta>45^\circ} + \left|\frac{\Delta DE_{3,1}^{50\%}}{\Delta\theta}\right|_{\theta>45^\circ}. \tag{3.3}$$

The better candidates will have high values of angular selectivity for the diffracted and transmitted orders and zero backward diffraction and reflection, maximizing Ω. The sum of the maximum variations in all forward and backward orders for 5% variations in thickness and fill factor, Φ, is

$$\Phi = \Phi_d + \Phi_F, \tag{3.4}$$

where

$$\Phi_d = \left|\Delta DE_{1,0}^{\max}\right|_{d\pm5\%} + \left|\Delta DE_{1,1}^{\max}\right|_{d\pm5\%} + \left|\Delta DE_{3,0}^{\max}\right|_{d\pm5\%} + \left|\Delta DE_{3,1}^{\max}\right|_{d\pm5\%} \tag{3.5}$$

and

$$\Phi_F = \left|\Delta DE_{1,0}^{\max}\right|_{F\pm5\%} + \left|\Delta DE_{1,1}^{\max}\right|_{F\pm5\%} + \left|\Delta DE_{3,0}^{\max}\right|_{F\pm5\%} + \left|\Delta DE_{3,1}^{\max}\right|_{F\pm5\%}. \tag{3.6}$$

The value of Φ is minimized with superior fabrication tolerances. The goal reflected in this figure of merit is to obtain the candidate with the greatest angular selectivity off the Bragg angle and the most lenient fabrication tolerances. As listed in Table 3.3, the chosen preliminary candidate with the greatest figure of merit is candidate four, with the angular behavior depicted in Fig. 3.12.

While this gives a grating with the desired linear, monotonic behavior, the angle at which this is achieved is shifted from the 45° incident angle. A bias angle must be determined at which the Bragg condition is fulfilled and the desired behavior is achieved at 45° incidence.

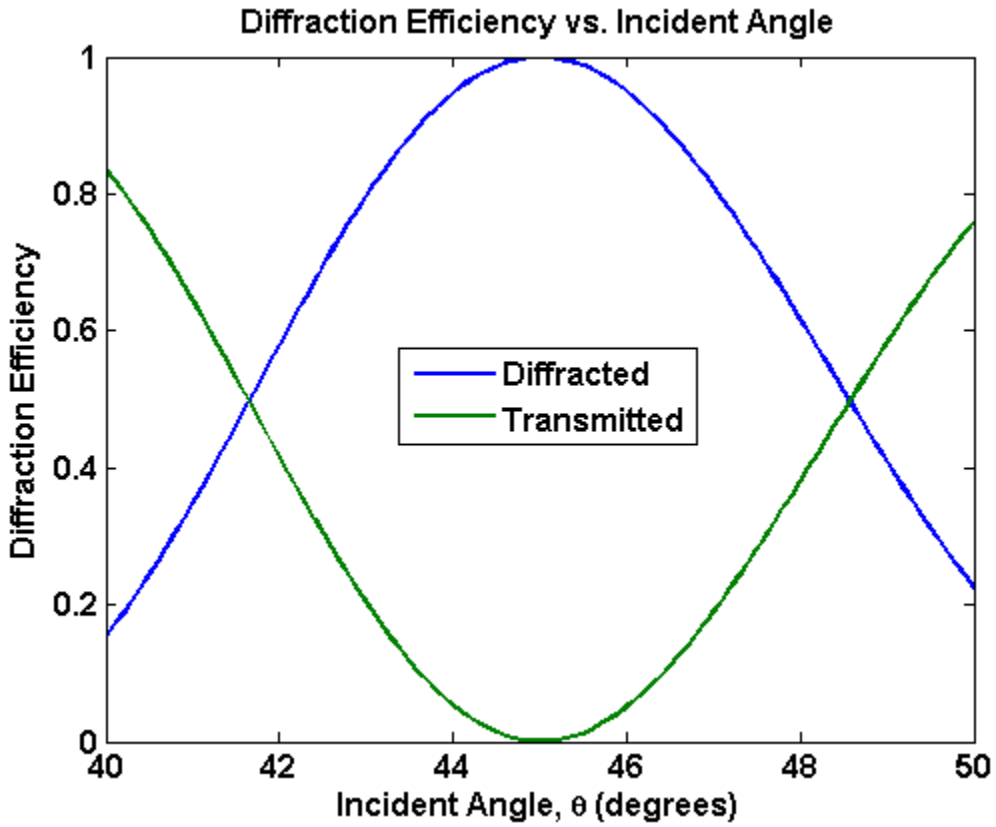

Figure 3.12: Angular sensitivity of preliminary candidate 4 for the secondary grating. Grating is optimized for 100% diffraction efficiency at $\theta = 45°$. Both backward orders, $DE_{1,0}$ and $DE_{1,1}$, remain near zero over the entire range of incident angles.

From Fig. 3.12, the desired linear, monotonic behavior is observed at points where both the transmitted and diffracted efficiencies are 50%. This condition is fulfilled on both the left ($\theta < 45°$) and right ($\theta > 45°$) sides of the curve for bias angles of $\theta_{bias} = 41.65°$ and $\theta_{bias} = 48.55°$ respectively. The grating periods required to fulfill the Bragg condition at these bias angles are $\Lambda = 0.498\mu m$ for $\theta_{bias} = 41.65°$ and $\Lambda = 0.442\mu m$ for $\theta_{bias} = 48.55°$. Since fabrication of a grating with a larger period is generally easier, the bias angle of $\theta_{bias} = 41.65°$ is chosen. This design process has also been completed for the alternate bias angle of $\theta_{bias} = 48.55°$. The end result is of the same quality with the

only difference being the size of the grating period. With the bias angle chosen and the appropriate grating period determined, RCWA simulations are run for a new set of thickness and fill factor points similar to those of candidate four. The figure of merit from Eq. (3.1) is evaluated with $DE_{1,0}^{T} = 0$, $DE_{1,1}^{T} = 0$, $DE_{3,0}^{T} = 0.0$, and $DE_{3,1}^{T} = 1.0$. The resulting color plot is presented in Fig. 3.13.

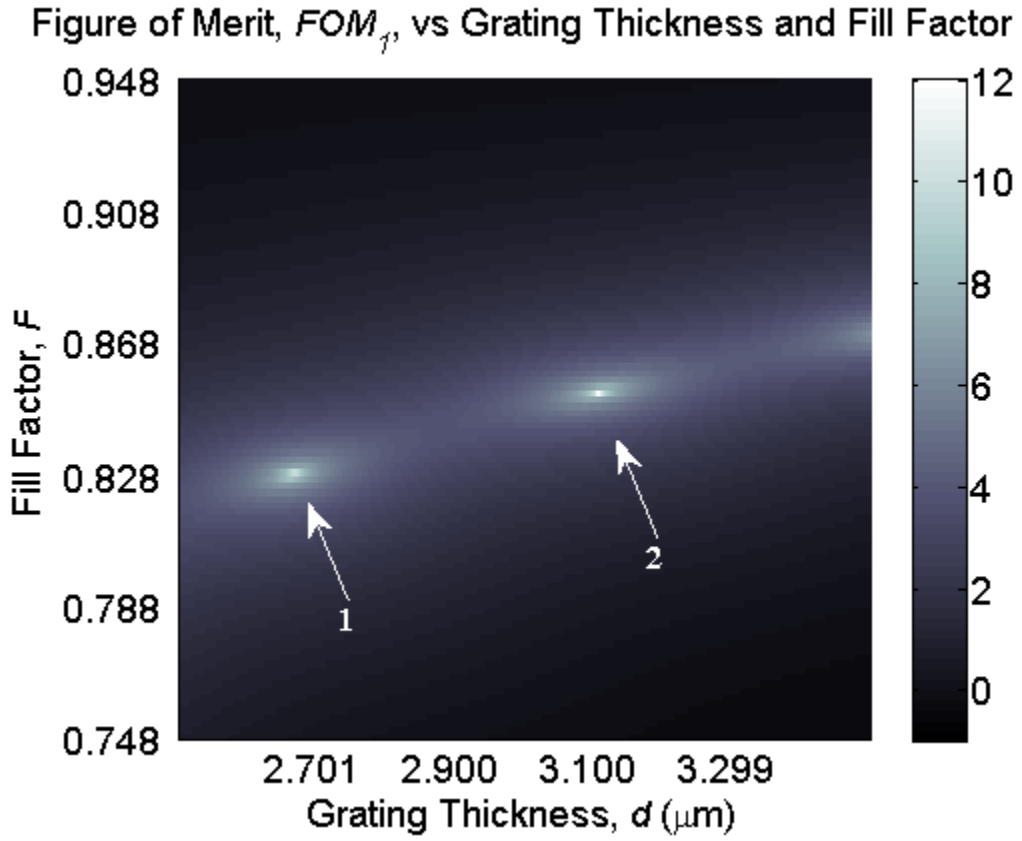

Figure 3.13: Plot of figure-of-merit, FOM_1, vs. grating thickness and fill factor for a target diffraction efficiency of 100%. Numbered regions with potential candidates for the secondary grating design starting point are highlighted.

Two candidates are identified and examined. Candidate one has a thickness of $2.665\mu m$ and a fill factor of 0.827. Candidate two has a thickness of $3.105\mu m$ and a fill factor of 0.852. To determine which candidate has the most desirable behavior at $\theta = 45°$, RCWA

data is generated for variation in incident angle from 40° to 50°. Additionally, the thickness and fill factor sensitivities are investigated to determine fabrication tolerances. These responses are plotted in Fig. 3.14.

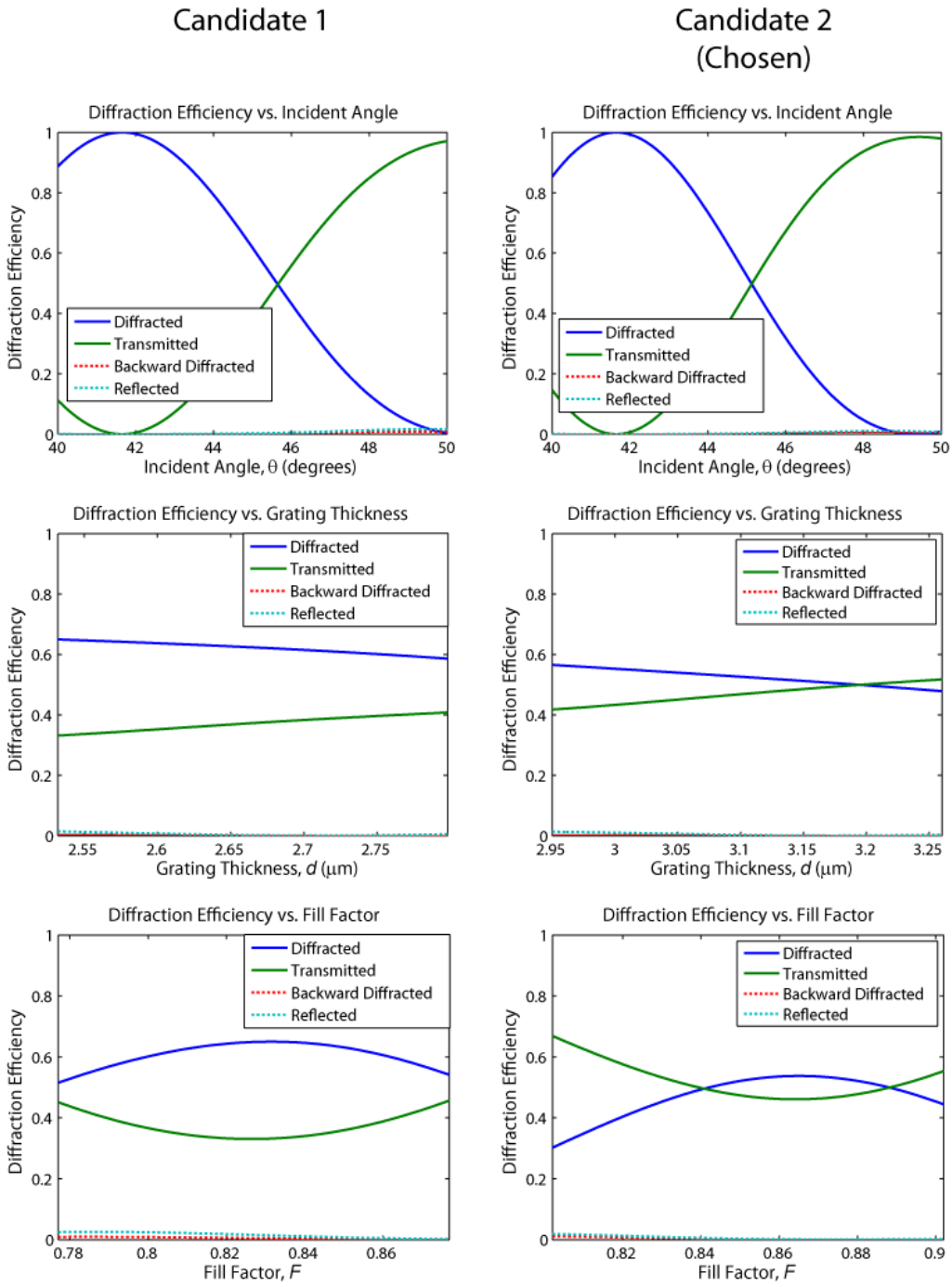

Figure 3.14: Incident angle, thickness, and fill factor sensitivities of candidates for the secondary grating with a bias angle of $\theta_{bias} = 41.65°$.

The transmitted and diffracted efficiencies at $\theta = 45°$ should be at or near 50% with a diffraction efficiency slope near that of the original candidate. If neither candidate is suitable, the one with the most appropriate diffraction efficiency slope is chosen, a new bias angle is determined by taking the angular shift needed achieve a diffraction efficiency of 50% at $\theta = 45°$, and the process is repeated. In this case, the diffraction efficiency of candidate two is suitably close to 50% at $\theta = 45°$ and no iteration is necessary. The choice of the secondary grating design parameters and the resulting diffraction efficiencies is summarized in Table 3.2. The angular sensitivity as plotted in Fig. 3.14 is determined to be $21.35\% DE / °$.

FDTD analysis with plane-wave and Gaussian beam incidence is used to simulate secondary grating operation under realistic conditions. The analyses for RCWA and FDTD plane-wave analysis are in good agreement. Simulated results are within two percent for the diffracted and transmitted orders as presented in Table 3.2. The efficiencies of backward-diffracted and reflected orders are within half a percent of those predicted by RCWA. This agreement extends to FDTD simulation for incident angle, thickness, fill factor, and surrounding refractive index sensitivities as shown in Fig. 3.15. These small discrepancies are primarily thought to be due to the high angular sensitivity of the grating coupled with the discretization of space required to perform the FDTD analysis with manageable computation time. Since the discrepancies are small, it is concluded that the secondary grating is modeled with sufficient accuracy in the FDTD simulation space. The FDTD analysis with Gaussian beam incidence shows a larger discrepancy for the diffracted and transmitted orders of about four percent as presented in Table 3.2.

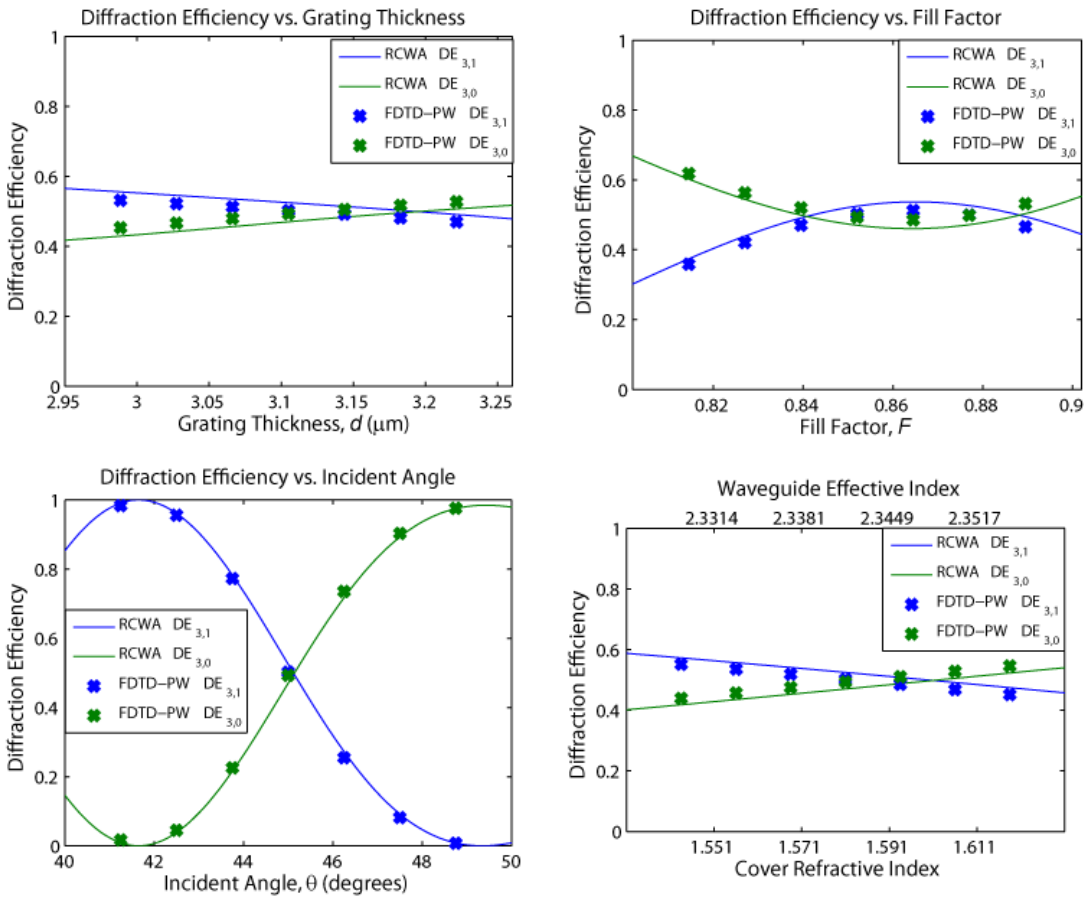

Figure 3.15: FDTD plane-wave incidence sensitivity data for the secondary grating. Plots include sensitivities for thickness (top left), fill factor (top right), incident angle (bottom left), and surrounding refractive index (bottom right).

Discrepancies in the backward-diffracted and reflected orders remain at less than half a percent. This level of agreement extends to the simulated sensitivities of thickness, fill factor, and surrounding refractive index, but the effect of Gaussian incidence is apparent when considering the sensitivity to incident angle in Fig. 3.16. The angular sensitivity for the FDTD Gaussian beam analysis is determined to be $13.92\%DE/°$. This is a $7.43\%DE/°$ decrease from the angular selectivity obtained with RCWA. The additional angular components from a Gaussian beam inherently decrease the angular selectivity. It is important to note that the desired linear, monotonic behavior is still achieved about the

incident angle of 45°. This behavior is expected and again indicates that RCWA is an effective and efficient tool for this design process.

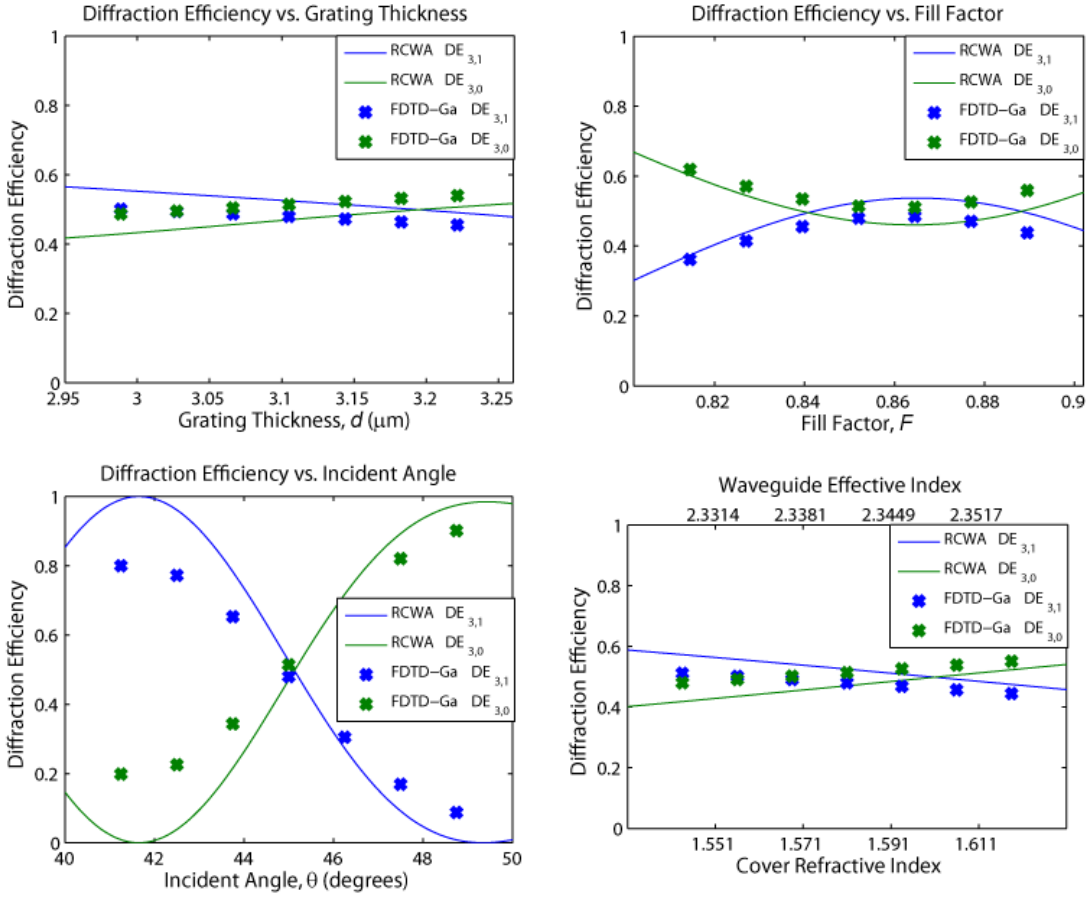

Figure 3.16: FDTD Gaussian incidence sensitivity data for the secondary grating. Plots include sensitivities for thickness (top left), fill factor (top right), incident angle (bottom left), and surrounding refractive index (bottom right).

3.3 Simulated Sensor Response

A preliminary evaluation of sensor performance is calculated with RCWA analysis. The refractive index of the immobilization layer (PBIBMA) is varied by ±0.01, which would be the range of a typical response to analyte immobilization [83, 120]. The effective indices are recalculated and the new diffracted angles are determined with Eq. (2.8). The output angle variation is calculated to be $0.0497° / mRIU$ in terms of the effective index.

With the calculated angular selectivity of the secondary grating, $21.35\%DE/°$, the sensor responsivity is $-1.061\%DE/mRIU$. Taking a typical source power of $1mW$ divided amongst 4 sensors and a monitor photodiode in a linear sensor array, the incident power is taken as $0.2mW$ per sensor. With a published SOI photodetector responsivity of $0.8A/W$ [95] and a reasonable current detection resolution of $10pA$, the sensor resolution is calculated to be $5.89\times10^{-9}RIU$. This number neglects detector noise, but provides an upper limit for the platform sensitivity. Since the secondary grating is designed to operate linearly, this would also be the minimum detectable level.

Since it has been shown that Gaussian beam incidence has a significant effect on the performance of the secondary grating, sensor performance is also analyzed by FDTD analysis with Gaussian incidence. The simulation is illustrated for the sensor with a primary grating designed for 50% diffraction efficiency in Fig. 3.17.

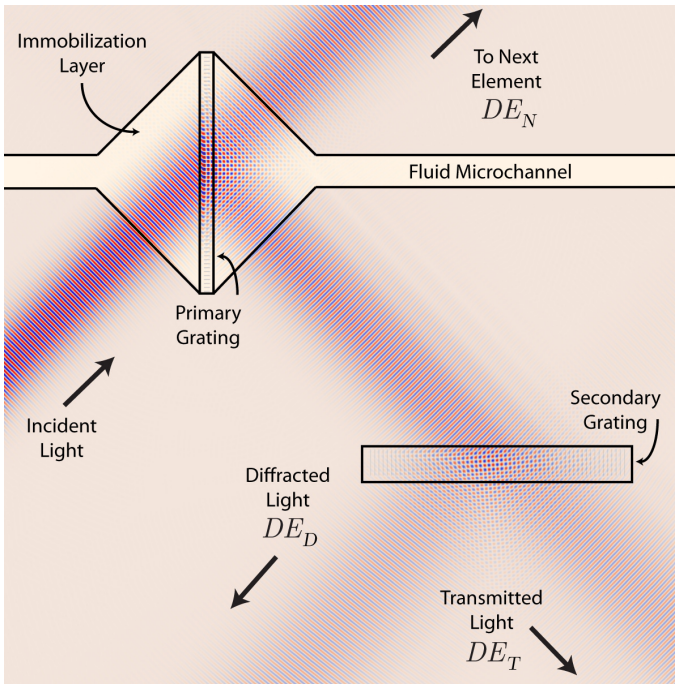

Figure 3.17: FDTD simulation for sensor with the 50% primary grating and Gaussian beam incidence. The index of the immobilization region is varied to determine sensor performance.

The preceeding analysis is done for all of the primary grating designs. The refractive index of the immobilization layer (PBIBMA) is varied by ± 0.01 and the effective indices are recalculated. The simulation results are summarized in Table 3.4. Variations in the output ratio are the same for all primary grating cases since the output angle variation is dependent on the grating periodicity. Calculating with the same parameters used for RCWA analysis, sensor resolution and minimum detectable level are determined to be $9.80 \times 10^{-9}\, RIU$. This upper limit on sensor resolution indicates that the CSDS platform is competitive with the state-of-the-art integrated optical sensor technologies.

Table 3.4: Sensor FDTD simulation results with Gaussian beam incidence.

FDTD Gaussian Sensor Results					
Immobilization Layer Refractive Index	**Effective Index** N_{eff}	**Diffracted Light** DE_D (%)	**Transmitted Light** DE_T (%)	**To Next Element** DE_N (%)	**Measurement** $\frac{DE_D}{DE_D + DE_T}$
Primary Grating $DE_{3,1}^T = 20\%$					
1.461	2.302	8.96	10.16	79.93	0.4686
1.471	2.305	8.41	10.43	80.28	0.4464
1.481	2.308	7.87	10.69	80.62	0.4240
Primary Grating $DE_{3,1}^T = 25\%$					
1.461	2.302	11.19	12.69	75.00	0.4686
1.471	2.305	10.49	13.01	75.44	0.4464
1.481	2.308	9.82	13.34	75.87	0.4240
Primary Grating $DE_{3,1}^T = 33\%$					
1.461	2.302	14.88	16.87	66.80	0.4686
1.471	2.305	13.96	17.31	67.39	0.4464
1.481	2.308	13.06	17.74	67.97	0.4240
Primary Grating $DE_{3,1}^T = 50\%$					
1.461	2.302	22.25	25.23	50.46	0.4686
1.471	2.305	20.87	25.88	51.34	0.4464
1.481	2.308	19.52	26.51	52.20	0.4240

CHAPTER 4

DEVICE FABRICATION

Accurate fabrication of the primary and secondary gratings is critical to the function of the CSDS platform. The grating grooves etched into the silicon device layer of the SOI substrate must be precisely fabricated to ensure that the desired grating characteristics are achieved. These grooves need to be spaced correctly to achieve the designed grating period. Variations in the fabricated grating period affect many aspects of grating operation, including the diffracted angle as given by Eqs. (2.8) and (2.13) and the resulting diffraction efficiencies. A shift in the angle of the beam diffracted by the primary grating could lead to an erroneous measured value. Accurate reproduction of the secondary grating period is important to obtain the designed angular selectivity characteristics. The grating grooves must also have the proper thickness and fill factor to attain the designed diffraction efficiencies. As discussed previously, the designed gratings are relatively insensitive to thickness variations, but exhibit significant sensitivities for fill factors varying by $\pm 5\%$ or more. With the designed fill factors and grating periods from Table 3.2, the fabricated groove widths range from $w = 74nm$ to $w = 128nm$. To remain within ten percent of the desired diffraction efficiencies, the fabricated groove widths should be within $5nm$ of the designed values. Additionally, the sidewall angle, ϕ, of each groove should be as near $90°$ as possible. As the sidewall angle deviates from $\phi = 90°$, the width varies at the top and bottom of the groove. With the silicon device layer thickness of $250nm$, a typical sidewall angle of $\phi = 80°$ results in a width difference of $43nm$. This corresponds to a variation in fill factor over 8% for primary and

secondary gratings. This presents significant challenges in fabrication which are addressed in this chapter.

Gratings are fabricated in a cleanroom environment in the Pettit Microelectronics building, which is part of the Georgia Tech Institute for Electronics and Nanotechnology (IEN). Precise patterning of the grating grooves is achieved with electron-beam lithography (EBL). Transfer of these patterns to the silicon device layer is done with an inductively-coupled plasma (ICP) etch. A Bosch process is used to achieve the highest possible sidewall angles and to improve etch selectivity. The primary grating boundaries are patterned in the SU-8 cladding via conventional optical lithography with a mask aligner. All steps are performed sequentially within the cleanroom environment in a time frame of approximately eight hours to avoid possible contamination.

For the proof-of-concept toluene sensor, PBIBMA is dip-coated onto the sensor at the Georgia Tech Research Institute Electro-Optical Systems Laboratory. After removing excess PBIBMA, microfluidic channels are assembled and bonded to the sensor. The process requires approximately two hours with pre-assembled microfluidic channels, but the adhesive requires an additional 24 hours to cure.

4.1 Electron-Beam Lithography

Gratings are patterned with the JEOL [121] JBX-9300FS electron-beam lithography (EBL) tool. The tool is configured to operate with an accelerating voltage of $100kV$ and a beam current of $2nA$. All fabricated patterns have a shot pitch of $5nm$. Two resists were considered for patterning, ZEP-520a from Zeon Chemicals [122] and hydrogen silsesquioxane (HSQ). HSQ is a negative resist capable of producing feature sizes as small as $10nm$ [123]. It has been shown to have a high etch selectivity to silicon and is

used in many SOI applications [124]. In most cases, the resist is not removed after etching, but is instead left to act as a cladding. For CSDS fabrication, the EBL resist must be removed after etching for deposition of the SU-8 overcoat layer. This presents an issue in that removal of HSQ will also remove any exposed oxide, including that within the etched grating grooves. It is for this reason that a silicon dioxide hard mask is also not an option. Furthermore, HSQ is a negative resist which greatly increases exposure time for CSDS fabrication. For these reasons, ZEP-520a is chosen. ZEP-520a is a positive resist capable of producing feature sizes as small as $15nm$ [125]. It is easily removed with Shipley Microposit [126] 1165 remover after etching. However, the best etch selectivity to silicon achieved at the IEN facilities is approximately $\rho \approx 0.7:1$ [(etch rate of silicon):(etch rate of ZEP-520a)]. With a silicon device layer thickness of $250nm$, a ZEP layer of approximately $400nm$ would be necessary. Since the smallest grating groove width is $w = 74nm$ for the secondary grating, the resulting aspect ratio would be 5.4:1. This presents a practical challenge in preventing sidewall collapse. This effect is illustrated in Appendix C for a ZEP thickness of $350nm$. With the ICP Bosch etch process detailed in the next section, the improved selectivity allows for a ZEP layer thickness of $55nm$. This results in an aspect ratio less than one, preventing sidewall collapse.

To determine the proper exposure dose (*Coulombs* per unit *area*), D, test gratings are patterned with doses from $160\mu C/cm^2$ to $240\mu C/cm^2$. Images for each dose are presented in Appendix C. A dose of $D = 220\mu C/cm^2$ is determined to be sufficient for defining the CSDS grating grooves. The SOI pieces used are cleaved to a size of $15mm$

by 20*mm* and patterned according to the process steps in Appendix D. Following this process, the sample is ready for etching.

4.2 Inductively Coupled Plasma Etching with Bosch Process

Reduction of the EBL-patterned aspect ratio and fabrication of vertical sidewalls without the use of HSQ or a silicon dioxide hard mask requires a different approach from a standard chlorine-based silicon ICP etch. A Bosch process is widely used for obtaining vertical sidewalls with a high etch selectivity. However, when working with nanometer scale features, scalloping from each etch cycle and undercutting are normally prohibitive. Work has been done to scale down the Bosch process for nano-scale applications by reducing the etch strength of each cycle. This has been accomplished by reducing the etch and passivation cycle times, gas flow rates, and platen power [127, 128]. Recent work at the IEN [129] by Brown has produced $43nm$ lines with a $60nm$ pitch with ZEP as a resist by modifying these parameters. An aspect ratio of 24:1 with an etch rate of $27nm/cycle$ and a selectivity of $\rho = 11:1$ (silicon:ZEP) was achieved. The edge roughness due to scalloping was limited to $3.9nm$ and undercutting was not observed. This process is well suited to CSDS fabrication since it allows for a thinner ZEP resist layer to prevent sidewall collapse during resist development. Also, it creates nearly vertical sidewalls. For these reasons, this process is used for fabricating the grating grooves.

The Bosch etch process is performed with a Surface Technology Systems Plc. (STS) [130] ICP tool. The process parameters used are summarized in Table 4.1.

Table 4.1: Process parameters for the ICP nano-scale Bosch etch for CSDS gratings. Gas flows are in standard cubic centimeters per minute (*sccm*).

STS ICP Nano-scale Bosch Etch Parameters		
Parameter	**Etch Cycle**	**Passivation Cycle**
Pressure	$6.0mTorr$	$6.0mTorr$
Cycle Time	$5s$	$6s$
C_4F_8 Gas Flow	$0sccm$	$50sccm$
SF_6 Gas Flow	$20sccm$	$0sccm$
13.56MHz Coil Power	$600W$	$600W$
380kHz Platen Power	$14W$ (variable)	$0W$
Etch Rate	$30nm/cycle$ (variable)	
Selectivity	$\rho = 8:1$ (Silicon:ZEP)	

The etch cycle platen power is indicated as being variable to account for fluctuations in the tool's etch rate over time. As the etch rate increases, the scalloping amplitude and therefore surface roughness also increase. If the etch rate is too small, the etch depth might be limited and the pattern not fully etched. Altering the cycle times and gas flows can limit the etch rate as necessary, however it is far more likely that these changes can disrupt the etch/passivation balance and prevent proper etching. Attempts to alter significantly these values in this work have resulted in either a complete lack of detectable etching or obliteration of the resist layer and uniform etching of the silicon device layer. Reduction of the process pressure can also reduce the etch rate, however it is observed that at lower pressures the etch depth is limited. This results in a decreased sidewall angle and pinched-off grooves. An example of this effect is presented in Appendix C for a pressure of $5mTorr$.

For each fabrication, two test silicon pieces are coated with ZEP and patterned with test gratings and $100\mu m$ squares. These test pieces are etched at various platen

powers to determine the etch rates and selectivities. The Nanospec refractometer [131] is used to measure the remaining ZEP thickness and a Tencor P15 Profilometer [132] is used to measure the depth of the $100\mu m$ squares. The most appropriate platen power is then chosen for the actual fabrication to provide an etch rate around $30nm/cycle$ and the number of cycles is determined for a 15-20% over-etch.

When the patterned grooves are etched, there is a biased difference between the patterned groove width and the etched groove width. Typically, the etched width is greater due to erosion of the resist sidewall during etching. To obtain the desired grating groove widths, the etch bias must be determined. To do this, grating patterns are patterned in EBL with several biased widths. These patterns are etched and the resulting groove widths are measured with an SEM for both top-down and cross-sectional views. A summary of the determined etch biases and the resulting patterned groove widths to achieve designed values is presented in Table 4.2. SEM images of the fabricated grating designs are presented in Figs. 4.1 and 4.2.

Table 4.2: Fabricated etch biases for CSDS gratings and the corrected pattern widths.

Fabricated Grating Etch Biases			
Grating Design	**Groove Width** w (nm)	**Etch Bias** w_{bias} (nm)	**Corrected EBL Groove Width** $w_c = w - w_{bias}$ (nm)
20% Primary Grating	90	20	70
25% Primary Grating	98	22	76
33% Primary Grating	109	25	84
50% Primary Grating	128	27	101
Secondary Grating	74	20	54

The grating thicknesses and fill factors are within one percent of designed values listed in Table 3.2. Sidewalls are nearly vertical with measured values of $\phi > 89°$. The amount of sidewall scalloping is below $10nm$. This fabrication is very reproducible when the platen power is appropriately adjusted to keep the etch rate near $30nm/cycle$. The results show that the ICP nano-scale Bosch process accurately produces the designed gratings while relieving the issues of the EBL patterned aspect ratio and sidewall angle without a hard mask.

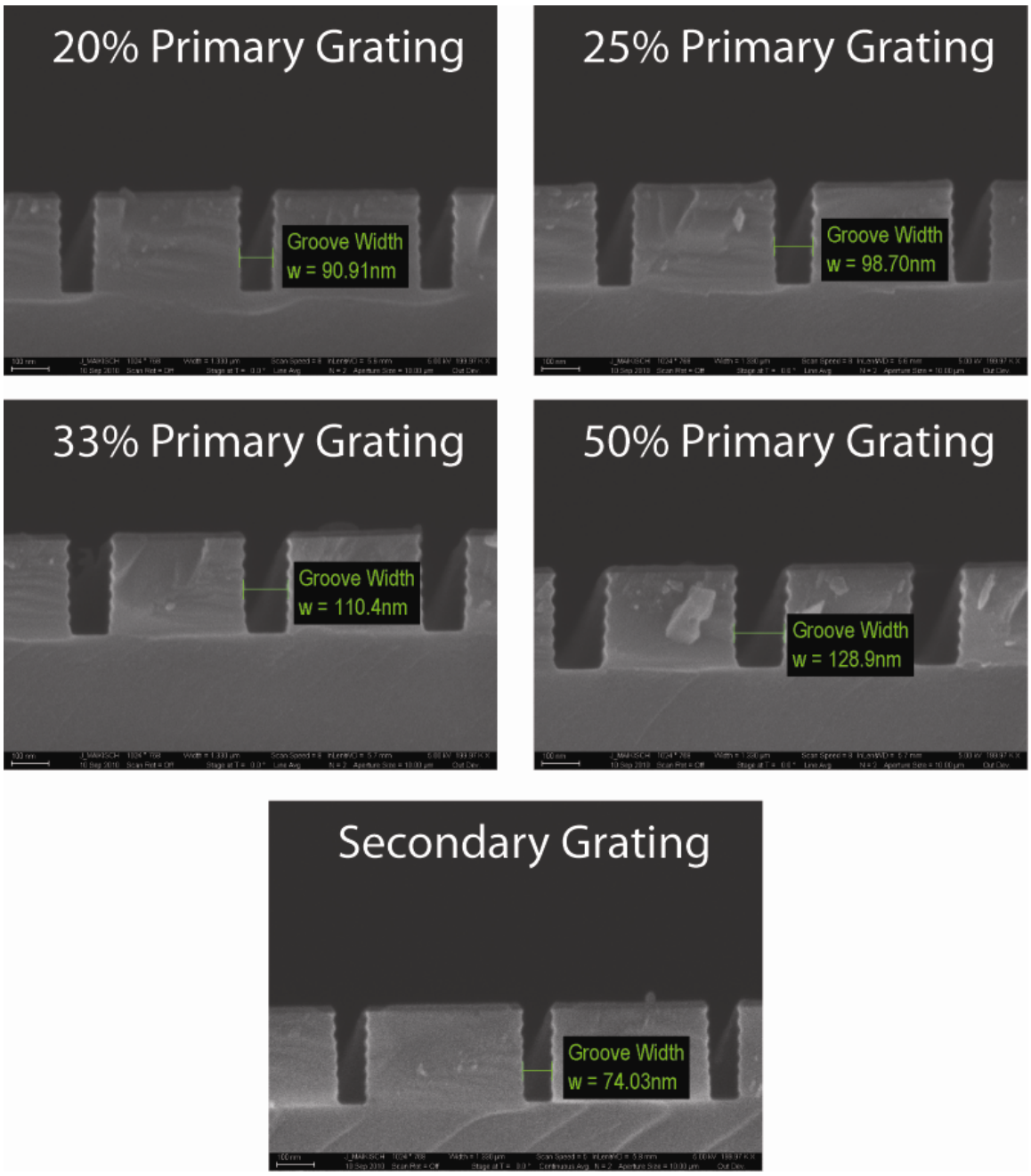

Figure 4.1: SEM images of etched grating cross sections corrected for etch bias.

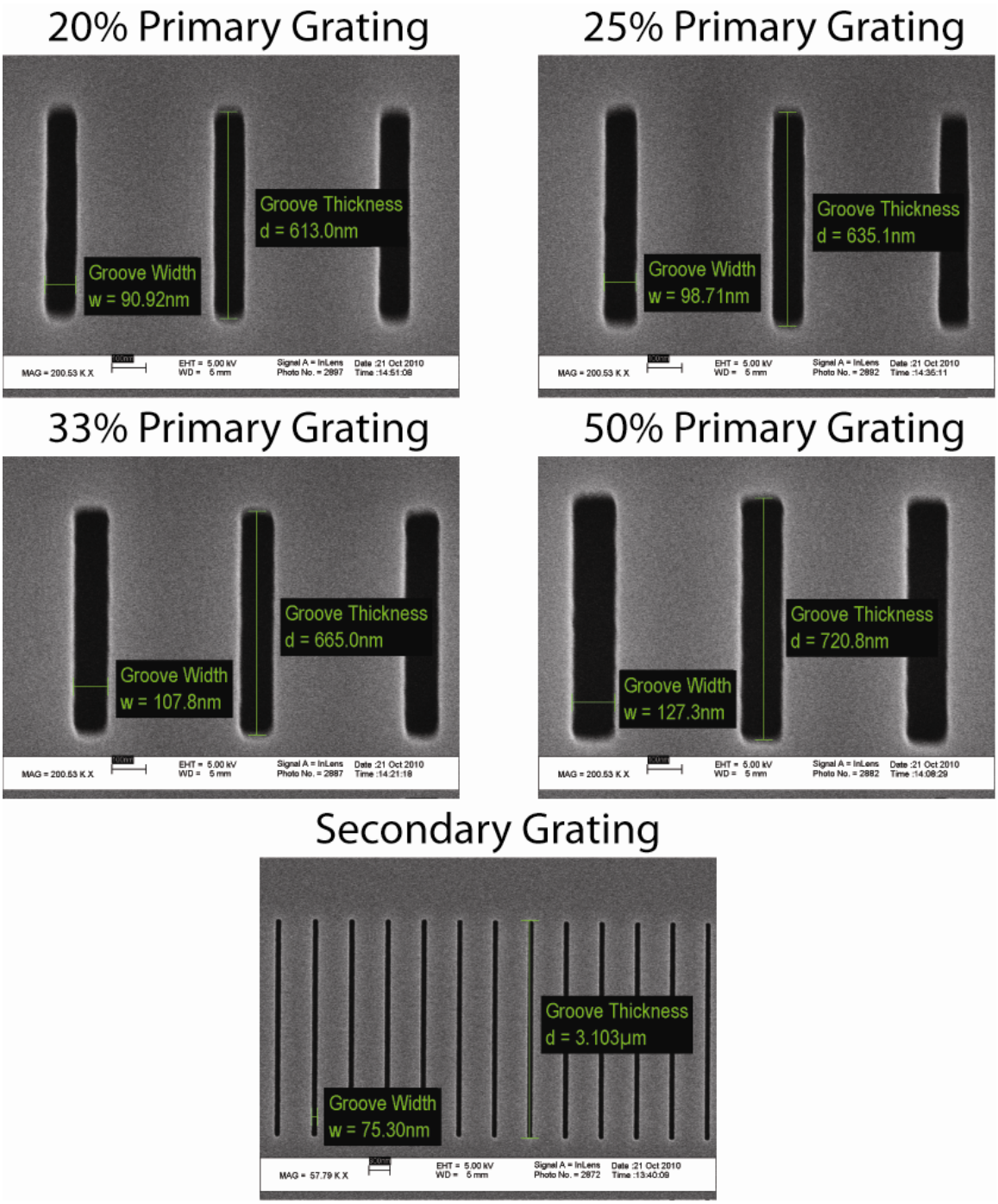

Figure 4.2: SEM images of fabricated grating designs corrected for etch bias.

4.3 Overcoat Layer Deposition and Optical Lithography

The primary grating boundary is defined in the SU-8 cladding layer. Deposition of SU-8 follows the process steps outlined in Appendix D. SU-8 is spun to a thickness of $2.9\mu m$ and patterned with ultraviolet (UV) exposure ($365nm$). For exposure, a Karl Suss MA-6 Mask Aligner [133] is used. The masks used are fabricated at the IEN mask shop. These masks are clear field and patterned with chrome. Curing of SU-8 is important to lock in its thermal characteristics. Over time, if uncured SU-8 is exposed to heat, its mechanical and optical properties can change. Additionally, a curing step is beneficial in annealing any cracks that may have formed during deposition and development. It is important that the curing temperature is above the maximum expected operation temperature and the lowest recommended cure temperature of $150°C$ from the manufacturer fulfills this requirement. SU-8 is cured at $150°C$ following the process in Appendix D.

Since the SU-8 overcoat completely covers the secondary grating, a critical question is whether the SU-8 adequately fills the grating grooves. The SU-8 2002 formula used is filtered to a $0.2\mu m$ particle size, however the secondary grating grooves are only $74nm$ wide. If the grooves are only partially or non-uniformly filled, grating operation can be adversely affected in ways that are difficult to anticipate. To determine how well the secondary grating grooves are filled, a test sample was fabricated and SU-8 was deposited following the procedures detailed in Appendix D. An SEM image of the cleaved cross section is presented in Fig. 4.3. In the cross-sectional image, some separation effects are observed in the SU-8 layer above the grating as a result of the cleaving process. However, it is apparent that the grating grooves are completely filled

with SU-8. This indicates that the SU-8 2002 formula and the process used are appropriate for CSDS fabrication.

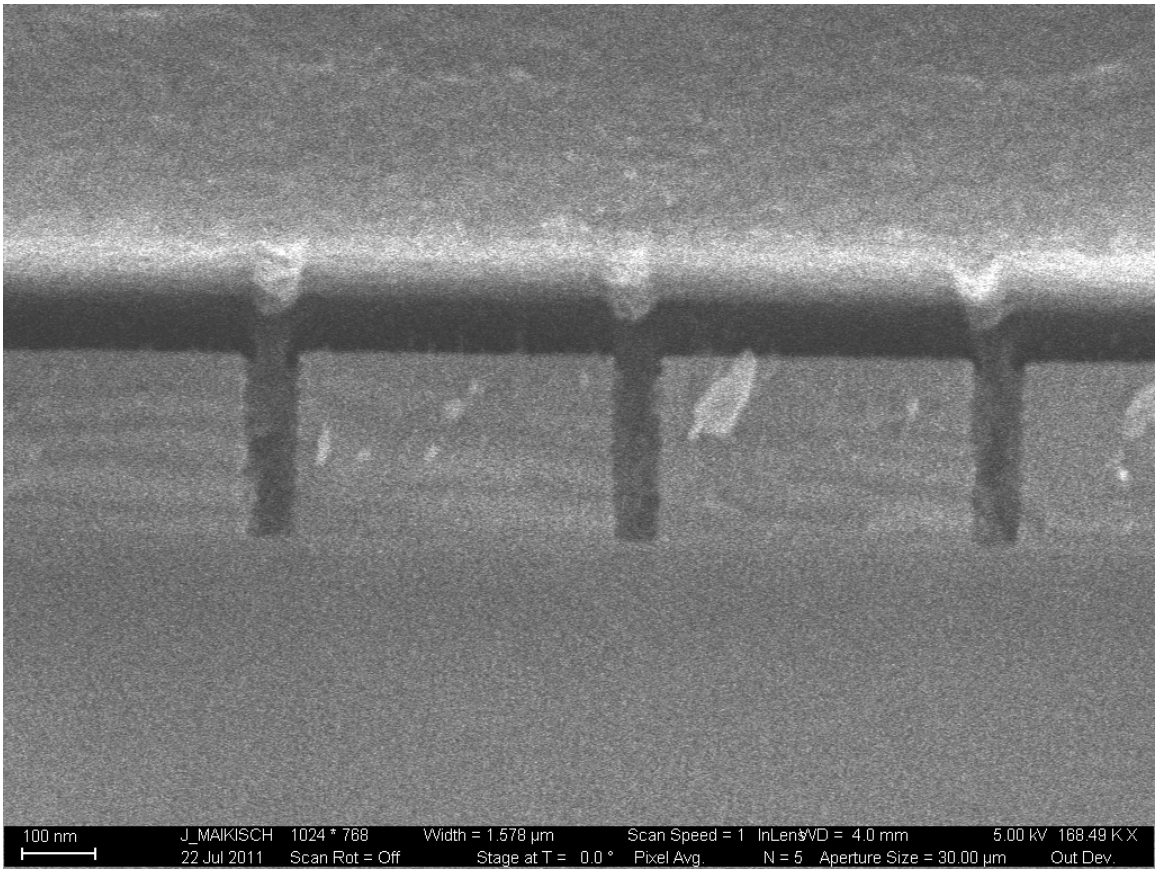

Figure 4.3: SEM cross section of secondary grating grooves filled with SU-8. Some separation is observed above the gratings from cleaving, but the grooves are completely filled.

4.4 Immobilization Layer and Microfluidic Channel Fabrication

For a functional demonstration of toluene sensing, the PBIBMA immobilization layer is deposited with a dip process. The steps in this process are listed in Appendix D. The substrate is dipped in a solution of PBIBMA in toluene at a concentration of $35 mg/ml$ and motor-drawn at a constant speed of $0.7 mm/\sec$. This produces a $70 nm$

PBIBMA layer. Excess PBIBMA is carefully removed with an acetone-soaked wipe to ensure proper adhesive bonding.

Microfluidic channels are fabricated in sheets of Teflon PFA to deliver toluene to the PBIBMA immobilization layer for sensing. The fabrication steps are listed in Appendix D. The process of fabricating the microchannel assembly and bonding it to the sensor is shown in Fig. 4.4. The microchannels are patterned in a sheet of Teflon PFA and then capped with an additional sheet. The sheets are bonded with Loctite 401 adhesive after applying the 770 surface primer and allowed to cure for 24 hours. The resulting microchannels are $3mm$ wide and $254\mu m$ thick (the thickness of one Teflon PFA sheet). The microchannel assembly is then secured to the sensor with Loctite 401 and allowed to cure for an additional 24 hours. The 770 surface primer is only applied to the Teflon PFA. A bond strength of $100\,psi$ for Teflon PFA with Loctite 401 and the 770 surface primer is reported [103]. Assembled microchannels maintained structural integrity with flow rates in excess of $1ml/\min$. More permanent microchannels for a commercially offered sensor can be fabricated directly in the SU-8 cladding. This method of microchannel fabrication is discussed in Chapter 8.

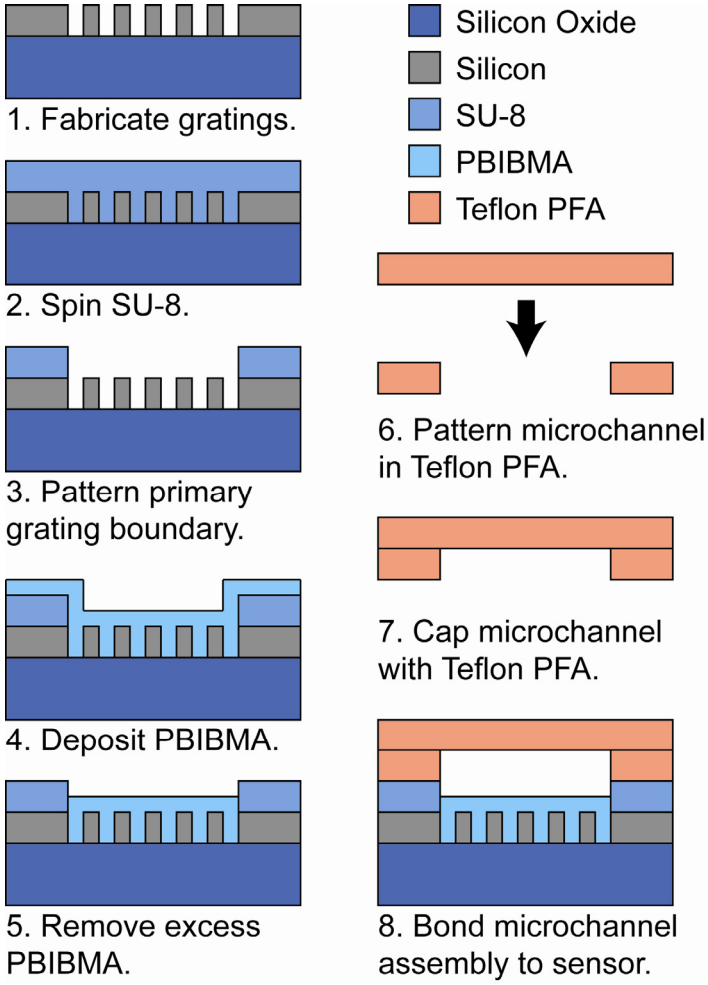

Figure 4.4: Deposition of the PBIBMA immobilization layer and fabrication of the Teflon PFA microfluidic assembly.

CHAPTER 5

EXPERIMENTAL APPARATUS AND METHODOLOGY

Characterization of the CSDS gratings and the functional demonstration of a toluene sensor require a robust experimental apparatus. Since light is diffracted by the grating into multiple directions, accurate detection is a challenge. To accomplish detection in the plane of operation, multiple photodetectors must be used. Each must be individually aligned and calibrated. This configuration is further complicated by the required optics to image the output onto the photodetector. Errors in alignment or calibration can result in erroneous measurements. A vertical detection scheme is preferable to an in-plane configuration. This allows use of an infrared camera to detect simultaneously all the diffracted orders. This relieves the limitations of using multiple external photodetectors. To accomplish this, vertical out-coupling gratings were designed. Also, light incident upon the gratings must be a slab-confined beam with finite width. Coupling of light into the SOI piece requires use of a 2-D waveguide. The transition from the 2-D input waveguide to the 1-D slab structure must minimize beam divergence and radiative loss. This requires careful design of the input waveguide.

The method of measurement must be accurate. In addition, the method should be capable of performing measurements in real-time. In the vertical detection scheme used, all diffraction orders are concurrently captured by the infrared camera. Analyzing the captured image with a Labview [134] program enables the desired diffracted order intensities to be measured in real-time. This program is configured to remove background pixel levels and calculate the recorded diffraction efficiencies in real time.

A functional demonstration of a toluene sensor requires microfluidic delivery. Fabrication of microfluidic channels with Teflon PFA was detailed in Chapter 4. Delivery of the analyte to the microchannels is accomplished with syringe pumps. Employing two syringe pumps enables the concentration to be varied while maintaining a constant fluid flow rate. A constant flow rate is critical in comparing measurements for various toluene concentrations.

Presented here is the developed experimental apparatus, including the designed out-coupling gratings and input waveguide, and measurement methodology. This apparatus is employed for characterization of the primary and secondary gratings in Chapter 6. It is also employed for characterization of the sensor response for an individual sensor and a linear array of sensors in Chapter 7. Also presented is the apparatus for fluid delivery to the sensor microchannels. This apparatus is employed for the functional toluene sensor demonstration in Chapter 7.

5.1 Experimental Apparatus

The experimental apparatus is illustrated in Fig. 5.1. Monochromatic light at 1550*nm* is provided by a Hewlett Packard [28] 81689A tunable laser. The line width of the source is 1*nm* at 1550*nm* as determined by an Agilent [28] 86142B optical spectrum analyzer. This source is capable of producing up to 5*mW* of optical power. The source light polarization is controlled by a Hewlett Packard 11896A polarization controller. The light is coupled into the sample under test by a tapered fiber acquired from OZ Optics [135].

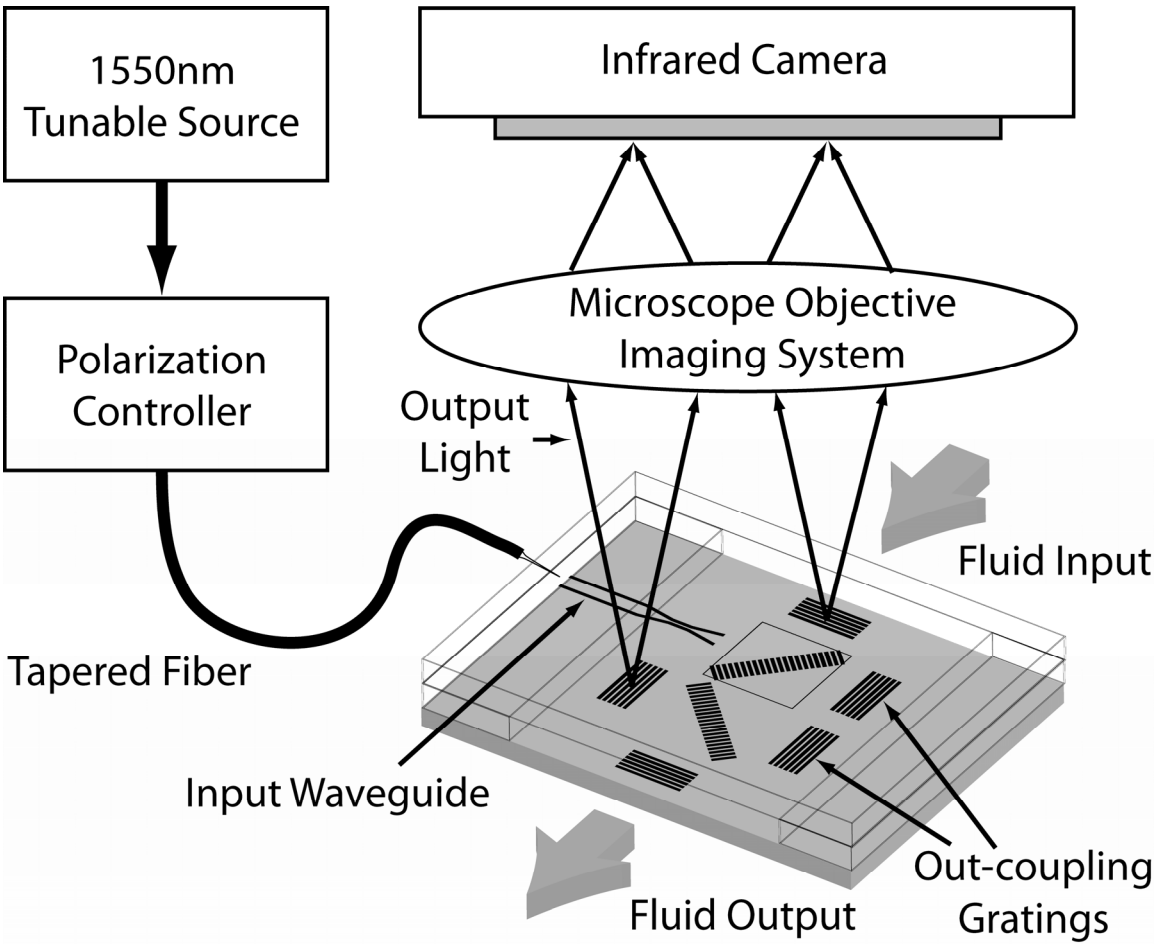

Figure 5.1: Experimental apparatus for the functional toluene sensor demonstration. Polarization-controlled monochromatic light is coupled to the sample by tapered fiber. Diffracted light is coupled out-of-plane by out-coupling gratings. It is then imaged by a microscope objective to an infrared camera for measurement.

The tapered fiber is polarization-maintaining to minimize variations in the incident polarization. It produces a light spot diameter of $2.5 \pm 0.5 \mu m$ and has a working distance of $14.0 \pm 2.0 \mu m$. An anti-reflective (AR) coating at $1550 nm$ is also incorporated to maximize the optical power coupled into the sample. Light coupled out of the sample by the out-coupling gratings is imaged by a Mitutoyo [136] microscope. The objective lenses used have magnifications of 10x, 20x, and 50x with corresponding numerical apertures (NA) of 0.28, 0.42, and 0.42. The image is then recorded by a Hamamatsu

[137] C2741 infrared camera with a resolution of 640x480 pixels and 8-bits per pixel. For the grating and sensor characterization, refractive index oils obtained from Cargille Laboratories [138] are flowed into the primary grating boundary. For the functional toluene sensor demonstration, a microchannel is fabricated and fluid is delivered by two KD Scientific [139] syringe pumps. The fluid is coupled into and out of the microchannel by Upchurch Scientific [140] NanoPorts. Microfluidic delivery is detailed later in this chapter. The configuration in the W417 Optics Laboratory in the Van Leer building is pictured in Fig. 5.2.

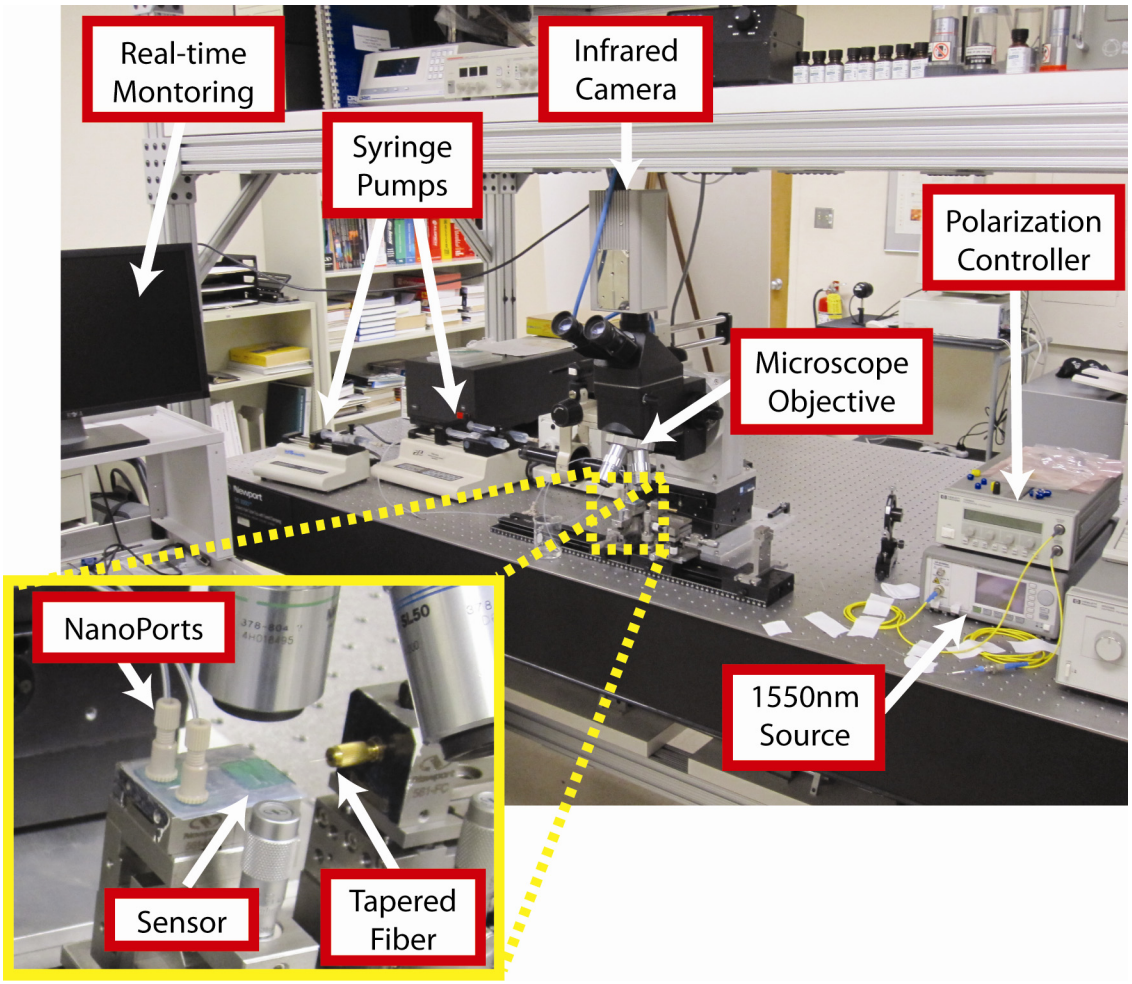

Figure 5.2: Experimental apparatus for the functional toluene sensor demonstration in the W417 Optics Laboratory.

The infrared camera is connected to a personal computer. Captured images are analyzed and the results are recorded in real-time by a custom Labview program. The Labview program and measurement methodology are discussed later in this chapter. Before measurements are taken, the appropriate polarization is established with the tapered fiber and a Glan-air polarizer. The polarizer is oriented to pass horizontally polarized light. By adjusting the polarization controller for a null in intensity, the desired vertical polarization is achieved. This polarization is normally stable for several hours, though for long duration measurements it is checked after 2 hours.

5.2 Out-coupling Grating Design

The out-coupling grating is designed to couple light vertically out-of-plane for detection. The configuration is shown in Fig. 5.3.

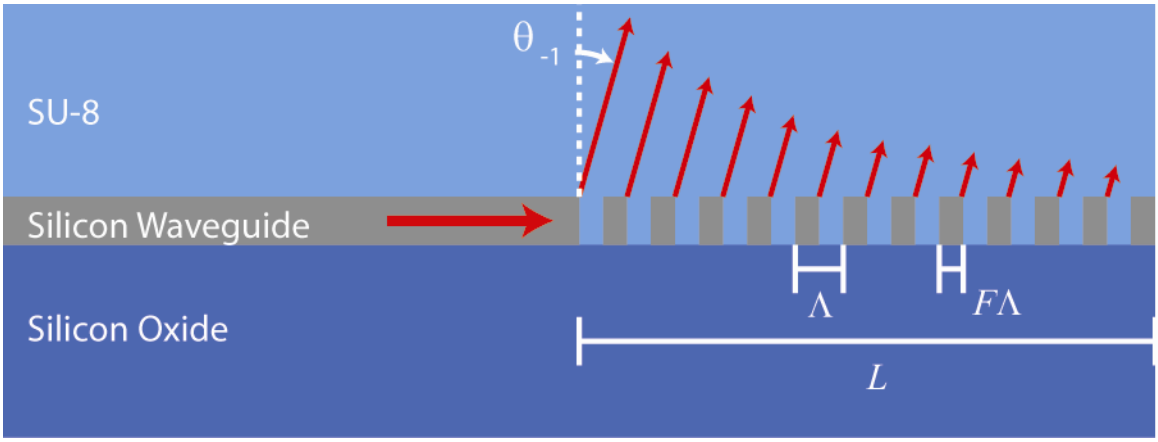

Figure 5.3: Configuration of the out-coupling grating. Grating grooves are etched to the buried-oxide layer for concurrent fabrication with CSDS gratings. The grating period is Λ, the fill factor is F, and the interaction length is L. The output angle is θ_{-1}.

The grating grooves are etched down to the buried-oxide (BOX) layer for concurrent fabrication with the CSDS gratings. The propagation constant of the diffracted light is

$$\beta_m = \beta_0 + 2m\pi / \Lambda, \tag{5.1}$$

where β_0 is the waveguide propagation constant, Λ is the grating period, and *m* is an integer. The diffracted output angle is

$$\theta_m = \sin^{-1}\left(\frac{\beta_m}{n_{SU-8}k_0}\right), \tag{5.2}$$

where $k_0 = 2\pi / \lambda$ is the freespace wavenumber and $n_{SU-8} = 1.581$ is the refractive index of the SU-8 cladding. The conditions for a single output beam have been reported by Tamir [141]. For the output angle to be real, $m < 0$. Output at $m = -1$ requires

$$\left|N_{eff} - (\lambda / \Lambda)\right| < n_{SU-8}, \tag{5.3}$$

where $N_{eff} = 2.341$ is the effective index of the waveguide when no grating is present. For no output beam with $m \le -2$,

$$2(\lambda / \Lambda) - N_{eff} > n_{SU-8}. \tag{5.4}$$

The half angular aperture of the microscope objective is

$$\alpha = \sin^{-1}(NA / n_{SU-8}), \tag{5.5}$$

where NA is the numerical aperture. Using the 20x microscope objective with $NA = 0.42$, $\alpha = 15.41°$. This represents the maximum value for the grating coupler output angle, θ_{-1}. These constraints yield the grating period condition, $0.3952\mu m < \Lambda < 0.7904\mu m$. However, care must be exercised to avoid the case, $\Lambda = N_{eff}d = 0.6621\mu m$. This case represents a resonant Bragg reflector with $\beta_0 d = 2\pi$ and $\theta_{-1} = 0$ [141].

The grating period, Λ, and fill factor, *F*, are determined with the cavity modeling framework (CAMFR) software developed at Ghent University [142, 143]. The CAMFR

software is a full-vectorial implementation of Maxwell's equations based on eigenmode expansion. The designed out-coupling grating has a period of $\Lambda = 0.733\mu m$ and a fill factor of $F = 0.93$. This gives an output angle of $\theta_{-1} = 8.23°$. With 200 grating periods, 65.57% of the incident light is coupled out-of-plane in the designed order. Of the remainder, 8.67% is reflected, 0.35% is transmitted, and 25.41% is lost to the substrate.

5.3 Input Waveguide Design

The input waveguide accepts light from the tapered fiber and produces an output beam confined by the 1-D slab waveguide. The configuration of the designed input waveguide is shown in Fig. 5.4.

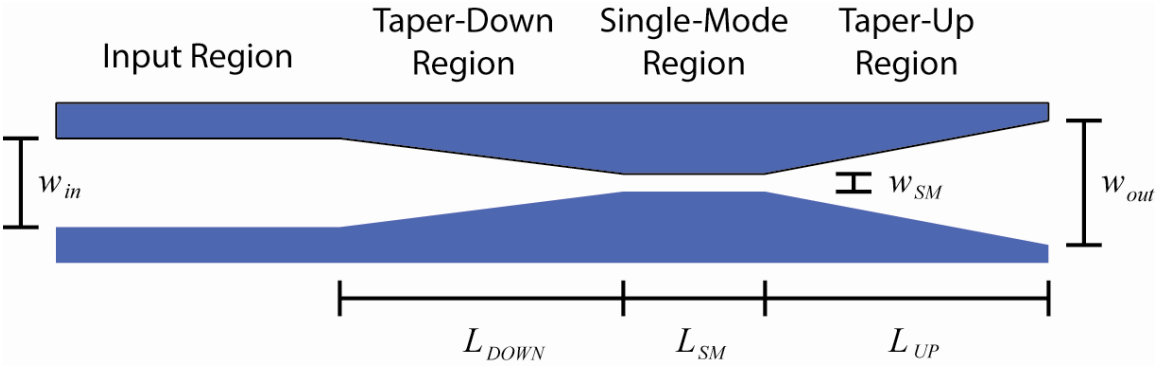

Figure 5.4: Configuration of the input waveguide. The input region accepts light from the tapered fiber. The waveguide is then tapered down to a single-mode region to reject higher-order modes. The waveguide is then tapered up to the desired width of the finite output beam.

Light is coupled into the input region via the tapered fiber. The waveguide width, w_{in}, to maximize coupling must be determined. This was done via experiment for waveguide widths of $4\mu m$, $6\mu m$, $8\mu m$, and $10\mu m$. In this experiment, light is coupled into the waveguide by the tapered fiber and coupled out via out-coupling gratings. The normalized power, P_N, detected is shown in Fig. 5.5. The chosen input waveguide with

width of $w_{in} = 6\mu m$ has the best coupling efficiency. Following the input region, the waveguide tapers down to a single-mode region. The length of this taper-down region is $L_{DOWN} = 200\mu m$ to minimize radiative loss. The single-mode region rejects higher-order modes to ensure only the fundamental mode appears at the output. The single-mode cutoff width for the waveguide is $w_{CO} = 250nm$.

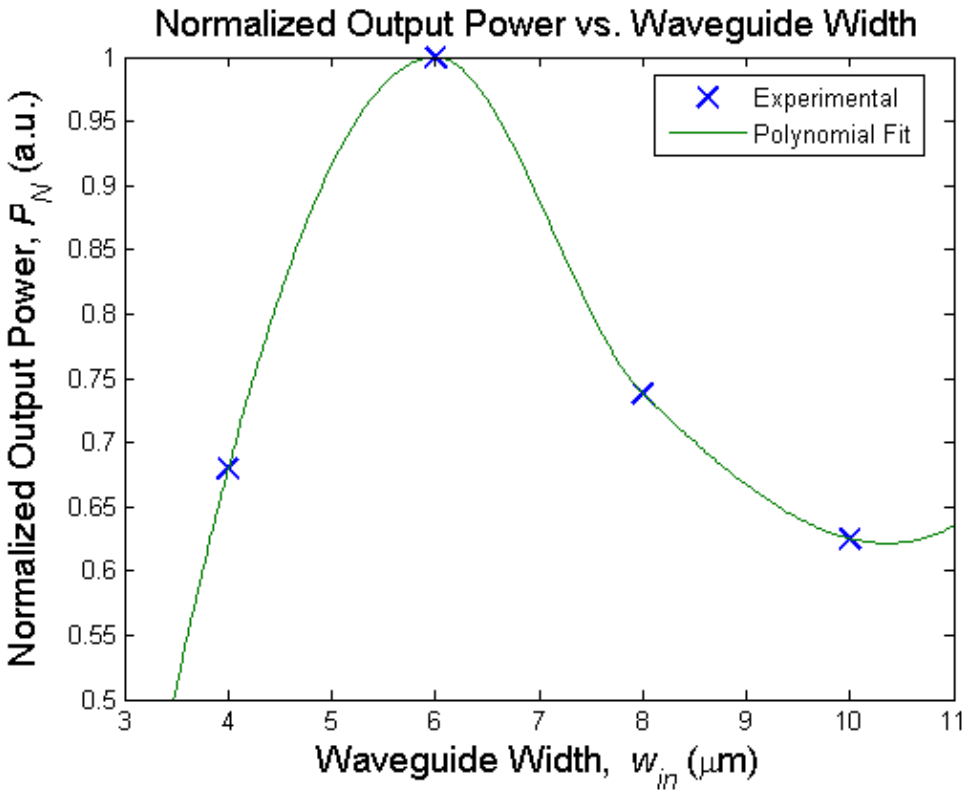

Figure 5.5: Plot of normalized output power, P_N, vs. waveguide width, w_{in}, for the input waveguide. Experiments are done for widths of $4\mu m$, $6\mu m$, $8\mu m$, and $10\mu m$.

After the single-mode region, the waveguide tapers up to the desired beam width. Single-mode region widths of $w_{SM} = 250nm$, $300nm$, and $400nm$ are fabricated and tested with an output width of $w_{out} = 10\mu m$. The single-mode region length is $L_{SM} = 100\mu m$ and the

taper-up region length is $L_{UP} = 200\mu m$. A width of $w_{SM} = 300nm$ is found to pass sufficient optical power while rejecting higher-order modes.

The taper-up region shapes the output beam to the desired width. The length and output width of the taper-up region should minimize beam divergence while not coupling to higher-order modes. Taper-up region output widths, w_{out}, and lengths, L_{UP}, are simulated with 2-D FDTD. Widths of $4-20\mu m$ and lengths of $100-500\mu m$ are simulated. A width of $w_{out} = 10\mu m$ and a length of $L_{UP} = 200\mu m$ produced the best results with a beam divergence of $5.2°$. Simulation of the design is illustrated in Fig. 5.6.

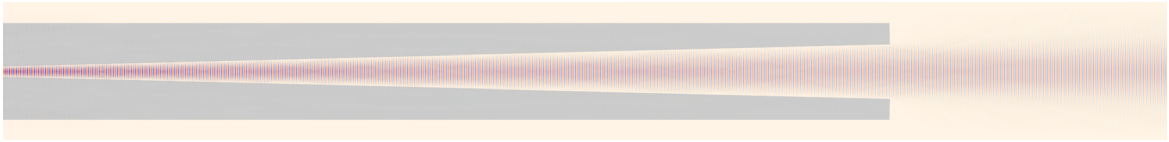

Figure 5.6: 2-D FDTD simulation of the single-mode and taper-up input waveguide regions. The single-mode region has a width of $w_{SM} = 300nm$ and a length of $L_{SM} = 100\mu m$. The taper-up region has a width of $w_{out} = 10\mu m$ and a length of $L_{UP} = 200\mu m$.

5.4 Measurement Methodology

Images captured by the infrared camera are relayed to a personal computer as depicted in Fig. 5.2. A custom Labview program analyzes the images and determines simultaneously the intensities of the diffracted orders. The program removes the background pixel levels, calculates the diffracted-order efficiencies, and records the results in a text file for further analysis. This provides an accurate measurement of the diffraction efficiencies in real-time.

A measurement of the diffracted-order intensities is illustrated in Fig. 5.7, where $I_{3,1}$ is the diffracted intensity, $I_{3,0}$ is the transmitted intensity, and $I_{1,0}$ is the reflected intensity. The measured intensity for each order is expressed as

$$I_{i,j} = \sum_{x,y} (p_{x,y} - p_{bg}), \tag{5.6}$$

where $p_{x,y}$ is a pixel in the area designated for $I_{i,j}$ in Fig. 5.7 and p_{bg} is the background pixel level.

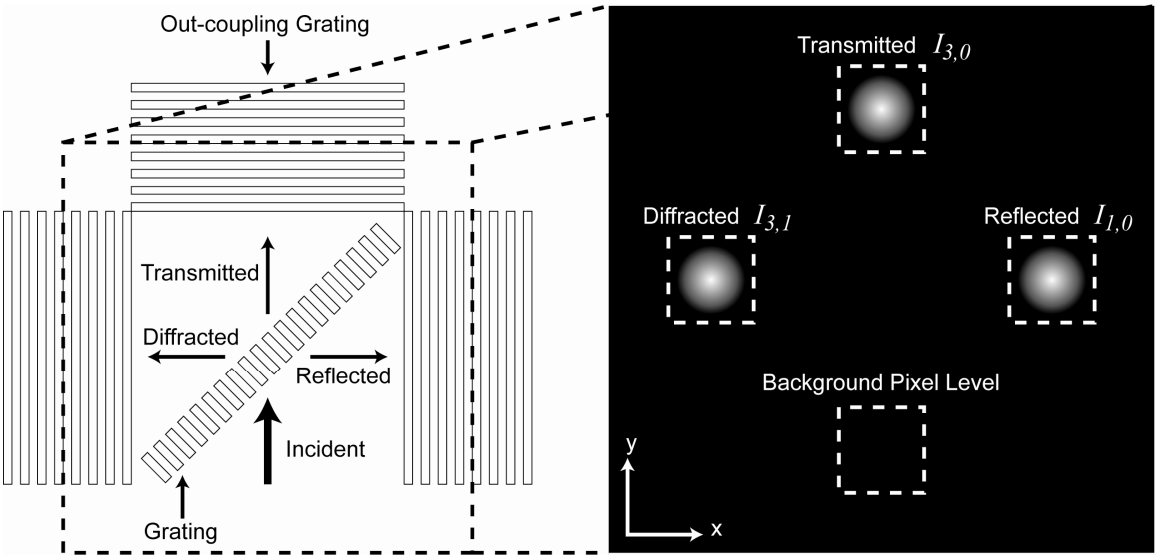

Figure 5.7: Measurement configuration with vertical coupling to an infrared camera. The background pixel level is obtained by averaging the pixel values in the designated area. The intensities for each diffracted order are obtained by summing the pixel values within the designated areas after subtracting the background pixel level.

The background pixel level is determined by averaging the pixels in the designated area with no detected light. The measured intensities are in the units of pixel value. It is unnecessary to convert the intensities to real units since the desired diffraction efficiencies are relative values. The diffraction efficiency is defined as

$$DE_{i,j} = I_{i,j} / (I_{1,0} + I_{3,0} + I_{3,1}). \tag{5.7}$$

The program records the measured diffraction efficiencies to a text file for further analysis every 33 milliseconds. It is possible to configure the program to average results over specified periods of time or apply low-pass filtering to minimize noise. In this research, only the raw data is recorded. Results for externally applying a low-pass filter are discussed for the functional toluene sensor demonstration in Chapter 7.3.

To characterize the grating (Chapters 6.1 and 6.2), sensor (Chapter 7.1), and linear array (Chapter 7.2) responses, refractive index oils are flowed into the primary grating boundary and the diffraction efficiencies are measured. After each measurement, the sample is cleaned with isopropyl alcohol and the refractive index oil for the next measurement is flowed. For the functional toluene sensor demonstration, the apparatus and methodology in the next section are used.

5.5 Microfluidic Delivery of Toluene

Functionally demonstrating a toluene sensor requires microfluidic delivery. This is accomplished with the configuration in Fig. 5.8. Fluid flow is controlled by two KD Scientific syringe pumps. This enables variation of the toluene concentration while maintaining a constant flow rate. A constant flow rate is critical in making accurate comparisons of measurements for differing toluene concentrations. The syringes used are made from polytetrafluoroethylene (PTFE). Fluid is transported through fluorinated ethylene propylene (FEP) tubing. PTFE and FEP are widely used thermopolymers that provide excellent solvent resistance [102]. Flows from each syringe pump are combined with a y-connector. The combined flow is then coupled to the fabricated microchannel inlet via NanoPort [140]. An additional NanoPort provides a connection to the microchannel outlet for waste fluid collection. The NanoPorts, y-connector, and syringe

adapters are made from polyether ether ketone (PEEK). PEEK is another thermopolymer with excellent solvent resistance [144].

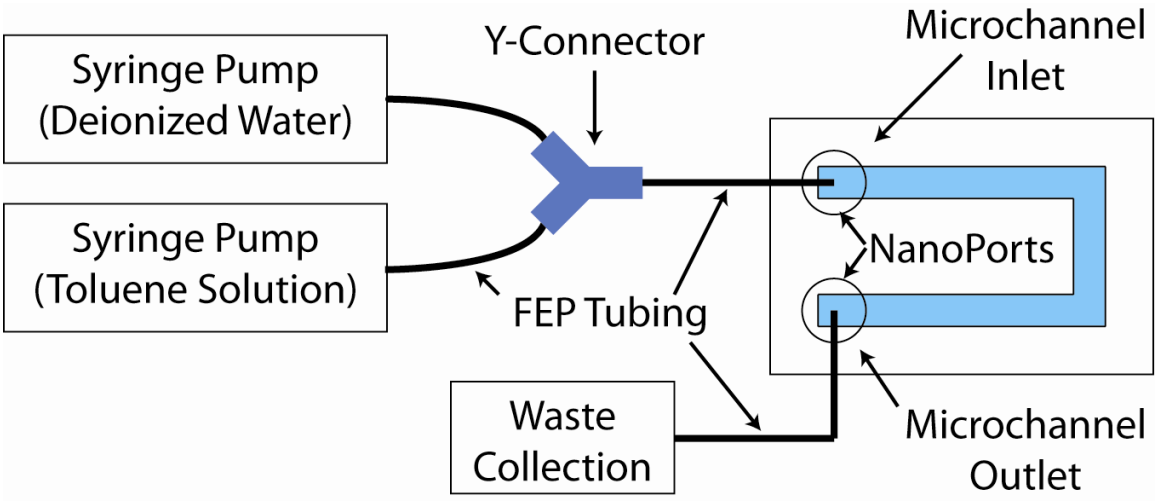

Figure 5.8: Apparatus for microfluidic delivery of toluene. Deionized water and a solution of toluene in deionized water are delivered by syringe pump. The flow rate of each pump is controlled to achieve the desired toluene concentration.

Toluene is dissolved in deionized water at a saturated concentration of $C_{sat} = 535\text{ppm}$. Delivery of this solution is controlled by one syringe pump. The remaining syringe pump delivers pure deionized water. The delivered toluene concentration is controlled by adjusting the flow rates of the two syringe pumps. The combined flow rate is chosen to maintain a flow pressure, P_F, below $1 psig$ within the microchannel. This minimizes the chance of leakage. The maximum flow pressure within the microchannel is, $P_F = \Delta P_O + \Delta P_C$, where ΔP_O is the pressure drop in the outlet tubing and ΔP_C is the pressure drop in the microchannel. The pressure drops are determined by solving Poiseuille's equation [145] for laminar flow,

$$\Delta P = \frac{128 \mu L Q}{\pi D_H^4} \tag{5.8}$$

where $\mu = 1.0 cP$ is the dynamic viscosity of water, L is the length of the section (50mm for the microchannel and 200mm for the outlet tubing), and Q is the volumetric flow rate. The hydraulic diameter is defined as $D_H = 4A / L_P$, where A is the cross-sectional area and L_P is the wetted perimeter. The hydraulic diameter is $468 \mu m$ for the microchannel and $508 \mu m$ for the outlet tubing. A combined flow rate of $Q = 500 \mu L / \min$ is chosen to maintain a maximum pressure of $P_F = 0.199 psig$ which is well below the 1$psig$ threshold. The necessary flow rate for the toluene syringe to deliver a concentration C is $Q_{toluene} = (C / C_{sat}) Q$. The corresponding flow rate for the water syringe is $Q_{water} = Q - Q_{toluene}$. Toluene concentrations of 100ppm, 200ppm, and 500ppm are measured in the functional demonstration detailed in Chapter 7.3.

CHAPTER 6

EXPERIMENTAL GRATING CHARACTERIZATION

Presented here is the characterization of the CSDS gratings with the experimental apparatus detailed in Chapter 5. The primary gratings are characterized as a function of variations in the refractive index of the surrounding bounded region. The secondary grating is characterized for variations in the incident angle. These characterizations represent the primary functions of the respective gratings in the CSDS platform. Experiments are performed with the Optics Laboratory facilities in room W417 of the Van Leer building. Also presented is a simulation of the observed grating reflection. Refinements to limit these reflections are introduced and simulated.

6.1 Primary Grating Characterization

The primary grating designs are fabricated in the configuration shown in Fig. 6.1. Light is shaped by the input waveguide and is incident upon the grating. Out-coupling gratings capture the diffracted, transmitted, and reflected light for detection. A $100\mu m$ square is defined in the SU-8 cladding for the grating boundary. Refractive index oils are flowed in the grating boundary region. The oils used have refractive indices of $n = 1.4318$, 1.4514, 1.4712, 1.4910, and 1.5108. After each measurement, the sample is cleaned with isopropyl alcohol and the next oil is flowed through the defined square. Experimental results are compared with FDTD simulation with Gaussian beam incidence. Results are shown in Figs. 6.2 and 6.3.

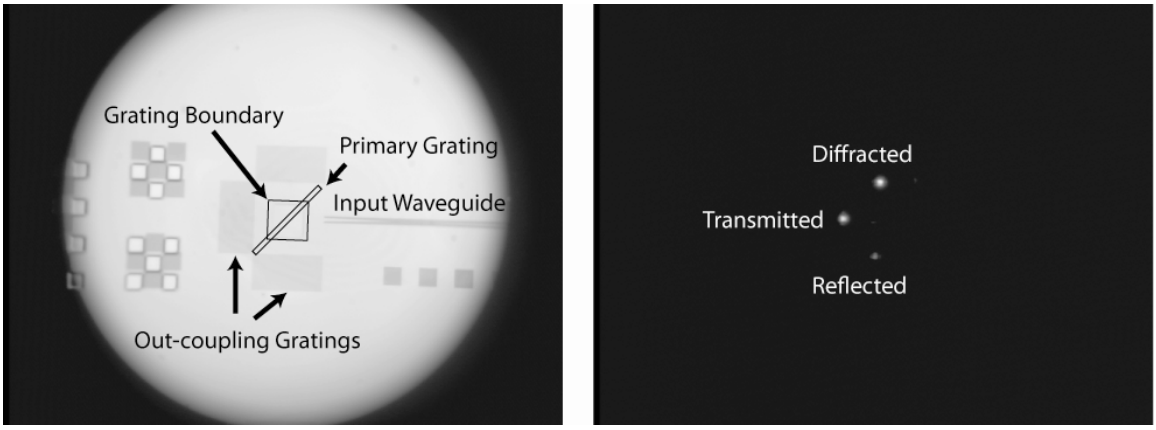

Figure 6.1: Primary grating experimental configuration (left) and measurement (right) for the 50% primary grating with the $n = 1.4318$ refractive index oil within the grating boundary.

There is a significant reflection which subtracts from the transmitted power. Characterization of this undesired reflection is discussed in Chapter 6.3. This reflection is undesirable, but does not detract from the primary grating's variable-diffracted-angle function. The efficiency of the diffracted order is in good agreement with the simulations. The diffracted order efficiency is within 4% of the simulated values. As designed, the primary grating diffraction efficiencies vary little, even with large refractive index changes. This experiment demonstrates that the primary gratings serve their designed function in the CSDS platform.

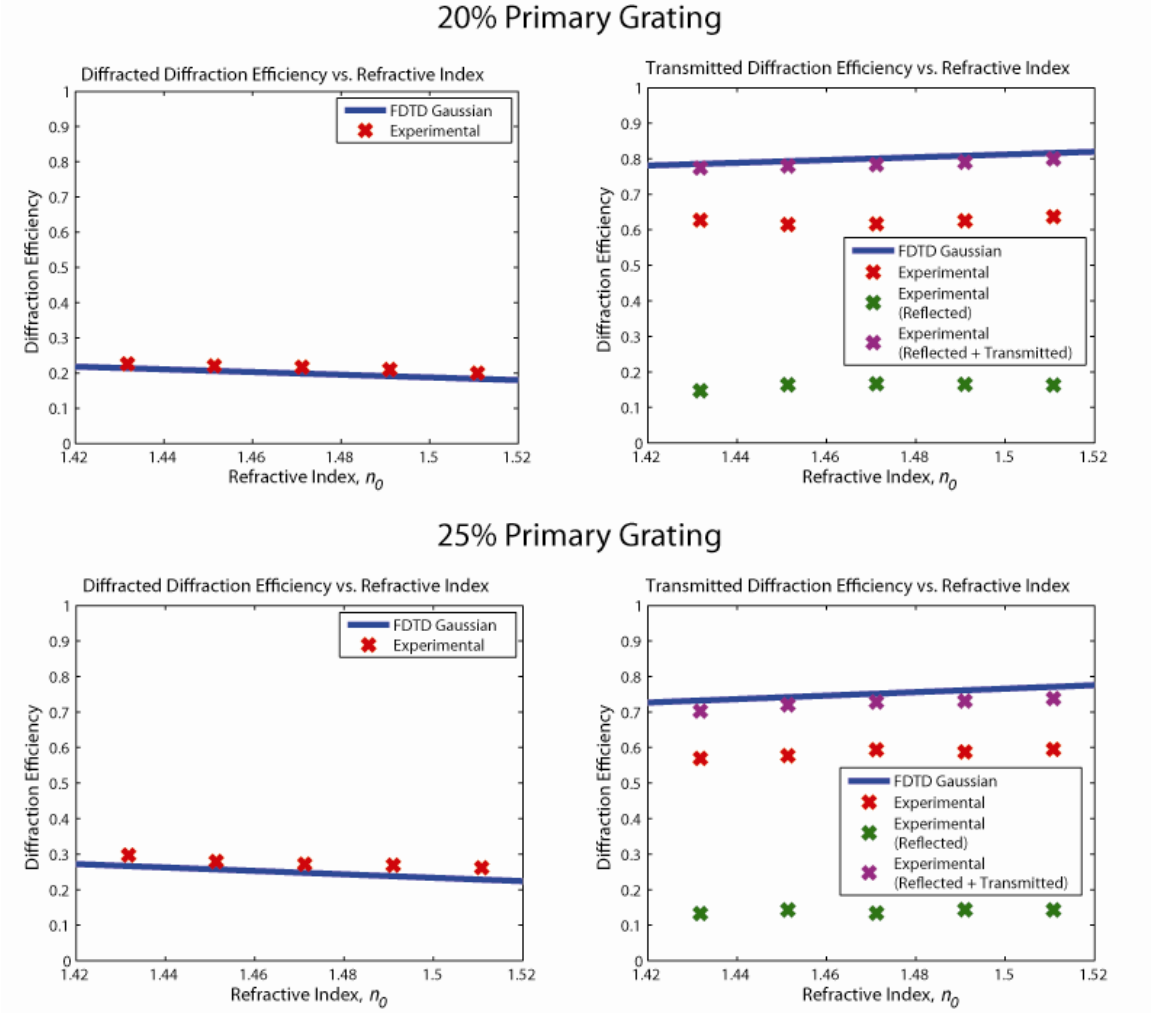

Figure 6.2: Experimental results compared with FDTD simulation with Gaussian beam incidence for the 20% and 25% primary grating designs. The diffraction efficiency is in good agreement. A significant reflection subtracts from the transmitted power.

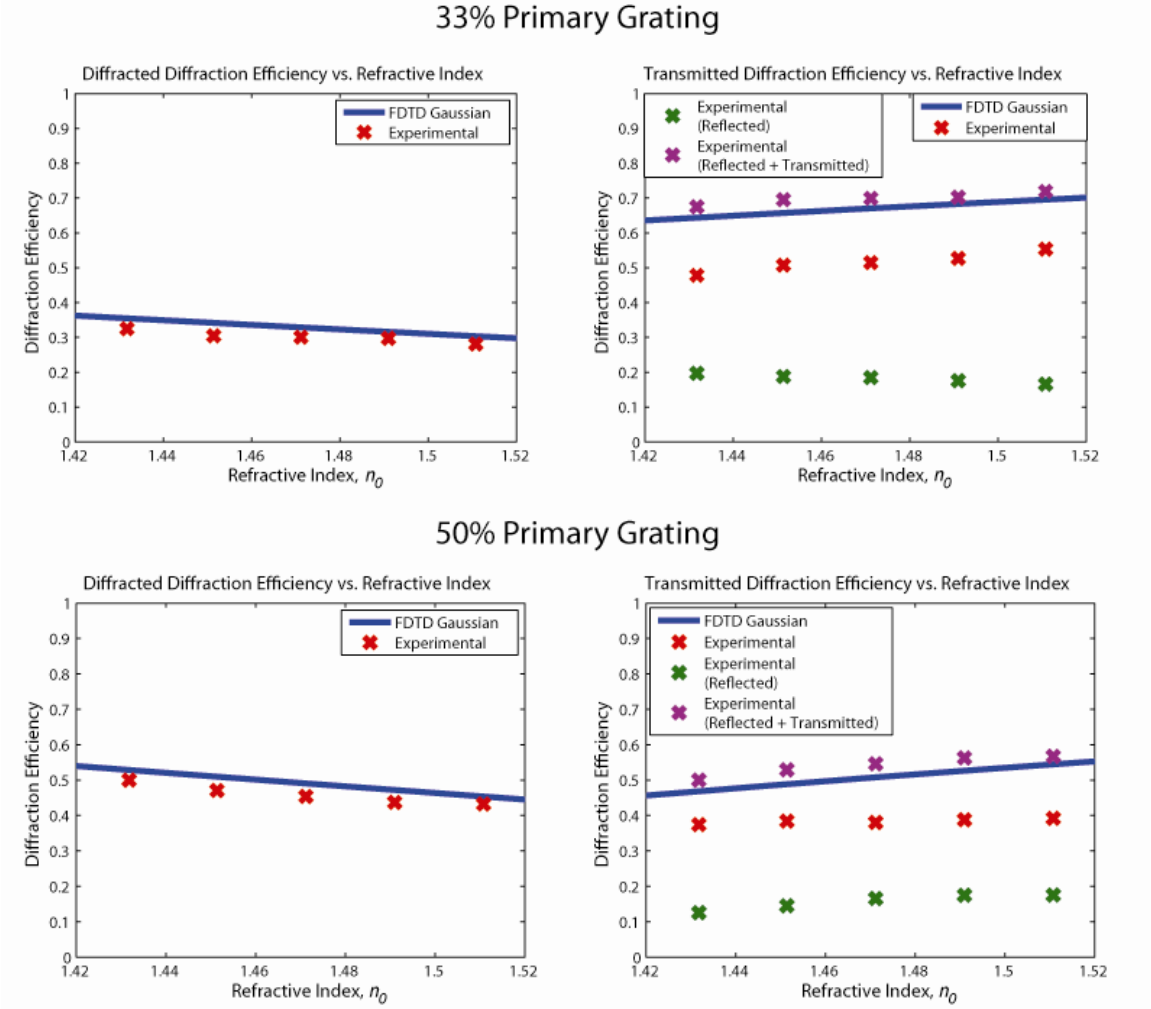

Figure 6.3: Experimental results compared with FDTD simulation with Gaussian beam incidence for the 33% and 50% primary grating designs. The diffraction efficiency is in good agreement. A significant reflection subtracts from the transmitted power.

6.2 Secondary Grating Characterization

The secondary grating is fabricated in the configuration shown in Fig. 6.4. This configuration is the similar to that for the primary grating. There is no grating boundary and the entire device is clad with SU-8. The out-coupling grating for the diffracted order is oriented at 38.5° to match the diffracted angle. Several gratings are fabricated in the same sample to accommodate different incident angles. Light is incident upon the

secondary grating at angles ranging from $\theta = 43°$ to $47°$ in $0.5°$ increments. Bends in the single-mode regions of the input waveguides orient incident light to the desired angle. Experimental results are compared with FDTD simulation with Gaussian beam incidence in Fig. 6.5.

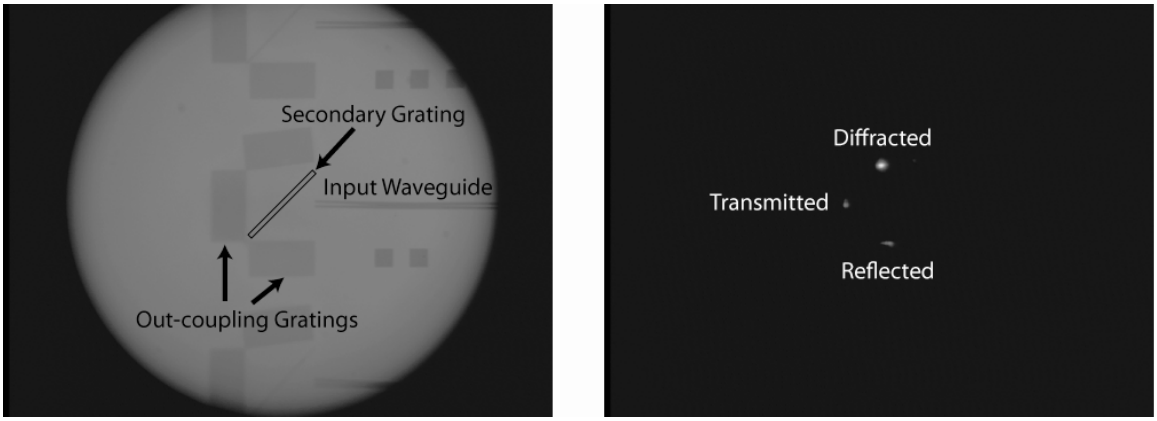

Figure 6.4: Secondary grating experimental configuration (left) and measurement (right) for an incident angle of $\theta = 43.5°$.

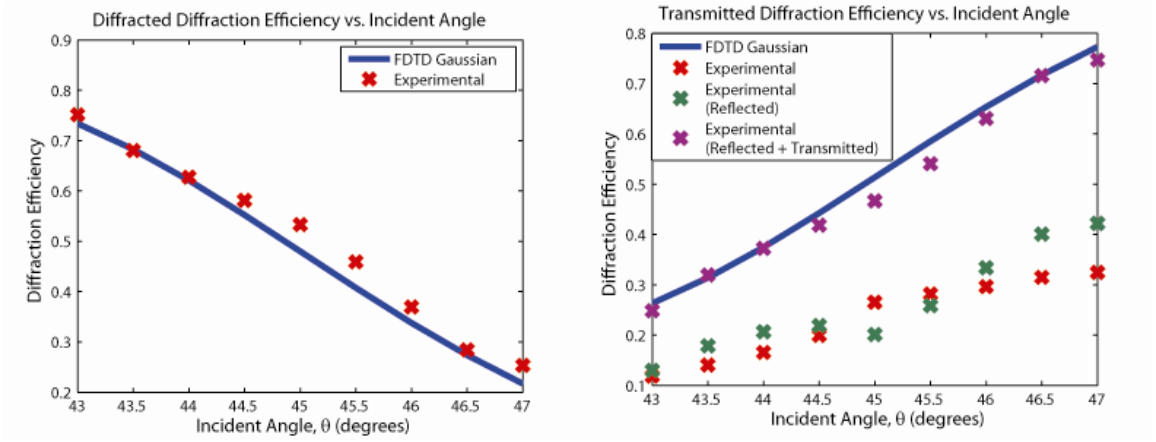

Figure 6.5: Experimental results compared with FDTD simulation with Gaussian beam incidence for the secondary grating design. The diffraction efficiency is in good agreement. A significant reflection subtracts from the transmitted power.

As with the primary grating results, there is a significant reflection which subtracts from the transmitted power. Characterization of this undesired reflection is discussed in the next section. The efficiency of the diffracted order is in good agreement with the simulations. The diffracted order efficiency was within 5% of the simulated values. This reflection is undesirable, but does not diminish the quality of measurement. The desired linear, monotonic behavior is observed. Detection of the diffraction efficiency will give an accurate measurement. This demonstrates that the secondary grating serves its designed function in the CSDS platform.

6.3 Characterization of Grating Reflection

The gratings characterized in Chapters 6.1 and 6.2 exhibit significant unwanted reflections. The diffracted efficiencies agree well with the simulation data and the gratings perform their designed functions, but it is desirable to minimize or eliminate these reflections. Here, these reflections are investigated and refinements to minimize them are introduced and simulated.

6.3.1 2-D FDTD Grating Simulation

In Chapter 3, the designed gratings were simulated with 2-D FDTD analysis with Gaussian beam incidence. The experimentally observed reflections do not appear as illustrated in Fig. 3.8. It is necessary to determine the source of these reflections and if they are unique to the fabricated gratings. An anti-reflection (AR) layer is a simple one-layer structure that removes the grating parameters of thickness, period, and fill factor. Experimental and simulated results for a fabricated AR layer are presented in the next section.

6.3.2 Test Anti-Reflection Layer

An anti-reflection layer was designed with a thickness of $729nm$ and an incident angle of $30°$. This AR layer was fabricated with the process detailed in Chapter 4 and tested with the apparatus detailed in Chapter 5. A similar unwanted reflection was detected in Fig. 6.6. Over 61% of the incident power was reflected.

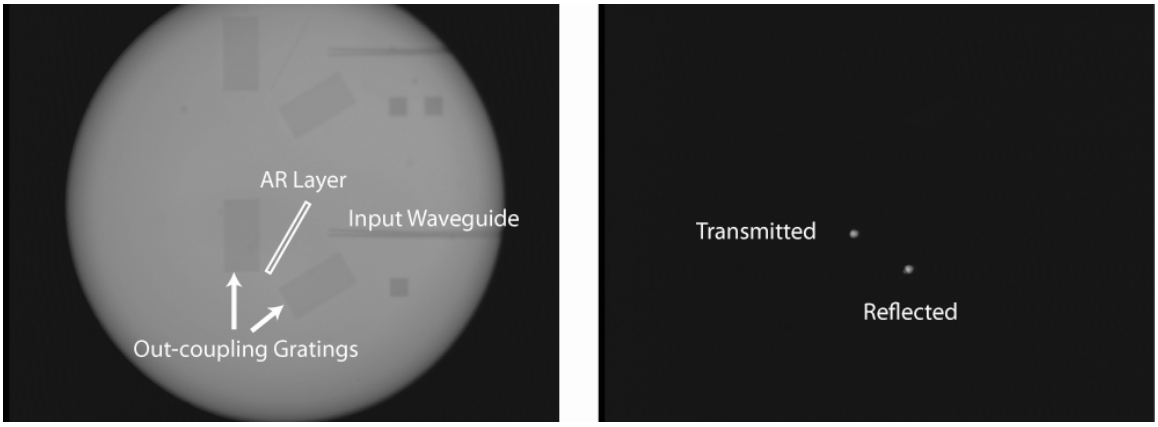

Figure 6.6: Fabricated AR layer with input waveguide and out-coupling gratings (left). The transmitted and reflected light are coupled out-of-plane by the out-coupling gratings and detected (right). Significant unwanted reflection is observed.

The AR layer and input waveguide were simulated with 2-D FDTD analysis in Fig. 6.7. The simulation space was constructed to match the fabricated device. Similar to the 2-D FDTD grating simulations, no reflection was observed. This indicates that the source of these reflections is not unique to the fabricated gratings. It also indicates that the input waveguide structure is not the cause.

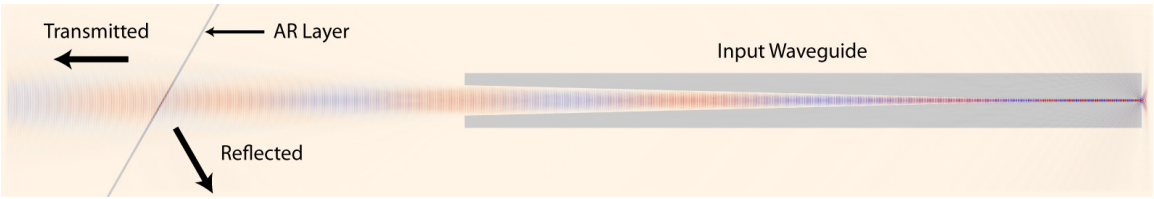

Figure 6.7: 2-D FDTD simulation of input waveguide and AR layer. The simulation shows no reflection at the AR layer.

To reproduce and analyze these reflections, 3-D FDTD simulation with Gaussian beam incidence was used. The result for the simulated AR layer is shown in Fig. 6.8.

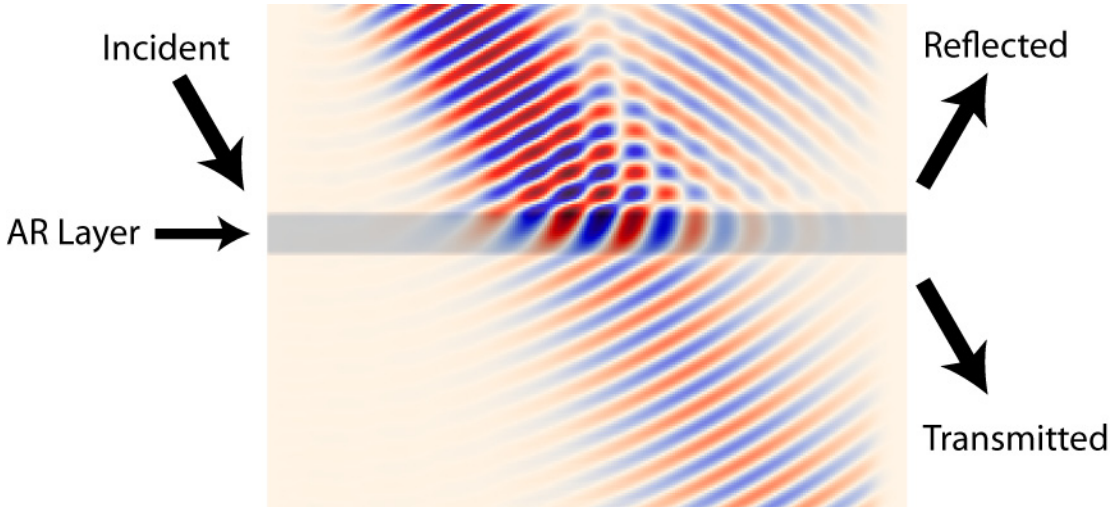

Figure 6.8: 3-D FDTD simulation of the fabricated AR layer. The experimentally observed reflection is present.

The simulated reflection is 43%. This shows that 3-D FDTD simulation is capable of reproducing the undesired reflections. The grating designs are simulated with 3-D FDTD in the next section.

6.3.3 3-D FDTD Grating Simulation

The primary and secondary gratings were simulated with 3-D FDTD analysis with Gaussian beam incidence. The result for the 20% primary grating is shown in Fig. 6.9.

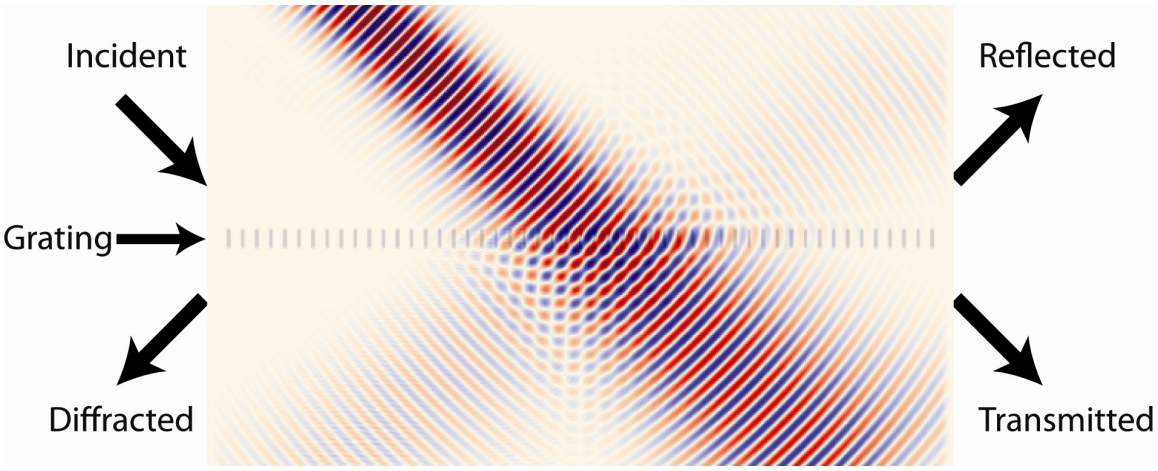

Figure 6.9: 3-D FDTD simulation of the 20% primary grating. The experimentally observed reflection is present.

The simulated diffracted-order efficiencies are summarized in Table 6.1. The simulated reflections are reasonably close to experimental observation. These simulations indicate that the undesired reflections are a result of mode-field mismatch between the slab waveguide region and the grating region. This is due to the large refractive index contrast between the grating grooves and ridges. To reduce the refractive index contrast, alternate shallow-groove gratings are introduced in the next section.

Table 6.1: Gratings simulated with 3-D FDTD analysis with Gaussian beam incidence. Normal gratings are the designs presented in Chapter 3 with a groove depth $d_G = 250nm$. Shallow gratings have a groove depth of $d_G = 50nm$.

Primary Grating ($\lambda = 1.55\mu m$, $\Lambda = 0.475\mu m$)						
Grating Parameters			**Diffraction Efficiencies**			
Target Diffraction Efficiency $DE_{3,1}^{T}$ (%)	Thickness d (μm)	Fill Factor F	Diffracted $DE_{3,1}$ (%)	Transmitted $DE_{3,0}$ (%)	Backward Diffracted $DE_{1,1}$ (%)	Reflected $DE_{1,0}$ (%)
20% Normal	0.615	0.811	18.77	71.59	0.00	9.63
20% Shallow	1.112	0.790	17.51	81.75	0.00	0.74
25% Normal	0.636	0.794	23.14	68.47	0.01	8.38
25% Shallow	1.109	0.760	22.85	76.56	0.00	0.59
33% Normal	0.668	0.770	32.19	56.51	0.01	11.29
33% Shallow	1.132	0.720	31.15	68.18	0.00	0.66
50% Normal	0.725	0.731	44.64	46.21	0.00	9.15
50% Shallow	1.240	0.658	43.51	55.57	0.00	0.92
Secondary Grating ($\lambda = 1.55\mu m$, $\Lambda = 0.498\mu m$)						
Normal	3.105	0.852	42.84	39.58	0.23	17.35
Shallow	3.070	0.780	46.32	52.78	0.19	0.71

6.3.4 Simulation of Alternate Shallow-Groove Gratings

Gratings were designed with shallow grooves that are 50*nm* deep rather than extending the entire silicon device layer thickness as in Fig. 6.10. This greatly reduces the refractive index contrast between the gratings grooves and ridges. This approach was used for an alternate AR layer design and resulted in a simulated reflection of only 3%. The design process for these shallow-groove gratings is the same as that for the gratings designed in Chapter 3.

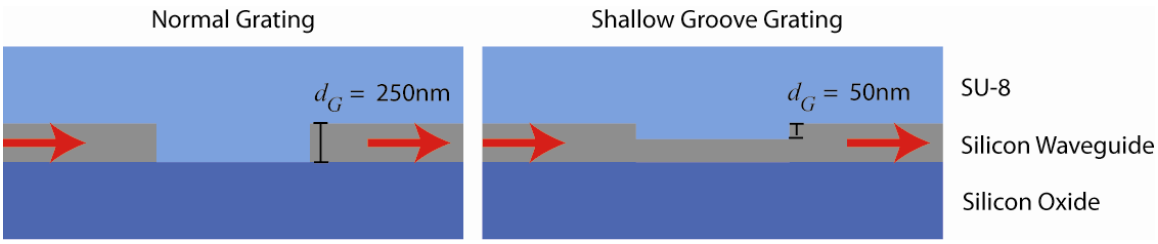

Figure 6.10: Grating groove profile for normal gratings (left) and shallow gratings (right). Normal gratings have grooves extending the entire silicon device layer thickness ($d_G = 250nm$) and shallow gratings have a groove depth of $d_G = 50nm$.

These shallow-groove gratings were simulated and the results are summarized in Table 6.1. The result for the 20% primary shallow groove grating is shown in Fig. 6.11. The undesired reflections are greatly reduced. This indicates that these reflections can be minimized by designing gratings with shallow grooves. A method of fabricating these shallow gratings is discussed in Chapter 8.

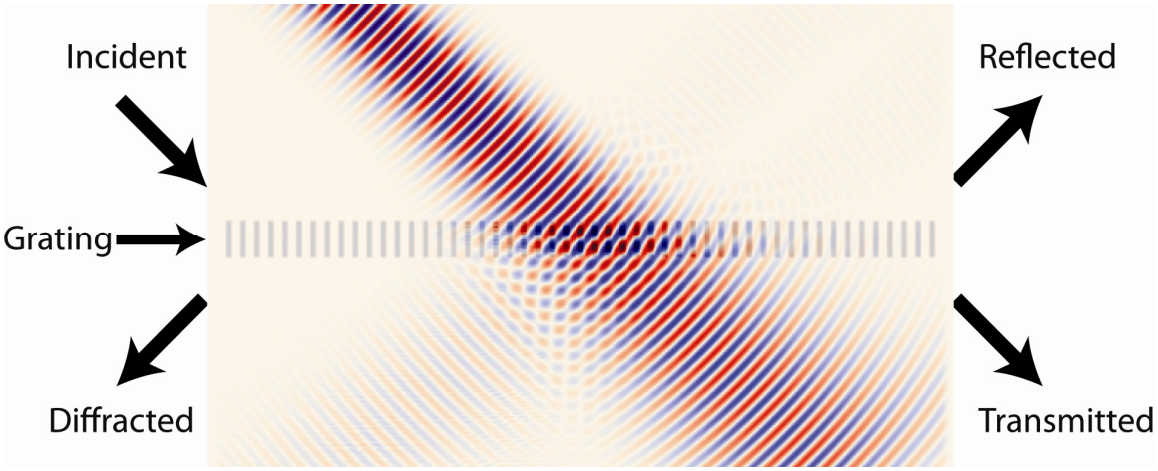

Figure 6.11: 3-D FDTD simulation of the 20% primary grating with shallow grooves. The unwanted reflection is reduced with this design.

CHAPTER 7

EXPERIMENTAL SENSOR RESULTS

Presented here are experimental results for the CSDS sensor with the apparatus detailed in Chapter 5. Sensors with each primary grating design are characterized. The sensor response is measured by flowing refractive index oils into the primary grating boundary region. Linear arrays of CSDS sensors are also characterized. Sensors in an array are individually addressed with various refractive index oils. Linear sensor arrays form the basis of 2-D sensor arrays. These experiments demonstrate the sensor response to changes in refractive index and the functionality required for 2-D sensor arrays. A toluene sensor is functionally demonstrated with the experimental apparatus and microfluidic delivery detailed in Chapter 5. The toluene sensor is shown detecting toluene concentrations as low as 100ppm. This experiment demonstrates the functionality of the CSDS platform. Experiments are performed with the Optics Laboratory facilities in room W417 of the Van Leer building.

7.1 Sensor Characterization

Sensors with each primary grating design are fabricated in the configuration shown in Fig. 7.1. Light is shaped by the input waveguide and is incident upon the primary grating. Diffracted light is then incident upon the secondary grating. Out-coupling gratings capture the light diffracted, transmitted, and reflected by the secondary grating for detection. A $100\mu m$ square is defined in the SU-8 cladding for the primary grating boundary. Refractive index oils are flowed in the primary grating boundary region. The oils used have refractive indices of $n = 1.4318$, 1.4514, 1.4712, 1.4910, and 1.5108. After

each measurement, the sample is cleaned with isopropyl alcohol and the next oil is flowed through the defined square.

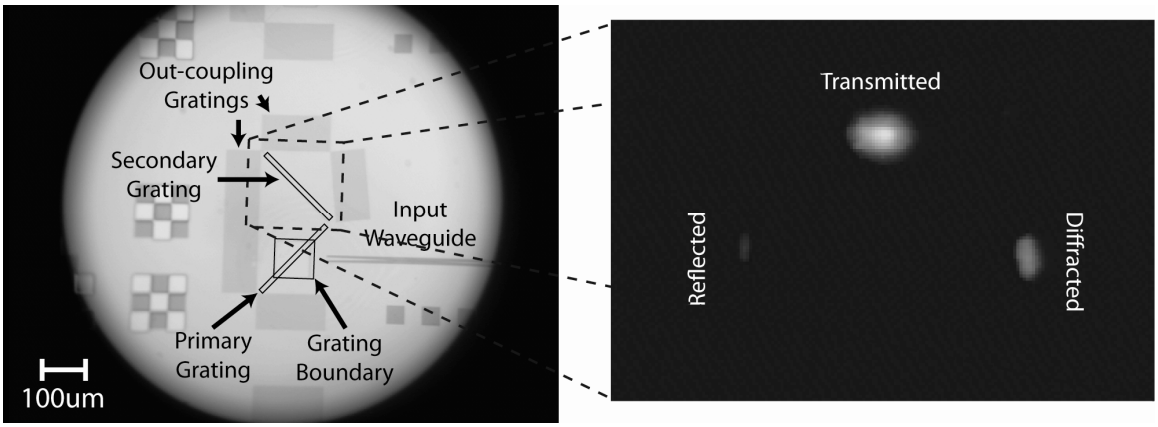

Figure 7.1: Experimental configuration (left) and measurement (right) for the sensor with a 20% primary grating and the $n = 1.4318$ refractive index oil within the primary grating boundary.

Experimental results were compared with FDTD simulation with Gaussian beam incidence. The simulations have been adjusted for the measured silicon device layer thickness of 254*nm*. This is necessary to account for the change in effective index of the slab waveguide structure. This change preserves the designed linear, monotonic behavior, but introduces a bias in the diffraction efficiency. Results are shown in Fig. 7.2. The secondary grating diffraction efficiencies are in excellent agreement with the simulated data. The measurements are within 4% of the simulated diffraction efficiencies. The most critical metric is the diffraction efficiency responsivity. The simulated responsivity is $0.181\%DE/mRIU$ in terms of the cladding refractive index. The measured responsivity of all the sensors is $0.179\%DE/mRIU$, differing less than 2% from simulation. These

experiments demonstrate the ability of the designed CSDS sensor to respond to variations in refractive index.

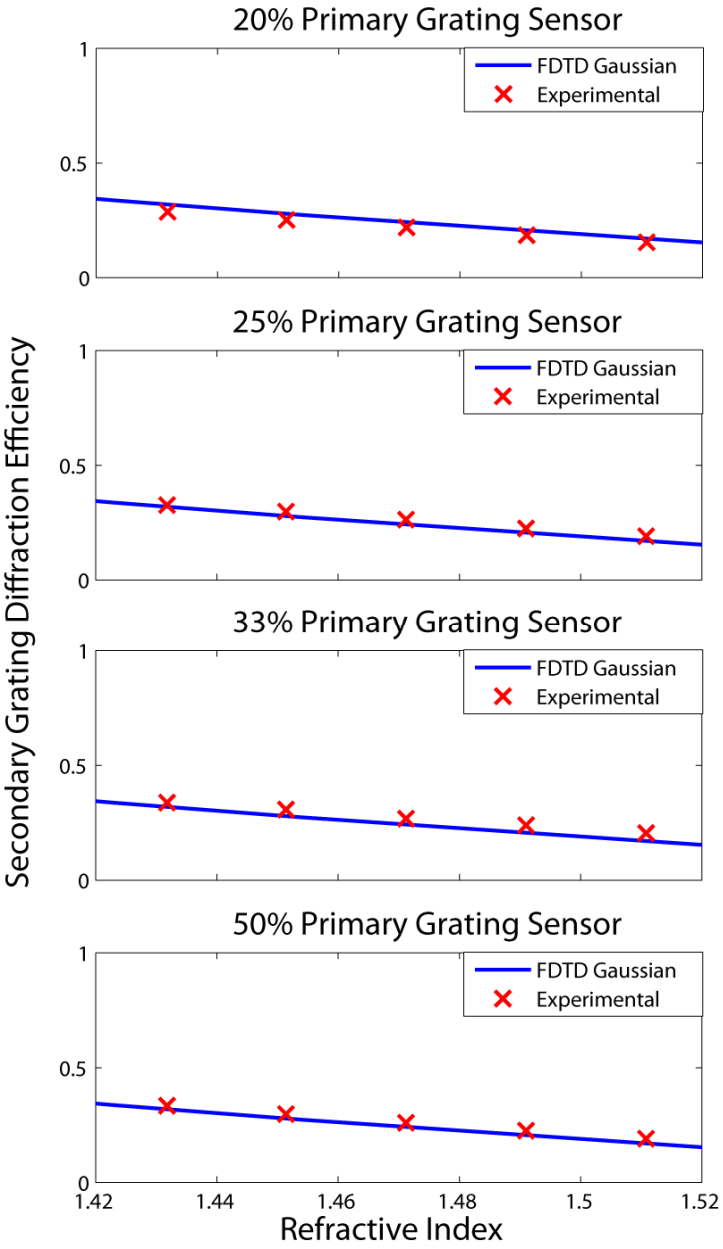

Figure 7.2: Experimental results compared with FDTD simulation with Gaussian beam incidence for the CSDS sensor with each primary grating design. The diffraction efficiencies for the secondary grating are in very good agreement.

7.2 Linear Sensor Array Prototype

A linear array of sensors is fabricated in the configuration shown in Fig. 7.3. Coupled light is incident upon each sensor in the sequence. Sensor primary gratings have diffraction efficiencies of 20%, 25%, 33%, and 50% in order of incidence. Light diffracted, transmitted, and reflected by each secondary grating is captured by out-coupling gratings fabricated for each sensor. Four $100\mu m$ squares are defined in the SU-8 cladding for the primary grating boundaries. Each sensor was tested individually. The sensor under test was addressed with various refractive index oils flowed into the corresponding primary grating boundary region. The oils used have refractive indices of $n = 1.4318$, 1.4514, 1.4712, 1.4910, and 1.5108. The refractive index oil with $n = 1.4712$ was flowed into the primary grating boundary regions of the sensors not addressed. This refractive index value represents no analyte immobilization.

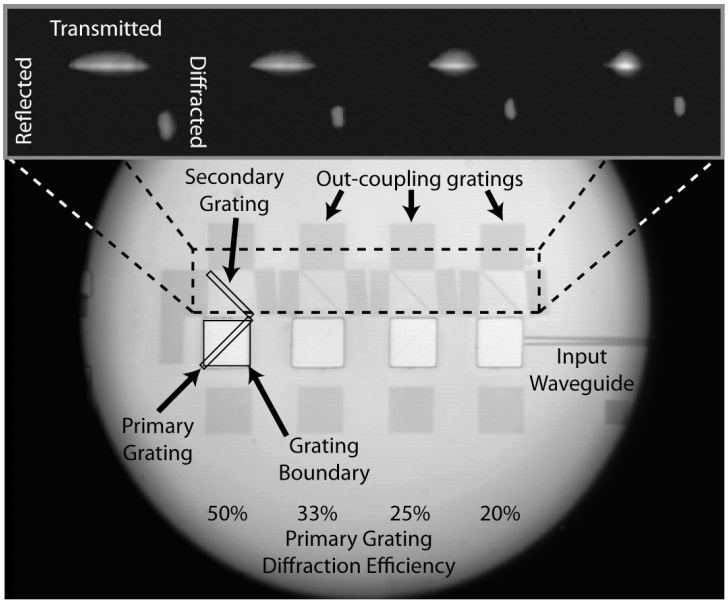

Figure 7.3: Fabricated linear sensor array configuration and measurement. In order of incidence, primary gratings have diffraction efficiencies of 20%, 25%, 33%, and 50%.

Experimental results were compared with FDTD simulation with Gaussian beam incidence. As with the sensor in the previous section, the simulations have been adjusted for the measured silicon device layer thickness of 254*nm*. Results are shown in Figs. 7.4 and 7.5. The secondary grating diffraction efficiencies are in excellent agreement with the simulated data. The measurements are within 3% of the simulated diffraction efficiencies. The measured diffraction efficiency responsivities are $0.181\%DE/mRIU$, $0.182\%DE/mRIU$, $0.182\%DE/mRIU$, and $0.183\%DE/mRIU$ for the 20%, 25%, 33%, and 50% primary grating sensors respectively. These results are within 2% of the simulated responsitivity of $0.181\%DE/mRIU$. The diffraction efficiencies of unaddressed sensors do not deviate as the refractive index oil in the primary grating boundary region of the addressed sensor varies. This independent operation demonstrates individual sensor addressability. This functionality is critical in ensuring that a measurement at one sensor does not affect measurements of other sensors in the linear sequence. These experiments successfully prototype linear sensor arrays. Multiple linear sensor arrays can be combined to form the 2-D sensor array from Fig. 2.2 for multiplexed and redundant sensing.

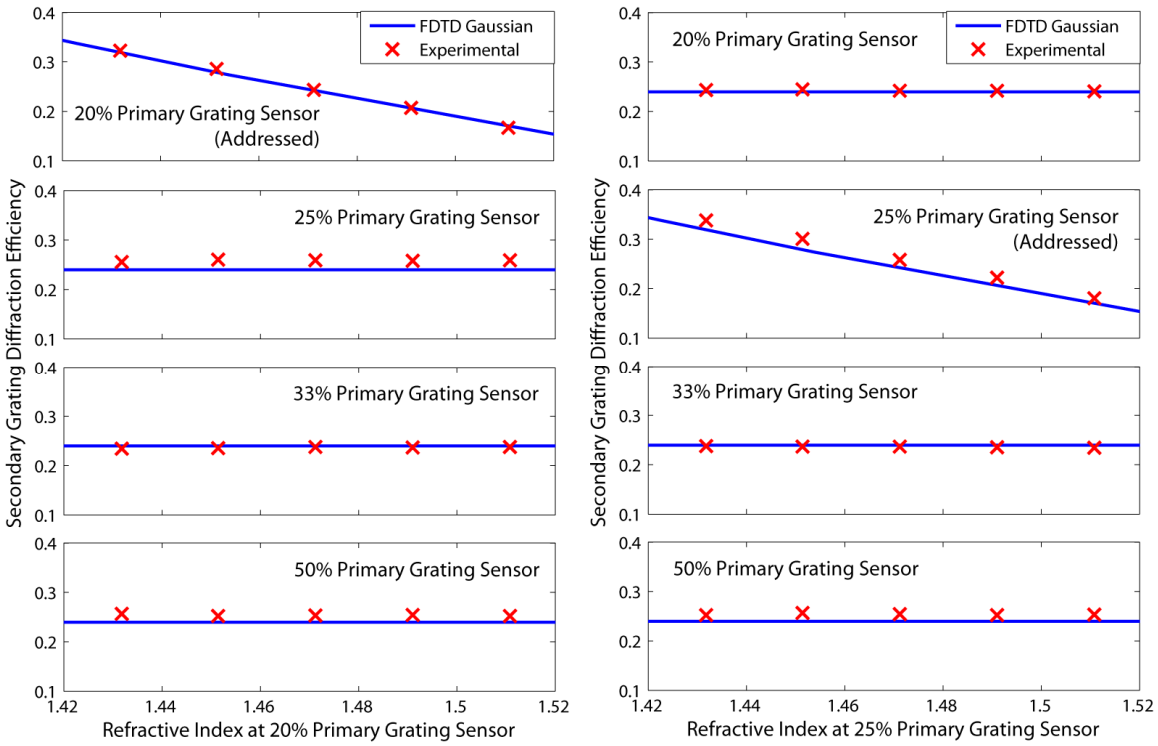

Figure 7.4: Experimental results compared with FDTD simulation with Gaussian incidence for the linear sensor array prototype testing the sensors with a 20% primary grating (left) and a 25% primary grating (right). Sensors under test were addressed with refractive index oils ranging from n = 1.432 to n = 1.511 flowed into the primary grating boundary. Refractive index oil of n = 1.471 is flowed for the unaddressed sensors. The secondary grating diffraction efficiencies are in very good agreement with simulation.

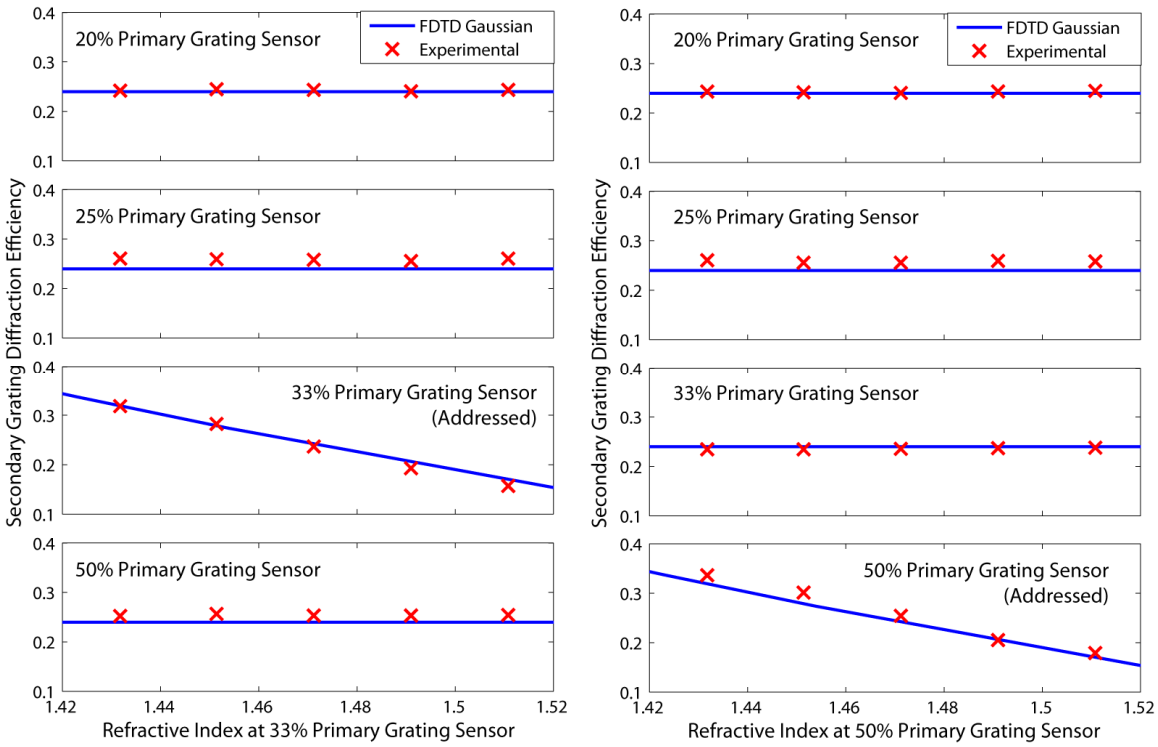

Figure 7.5: Experimental results compared with FDTD simulation with Gaussian incidence for the linear sensor array prototype testing the sensors with a 33% primary grating (left) and a 50% primary grating (right). Sensors under test were addressed with refractive index oils ranging from n = 1.432 to n = 1.511 flowed into the primary grating boundary. Refractive index oil of n = 1.471 is flowed for the unaddressed sensors. The secondary grating diffraction efficiencies are in very good agreement with simulation.

7.3 Functional Demonstration of Toluene Sensor

The toluene sensor with each primary grating design is fabricated in the configuration shown in Fig. 7.6. The primary grating boundary is formed by a 100μm square in the SU-8 cladding. The PBIBMA immobilization layer is dip-coated into the primary grating boundary. The microchannel is fabricated and bonded to the sensor as detailed in Chapter 4. Coupled light is shaped by the input waveguide and is incident upon the sensor. The diffracted, transmitted, and reflected orders are captured by the out-coupling gratings at the secondary grating for detection.

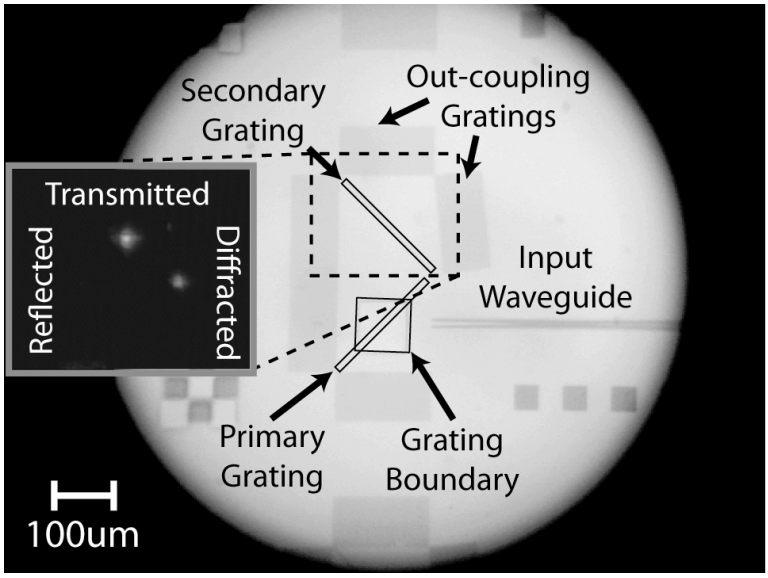

Figure 7.6: Fabricated toluene sensor configuration and measurement for the 50% primary grating.

Toluene dissolved in deionized water is delivered with the microfluidic apparatus described in Chapter 5. Various toluene concentrations are flowed to the sensor with a flow rate of $Q = 500 \mu L / \min$ to maintain a microchannel pressure below 1*psig*. The concentration of toluene is controlled by changing the ratio of syringe pump flow rates as described in Chapter 5. Results for toluene concentrations of 100ppm, 200ppm, and 500ppm are presented in Figs. 7.7 and 7.8 for sensors with the 20%, 25%, 33%, and 50% primary gratings. The infrared camera produces a significant amount of high frequency noise. This noise is removed with an ideal low-pass filter in Matlab after the data are recorded. The filter time constant is 4.1 seconds. This type of filter is analogous to internal filtering by the camera and can be applied in real time for commercial applications. The results after applying the filter are presented in Figs. 7.7 and 7.8. The clarity of the data is significantly enhanced.

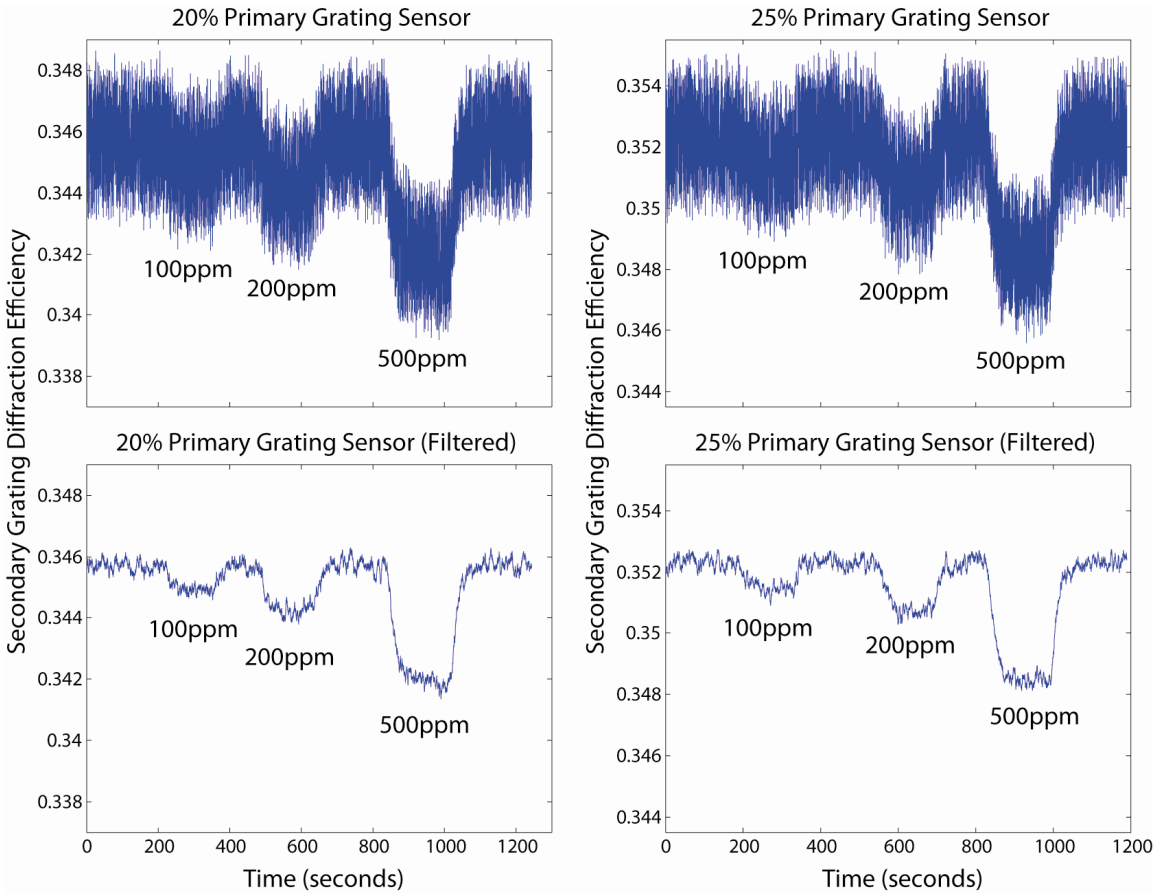

Figure 7.7: Experimental results for the toluene sensors with 20% (left) and 25% (right) primary gratings. The top plot is the measured data. The bottom plot shows the result after applying an ideal low pass filter to remove noise from the infrared camera. Toluene is measured in concentrations of 100ppm, 200ppm, and 500ppm.

The observed response time to reach equilibrium is about one minute. This response time is typical for sensors immobilizing solvents with the free-volume filling mechanism [82, 83]. It is also typical of other sensing mechanisms such as diffusion in low-glass-transition-temperature polymers [146]. The response time can be further enhanced by increasing the flow rate. Care must be taken to ensure that the microfluidic channels can handle the increased pressure from greater flow rates. The observed change in diffraction efficiency is in excellent agreement with simulated results. The measured changes in diffraction efficiency are $0.077\%DE/100\text{ppm}$, $0.078\%DE/100\text{ppm}$,

$0.078\%DE/100\text{ppm}$, and $0.079\%DE/100\text{ppm}$ for the 20%, 25%, 33%, and 50% primary grating sensors respectively.

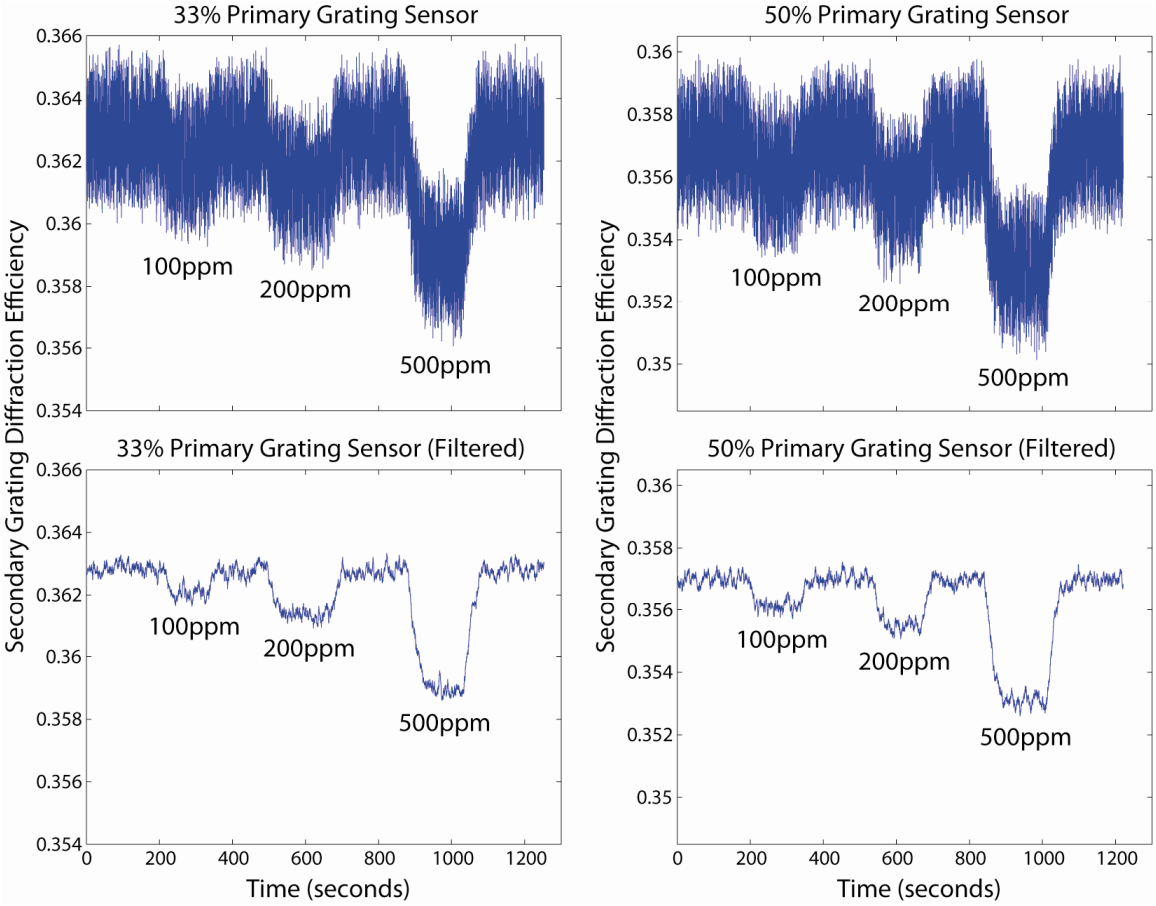

Figure 7.8: Experimental results for the toluene sensors with 33% (left) and 50% (right) primary gratings. The top plot is the measured data. The bottom plot shows the result after applying an ideal low pass filter to remove noise from the infrared camera. Toluene is measured in concentrations of 100ppm, 200ppm, and 500ppm.

The results are within 4% of the simulated change in diffraction efficiency of $0.080\%DE/100\text{ppm}$. The smallest concentration sensed in this functional demonstration was 100ppm. Typical detected concentrations for toluene and similar solvents by other sensors are on the order of parts-per-million [82, 83, 146]. More finely-tuned sensors with larger device sizes can detect concentrations on the order of hundreds of parts-per-billion [147]. The corresponding change in cladding refractive index for the smallest

concentration sensed (100ppm) is $3\times10^{-4}\,RIU$. This is comparable to published values on the order of $10^{-4}\,RIU$ for SPR sensors [6, 7] and Mach Zehnder sensors [8, 10] with millimeter-scale device sizes. Published values for microring resonator sensors are on the order of $10^{-5}\,RIU$ [11, 60] but require spectral detection. The sensitivity of the demonstrated CSDS sensor is primarily limited by noise in the infrared camera. Simulations in Chapter 3 indicate that the sensitivity may be improved by three or four orders of magnitude with the inclusion of integrated photodiodes and other refinements. These refinements are discussed in Chapter 8. These experiments functionally demonstrate the CSDS platform accurately detecting the concentration of toluene in solution.

CHAPTER 8

CONCLUSIONS

The primary objective of this research was to develop a class of integrated compact silicon diffractive sensors (CSDS) based on in-plane diffraction gratings. This was accomplished by combining constant-diffraction-efficiency and highly-angularly-selective in-plane resonance-domain diffraction gratings. The grating design and optimization process with rigorous coupled-wave analysis (RCWA) was detailed. Grating designs were optimized for a proof-of-concept toluene sensor. These designs were verified with finite-difference time-domain (FDTD) simulation with Gaussian beam incidence. Grating fabrication was accomplished with electron-beam lithography and the developed nano-scale Bosch etch process. A measurement methodology and experimental apparatus were developed. This apparatus uses a vertical detection scheme and a custom Labview program for real-time measurements. The designed gratings were experimentally characterized to verify that the desired performance is achieved. Individual and linearly arrayed sensors were characterized with refractive index oils to verify the diffraction efficiency responsivity and array functionality. The designed proof-of-concept sensor was functionally demonstrated with microfluidic delivery of toluene in solution.

In this chapter, the main accomplishments and contributions of this research are summarized. Planned efforts to improve sensitivity, refine analyte delivery, and develop high-throughput fabrication are also discussed.

8.1 Summary of Results

8.1.1 Review of Integrated Optical Sensing Platforms

Current state-of-the-art integrated optical sensing platforms were reviewed, including surface plasmon resonance (SPR) sensors, Mach Zehnder interferometric (MZI) sensors, and microring resonator sensors. The requirements of an integrated optical sensing platform suitable for field-deployable lab-on-a-chip (LOAC) devices were discussed. These requirements include micron-scale device sizes, robust intensity-based detection (as opposed to spectral-based), and two-dimensional sensor array capability. Micron-scale device sizes enable dense sensor population. SPR and MZI sensors are limited to devices sizes of millimeters. Microring resonator sensors meet this requirement with device sizes of microns or tens of microns. Intensity-based detection reduces cost and enables use of integrated sources and photodetectors. SPR, MZI, and microring resonator sensors are capable of intensity-based detection with measurement of optical attenuation. However, attenuation measurements are susceptible to degradation of the optical signal. A robust platform requires intensity-based measurement that is unaffected by source fluctuations. A 2-D sensor array configuration enables multiplexed and redundant sensing. Integration in a 2-D sensor array requires multiple sensors in a linear sequence to share source power. Ideally, this should be accomplished without the addition of optical splitters or complex geometries. SPR, MZI, and microring resonator sensors have not been demonstrated with this capability with intensity-based measurements. An integrated optical sensing platform for field-deployable LOAC applications must simultaneously meet these requirements and demonstrate a high level of sensitivity.

8.1.2 Compact Silicon Diffractive Sensor Design

A new class of integrated compact silicon diffractive sensors was developed and presented. Sensing is achieved by combining constant-diffraction-efficiency and highly-angularly-selective in-plane resonance-domain diffraction gratings [23]. This class of sensors addresses the requirements for field-deployable LOAC devices. The substrate is silicon-on-insulator (SOI) substrate to limit costs, exploit established fabrication processes, enable integration of supporting electronics, and use the well-understood telecommunications wavelength of $\lambda = 1.55 \mu m$. Device sizes are small with grating thicknesses of typically only a few microns. Measurement of the grating diffraction efficiencies is intensity-based. Since diffraction efficiency is a ratio, the measurement is attenuation independent. Careful design of the in-plane gratings allows intrinsic splitting of source light. Light is used by multiple sensors in a linear sequence without the addition of optical splitters. Linear sensor arrays fabricated in parallel enable compact 2-D sensor arrays for multiplexed and redundant sensing.

Material selections were discussed for a proof-of-concept toluene sensor. SU-8 was chosen for the cladding because of its thermal and mechanical stability. PBIBMA was chosen for the immobilization layer material to collect toluene with a free-volume filling mechanism. Optically transparent sheets of Teflon PFA were chosen to fabricate microchannels for their bonding capabilities and solvent resistance. The refractive indices of the relevant materials were experimentally determined.

The layout and design requirements for the primary and secondary gratings were discussed. Gratings are designed to accept incident light at an angle of 45° to enable perpendicular device orientations. This simplifies fabrication. The primary grating

requires a constant diffraction efficiency, even with a change in the surrounding refractive index. The change in diffraction efficiency was minimized by perpendicularly orienting the primary grating boundaries for normal incidence with respect to the incident and diffracted beams. It was determined that suitable designs could be optimized with grating thicknesses less than $2\mu m$ and fill factors greater than 0.5. The secondary grating requires a high angular selectivity and manageable fabrication tolerances. Furthermore, the secondary grating response to changes in incident angle must be linear and monotonic. This enables detection of both positive and negative changes in incident angle. This requires the grating to operate at a controlled angular shift from the Bragg condition.

8.1.3 In-Plane Diffraction Grating Optimization

The primary and secondary grating design and optimization processes with RCWA were presented [23]. RCWA is an exact analysis that is easy to implement with manageable computation times. It has been used extensively in diffraction grating design [106]. Primary grating design candidates for the proof-of-concept toluene sensor were identified. Sensitivity analysis was performed to determine the most suitable designs with the most lenient fabrication tolerances and smallest change in diffraction efficiency with variations in the surrounding refractive index. The process of designing the secondary grating with a controlled angular shift from the Bragg condition was detailed. Secondary grating design candidates for the proof-of-concept toluene sensor were identified and evaluated with sensitivity analysis. The most suitable candidate was chosen to strike a balance between the desired linear, monotonic response and manageable fabrication tolerances.

The designed grating diffraction efficiencies were verified with FDTD simulation with Gaussian incidence [23]. RCWA is an exact analysis, however it is only applicable to plane-wave incidence. Results for the primary grating designs show excellent agreement within 1%. The sensitivity analysis is within 2%, also showing excellent agreement. Results for the secondary grating are in good agreement within 5%. The simulated angular responsivitity is smaller by $7.43\% DE/^\circ$. These differences are due to the multiple angular components of the Gaussian beam and the high angular selectivity of the grating. However, the desired linear, monotonic response is preserved. These results indicate that RCWA is an efficient and accurate design tool for the CSDS gratings.

The CSDS sensor with both gratings was simulated with FDTD with Gaussian beam incidence to determine the refractive index response [23]. The refractive index within the primary grating boundary was varied and the diffraction efficiencies at the secondary grating were recorded. The lower limit of detection was simulated to be $10^{-8} RIU$. This potential level of sensitivity is highly competitive with predicted values for state-of-the-art integrated optical sensors.

8.1.4 Sensor Fabrication

Fabrication of the CSDS toluene sensor was presented and detailed [23]. In-plane diffraction gratings were patterned with electron-beam lithography (EBL). The grating patterns were transferred to the silicon device layer with a nano-scale ICP Bosch process. This fabrication methodology repeatably yields grating features within 1% of their target values. The fabricated sidewall angles are greater than 89° and the magnitude of scalloping is less than $10nm$. The smallest grating grooves fabricated were $74nm$ wide and $250nm$ deep, resulting in an aspect ratio of 3.4:1. The primary grating boundaries

were defined in the SU-8 cladding layer with conventional optical lithography. Care was taken to ensure that the SU-8 completely filled the secondary grating grooves.

The process of depositing the immobilization layer and constructing microfluidic channels for the proof-of-concept toluene sensor was presented [24]. PBIBMA was dip-coated to create a 70*nm* immobilization layer. Microfluidic channels were patterned in sheets of Teflon PFA and bonded with Loctite 401 cyanoacrylate. After removing excess PBIBMA, the microfluidic assembly is bonded to the sensor. The fabricated microchannels are low in cost, high in bond strength, and high in solvent resistance.

8.1.5 Experimental Apparatus and Methodology

The developed experimental apparatus and measurement methodology were presented and discussed [23]. Diffraction efficiencies were simultaneously measured with a vertical detection scheme. This relieves the limitations of using multiple external photodetectors. Out-coupling gratings were designed to couple light out-of-plane. This light is imaged by a microscope objective and captured by an infrared camera. Input waveguides were designed to couple light from a tapered fiber to the slab waveguide structure. Careful design of this waveguide shapes the beam incident to the sensor and minimizes beam divergence. Measurements are recorded with a custom Labview program. This program simultaneously captures the pixel value intensity of each diffracted order, removes the background pixel level, calculates the diffraction efficiencies, and writes the results to file every 33 milliseconds.

The microfluidic delivery apparatus for the toluene sensor functional demonstration was presented [24]. Fluid flow is controlled by two syringe pumps joined with a y-connector. Fluid is coupled into and out of the microchannel via NanoPorts. The

toluene concentration is controlled by varying the flow rate ratio of the two syringe pumps. This enables a constant flow rate for different toluene concentrations. A fluid flow rate of $500\mu L/\min$ was chosen to maintain a pressure below 1*psig* within the microchannel.

8.1.6 Experimental Grating Characterization

Characterizations of the primary and secondary gratings were presented [23]. The primary gratings were characterized by flowing oils of varying refractive indices into the primary grating boundary. A significant reflection was observed, but the diffracted order efficiencies remained within 4% of the simulated values. The change in diffraction efficiency was minimal with varying refractive index. These experiments demonstrated the primary gratings successfully performing the designed function. The secondary grating was characterized by varying the incident angle. Multiple gratings with input waveguides oriented to different angles were fabricated. A significant reflection was observed, but the diffracted order efficiency remained within 5% of the simulated values. The desired linear, monotonic response to changes in incident angle was observed. This experiment successfully demonstrated the secondary grating performing its designed function.

The source of the experimentally observed reflections was investigated and refinements to minimize these reflections were introduced. It was found that 3-D FDTD simulation could reproduce the reflections whereas 2-D FDTD simulation could not. It was determined that the cause was the large refractive index contrast between the grating ridges and grooves. To limit the refractive index contrast, alternative shallow-groove

gratings were introduced. Simulations with 3-D FDTD analysis result in reflected efficiencies less than 1% for these shallow-groove gratings.

8.1.7 Experimental Sensor Characterization and Functional Demonstration

Experimental characterizations of the designed CSDS sensors with different primary grating diffraction efficiencies were presented [23]. Varying refractive index oils were flowed into the primary grating boundary regions and the diffraction efficiency of the secondary grating was measured. The secondary grating diffraction efficiencies are in excellent agreement with the simulated data. The measurements are within 4% of the simulated diffraction efficiencies and the diffraction efficiency responsivities are within 2% of simulation. These experiments successfully demonstrated the CSDS sensors responding to changes in refractive index.

Experimental characterizations of the designed CSDS sensors configured in a linear sensor array were presented [24]. Individual sensors were addressed by flowing varying refractive index oils into the corresponding primary grating boundary. An oil representing no analyte immobilization was flowed into the primary grating boundary of sensors not addressed. The secondary grating diffraction efficiencies are in excellent agreement with the simulated data. The measurements are within 3% of the simulated diffraction efficiencies and the diffraction efficiency responsivities are within 2% of simulation. The diffraction efficiencies of unaddressed sensors do not deviate as the refractive index oil in the primary grating boundary region of the addressed sensor varies. This independent operation successfully demonstrates individual sensor addressability in the linear sensor array prototype.

The designed CSDS toluene sensors were functionally demonstrated sensing toluene in solution with microfluidic delivery [24]. Toluene concentrations of 100ppm, 200ppm, and 500ppm were detected. The observed response time to reach equilibrium was about one minute with a $500\mu L$ / min fluid flow rate. This response time was typical, but can be improved with higher flow rates. The observed change in diffraction efficiency is in excellent agreement with simulated results. The measured change in diffraction efficiency was within 4% of the simulated value. The smallest change in cladding refractive index measured was $3\times10^{-4}\,RIU$ which corresponds to the 100ppm toluene concentration. This level of sensitivity is typical of other state-of-the-art integrated optical sensors with intensity-based detection. Simulations indicate that the sensitivity may be improved by three or four orders of magnitude with the inclusion of integrated photodiodes, integrated sources, and minimization of grating reflections. These experiments functionally demonstrate the CSDS platform accurately detecting the concentration of toluene in solution.

8.2 Future Work

The results presented in this thesis verify the functionality of the CSDS platform. However, more work is necessary to realize the CSDS platform's full potential for field-deployable LOAC applications. The long-term goal of this research is to develop a fully integrated optical sensing platform with high sensitivity, integrated sources, integrated photodetection, networked microfluidic delivery, and low-cost, high-throughput fabrication. Planned efforts to achieve these goals are discussed in this section.

8.2.1 Shallow-Groove Grating Fabrication

As discussed in Sec. 6.3, a significant undesired reflection is experimentally observed for the fabricated gratings. This reflection was simulated with 3-D FDTD analysis and alternative shallow-groove grating designs were presented. With grooves extending only 50*nm* into the silicon device layer, the developed nano-scale Bosch process may not be suitable for etching the grating grooves. Grating fabrication would only require one or two etch cycles, and guaranteeing a 50*nm* groove depth without an etch-stop layer (such as the buried oxide layer for the nano-scale Bosch process) would be prohibitively difficult. However, the shallow grooves may be fabricated with a standard chlorine etch if HSQ is used as the electron-beam resist. As discussed in Sec. 4.1, the primary issue with HSQ as a resist was that removal would harm the exposed buried oxide (BOX) layer. With shallow-groove gratings, the BOX layer is not exposed and the HSQ can be removed without issue. Because of the strong etch selectivity between silicon and HSQ [124], the patterned aspect ratios will be manageably small. However, work must be done to develop the shallow-groove grating fabrication process. A nearly vertical sidewall angle was achieved with the developed nano-scale Bosch process. The sidewall angle must be maximized with HSQ and a chlorine-based etch, with vertical sidewalls as the goal. It is critically important that the developed process accurately and repeatably reproduce the designed shallow-groove gratings.

8.2.2 Integrated Silicon-on-Insulator Source and Photodetection

Enhancement of the CSDS platform's sensitivity and portability requires integration of optical sources and photodetection. High sensitivity and increased portability are critical in field-deployable LOAC applications. To accomplish this, work must be completed to

evaluate emerging integrated source and detection technologies. Furthermore, work must be completed to merge the fabrication processes of these technologies with the existing CSDS fabrication process. In this section, methods of integrating optical sources and photodiodes into the SOI substrate are discussed and the potential impact on device fabrication is explored.

8.2.2.1 Heterogeneously Integrated III-V Lasers

Integration of the optical source decreases the overall device size and increases portability. Furthermore, it removes the need for externally coupling light into the device and increases robustness. Light at telecommunications wavelengths (specifically $\lambda = 1550nm$ in this case) is typically produced by a III-V laser. The primary challenge in source integration is the coupling of light from the III-V material to the silicon substrate. Heterogeneously integrated III-V lasers have been developed to meet this challenge [93, 94]. These lasers are bonded to the SOI substrate with benzocyclobutene (BCB). This relieves the alignment limitations of flip-chip bonding and the potential defect limitations of hetero-epitaxial growth. Fabricated lasers have been demonstrated by Lamponi to generate light at wavelengths near $1550nm$ and output powers near $1mW$ within the SOI waveguide [93].

Work must be done to merge the laser fabrication and bonding steps with the fabrication of the CSDS gratings, immobilization layer, and microfluidic channels. Laser bonding must be done after the other CSDS components have been fabricated to preserve their integrity. The SU-8 cladding will serve as a protective layer for the other sensor components. The bonding area can be defined in the SU-8 cladding with optical lithography. Since laser performance is strongly dependent on the quality, thickness, and

uniformity of the bonding layer, work must be done to ensure the desired bonding layer characteristics are achieved. Furthermore, work is necessary to achieve the desired light generation and coupling to the SOI waveguide.

8.2.2.2 Integrated Silicon-on-Insulator Photodiodes

Integrated photodetection eliminates the need for out-coupling gratings and external imaging to measure the diffracted order intensities. This reduces overall device size and increases robustness. Furthermore, integrated photodetection may improve the refractive index sensitivity by three or four orders of magnitude as indicated by simulations in Sec. 3.3. Fabricated SOI p-i-n photodiodes have been demonstrated by Geis with a responsivity of $0.8 A/W$ at $1550nm$ [95]. This was achieved by reducing the waveguide size to $220nm$ by $550nm$ and optimizing the ion implantation process. The waveguides used are similar in size to the single-mode region of the CSDS input waveguide from Sec. 5.3.

Work must be done to merge the photodiode fabrication process with the fabrication of the CSDS gratings, immobilization layer, and microfluidic channels. The annealing temperature required after doping with phosphorus and boron is $1000°C$. To prevent damage to the deposited immobilization layer and fabricated microchannels, it is necessary to fabricate the photodiodes before the CSDS components. Geis has demonstrated that annealing temperatures up to $300°C$ after fabrication do not significantly affect operation. This temperature is compatible with the developed grating fabrication process and the discussed fabrication of shallow-groove gratings in Sec. 8.2.1. Furthermore, work is necessary to design the waveguide structure that couples diffracted light into the photodiode. This may be accomplished with a structure similar to the CSDS

input waveguide. Finally, work must be done to ensure that the desired responsivity and noise characteristics are achieved.

8.2.3 Microchannel Fabrication in SU-8 Cladding

The Teflon PFA microchannels fabricated in Sec. 4.4 are suitable for device prototyping. However, a commercially available device must have a more rigid and permanent microchannel structure. Furthermore, the patterned microchannel size should be on the order of tens of microns. Microchannels of this size are necessary to develop microfluidic delivery networks. Networked delivery enables different test fluids to be measured by individual or by multiple sensors in a 2-D sensor array as discussed in Sec. 2.1. Also, the microchannel fabrication process must be monolithically integrated into the CSDS grating fabrication. This is necessary to permit bonding of an integrated source as discussed in Sec. 8.2.2.1. Finally, the microchannel material must feature a strong resistance to solvents, acids, and bases as well as strong thermal and mechanical stability. SU-8 from MicroChem [97] has these features and has been used extensively in microchannel fabrication.

There are two promising methods of monolithic SU-8 microchannel fabrication for the CSDS platform. The first was developed by Dang and involves use of a sacrificial polymer that can be decomposed at temperatures below $200°C$ [148, 149]. Microchannels could be defined in the SU-8 cladding with optical lithography and filled with the sacrificial polymer. The structure could then be machined down to the desired microchannel height and an additional SU-8 layer deposited to cap the microchannel. The sacrificial polymer could then be heated and evacuated to complete the microchannel fabrication. This method reliably produces rigid and watertight microchannels. To realize

these microchannels in the CSDS platform, work must be done to ensure that the evacuation process does not destroy the deposited immobilization layer. It is necessary that the immobilization layer is able to withstand the evacuation temperature. Furthermore, work must be done to ensure that the immobilization layer is fully exposed after evacuation to ensure proper measurement. Because the immobilization layer is application-specific, this process may not be suitable for all applications.

The second method was developed by Yang [150]. Nano-imprint lithography is used to pattern the SU-8 microchannels. An additional SU-8 capping layer is bonded with an optimized bonding temperature and pressure. This method is able to produce rigid and watertight microchannels, though surface defects and contamination can adversely affect the bonding quality. The maximum temperature used in the bonding process is $90°C$, which is compatible with a larger pool of immobilization layer materials. To realize these microchannels in the CSDS platform, work must be done to fabricate reliably these structures. Also, work must be done to ensure that the immobilization layer integrity is preserved. Finally, work must be done to achieve alignment between the bonded layers such that access can be had for integrated source and photodiode fabrication.

8.2.4 High-Throughput Fabrication with Nano-Imprint Lithography

In the presented research, gratings were fabricated with electron-beam lithography. This method of fabrication is suitable for prototyping, but too slow and costly for commercial manufacture. To realize the CSDS platform commercially, grating fabrication must be low in cost and high in throughput. Nano-imprint lithography (NIL) is well positioned to meet these requirements. With NIL, a fabricated stamp transfers the desired pattern to a substrate through the application of heat and pressure. If the stamp is transparent to

ultraviolet light (such as a quartz stamp), UV-curable materials can be exposed while the stamp is held in contact. Stamps are typically patterned with EBL, but are reusable for reduced cost. Because the entire pattern is transferred at once, the throughput is high. NIL has been demonstrated to pattern gratings accurately and reliably with periods as low as 200*nm* [151-153]. This resolution is suitable for fabrication of the CSDS gratings.

To use NIL for CSDS grating fabrication, work must be done to evaluate resists for accuracy in reproducing the grating patterns. Furthermore, work must be done to adapt the developed fabrication process to the resist chosen. It is critical that the gratings are accurately patterned and that the fabricated sidewalls of the grating grooves are nearly vertical.

8.3 Concluding Remarks

The research presented in this thesis developed and functionally demonstrated a new class of integrated compact silicon diffractive sensors (CSDS) based on in-plane diffraction gratings. This was accomplished by combining constant-diffraction-efficiency and highly-angularly-selective in-plane resonance-domain diffraction gratings. This class of sensors uses a silicon-on-insulator substrate to limit costs, exploit established fabrication processes, enable integration of supporting electronics, and use the well-understood telecommunications wavelength of $\lambda = 1.55 \mu m$. The CSDS platform offers many advantages for integrated optical sensing. Device sizes are small with grating thicknesses of typically only a few microns. Measurement of the grating diffraction efficiencies is intensity-based. Since diffraction efficiency is a ratio, the measurement is attenuation independent. Careful design of the in-plane gratings allows intrinsic splitting of source light. Light is used by multiple sensors in a linear sequence without the addition

of optical splitters. Linear sensor arrays fabricated in parallel enable compact 2-D sensor arrays for multiplexed and redundant sensing.

The features of the CSDS platform are highly desirable for a field-deployable LOAC device. The research presented in this thesis successfully demonstrates the platform's functionality. Planned efforts to improve sensitivity, refine analyte delivery, and develop high-throughput fabrication will position the CSDS platform to meet commercial demand for portable, robust, low-cost devices with high sensitivity.

APPENDIX A

PRIMARY GRATING BOUNDARY ORIENTATION

The in-plane bounded grating configuration is illustrated in Fig. 2.4. The diffracted output angle, θ_m, will follow the forward-diffraction equation,

$$n_0 \sin\gamma - n_0 \sin(-\gamma_m) = m\frac{\lambda}{\Lambda}. \tag{A.1}$$

The diffracted order of interest corresponds to $m = 1$ since these are resonance-domain gratings with only one diffracted order. Snell's law relation is used to express the interior angles, γ and γ_m, in terms of the exterior angles, θ and θ_m. This is accomplished with the intermediate angles, β, β_m, ξ, and ξ_m, defined in Fig. A.1.

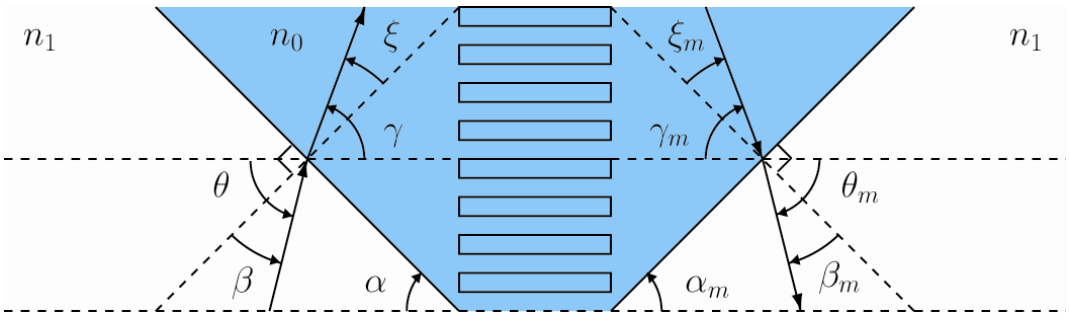

Figure A.1: Bounded in-plane grating configuration with intermediate angles, β, β_m, ξ, and ξ_m, defined.

The intermediate angles are expressed as

$$\begin{aligned} \beta &= \theta + \alpha - \pi/2 \qquad & \beta_m &= \theta_m + \alpha_m - \pi/2 \\ \xi &= \gamma + \alpha - \pi/2 \qquad & \xi_m &= \gamma_m + \alpha_m - \pi/2 \end{aligned}. \tag{A.2}$$

Snell's relations for the intermediate angle are

$$n_1 \sin\beta = n_0 \sin\xi \qquad n_1 \sin\beta_m = n_0 \sin\xi_m \,. \tag{A.3}$$

Substituting Eq. (A.2) into Eq. (A.3) and simplifying yields

$$n_1 \cos(\theta+\alpha) = n_0 \cos(\gamma+\alpha) \qquad n_1 \cos(\theta_m+\alpha_m) = n_0 \cos(\gamma_m+\alpha_m). \qquad \text{(A.4)}$$

Solving Eq. (A.4) for the interior angles, γ and γ_m, gives

$$\gamma = \cos^{-1}\left[\frac{n_1}{n_0}\cos(\theta+\alpha)\right]-\alpha \qquad \gamma_m = \cos^{-1}\left[\frac{n_1}{n_0}\cos(\theta_m+\alpha_m)\right]-\alpha_m. \qquad \text{(A.5)}$$

Substituting this into the forward diffraction equation yields

$$\sin\left\{\cos^{-1}\left[\frac{n_1}{n_0}\cos(\theta+\alpha)\right]-\alpha\right\}+\sin\left\{\cos^{-1}\left[\frac{n_1}{n_0}\cos(\theta_m+\alpha_m)\right]-\alpha_m\right\}=\frac{\lambda}{n_0\Lambda}, \quad \text{(A.6)}$$

which when solved for grating period, Λ, leaves

$$\Lambda = \frac{\lambda}{n_0}\left(\sin\left\{\cos^{-1}\left[\frac{n_1}{n_0}\cos(\theta+\alpha)\right]-\alpha\right\}+\sin\left\{\cos^{-1}\left[\frac{n_1}{n_0}\cos(\theta_m+\alpha_m)\right]-\alpha_m\right\}\right)^{-1}. \text{(A.7)}$$

This is the grating period necessary for the desired incident and diffracted angles. The output angle variation, $\Delta\theta_m$, is defined as $\Delta\theta_m = \theta_{mx} - \theta_m$. The new refractive index is defined as $n_{0x} = n_0 + \Delta n_0$ to reflect analyte immobilization. Replacing θ_m with θ_{mx} and n_0 with n_{0x} in Eq. (A.6) and substituting the expression for the grating period from Eq. (A.7), the new diffracted angle is

$$\theta_{mx} = \cos^{-1}\left\{\frac{n_{0x}}{n_1}\cos\left[\sin^{-1}\left(\frac{n_0}{n_{0x}}\Gamma-\sin\left\{\cos^{-1}\left[\frac{n_1}{n_{0x}}\cos(\theta+\alpha)\right]-\alpha\right\}\right)+\alpha_m\right]\right\}-\alpha_m, \text{(A.8)}$$

where Γ is the left side of the forward diffraction equation from Eq. (A.6),

$$\Gamma = \sin\left\{\cos^{-1}\left[\frac{n_1}{n_0}\cos(\theta+\alpha)\right]-\alpha\right\}+\sin\left\{\cos^{-1}\left[\frac{n_1}{n_0}\cos(\theta_m+\alpha_m)\right]-\alpha_m\right\}. \quad \text{(A.9)}$$

When the design is such that $\alpha = \alpha_m$, $\theta = \theta_m$, $\gamma = \gamma_m$, and the grating period, Λ, initially is given by the Bragg condition, then the Bragg dephasing parameter is

$\xi = (\gamma - \gamma_B)(\pi d / \Lambda)$, where γ_B is the interior incident angle that fulfills the Bragg condition for a given n_0. The rate of dephasing is

$$\Psi = \frac{\partial \xi}{\partial n_0} = \frac{\partial}{\partial n_0}(\gamma - \gamma_B)\frac{\pi d}{\Lambda}. \tag{A.10}$$

where γ is the actual interior incident angle and d is the grating thickness. When the Bragg condition is fulfilled, the grating period from Eq. (A.7) can be rewritten as

$$\Lambda = \frac{\lambda}{2n_{0c}}\left(\sin\left\{\cos^{-1}\left[\frac{n_1}{n_{0c}}\cos(\theta+\alpha)\right]-\alpha\right\}\right)^{-1}, \tag{A.11}$$

noting that n_0 has been replaced with n_{0c} to denote it remains constant in this expression for Λ since the grating period is fixed. For the PBIBMA cladding unperturbed by analyte presence, $n_{0c} = 2.305$. To determine γ_B, Eq. (A.1) is revisited, noting that $\gamma = \gamma_m = \gamma_B$, and rearranged yielding

$$\Lambda = \frac{\lambda}{2n_0}\sin\gamma_B. \tag{A.12}$$

Equating the grating periods in Eq. (A.11) with Eq. (A.12), γ_B can be determined, giving

$$\gamma_B = \sin^{-1}\left(\frac{n_{0c}}{n_0}\sin\left\{\cos^{-1}\left[\frac{n_1}{n_{0c}}\cos(\theta+\alpha)\right]-\alpha\right\}\right). \tag{A.13}$$

With γ from Eq. (A.5), the expression for the Bragg dephasing after performing the differentiation is

$$\Psi = \frac{\pi d}{\Lambda}\frac{\partial}{\partial n_0}(\gamma) + \frac{\pi d}{\Lambda}\frac{\frac{n_{0c}}{n_0^2}\sin(\gamma_c-\alpha)}{\left\{1-\left[\frac{n_{0c}}{n_0}\sin(\gamma_c-\alpha)\right]^2\right\}^{1/2}}, \tag{A.14}$$

where

$$\gamma_c = \cos^{-1}\left[\frac{n_1}{n_{0c}}\cos\left(\theta+\alpha\right)\right]-\alpha \tag{A.15}$$

and

$$\frac{\partial}{\partial n_0}\left(\gamma\right) = \frac{-\frac{n_1}{n_0^2}\cos\left(\theta+\alpha\right)}{\left\{1-\left[\frac{n_1}{n_0}\cos\left(\theta+\alpha\right)\right]^2\right\}^{1/2}}. \tag{A.16}$$

APPENDIX B

GRATING SIMULATION DATA

B.1 Primary Grating Design Candidates

B.1.1 Primary Grating with 20% Diffraction Efficiency

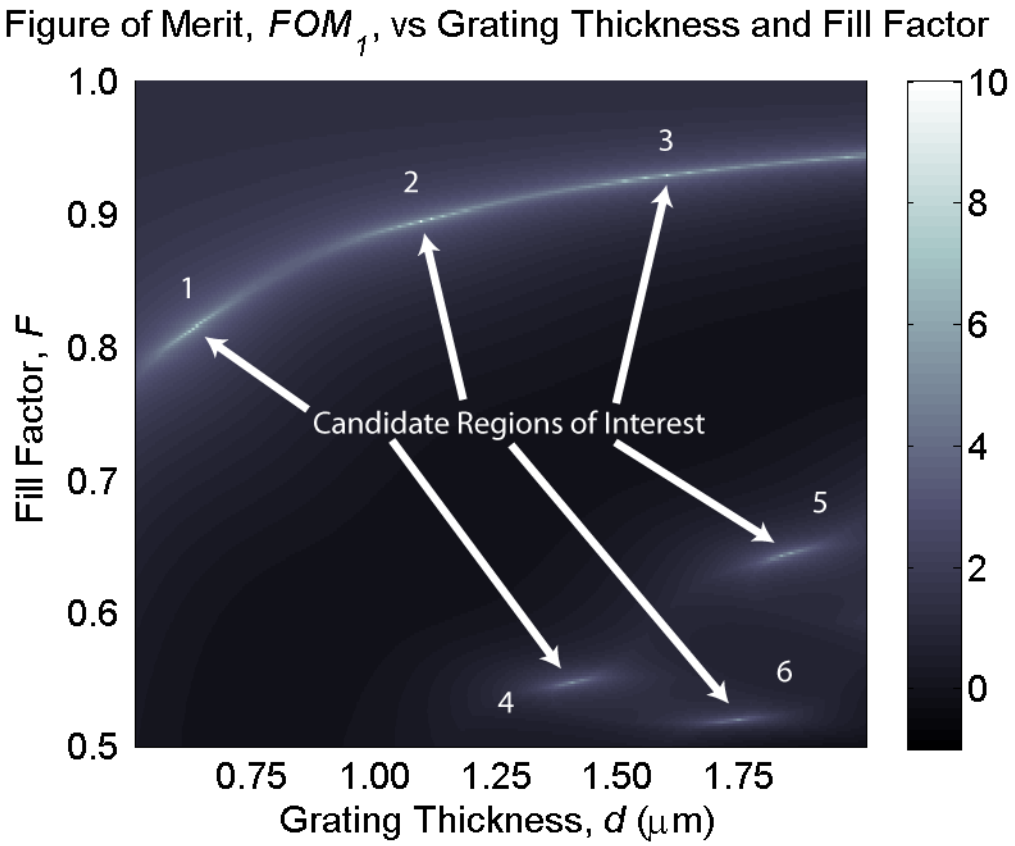

Figure B.1: A plot of figure-of-merit vs. grating thickness and fill factor for a primary grating target diffraction efficiency of 20%. Regions with potential design candidates are highlighted.

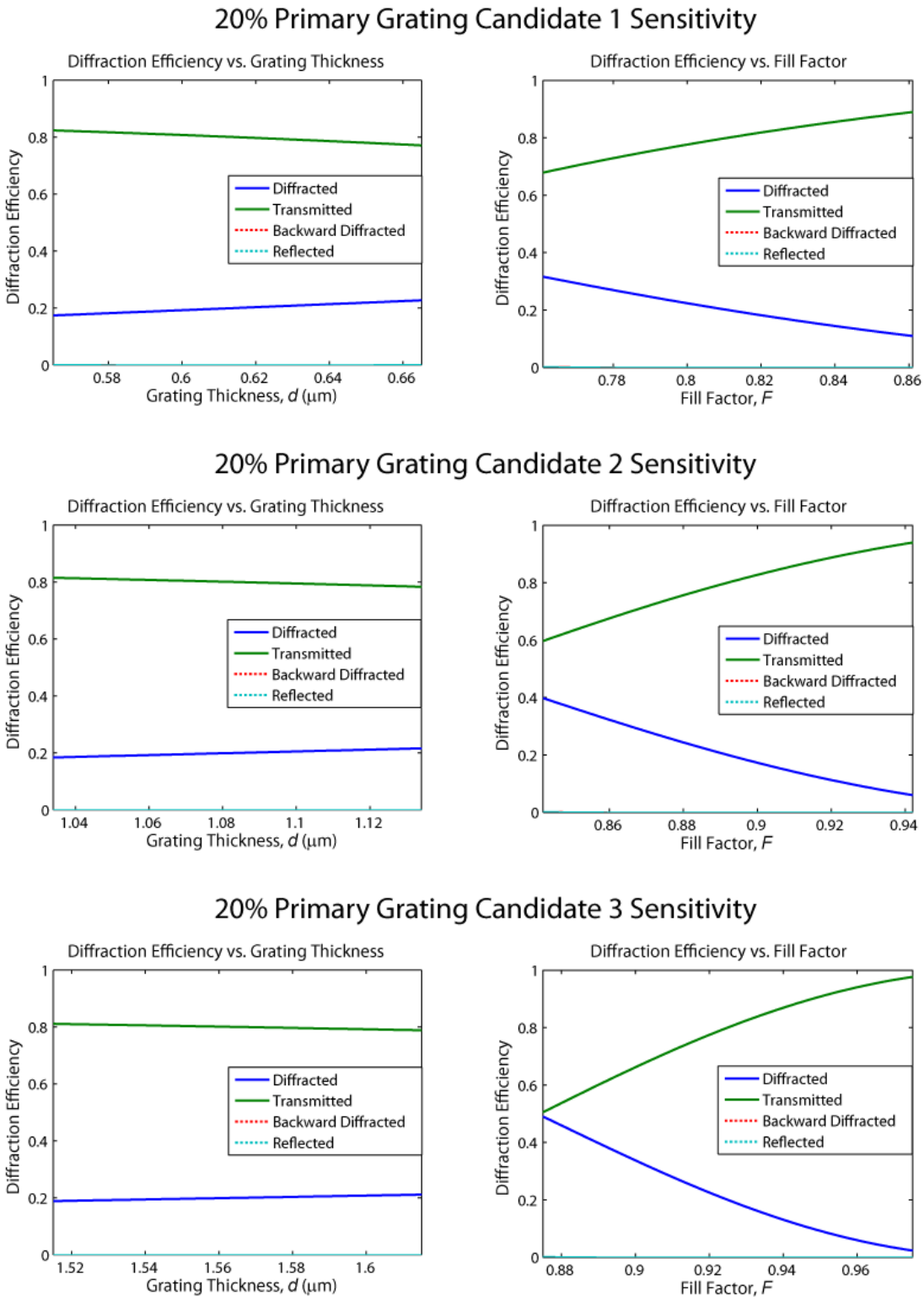

Figure B.2: RCWA grating thickness and fill factor sensitivities for primary grating candidates 1, 2, and 3 with target diffraction efficiencies of 20%.

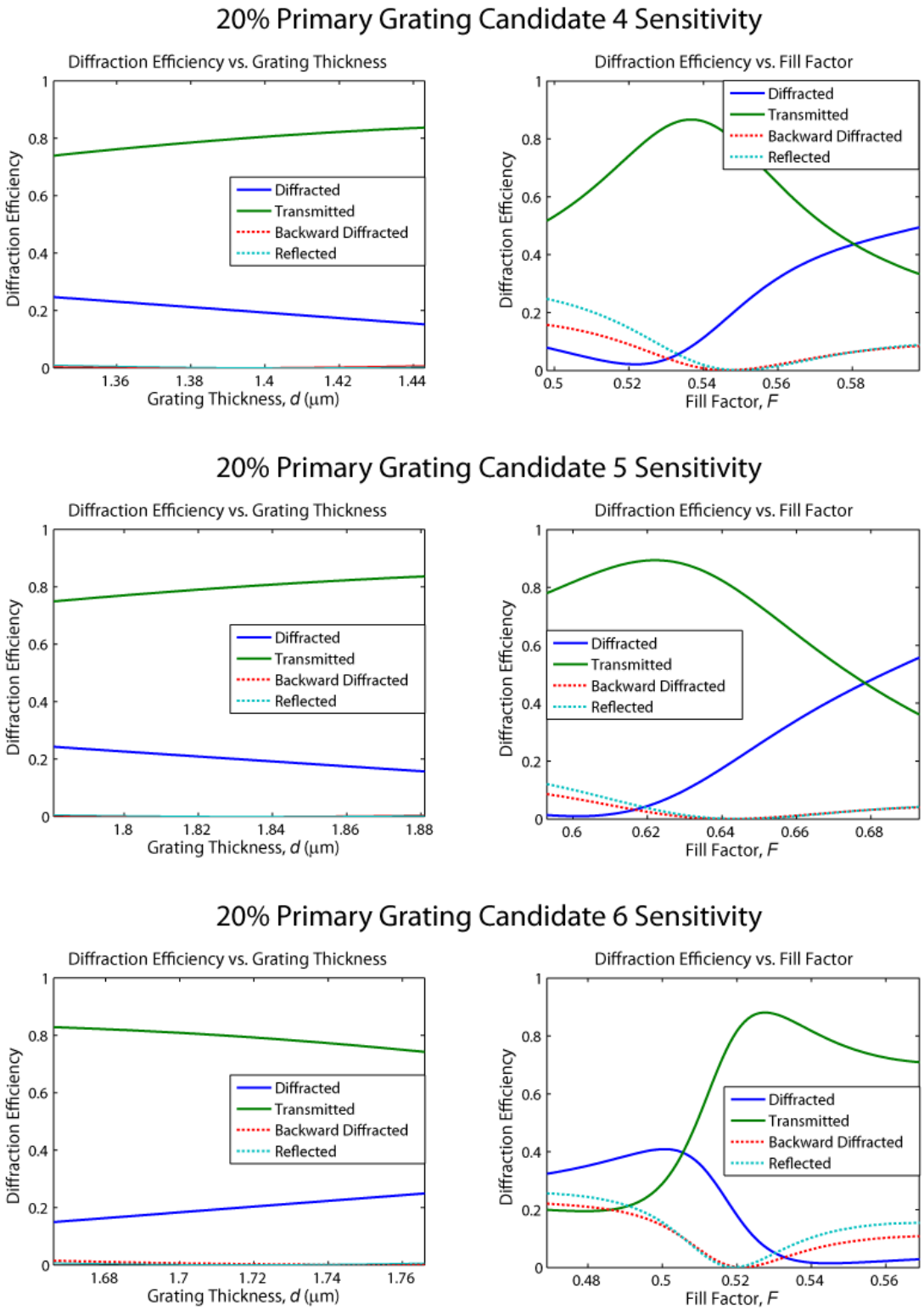

Figure B.3: RCWA grating thickness and fill factor sensitivities for primary grating candidates 4, 5, and 6 with target diffraction efficiencies of 20%.

B.1.2 Primary Grating with 33% Diffraction Efficiency

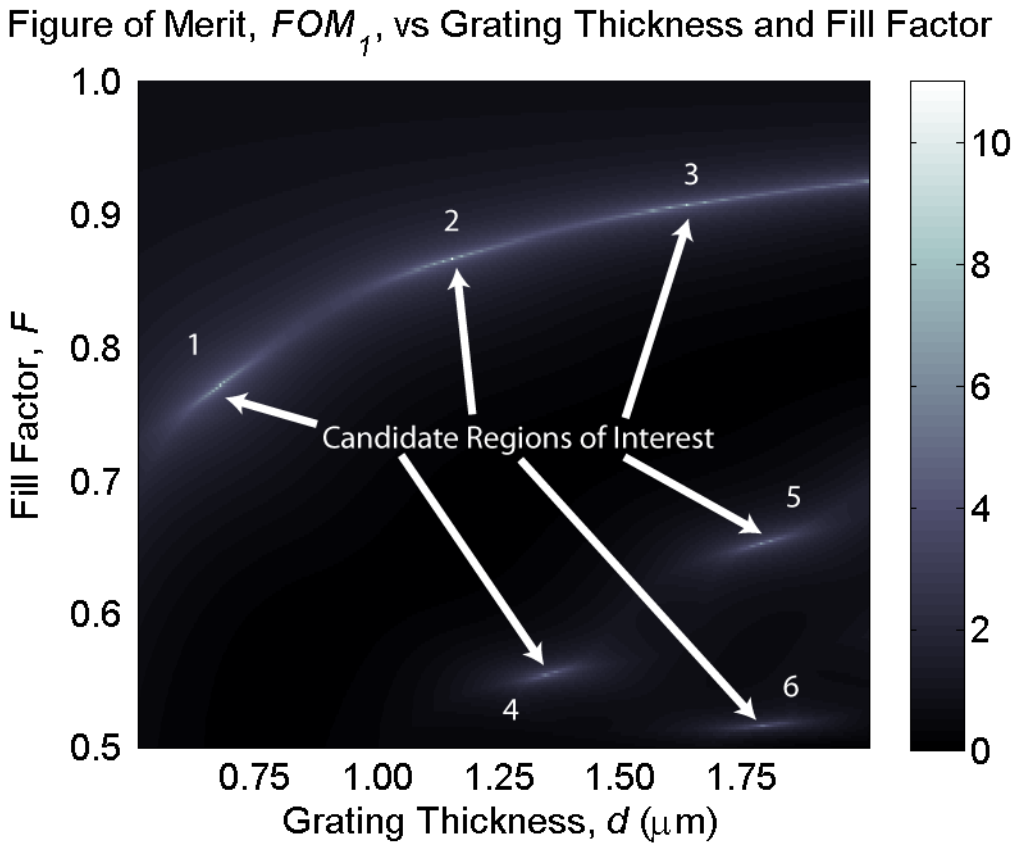

Figure B.4: A plot of figure-of-merit vs. grating thickness and fill factor for a primary grating target diffraction efficiency of 33%. Regions with potential design candidates are highlighted.

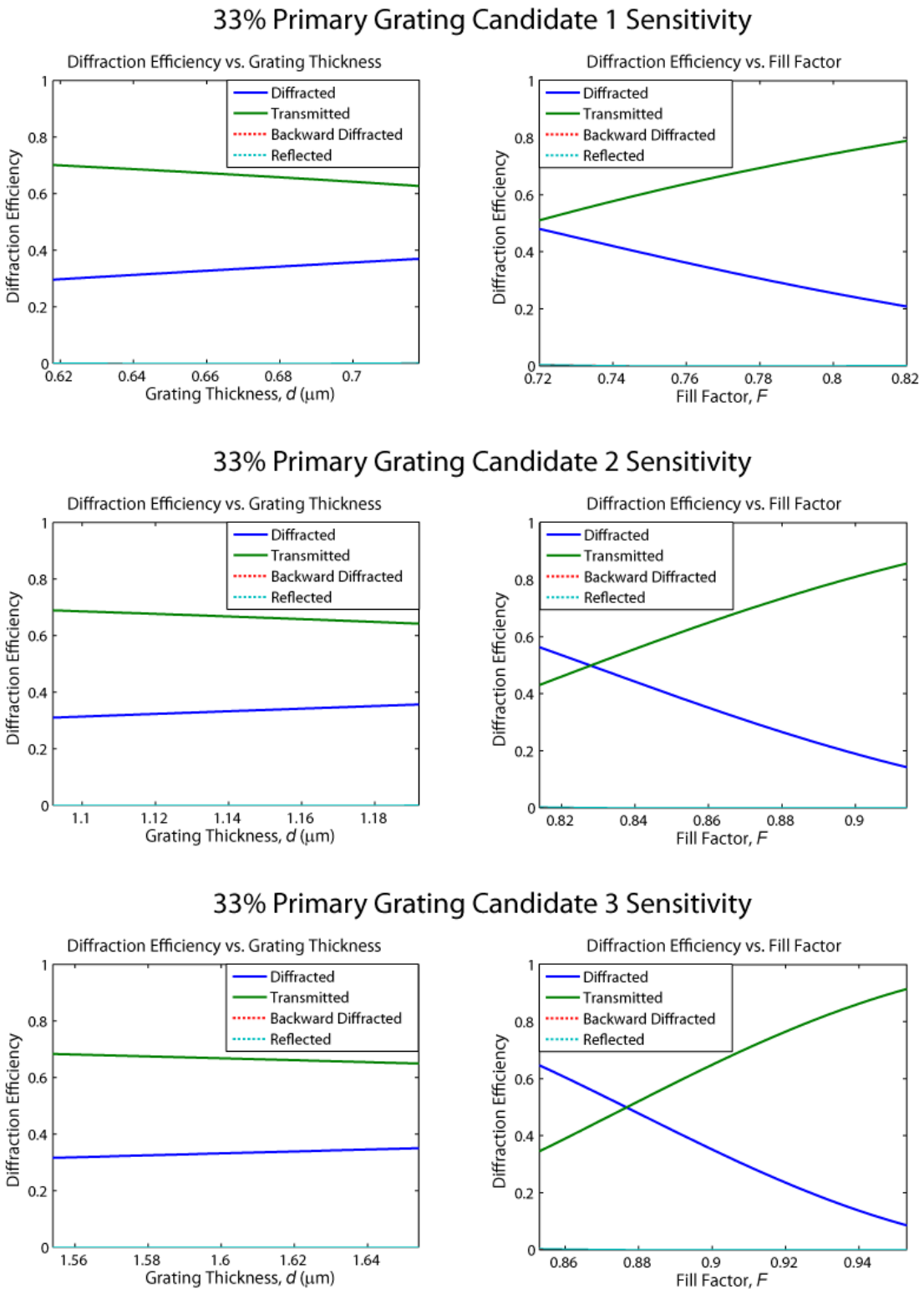

Figure B.5: RCWA grating thickness and fill factor sensitivities for primary grating candidates 1, 2, and 3 with target diffraction efficiencies of 33%.

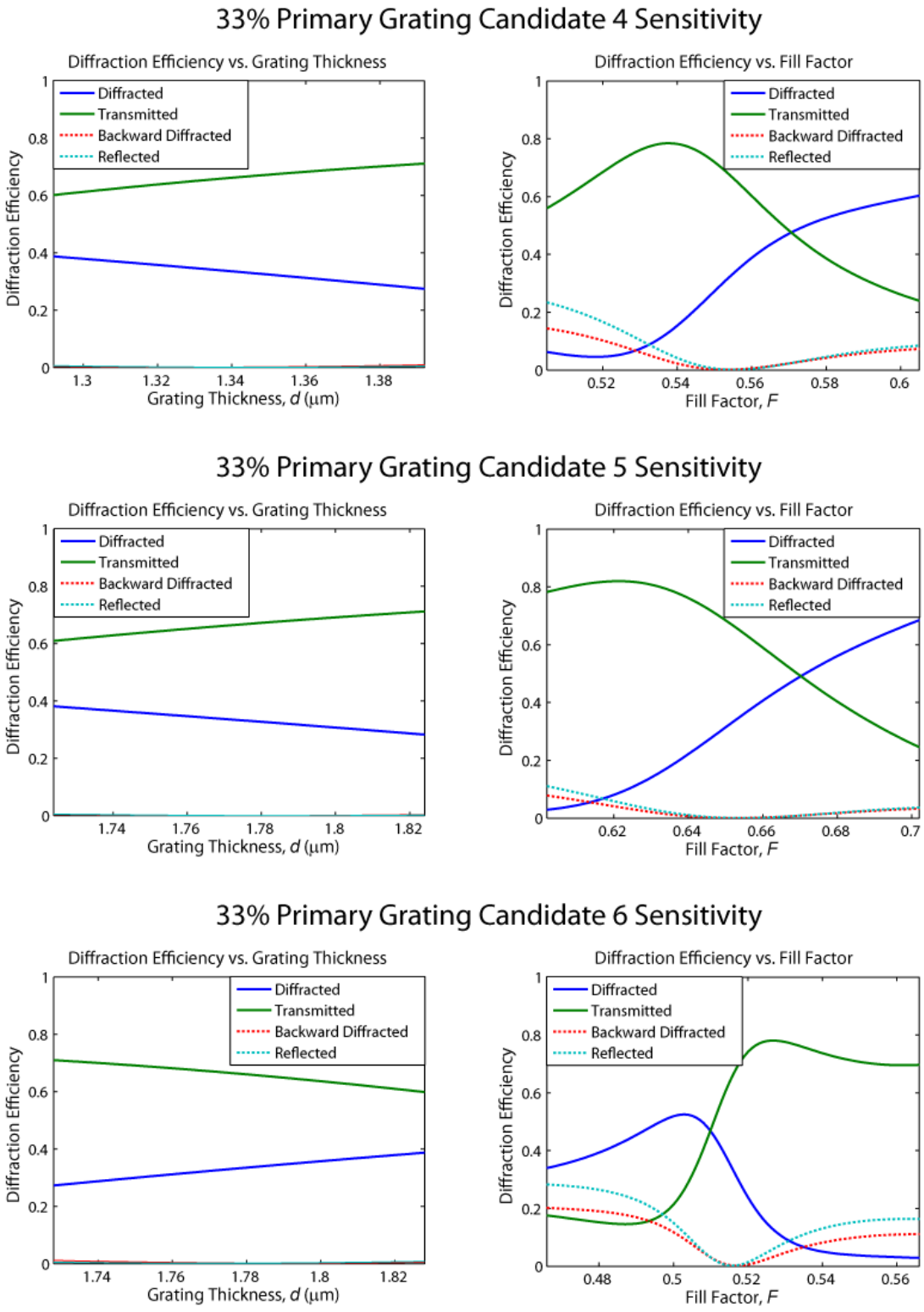

Figure B.6: RCWA grating thickness and fill factor sensitivities for primary grating candidates 4, 5, and 6 with target diffraction efficiencies of 33%.

B.1.3 Primary Grating with 50% Diffraction Efficiency

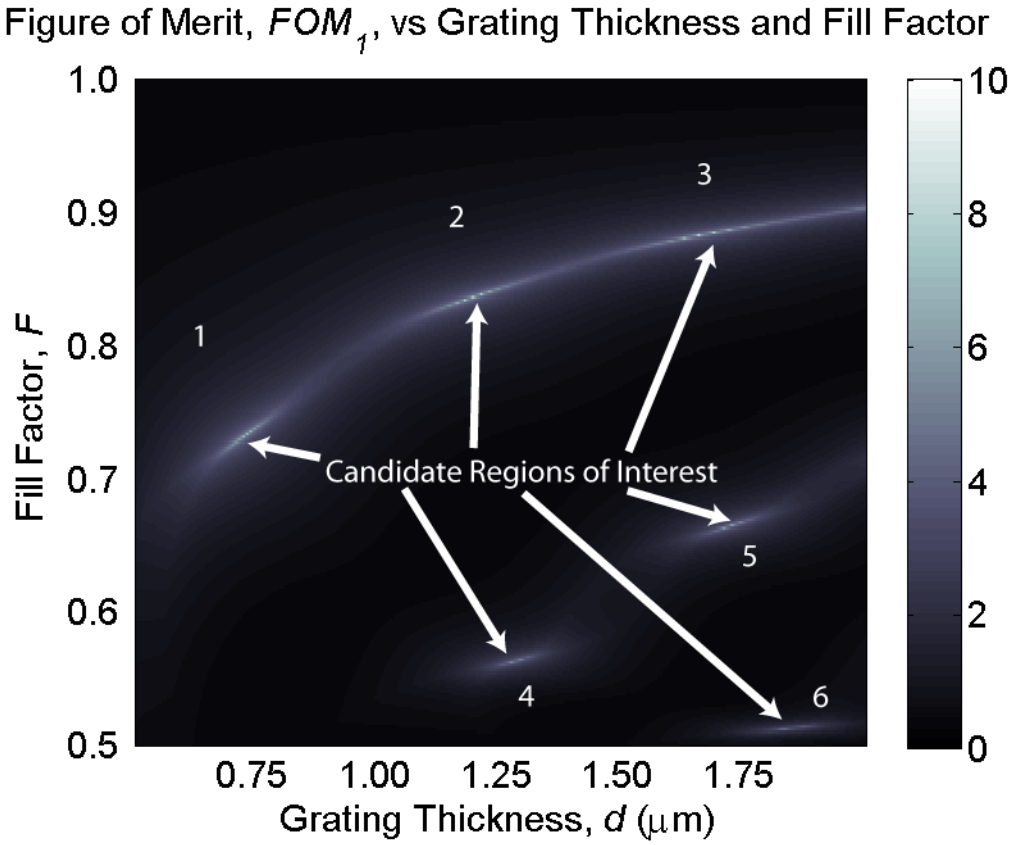

Figure B.7: A plot of figure-of-merit vs. grating thickness and fill factor for a primary grating target diffraction efficiency of 50%. Regions with potential design candidates are highlighted.

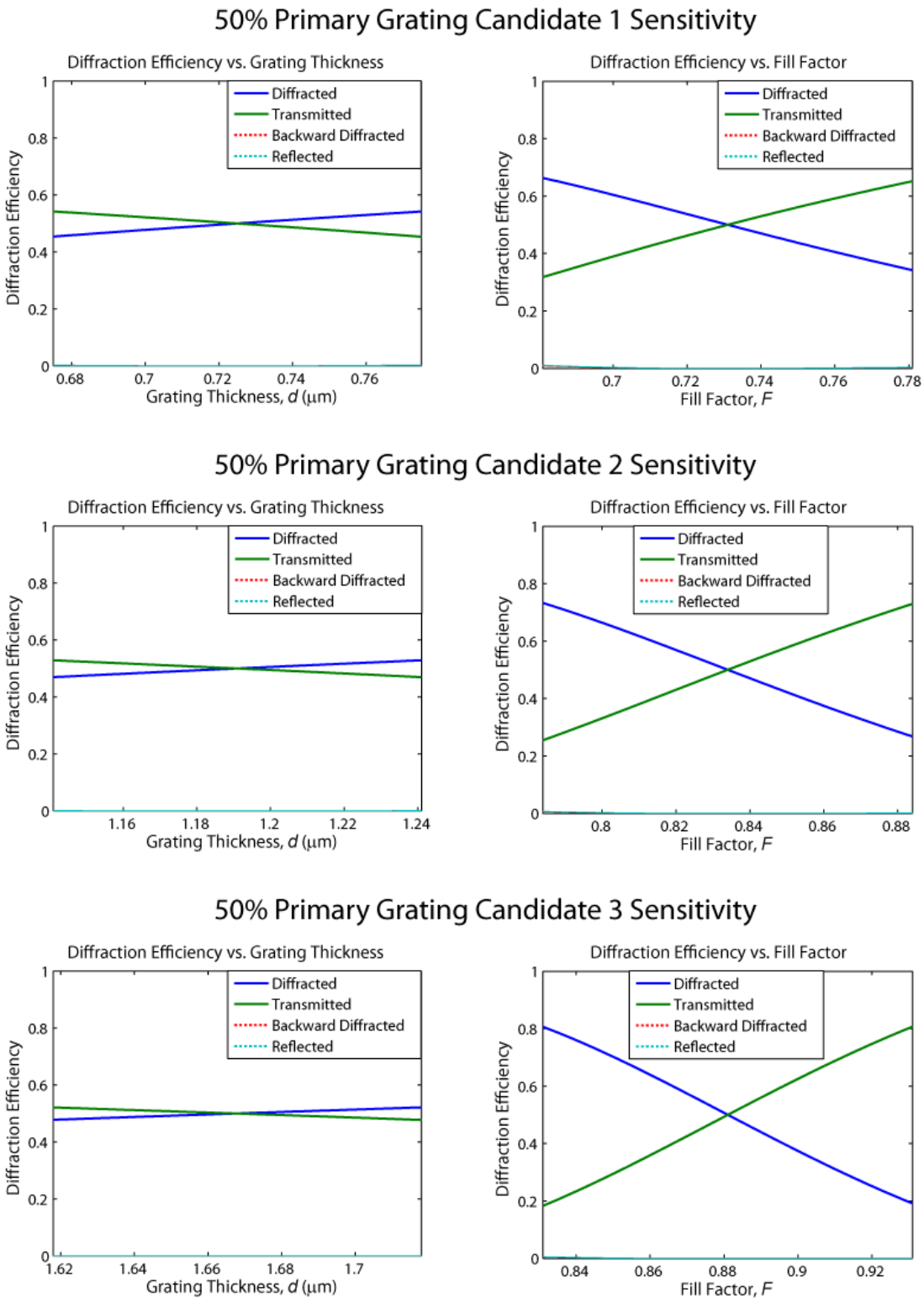

Figure B.8: RCWA grating thickness and fill factor sensitivities for primary grating candidates 1, 2, and 3 with target diffraction efficiencies of 50%.

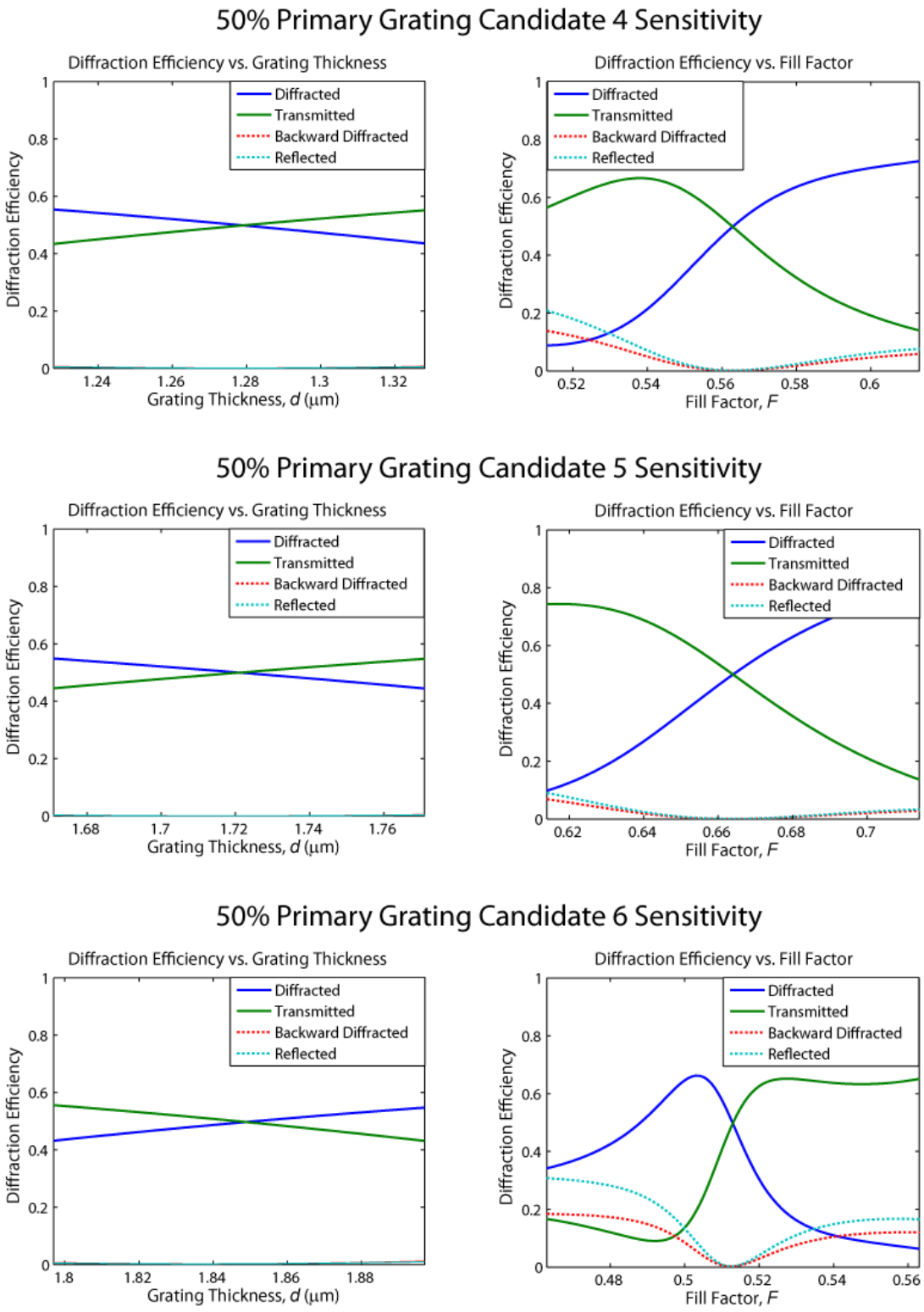

Figure B.9: RCWA grating thickness and fill factor sensitivities for primary grating candidates 4, 5, and 6 with target diffraction efficiencies of 50%.

B.2 Primary Grating Sensitivity Analysis

B.2.1 Primary Grating with 20% Diffraction Efficiency

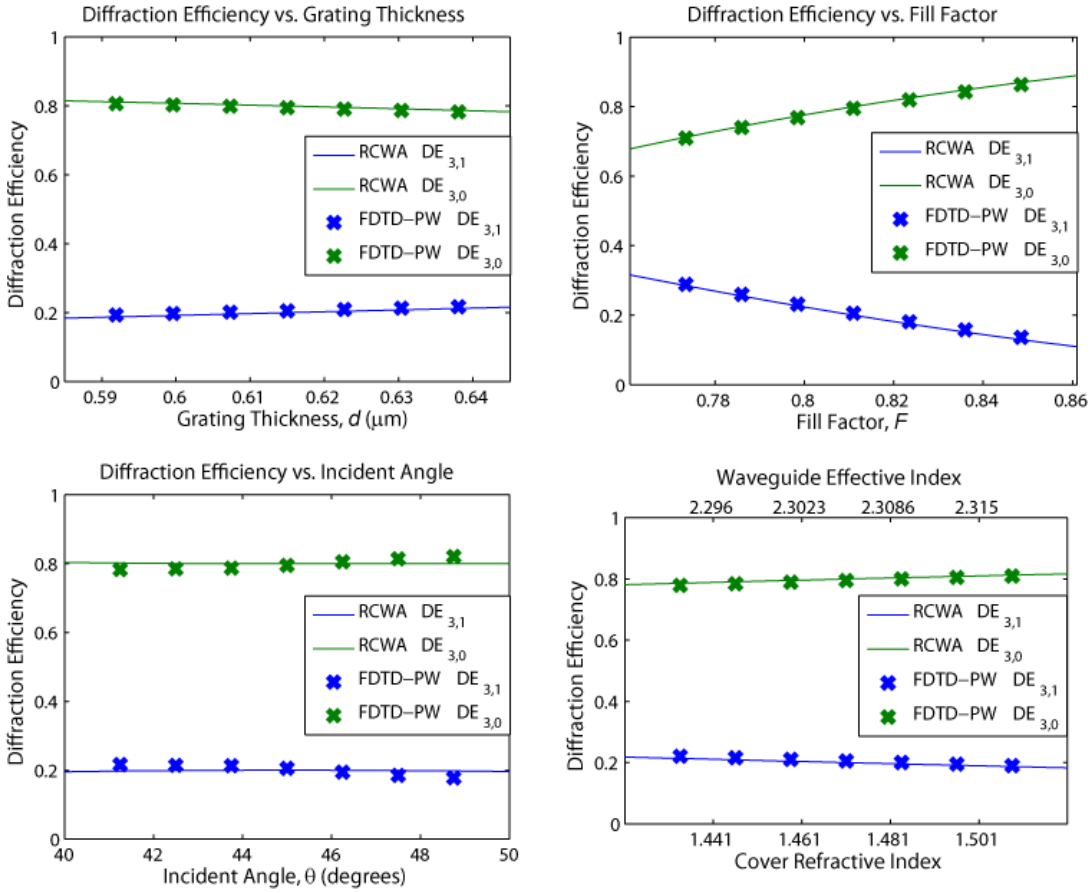

Figure B.10: FDTD plane-wave incidence sensitivity data for the primary grating design with 20% diffraction efficiency. Plots include sensitivities for thickness (top left), fill factor (top right), incident angle (bottom left), and surrounding refractive index (bottom right).

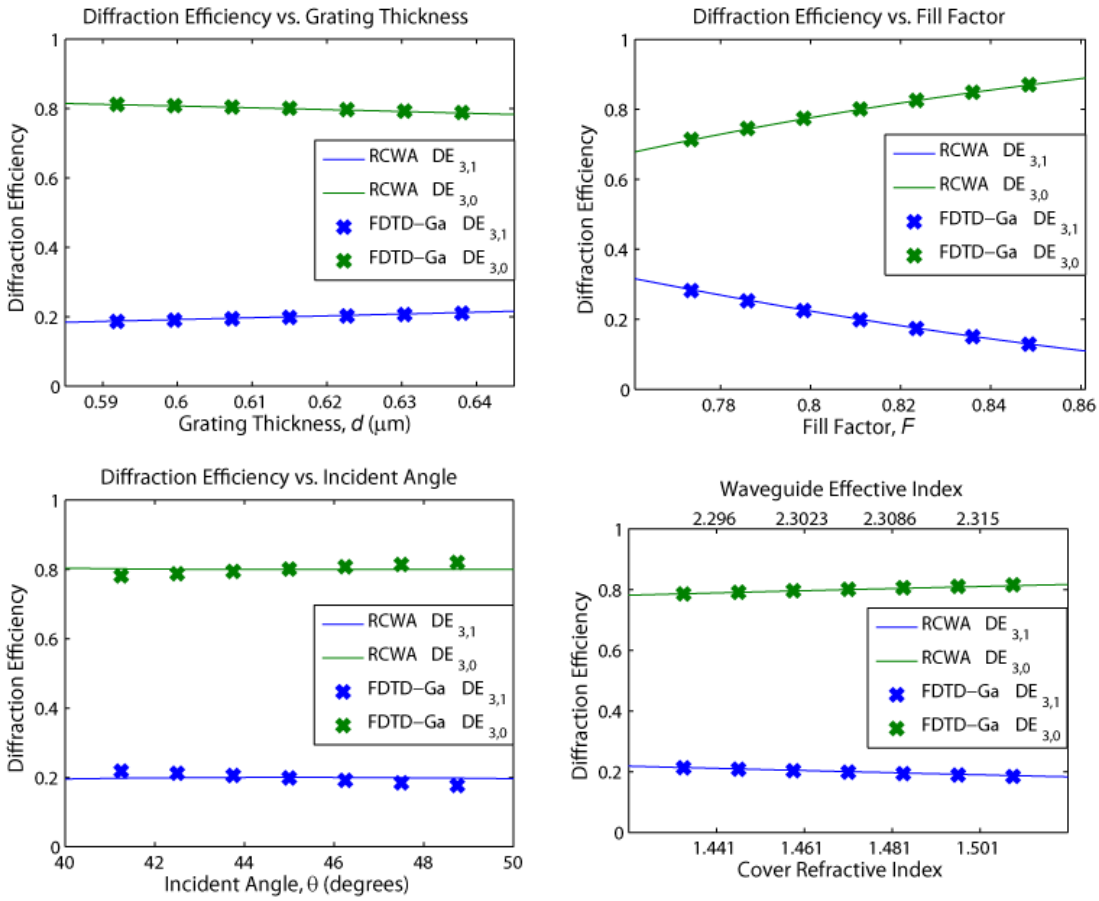

Figure B.11: FDTD Gaussian incidence sensitivity data for the primary grating design with 20% diffraction efficiency. Plots include sensitivities for thickness (top left), fill factor (top right), incident angle (bottom left), and surrounding refractive index (bottom right).

B.2.2 Primary Grating with 33% Diffraction Efficiency

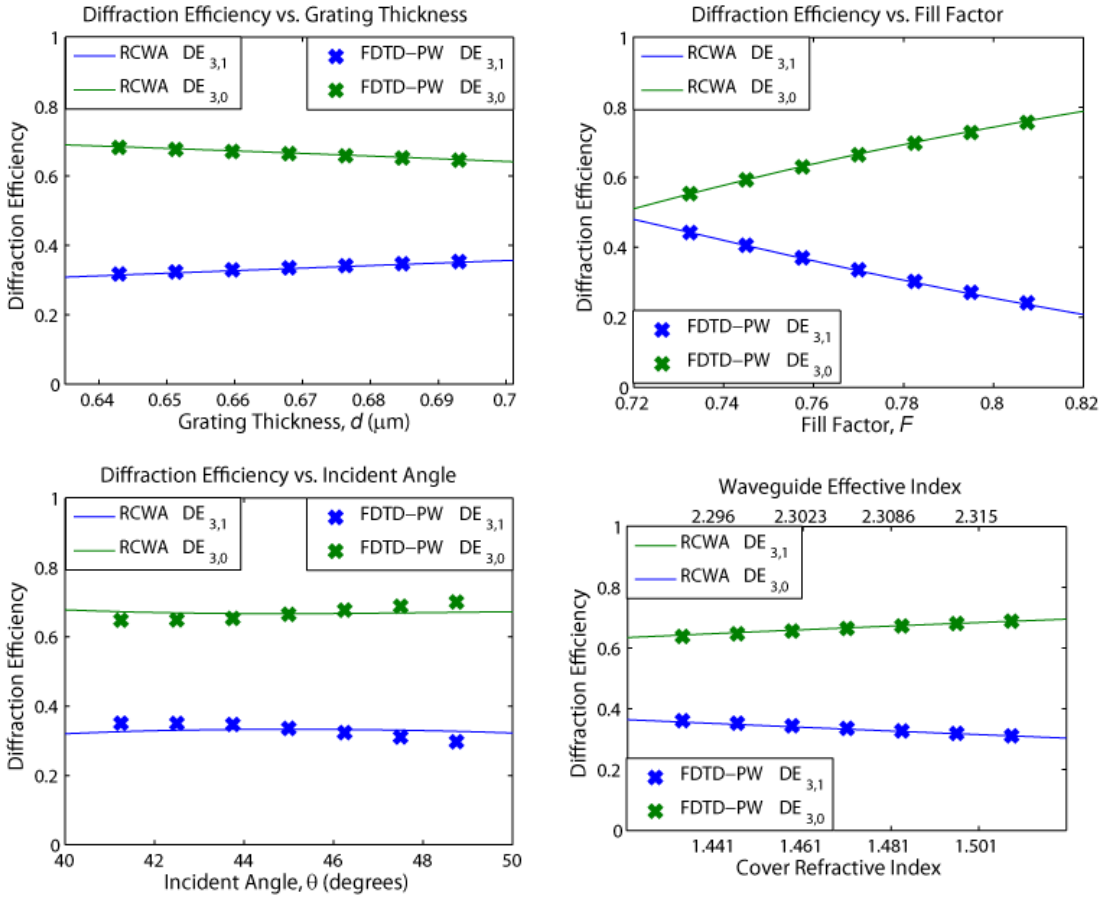

Figure B.12: FDTD plane-wave incidence sensitivity data for the primary grating design with 33% diffraction efficiency. Plots include sensitivities for thickness (top left), fill factor (top right), incident angle (bottom left), and surrounding refractive index (bottom right).

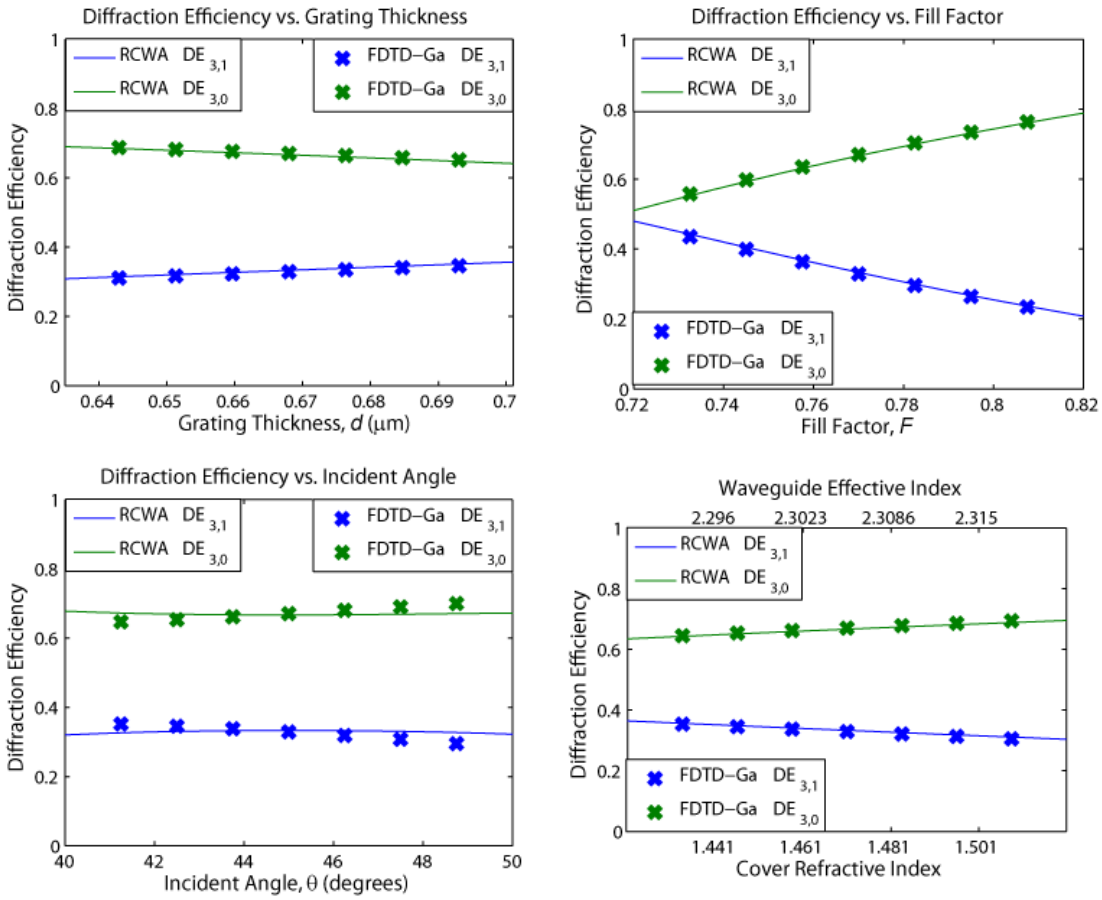

Figure B.13: FDTD Gaussian incidence sensitivity data for the primary grating design with 33% diffraction efficiency. Plots include sensitivities for thickness (top left), fill factor (top right), incident angle (bottom left), and surrounding refractive index (bottom right).

B.2.3 Primary Grating with 50% Diffraction Efficiency

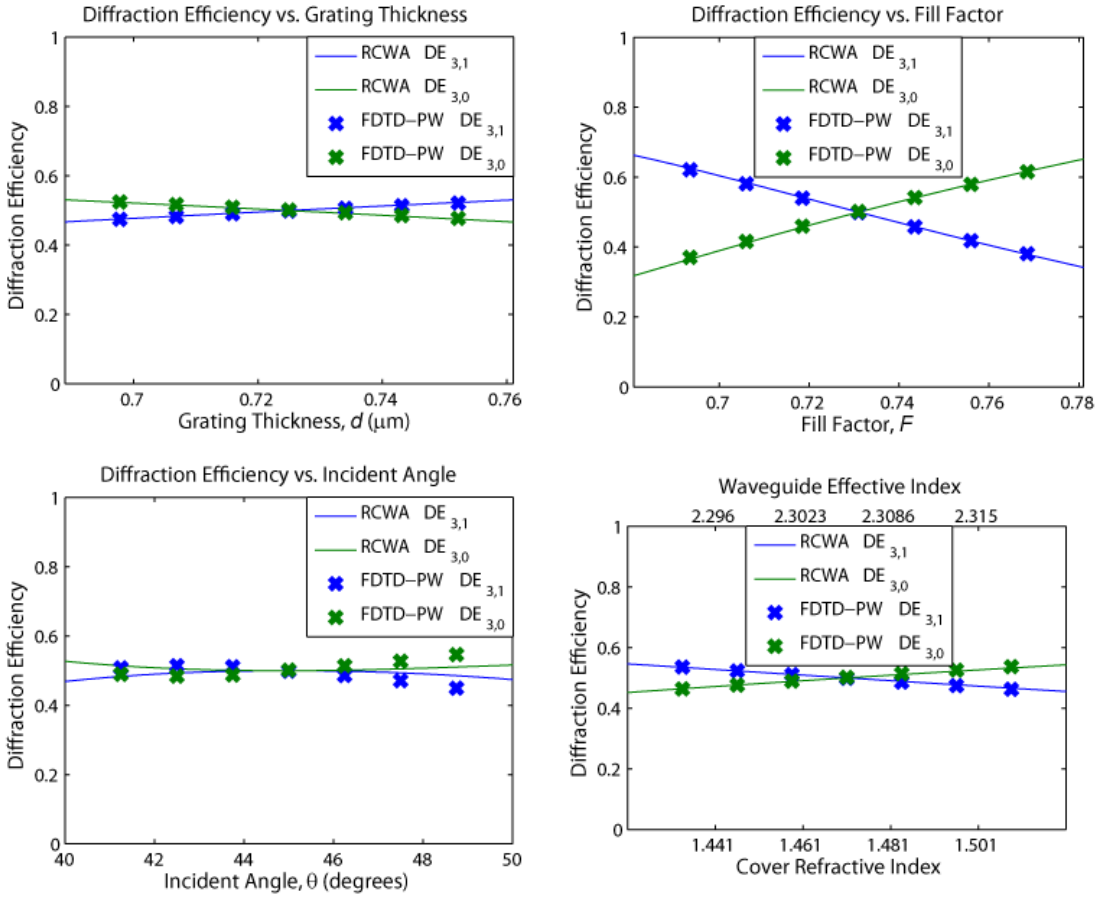

Figure B.14: FDTD plane-wave incidence sensitivity data for the primary grating design with 50% diffraction efficiency. Plots include sensitivities for thickness (top left), fill factor (top right), incident angle (bottom left), and surrounding refractive index (bottom right).

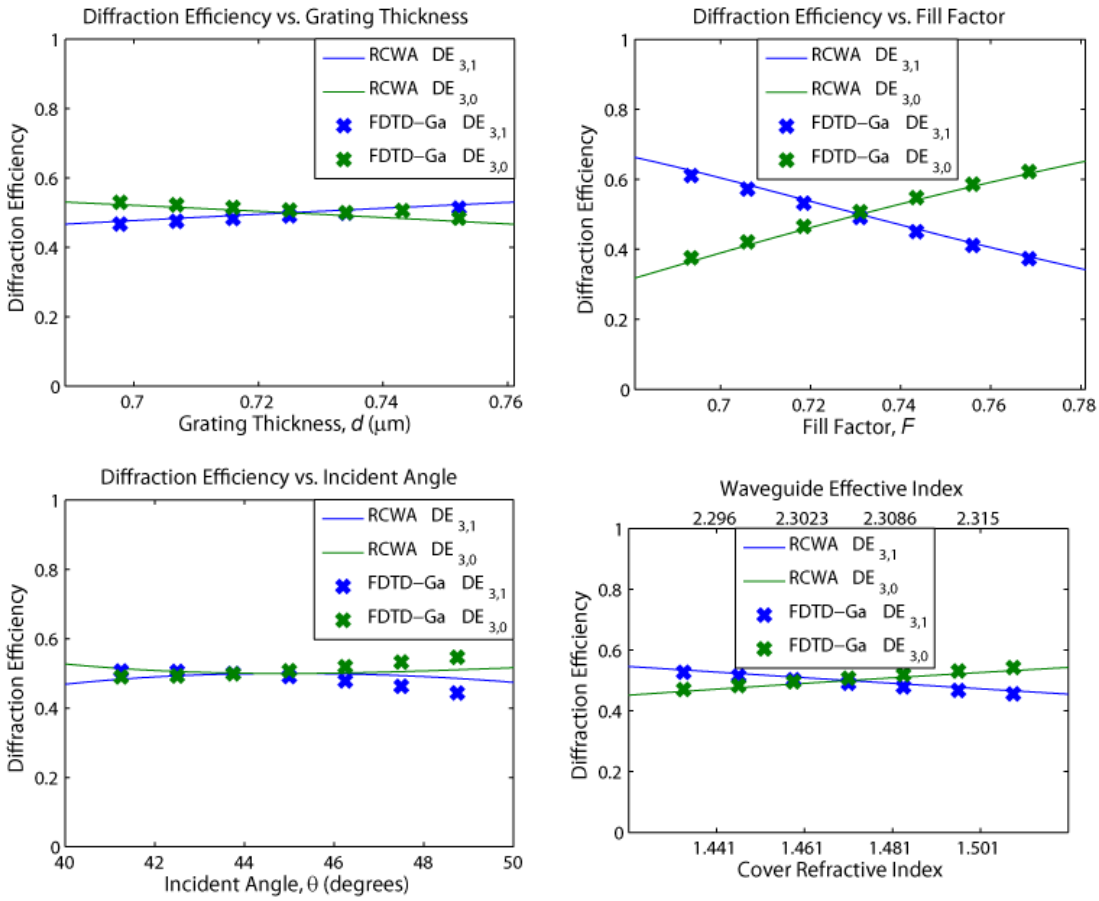

Figure B.15: FDTD Gaussian incidence sensitivity data for the primary grating design with 50% diffraction efficiency. Plots include sensitivities for thickness (top left), fill factor (top right), incident angle (bottom left), and surrounding refractive index (bottom right).

B.3 Secondary Grating Design Candidates

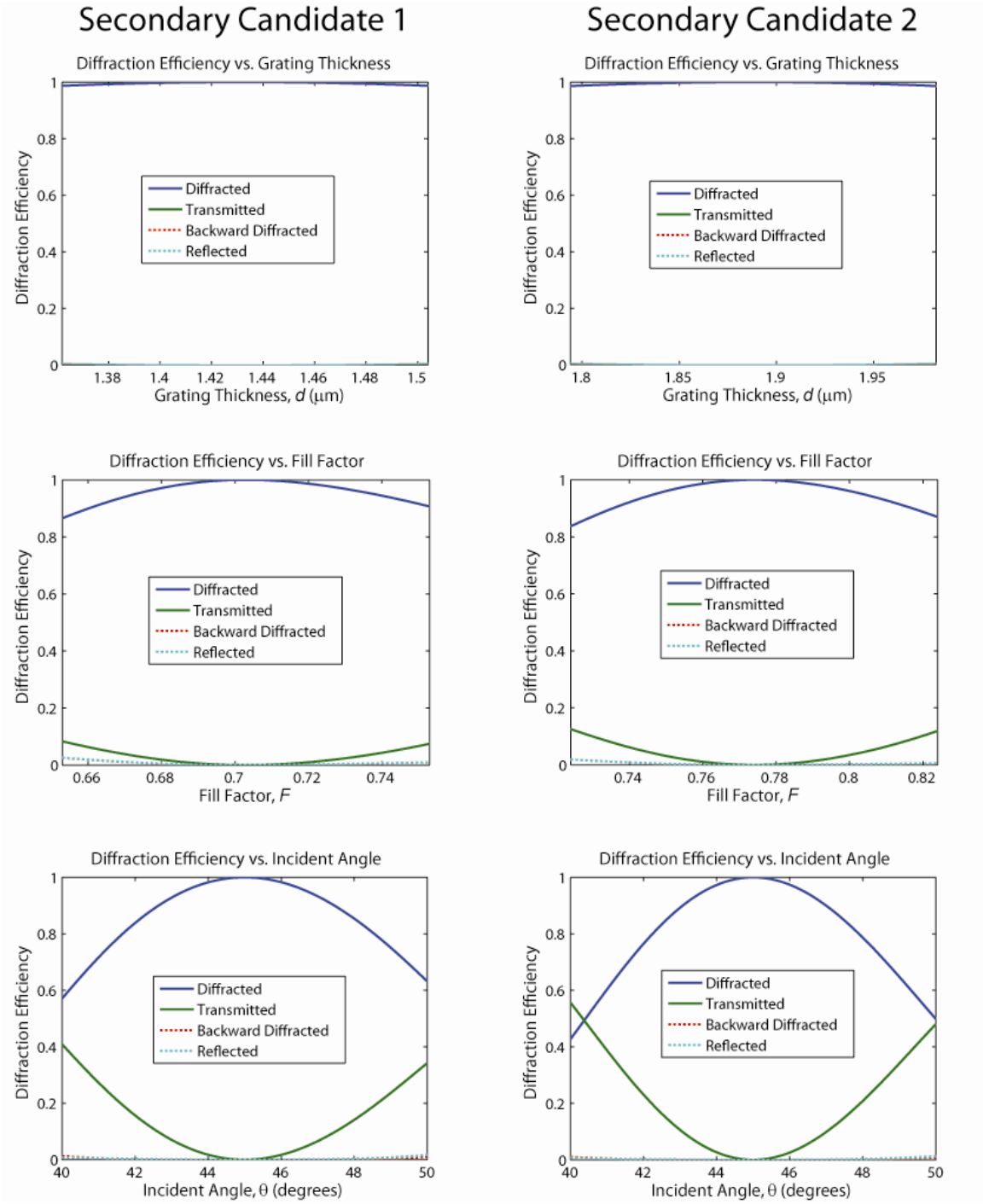

Figure B.16: RCWA grating thickness, fill factor, and incident angle sensitivities for secondary grating design candidates 1 and 2.

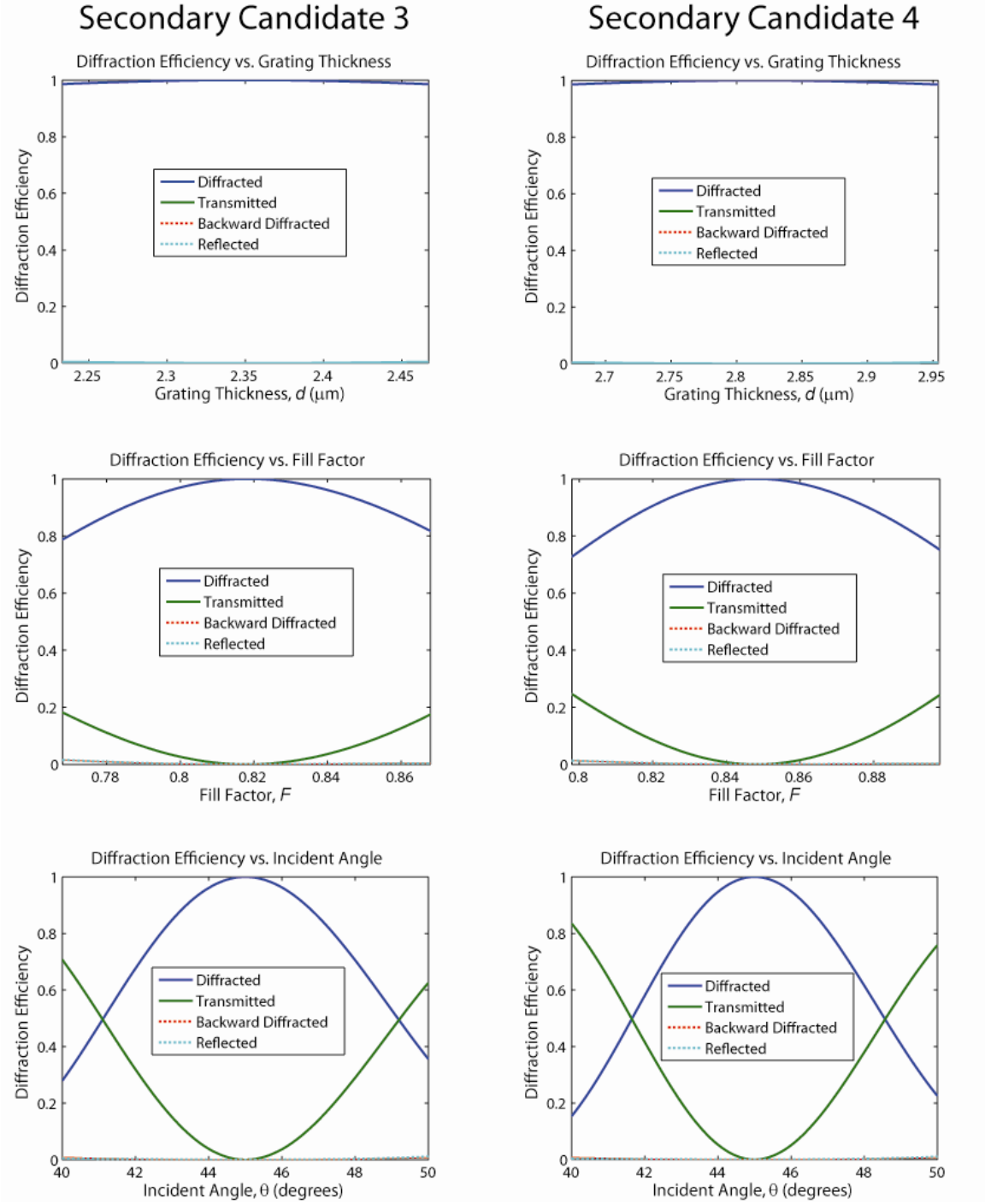

Figure B.17: RCWA grating thickness, fill factor, and incident angle sensitivities for secondary grating design candidates 3 and 4.

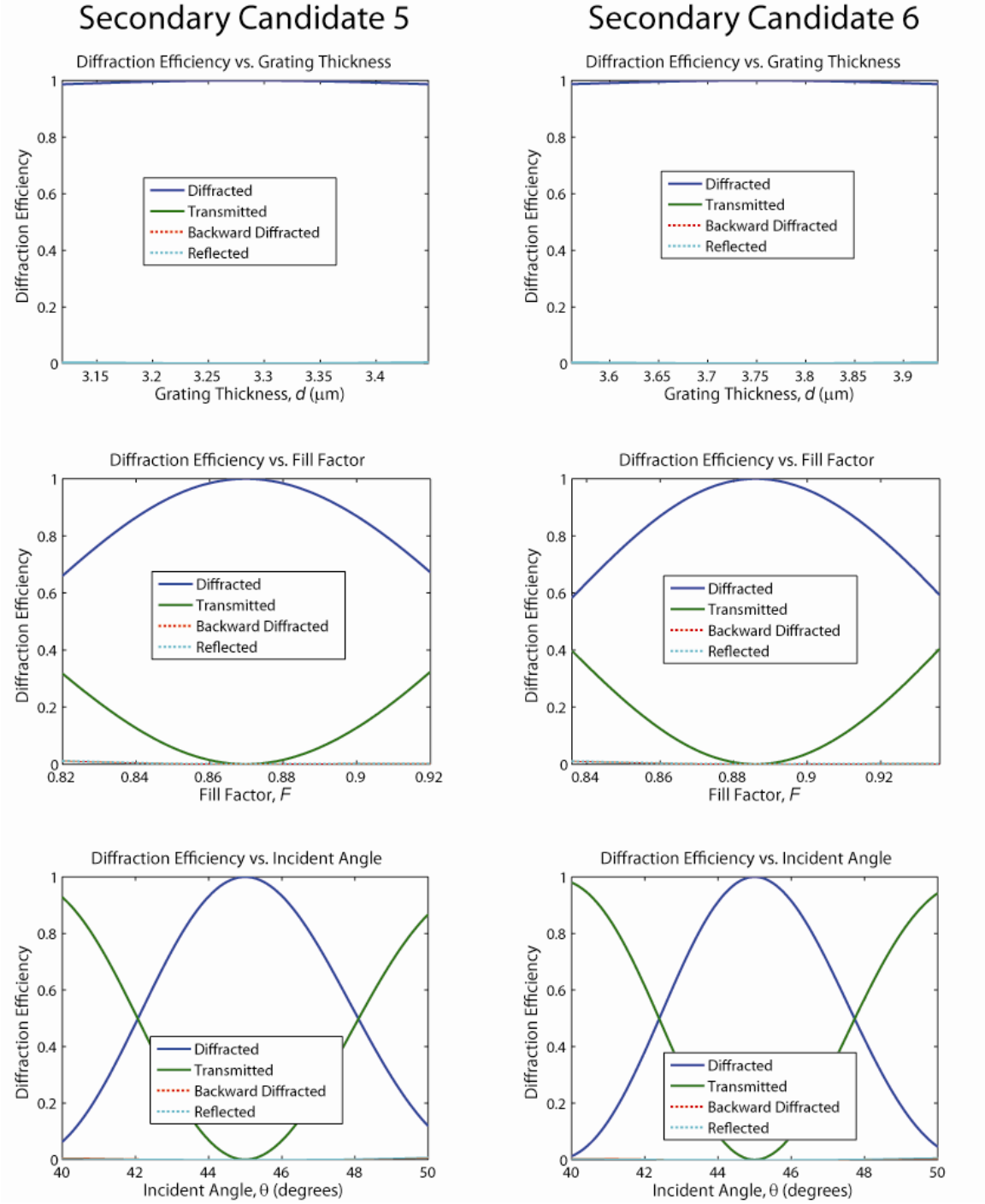

Figure B.18: RCWA grating thickness, fill factor, and incident angle sensitivities for secondary grating design candidates 5 and 6.

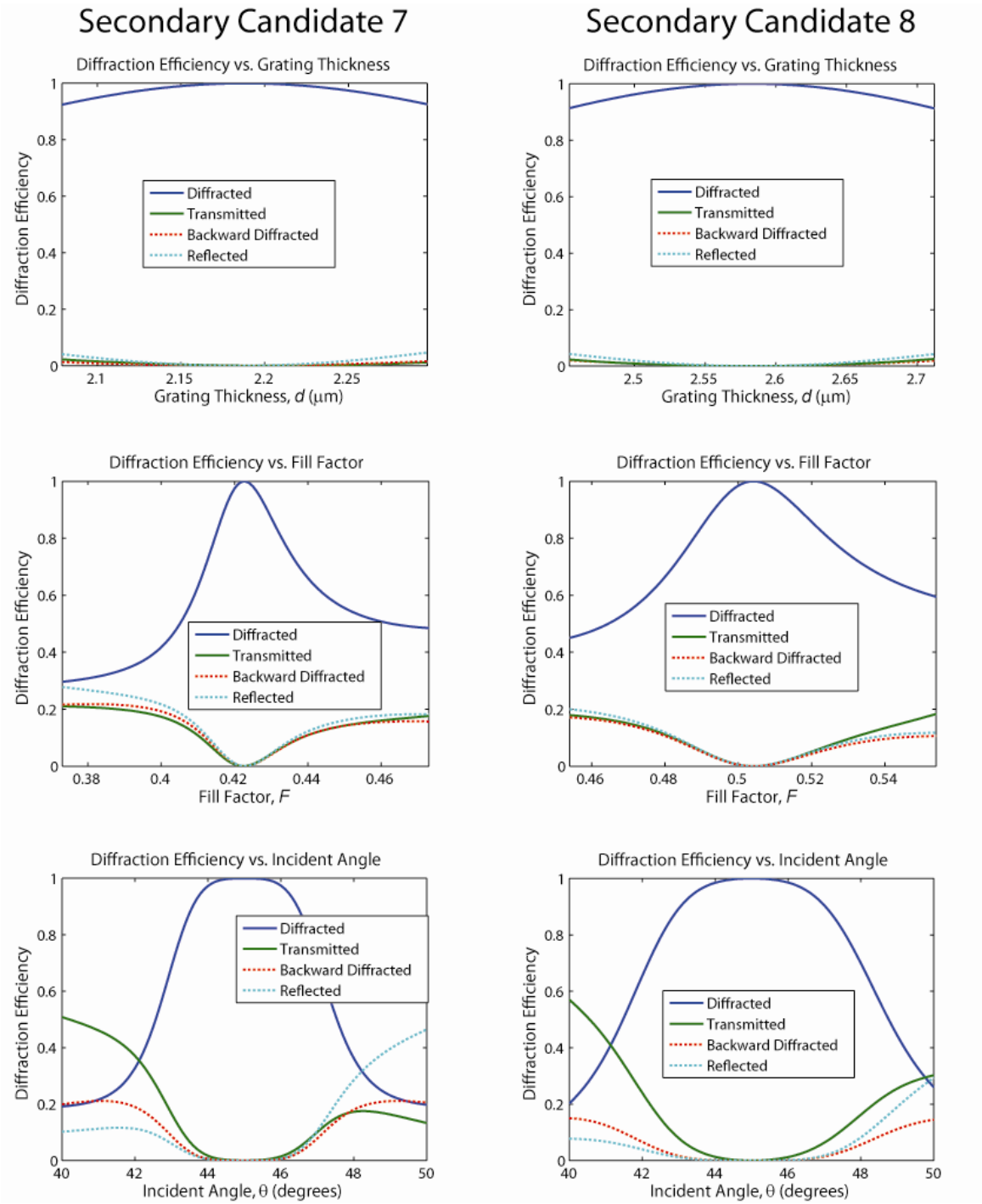

Figure B.19: RCWA grating thickness, fill factor, and incident angle sensitivities for secondary grating design candidates 7 and 8.

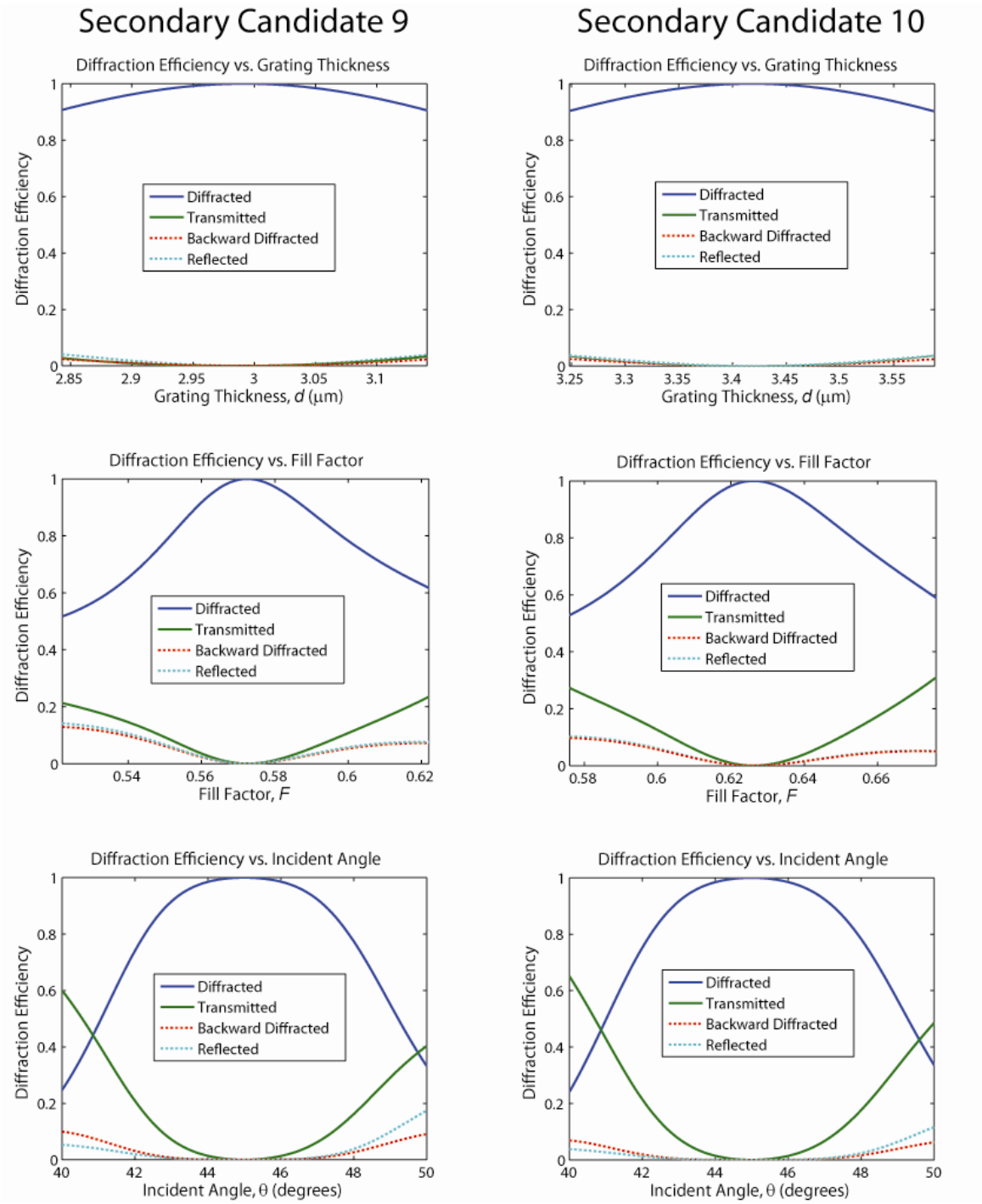

Figure B.20: RCWA grating thickness, fill factor, and incident angle sensitivities for secondary grating design candidates 9 and 10.

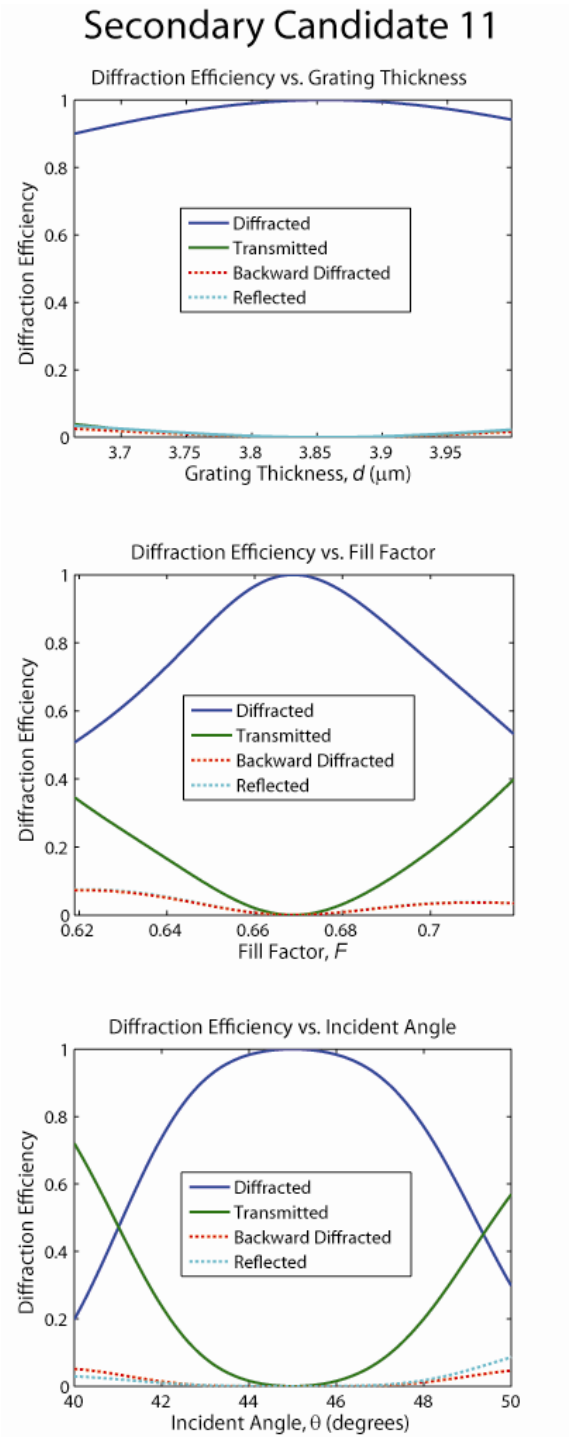

Figure B.21: RCWA grating thickness, fill factor, and incident angle sensitivities for secondary grating design candidate 11.

APPENDIX C

GRATING FABRICATION

C.1 Electron-Beam Resist Sidewall Collapse

With a silicon device layer thickness of $250nm$, a ZEP layer of approximately $400nm$ is necessary to perform a chlorine-based etch. This results in a patterned aspect ratio of 5.4:1 for the secondary grating. This presents a practical challenge in preventing sidewall collapse. This effect is illustrated in Fig. C.1 for a ZEP thickness of $350nm$.

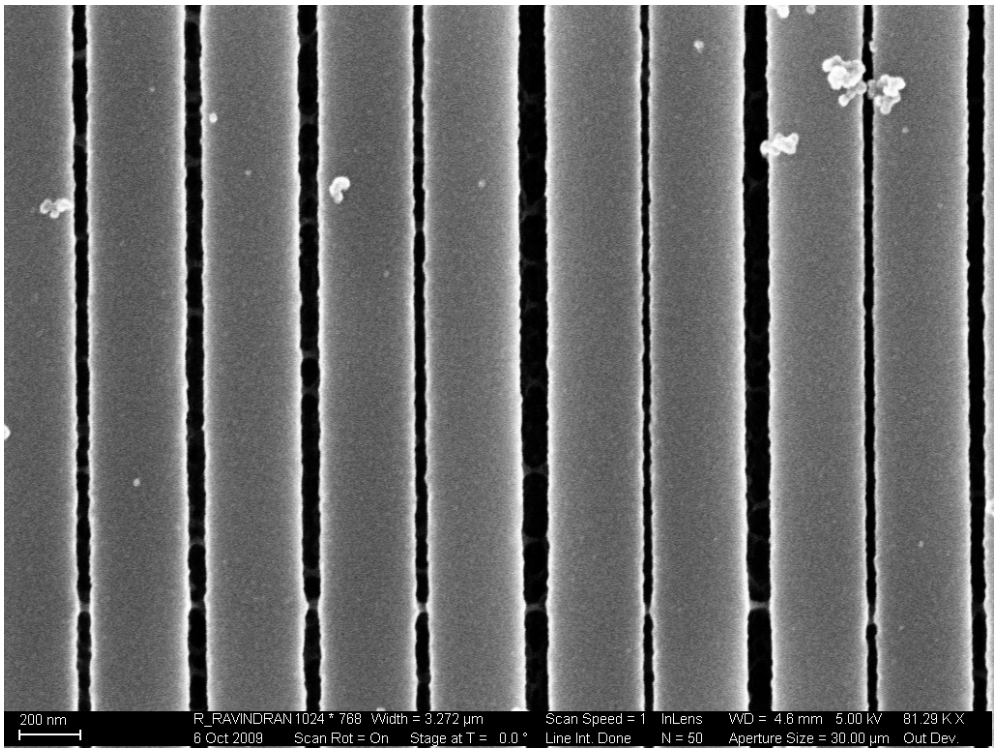

Figure C.1: SEM image of $74nm$ grating grooves patterned in $350nm$ of ZEP-520a. The high aspect ratio leads to sidewall collapse for a large variation in groove width.

C.2 Electron-Beam Lithography Dose Test

To determine the proper exposure dose, D, test gratings are patterned with doses from $160\mu C/cm^2$ to $240\mu C/cm^2$. Images for each dose are presented in Fig. C.2. A dose of $D = 220\mu C/cm^2$ is determined to be sufficient for defining the CSDS grating grooves.

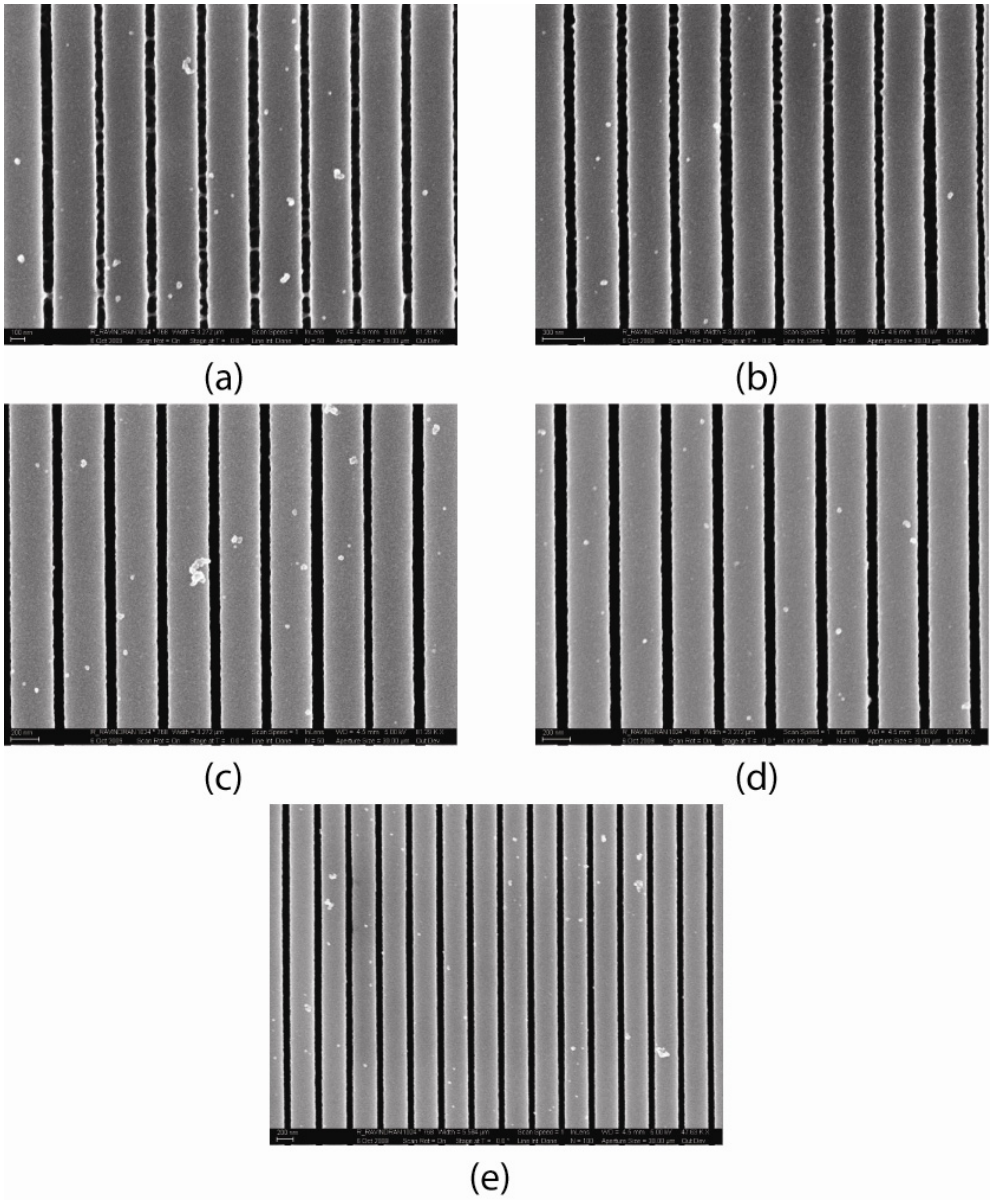

Figure C.2: Test grating patterns in ZEP-520a for exposure dosages of a) $D = 160\mu C/cm^2$, b) $D = 180\mu C/cm^2$, c) $D = 200\mu C/cm^2$, d) $D = 220\mu C/cm^2$, and e) $D = 240\mu C/cm^2$.

C.3 Low Pressure Etch Pinch-off Effect

The process pressure can be lowered to reduce the nano-scale Bosch process etch rate. However, it is observed that the etch depth is limited at lower pressures. This results in a decreased sidewall angle and pinched-off grooves. An example of this effect is presented in Fig. C.3 for a reduced pressure of 5*mTorr*.

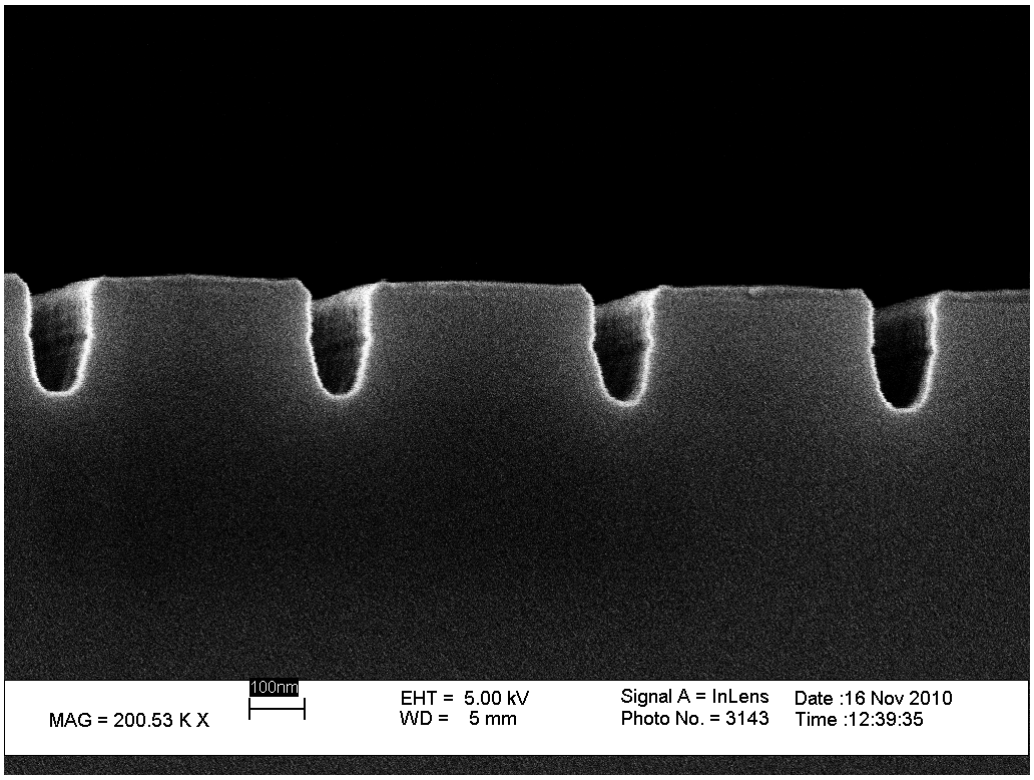

Figure C.3: Etched grating grooves with a lower process pressure of 5*mTorr* exhibiting the pinch-off effect.

APPENDIX D

FABRICATION PROCESS STEPS

D.1 Electron-Beam Lithography Process Steps

Samples are patterned with electron-beam lithography (EBL) according to the following process:

1) Wash sequentially in acetone, methanol, and isopropyl alcohol (AMI).
2) Wash in ultrasonic bath while submerged in acetone for 5*min*.
3) Wash in AMI.
4) Spin on ZEP-520a in a 4:1 anisole-to-ZEP dilution at 2000*rpm* for 60*sec.* with an initial acceleration of 1000*rpm/s*. This gives a ZEP layer of about 55*nm* for this piece size.
5) Soft bake at 180°*C* for 2*min*.

After the soft bake step, the layer thickness is measured with a NanoSpec 3000 refractometer. If the ZEP spin results are unacceptable because of particulates, adhesion, or improper layer thickness, the piece is submerged in Shipley Microposit [140] 1165 remover for 10 minutes and the process is restarted. If the layer thickness is acceptable and the sample looks free of particulates and color variations due to interference effects (indicating poor adhesion), it is loaded into the EBL tool for exposure. After EBL exposure, the resist is developed by the following process:

1) Submerse in n-amyl acetate for 2*min*.
2) Submerse in isopropyl alcohol for 30*sec*.
3) Dry gently with a nitrogen gun.

D.2 SU-8 Deposition Process Steps

Before the SU-8 overcoat can be deposited, the etched sample must be cleared of any ZEP residue and properly cleaned. The following steps are taken to prepare the sample:

1) Submerse in 1165 remover for 10*min*.
2) Wash in AMI.
3) Wash in ultrasonic bath while submerged in acetone for 5*min*.
4) Wash in AMI.

Since the remaining ZEP layer after etching is normally between 10*nm* and 20*nm* thick, it is unnecessary to heat the 1165 remover. Deposition of SU-8 takes place as follows:

1) Spin on SU-8 2002 initially at 500*rpm* for 10*sec.* with an initial acceleration of 100*rpm/s*.
2) Continue SU-8 2002 spin at 1000*rpm* for 30*sec.* with an initial acceleration of 300*rpm/s*. This gives an SU-8 thickness of about $2.9\mu m$ for this piece size.
3) Soft bake at $95°C$ for 1*min*.

The sample is then ready for ultraviolet (UV) exposure (365*nm*) to pattern the SU-8. For exposure, a Karl Suss MA-6 Mask Aligner is used. The masks used are fabricated at the NRC mask shop. These masks are clear field and patterned with chrome. For an SU-8 thickness of $2.9\mu m$, the appropriate UV dosage is $85mJ/cm^2$. After exposure, the following steps are taken to develop the SU-8:

1) Post-exposure bake at $95°C$ for 1*min*.
2) Submerse in SU-8 developer for 1*min.*
3) Rinse with fresh SU-8 developer for 10*sec*.
4) Rinse with isopropyl alcohol for 10*sec*.

5) Dry gently with a nitrogen gun.

The following steps are used in curing the SU-8:

1) Bake at $100°C$ for $5min$.
2) Bake at $125°C$ for $5min$.
3) Bake at $150°C$ for $20min$.

Cured samples are then removed from the hot plate and allowed to cool slowly on a non-conductive surface, such as a Texwipe, to prevent any new cracks from forming.

D.3 PBIBMA Deposition

Before deposition, a solution of PBIBMA in toluene is prepared with a concentration of $35mg/ml$ and filtered to a $0.2\mu m$ particle size. The sample is prepared with the following steps:

1) Rinse with isopropyl alcohol.
2) Dry with compressed air.
3) Repeat until all visible particulates are removed.

When dip-coating the sample, it is important to do a few dry runs to ensure that the desired draw speed is achieved. The sample is coated with the following steps:

1) Secure the sample to the motor-driven armature.
2) Lower the sample into the PBIBMA solution until the sensor is submerged.
3) Draw the sample at a speed of $0.7mm/\sec$. It is important not to disturb the armature or sample during the draw step. This typically yields a PBIBMA thickness of $70nm$.
4) Once the sample is completely removed from the solution, stop the motor and carefully remove it.

The sample is then examined with a Tencor profilometer to determine the PBIBMA thickness and inspect for particulates. If needed, the PBIBMA can be removed with acetone and the process can be restarted. After deposition, excess PBIBMA is removed with an acetone-soaked wipe. It is important to let excess acetone evaporate before using the wipe. This prevents excess acetone vapor from corrupting the functional PBIBMA surface.

D.4 Microfluidic Channel Assembly

Microfluidic channels are patterned with a razor knife in a small sheet of Teflon PFA. A capping sheet of the same size is patterned with access ports for fluid delivery. Before bonding, the sheets are prepared as follows:

1) Clean with acetone.
2) Clean with isopropyl alcohol.
3) Apply 770 surface primer. Allow to dry for one minute.

Proper bonding is essential to preventing leaks and ensuring that adhesive does not block the microchannel. The following steps are used to bond the Teflon PFA sheets:

1) Dispense small droplets of Loctite 401 around the microchannel perimeter.
2) Carefully align the capping sheet access ports to the microchannel sheet.
3) Establish contact between sheets in a smooth motion. It is critical that the sheets are aligned before this step as the fixture time is only a couple of seconds.
4) Inspect the assembly to ensure that the adhesive is evenly distributed around the microchannel and no adhesive has leaked into the microchannel.

Pressure can be applied to move adhesive into coverage gaps to a limited degree, but care must be taken to not push adhesive into the microchannel. If the bonding results are poor,

the sheets can be pried apart before curing. The adhesive can be removed with acetone to restart the process. If the results are acceptable, the microchannel assembly is allowed to cure for 24 hours.

To bond the microchannel assembly to the sensor, the same preparation steps are taken for the Teflon PFA. Particulates on the sensor are removed with compressed air. The sensor is not cleaned with any solvents and the 770 surface primer is not applied since this would destroy the PBIBMA immobilization layer. To minimize contamination, microchannels are preassembled and bonded to the sensor immediately following PBIBMA deposition. The bonding steps are similar, except that the adhesive is applied to the microchannel assembly and then the assembly is carefully flipped and aligned to the sensor. This is necessary since the SOI substrate is opaque. The sensor is then allowed to cure for 24 hours before use.

REFERENCES

[1] D. R. Reyes, D. Iossifidis, P.-A. Auroux, and A. Manz, "Micro total analysis systems. 1. Introduction, theory, and technology," *Anal. Chem.,* vol. 74, pp. 2623-2636, Jun. 15, 2002.

[2] E. M. J. Verpoorte, B. H. van der Schoot, S. Jeanneret, A. Manz, H. M. Widmer, and N. F. de Rooij, "Three-dimensional micro flow manifolds for miniaturized chemical analysis systems," *J. Micromech. Microeng.,* vol. 4, pp. 248-256, Dec. 1994.

[3] A. Manz, N. Graber, and H. M. Widmer, "Miniaturized total chemical analysis systems: a novel concept for chemical sensing," *Sens. Actuators B-Chem.,* vol. B1, pp. 244-248, Jan. 1990.

[4] P.-A. Auroux, D. Iossifidis, D. R. Reyes, and A. Manz, "Micro total analysis systems. 2. Analytical standard operations and applications," *Anal. Chem.,* vol. 74, pp. 2637-2652, Jun. 15, 2002.

[5] M. Iqbal, M. A. Gleeson, B. Spaugh, F. Tybor, W. G. Gunn, M. Hochberg, T. Baehr-Jones, R. C. Bailey, and L. C. Gunn, "Label-free biosensor arrays based on silicon ring resonators and high-speed optical scanning instrumentation," *IEEE J. Sel. Top. Quant.,* vol. 16, pp. 654-661, May/June 2010.

[6] J. R. Krenn, N. Galler, H. Ditlbacher, A. Hohenau, B. Lamprecht, E. Kraker, G. Jakopic, and T. Mayr, "Waveguide-integrated SPR sensing on an all-organic platform," *Proc. SPIE*, vol. 8073, pp. 80730F1-80730F1-6, 2011.

[7] R. D. Harris and J. S. Wilkinson, "Waveguide surface plasmon resonance sensors," *Sens. Actuators B-Chem.,* vol. 29, pp. 261-267, Oct. 1995.

[8] F. Prieto, B. Sepulveda, A. Calle, A. Llobera, C. Dominguez, A. Abad, A. Montoya, and L. M. Lechuga, "An integrated optical interferometric nanodevice based on silicon technology for biosensor applications," *Nanotechnol.,* vol. 14, pp. 907-12, Aug. 2003.

[9] L. M. Lechuga, K. Zinoviev, L. Fernandez, J. Elizalde, O. E. Hidalgo, and C. Dominguez, "Biosensing microsystem platforms based on the integration of Si Mach-Zehnder interferometer, microfluidics and grating couplers," *Proc. SPIE*, vol. 7220, pp. 72200L-1-72200L-8, 2009.

[10] B. Sepulveda, J. S. del Rio, M. Moreno, F. J. Blanco, K. Mayora, C. Dominguez, and L. M. Lechuga, "Optical biosensor microsystems based on the integration of

highly sensitive Mach-Zehnder interferometer devices," *J. Opt. A-Pure Appl. Op.,* vol. 8, pp. 561-566, July 2006.

[11] C.-Y. Chao, W. Fung, and L. J. Guo, "Polymer microring resonators for biochemical sensing applications," *IEEE J. Sel. Top. Quant. Electron.,* vol. 12, pp. 134-142, Jan./Feb. 2006.

[12] K. De Vos, I. Bartolozzi, E. Schacht, P. Bienstman, and R. Baets, "Silicon-on-insulator microring resonator for sensitive and label-free biosensing," *Opt. Express,* vol. 15, pp. 7610-7615, Jun. 6, 2007.

[13] J. Homola, *Surface Plasmon Resonance Based Sensors,* vol. 4. Berlin-Heidelberg: Springer, 2006.

[14] P. Debackere, D. Taillaert, K. De Vos, S. Scheerlinck, P. Bienstman, and R. Baets, "Si based waveguide and surface plasmon sensors," *Proc. SPIE*, vol. 6477, pp. 647719-1-647719-10, 2007.

[15] H. Sung-Hoon, K. Chang-Kyeng, K. Bo-Soon, L. Min-Woo, L. Seung-Gol, P. Se-Geun, L. El-Hang, and O. Beom-Hoan, "Implementation of surface plasmon resonance planar waveguide sensor system," *Microelectron. Eng.,* vol. 87, pp. 1315-1318, May 2010.

[16] L. U. Kempen and R. E. Kunz, "Replicated Mach-Zehnder interferometers with focusing grating couplers for sensing applications," *Sens. Actuators B-Chem.,* vol. 39, pp. 295-299, Mar.-Apr. 1997.

[17] B. Y. Shew, Y. C. Cheng, and Y. H. Tsai, "Monolithic SU-8 micro-interferometer for biochemical detections," *Sens. Actuators A-Phys.,* vol. 141, pp. 299-306, Feb. 15, 2008.

[18] J. Flueckiger, S. M. Grist, G. Bisra, L. Chrostowski, and K. C. Cheung, "Cascaded silicon-on-insulator microring resonators for the detection of biomolecules in PDMS microfluidic channels," *Proc. SPIE*, vol. 7929, pp. 79290I-1-79290I-10, 2011.

[19] J. S. Maikisch and T. K. Gaylord, "A compact integrated optical chemical/biological sensor," in *Frontiers in Optics*, Rochester, NY, 2008, p. FWT4.

[20] J. S. Maikisch and T. K. Gaylord, "Compact silicon-on-insulator diffractive sensor design," in *Frontiers in Optics*, San Jose, CS, 2009, p. FMJ4.

[21] J. S. Maikisch and T. K. Gaylord, "Compact silicon diffractive sensors," in *Frontiers in Optics*, Rochester, NY, 2010, p. FMJ2.

[22] J. S. Maikisch and T. K. Gaylord, "Compact silicon diffractive sensor characterization," in *Frontiers in Optics*, San Jose, CA, 2011, p. FThN3.

[23] J. S. Maikisch and T. K. Gaylord, "Compact silicon diffractive sensor: design, fabrication, and prototype," *Appl. Opt.,* vol. 51, pp. 4325-4332, Jul. 1, 2012.

[24] J. S. Maikisch and T. K. Gaylord, "Compact silicon diffractive sensor: functional demonstration and array prototype," *Appl. Opt.,* p. (in preparation), 2012.

[25] S. C. Terry, J. H. Jerman, and J. B. Angell, "A gas chromatographic air analyzer fabricated on a silicon wafer," *IEEE Trans. Electron Dev.,* vol. 26, pp. 1880-1886, Dec. 1979.

[26] Royal Society of Chemistry Publishing, Cambridge, UK, http://pubs.rsc.org/en/journals/journalissues/lc

[27] Biacore Life Sciences, Piscataway, NJ, www.biacore.com

[28] Agilent Technologies, Santa Clara, CA, www.agilent.com

[29] Epoch Biosciences, Bothell, WA, www.epochbio.com

[30] Caliper Technologies, Hopkinton, MA, www.caliperls.com

[31] Z. Z. Wang, T. Wilkop, D. K. Xu, Y. Dong, G. Y. Ma, and Q. Cheng, "Surface plasmon resonance imaging for affinity analysis of aptamer - protein interactions with PDMS microfluidic chips," *Anal. Bioanal. Chem.,* vol. 389, pp. 819-825, Oct. 2007.

[32] W. Budach, A. P. Abel, A. E. Bruno, and D. Neuschafer, "Planar waveguides as high-performance sensing platforms for fluorescence-based multiplexed oligonucleotide hybridization assays," *Anal. Chem.,* vol. 71, pp. 3347-3355, Jul. 2, 1999.

[33] H. Yu-Jie, H. Che-Wei, L. Tsung-Hsien, L. Chih-Ting, C. Li-Guang, H. Po-Yun, W. Bi-Ru, H. Hsiao-Ting, K. Bing-Jye, T. Hann-Huei, L. Hsin-Hao, J. Ying-Zong, W. Chorng-Kuang, and L. Shey-Shi, "A fully-integrated cantilever-based DNA detection SoC in a CMOS Bio-MEMS process," *Symp. VLSI Circuits*, Piscataway, NJ, pp. 50-51, 2011.

[34] A. J. Qavi and R. C. Bailey, "Multiplexed detection and label-free quantitation of microRNAs using arrays of silicon photonic microring resonators," *Angew. Chem., Int. Ed.,* vol. 49, pp. 4608-4611, Jun. 21, 2010.

[35] B. H. Schneider, J. G. Edwards, and N. F. Hartman, "Hartman interferometer: versatile integrated optic sensor for label-free, real-time quantification of nucleic acids, proteins, and pathogens," *Clin. Chem.,* vol. 43, pp. 1757-1763, Sept. 1, 1997.

[36] J. Xu, D. Suarez, and D. Gottfried, "Detection of avian influenza virus using an interferometric biosensor," *Anal. Bioanal. Chem.,* vol. 389, pp. 1193-1199, Aug. 21, 2007.

[37] H. Vaisocherova, K. Mrkvova, M. Piliarik, P. Jinoch, M. Steinbachova, and J. Homola, "Surface plasmon resonance biosensor for direct detection of antibody against Epstein-Barr virus," *Biosens. Bioelectron.,* vol. 22, pp. 1020-1026, Jun. 21, 2007.

[38] K. De Vos, J. Girones, T. Claes, Y. De Koninck, S. Popelka, E. Schacht, R. Baets, and P. Bienstman, "Multiplexed antibody detection with an array of silicon-on-insulator microring resonators," *IEEE Photonics J.,* vol. 1, pp. 225-235, Oct. 2009.

[39] J. Trevino, A. Calle, J. M. Rodriguez-Frade, M. Mellado, and L. M. Lechuga, "Determination of human growth hormone in human serum samples by surface plasmon resonance immunoassay," *Talanta,* vol. 78, pp. 1011-1016, May 15, 2009.

[40] J. W. Chung, R. Bernhardt, and J. C. Pyun, "Additive assay of cancer marker CA 19-9 by SPR biosensor," *Sens. Actuators B-Chem.,* vol. 118, pp. 28-32, Oct. 25, 2006.

[41] R. C. Bailey, A. L. Washburn, A. J. Qavi, M. Iqbal, M. Gleeson, F. Tybor, and L. C. Gunn, "A robust silicon photonic platform for multiparameter biological analysis," *Proc. SPIE*, vol. 7220, pp. 72200N-1-72200N-6, 2009.

[42] K. Campbell, T. McGrath, S. Sjolander, T. Hanson, M. Tidare, O. Jansson, A. Moberg, M. Mooney, C. Elliott, and J. Buijs, "Use of a novel micro-fluidic device to create arrays for multiplex analysis of large and small molecular weight compounds by surface plasmon resonance," *Biosens. Bioelectron.,* vol. 26, pp. 3029-3036, Feb. 15, 2011.

[43] B. J. Yakes, S. Prezioso, S. A. Haughey, K. Campbell, C. T. Elliott, and S. L. Degrasse, "An improved immunoassay for detection of saxitoxin by surface plasmon resonance biosensors," *Sens. Actuators B-Chem.,* vol. 156, pp. 805-811, Aug. 2011.

[44] K. A. Heyries, M. G. Loughran, D. Hoffmann, A. Homsy, L. J. Blum, and C. A. Marquette, "Microfluidic biochip for chemiluminescent detection of allergen-specific antibodies," *Biosens. Bioelectron.,* vol. 23, pp. 1812-1818, Jul. 15, 2008.

[45] J. Homola, K. Hegnerova, and M. Vala, "Surface plasmon resonance biosensors for detection of foodborne pathogens and toxins," *Proc. SPIE*, vol. 7167, pp. 716705-1-716705-10, 2009.

[46] K. Majer-Baranyi, A. Szekacs, I. Szendro, A. Kiss, and N. Adanyi, "Optical waveguide lightmode spectroscopy technique-based immunosensor development

for deoxynivalenol determination in wheat samples," *Eur. Food Res. Technol.,* pp. 1-7, Oct. 19, 2011.

[47] J. V. Samsonova, N. A. Uskova, A. N. Andresyuk, M. Franek, and C. T. Elliott, "Biacore biosensor immunoassay for 4-nonylphenols: Assay optimization and applicability for shellfish analysis," *Chemosphere,* vol. 57, pp. 975-985, Nov. 2004.

[48] E. S. Forzani, H. Zhang, W. Chen, and N. Tao, "Detection of heavy metal ions in drinking water using a high-resolution differential surface plasmon resonance sensor," *Environ. Sci. Technol.,* vol. 39, pp. 1257-1262, Mar. 1, 2005.

[49] P. Westerhoff, T. Nongjian, E. S. Forzani, and K. Foley, "Detection of arsenic in groundwater using a surface plasmon resonance sensor," *Sens. Actuators B-Chem.,* vol. 123, pp. 82-88, Apr. 10, 2007.

[50] M. Farre, E. Martinez, J. Ramon, A. Navarro, J. Radjenovic, E. Mauriz, L. Lechuga, M. P. Marco, and D. Barcelo, "Part per trillion determination of atrazine in natural water samples by a surface plasmon resonance immunosensor," *Anal. Bioanal. Chem.,* vol. 388, pp. 207-214, May 2007.

[51] E. Mauriz, A. Calle, J. J. Manclus, A. Montoya, and L. M. Lechuga, "Multi-analyte SPR immunoassays for environmental biosensing of pesticides," *Anal. Bioanal. Chem.,* vol. 387, pp. 1449-1458, Oct. 25, 2007.

[52] E. Mauriz, A. Calle, J. J. Manclus, A. Montoya, A. Hildebrandt, D. Barcelo, and L. M. Lechuga, "Optical immunosensor for fast and sensitive detection of DDT and related compounds in river water samples," *Biosens. Bioelectron.,* vol. 22, pp. 1410-1418, Feb. 15, 2007.

[53] N. R. Walker, M. J. Linman, M. M. Timmers, S. L. Dean, C. M. Burkett, J. A. Lloyd, J. D. Keelor, B. M. Baughman, and P. L. Edmiston, "Selective detection of gas-phase TNT by integrated optical waveguide spectrometry using molecularly imprinted sol-gel sensing films," *Anal. Chim. Acta,* vol. 593, pp. 82-91, Jun. 2007.

[54] A. Larsson, J. Angbrant, J. Ekeroth, P. Mansson, and B. Liedberg, "A novel biochip technology for detection of explosives - TNT: Synthesis, characterisation and application," *Sens. Actuators B-Chem.,* vol. 113, pp. 730-748, Feb. 26, 2006.

[55] O. Wan-Kyu, J. Yoon Seon, S. Jooyoung, and J. Jyongsik, "Fluorescent europium-modified polymer nanoparticles for rapid and sensitive anthrax sensors," *Biosens. Bioelectron.,* vol. 29, pp. 172-177, Nov. 15, 2011.

[56] S. Mostafa, I. Lee, S. K. Islam, S. A. Eliza, G. Shekhawat, V. P. Dravid, and F. S. Tulip, "Integrated MOSFET-embedded-cantilever-based biosensor characteristic for detection of anthrax simulant," *IEEE Electron. Dev. Letts.,* vol. 32, pp. 408-410, Mar. 2011.

[57] E. Botonjic-Sehic, T. L. Paxon, and H. Boudries, "Rapid and field-deployable biological and chemical Raman-based identification," *Proc. SPIE*, vol. 8032, pp. 80320G-1-80320G-9, 2011.

[58] P. Taranekar, A. Baba, P. Jin Young, T. M. Fulghum, and R. Advincula, "Dendrimer precursors for nanomolar and picomolar real-time surface plasmon resonance/potentiometric chemical nerve agent sensing using electrochemically crosslinked ultrathin films," *Adv. Funct. Mater.,* vol. 16, pp. 2000-2007, Oct. 4, 2006.

[59] S. M. Daly, M. Grassi, D. K. Shenoy, F. Ugozzoli, and E. Dalcanale, "Supramolecular surface plasmon resonance (SPR) sensors for organophosphorus vapor detection," *J. Mater. Chem.,* vol. 17, pp. 1809-1818, May 14, 2007.

[60] K. De Vos, P. Debackere, T. Claes, J. Girones, W. De Cort, E. Schacht, R. G. Baets, and P. Bienstman, "Label-free biosensors on silicon-on-insulator optical chips," *Proc. SPIE*, vol. 7397, pp. 739710-1-739710-8, 2009.

[61] F. Baldini, S. Martellucci, A. N. Chester, and J. Homola, *Optical Chemical Sensors*. Dordrecht, Netherlands: Springer, 2006.

[62] R. Narayanaswamy and O. S. Wolfbeis, *Optical Sensors: Industrial, Environmental, and Diagnostic Applications*. New York, NY: Springer, 2004.

[63] R. W. Wood, "Remarkable spectrum from a diffraction grating," *Philos. Mag.,* vol. 4, pp. 396-402, Sept. 1902.

[64] U. Fano, "Theory of anomalous diffraction gratings and of quasi-stationary waves on metallic surfaces (Sommerfeld's waves)," *J. Opt. Soc. Am.,* vol. 31, pp. 213-222, Mar. 1941.

[65] A. Otto, "Excitation of nonradiative surface plasma waves in silver by the method of frustrated total reflection," *Z. Phys. A, At. Nuclei,* vol. 216, pp. 398-410, 1968.

[66] E. Kretschmann and H. Raether, "Radiative decay of non radiative surface plasmons excited by light," *Z. Naturforsch. Pt. A,* vol. 23a, pp. 2135-2136, Dec. 1968.

[67] International Business Machines, Armonk, NY, www.ibm.com

[68] I. Pockrand, J. D. Swalen, J. G. Gordon, II, and M. R. Philpott, "Surface plasmon spectroscopy of organic monolayer assemblies," *Surf. Sci.,* vol. 74, pp. 237-244, May 1978.

[69] I. Pockrand, J. D. Swalen, R. Santo, A. Brillante, and M. R. Philpott, "Optical properties of organic dye monolayers by surface plasmon spectroscopy," *J. Chem. Phys.,* vol. 69, pp. 4001-4011, Nov. 1, 1978.

[70] J. Homola, "Surface plasmon resonance sensors for detection of chemical and biological species," *Chem. Rev.,* vol. 108, pp. 462-493, Jan. 30, 2008.

[71] H. Raether, *Surface Plasmons on Smooth and Rough Surfaces and on Gratings*. Berlin, Germany: Springer-Verlag, 1988.

[72] A. J. Benahmed and H. Chih-Ming, "Bandgap-assisted surface-plasmon sensing," *Appl. Opt.,* vol. 46, pp. 3369-3375, Jun. 1, 2007.

[73] S. M. Husson and L. Xiao, "Adsorption of dansylated amino acids on molecularly imprinted surfaces: A surface plasmon resonance study," *Biosens. Bioelectron.,* vol. 22, pp. 336-348, 2006.

[74] D. C. Cullen, R. G. W. Brown, and C. R. Lowe, "Detection of immuno-complex formation via surface plasmon resonance on gold-coated diffraction gratings," *Biosensors,* vol. 3, pp. 211-225, 1987.

[75] D. C. Cullen and C. R. Lowe, "Direct surface plasmon-polariton immunosensor. Preliminary investigation of the non-specific adsorption of serum components to the sensor interface," *Sens. Actuators B-Chem.,* vol. B1, pp. 576-579, Jun. 25-30, 1990.

[76] J. Homola, S. S. Yee, and G. Gauglitz, "Surface plasmon resonance sensors: review," *Sens. Actuators B-Chem.,* vol. 54, pp. 3-15, Sept. 16, 1999.

[77] B. H. Ong, X. Yuan, and S. C. Tjin, "Bimetallic silver-gold film waveguide surface plasmon resonance sensor," *Fiber Integrated Opt.,* pp. 229-240, 2007.

[78] P. Hyungseok, H. J. Cho, and P. L. Likamwa, "On-chip surface plasmon resonance sensor," *J. Nanosci. Nanotechnol.,* vol. 8, pp. 4968-4971, Oct. 2008.

[79] P. Hyungseok, P. L. Likamwa, and H. J. Cho, "Development of SPR sensor array based on optoelectronic platform for high throughput system," in *IEEE LEOS Ann. Mtg.*, Piscataway, NJ, 2008, pp. CFE6-1-CFE6-2.

[80] N. F. Hartman, "Optical sensing apparatus and method," U.S. Patent 4 940 328, Jul. 10, 1990.

[81] R. Bernini and A. Cusano, "Generalized Mach-Zehnder interferometers for sensing applications," *Sens. Actuators B-Chem.,* vol. 100, pp. 72-74, Jun. 1, 2004.

[82] J. J. Lillie, M. A. Thomas, N. M. Jokerst, S. E. Ralph, K. A. Dennis, and C. L. Henderson, "Multimode interferometric sensors on silicon optimized for fully integrated complementary-metal-oxide-semiconductor chemical-biological sensor systems," *J. Opt. Soc. Am. B,* vol. 23, pp. 642-651, Apr. 2006.

[83] D. P. Campbell, J. L. Moore, J. M. Cobb, N. F. Hartman, B. H. Schneider, and M. G. Venugopal, "Optical system-on-a-chip for chemical and biochemical sensing: the chemistry," *Proc. SPIE*, vol. 3540, pp. 153-161, 1999.

[84] N. F. Hartman, J. Cobb, J. G. Edwards, X. Yang, P. Katila, M. J. Leppihalme, A. Tervonen, and N. Peyghambarian, "Optical system-on-a-chip for chemical and biochemical sensing: the platform," *Proc. SPIE*, vol. 3537, pp. 302-309, 1999.

[85] P. L. Edmiston, D. P. Campbell, D. S. Gottfried, J. Baughman, and M. M. Timmers, "Detection of vapor phase trinitrotoluene in the parts-per-trillion range using waveguide interferometry," *Sens. Actuators B-Chem.,* vol. 143, pp. 574-82, Jan. 7, 2010.

[86] D. P. Campbell, J. L. Moore, J. M. Cobb, and J. G. Edwards, "Integrated optic sensor for pH and ammonia," *Proc. SPIE*, vol. 3537, pp. 327-335, 1999.

[87] M. Iodice, L. De Stefano, G. Coppola, V. Mocella, I. Rea, E. De Tommasi, E. Orabona, and I. Rendina, "Label-free biosensing by means of optical micro-ring resonator," *Proc. SPIE*, vol. 7356, pp. 735603-1-735603-11, 2009.

[88] C.-Y. Chao and L. J. Guo, "Biochemical sensors based on polymer microrings with sharp asymmetrical resonance," *Appl. Phys. Lett.,* vol. 83, pp. 1527-1529, Aug. 25, 2003.

[89] I. M. White, Z. Hongying, J. D. Suter, N. M. Hanumegowda, H. Oveys, M. Zourob, and F. Xudong, "Refractometric sensors for lab-on-a-chip based on optical ring resonators," *IEEE Sens. J.,* vol. 7, pp. 28-35, Jan. 2007.

[90] M. Soltani, S. Yegnanarayanan, and A. Adibi, "Ultra-high Q planar silicon microdisk resonators for chip-scale silicon photonics," *Opt. Express,* vol. 15, pp. 4694-4704, Apr. 3, 2007.

[91] J. Guo, M. J. Shaw, G. Allen Vawter, P. Esherick, G. Ronald Hadley, and C. T. Sullivan, "High-Q integrated on-chip micro-ring resonator," in *IEEE LEOS Ann. Mtg.*, Piscataway, NJ, 2004, pp. 745-746.

[92] Z. Xia, A. A. Eftekhar, M. Soltani, B. Momeni, Q. Li, M. Chamanzar, S. Yegnanarayanan, and A. Adibi, "High resolution on-chip spectroscopy based on miniaturized microdonut resonators," *Opt. Express,* vol. 19, pp. 12356-12364, Jun. 20, 2011.

[93] M. Lamponi, S. Keyvaninia, F. Pommereau, R. Brenot, G. de Valicourt, F. Lelarge, G. Roelkens, D. Van Thourhout, S. Messaoudene, J. M. Fedeli, and G. H. Duan, "Heterogeneously integrated InP/SOI laser using double tapered single-mode waveguides through adhesive die to wafer bonding," in *IEEE GFP Intl. Conf.*, Piscataway, NJ, 2010, pp. 22-24.

[94] G. Roelkens, Y. De Koninck, S. Keyvaninia, S. Stankovic, M. Tassaert, M. Lamponi, D. Guanghua, D. Van Thourhout, and R. Baets, "Hybrid silicon lasers," *Proc. SPIE*, vol. 7942, pp. 79420D-1-79420D-9, 2011.

[95] M. W. Geis, S. J. Spector, M. E. Grein, R. T. Schulein, J. U. Yoon, D. M. Lennon, S. Deneault, F. Gan, F. X. Kaertner, and T. M. Lyszczarz, "CMOS-compatible all-Si high-speed waveguide photodiodes with high responsivity in near-infrared communication band," *IEEE Photonic. Technol. Letts.,* vol. 19, pp. 152-154, Feb. 1, 2007.

[96] L. Colace, V. Sorianello, M. Romagnoli, L. Socci, and G. Assanto, "Optical power monitors in Ge monolithically integrated on SOI chips," *Microelectron. Eng.,* vol. 88, pp. 514-517, Apr. 2011.

[97] MicroChem Corp., Newton, MA, www.microchem.com

[98] J. A. Woollam Co., Inc., Lincoln, NE, www.jawoollam.com

[99] M. Bass, C. DeCusatis, G. Li, V. N. Mahajan, J. Enoch, and E. Van Stryland, *Handbook of Optics*, 3rd ed. vol. 4: McGraw-Hill, 2009.

[100] Soitec, Bernin, France, www.soitec.com

[101] H. Kogelnik and V. Ramaswamy, "Scaling rules for thin-film optical waveguides," *Appl. Opt.,* vol. 13, pp. 1857-1862, Aug. 1974.

[102] DuPont, Wilmington, DE, www.dupont.com

[103] Henkel Corporation, Dusseldorf, Germany, www.henkel.com

[104] H. Kogelnik, "Coupled wave theory for thick hologram gratings," *Bell Syst. Tech. J.,* vol. 48, pp. 2909-2947, Nov. 1969.

[105] S. M. Rytov, "Electromagnetic properties of a finely stratified medium," *Sov. Phys. JETP-USSR,* vol. 2, pp. 466-475, 1956.

[106] J. S. Maikisch and T. K. Gaylord, "Optimum parallel-face slanted surface-relief gratings," *Appl. Opt.,* vol. 46, pp. 3674-3681, Jun. 20, 2007.

[107] S.-D. Wu, T. K. Gaylord, J. S. Maikisch, and E. N. Glytsis, "Optimization of anisotropically etched silicon surface-relief gratings for substrate-mode optical interconnects," *Appl. Opt.,* vol. 45, pp. 15-21, Jan. 1, 2006.

[108] E. N. Glytsis and T. K. Gaylord, "Rigorous three-dimensional coupled-wave diffraction analysis of single and cascaded anisotropic gratings," *J. Opt. Soc. Am. A,* vol. 4, pp. 2061-2080, Nov. 1987.

[109] E. N. Glytsis and T. K. Gaylord, "Rigorous 3-D coupled wave diffraction analysis of multiple superposed gratings in anisotropic media," *Appl. Opt.,* vol. 28, pp. 2401-2421, Jun. 15, 1989.

[110] E. N. Glytsis and T. K. Gaylord, "Three-dimensional (vector) rigorous coupled-wave analysis of anisotropic grating diffraction," *J. Opt. Soc. Am. A,* vol. 7, pp. 1399-1420, Aug. 1990.

[111] M. G. Moharam and T. K. Gaylord, "Rigorous coupled-wave analysis of planar-grating diffraction," *J. Opt. Soc. Am.,* vol. 71, pp. 811-818, Jul. 1981.

[112] M. G. Moharam and T. K. Gaylord, "Rigorous coupled-wave analysis of grating diffraction-E-mode polarization and losses," *J. Opt. Soc. Am.,* vol. 73, pp. 451-455, Apr. 1983.

[113] M. G. Moharam and T. K. Gaylord, "Rigorous coupled-wave analysis of metallic surface-relief gratings," *J. Opt. Soc. Am. A,* vol. 3, pp. 1780-1787, Nov. 1986.

[114] M. G. Moharam, E. B. Grann, D. A. Pommet, and T. K. Gaylord, "Formulation for stable and efficient implementation of the rigorous coupled-wave analysis of binary gratings," *J. Opt. Soc. Am. A,* vol. 12, pp. 1068-1076, May 1995.

[115] M. G. Moharam, D. A. Pommet, E. B. Grann, and T. K. Gaylord, "Stable implementation of the rigorous coupled-wave analysis for surface-relief gratings: enhanced transmittance matrix approach," *J. Opt. Soc. Am. A,* vol. 12, pp. 1077-1086, May 1995.

[116] S.-D. Wu, T. K. Gaylord, E. N. Glytsis, and Y.-M. Wu, "Three-dimensional converging-diverging Gaussian beam diffraction by a volume grating," *J. Opt. Soc. Am. A,* vol. 22, pp. 1293-1303, Jul. 2005.

[117] A. F. Oskooi, C. Kottke, and S. G. Johnson, "Accurate finite-difference time-domain simulation of anisotropic media by subpixel smoothing," *Opt. Lett.,* vol. 34, pp. 2778-2780, Sep. 15, 2009.

[118] A. F. Oskooi, D. Roundy, M. Ibanescu, P. Bermel, J. D. Joannopoulos, and S. G. Johnson, "MEEP: A flexible free-software package for electromagnetic simulations by the FDTD method," *Comput. Phys. Commun.,* vol. 181, pp. 687-702, Nov. 20, 2010.

[119] A. Farjadpour, D. Roundy, A. Rodriguez, M. Ibanescu, P. Bermel, J. D. Joannopoulos, S. G. Johnson, and G. W. Burr, "Improving accuracy by subpixel smoothing in the finite-difference time domain," *Opt. Lett.,* vol. 31, pp. 2972-2974, Oct. 15, 2006.

[120] P. Adam, J. Dostalek, and J. Homola, "Multiple surface plasmon spectroscopy for study of biomolecular systems," *Sens. Actuators B-Chem.,* vol. 113, pp. 774-781, Feb. 27, 2006.

[121] JEOL Ltd., Tokyo, Japan, www.jeol.com

[122] Zeon Chemicals L.P., Louisville, KY, www.zeonchemicals.com

[123] A. E. Grigorescu, M. C. van der Krogt, C. W. Hagen, and P. Kruit, "10nm lines and spaces written in HSQ, using electron beam lithography," *Microelectron. Eng.,* vol. 84, pp. 822-824, May-Aug. 2007.

[124] C. C. Welch, A. L. Goodyear, T. Wahlbrink, M. C. Lemme, and T. Mollenhauer, "Silicon etch process options for micro- and nanotechnology using inductively coupled plasmas," *Microelectron. Eng.,* vol. 83, pp. 1170-1173, Apr.-Sept. 2006.

[125] H. Yang, L. Fan, A. Jin, Q. Luo, C. Gu, and Z. Cui, "Low-energy electron-beam lithography of ZEP-520 positive resist " in *IEEE NEMS Intl. Conf.*, Zhuhai, China, 2006, pp. 391-394.

[126] Shipley Co. L.L.C., Marlborough, MA

[127] X. Wang, W. Zeng, G. Lu, O. L. Russo, and E. Eisenbraun, "High aspect ratio Bosch etching of sub-0.25 um trenches for hyperintegration applications," *J. Vac. Sci. Technol. B,* vol. 25, pp. 1376-1381, Jul./Aug. 2007.

[128] Q. Li, L. Zhang, M. Chen, and S. Fan, "A process study of electron beam nano-lithography and deep etching with an ICP system," *Sci. China Ser. E,* vol. 52, pp. 1665-1671, Jun. 2009.

[129] D. K. Brown, "Nanometer scale Bosch process silicon etching," *IEEE Electron Ion Photon Beam and Nanofabrication Conference*, Anchorage, AK, 2010.

[130] SPTS Technologies, Newport, United Kingdom, www.spts.com

[131] Nanometrics Inc., Milpitas, CA, www.nanometrics.com

[132] KLA-Tencor Corp., Milpitas, CA, www.kla-tencor.com

[133] SUSS MicroTec AG, Garching, Germany, www.suss.com

[134] National Instruments Corporation, Austin, TX, www.ni.com

[135] OZ Optics, Ottowa, Canada, www.ozoptics.com

[136] Mitutoyo America Corp., www.mitutoyo.com

[137] Hamamatsu Corp., Bridgewater, NJ, www.hamamatsu.com

[138] Cargille Laboratories, Cedar Grove, NJ, www.cargille.com

[139] KD Scientific, Holliston, MA, www.kdscientific.com

[140] Upchurch Scientific, Oak Harbor, WA, www.upchurch.com

[141] T. Tamir and S. Peng, "Analysis and design of grating couplers," *Appl. Phys. A-Mater.,* vol. 14, pp. 235-254, 1977.

[142] P. Bienstman and R. Baets, "Waveguide and resonator modeling based on vectorial eigenmode expansion and perfectly matched layer boundery conditions," in *Pr. Electromagn. Res. S.*, Cambridge, MA, 2000, p. 175.

[143] P. Bienstman, "Rigorous and efficient modelling of wavelength scale photonic components," Ph.D. Dissertation, Dept.of Inform. Tech., Ghent University, Ghent, Belgium, 2001.

[144] IDEX Health & Science, Oak Harbor, WA, www.idex-hs.com

[145] B. J. Kirby, *Micro- and Nanoscale Fluid Mechanics: Transport in Microfluidic Devices*: Cambridge University Press, 2010.

[146] T. Shiquan, G. Shoufeng, J. C. Fanguy, and H. Xuemei, "The application of a light guiding flexible tubular waveguide in evanescent wave absorption optical sensing," *Sens. Actuators B-Chem.,* vol. 120, pp. 724-731, 2007.

[147] A. Crescitelli, M. Consales, M. Penza, P. Aversa, M. Giordono, and A. Cusano, "Toluene detection in aqueous phase by optical fiber sensors integrated with single-walled carbon nanotubes," *Open Environ. Bio. Monitoring J.,* vol. 1, pp. 26-32, 2008.

[148] B. Dang, M. S. Bakir, and J. D. Meindl, "Integrated thermal-fluidic I/O interconnects for an on-chip microchannel heat sink," *IEEE Electron Dev. Lett.,* vol. 27, pp. 117-119, Feb. 2006.

[149] B. Dang, M. S. Bakir, D. C. Sekar, C. R. King, Jr., and J. D. Meindl, "Integrated microfluidic cooling and interconnects for 2D and 3D chips," *IEEE Trans. Adv. Packag.,* vol. 33, pp. 79-87, Feb. 2010.

[150] R. Yang, L. Bing-Rui, W. Jing, X. Shen-Qi, C. Yifang, E. Huq, Q. Xin-Ping, and L. Ran, "Fabrication of micro/nano fluidic channels by nanoimprint lithography and bonding using SU-8," *Microelec. Eng.,* vol. 86, pp. 1379-1381, Apr.-June 2009.

[151] J. Lee, C. KeeBong, K. GeeHong, and L. SeungWoo, "The UV-nanoimprint lithography equipment with multi-head imprinting unit for sub-50nm half-pitch patterns," *Microelec. Eng.,* vol. 84, pp. 963-966, May-Aug. 2007.

[152] N. Khusnatdinov, G. Doyle, M. Miller, N. Stacey, M. Watts, and D. L. LaBrake, "Fabrication of nano and micro optical elements by step and flash imprint lithography," *Proc. SPIE*, vol. 6110, pp. 61100K-1-61100K-10, 2006.

[153] S.-Q. Xie, J. Wan, B.-R. Lu, Y. Sun, Y. Chen, X.-P. Qu, and R. Liu, "A nanoimprint lithography for fabricating SU-8 gratings for near-infrared to deep-UV application," *Microelec. Eng.,* vol. 85, pp. 914-917, May-June 2008.

VITA

Jonathan S. Maikisch was born in 1981 in Ridgewood, New Jersey. He concurrently received his Bachelors of Engineering and Masters of Engineering in Electrical Engineering in 2004 from Stevens Institute of Technology in Hoboken, New Jersey. While at Georgia Tech, Jonathan was the recipient of the Center of Organic Photonics and Electronics Fellowship and the Georgia Tech Research and Innovation Conference Travel Grant. During his time at Georgia Tech, Jonathan served as the main instructor of record for ECE 3710 Circuits and Electronics. For his efforts, Jonathan was recognized as the 2010 Electrical and Computer Engineering Outstanding Graduate Teaching Assistant and was a finalist for the 2010 Center for the Enhancement of Teaching and Learning Outstanding Teaching Assistant Award. Jonathan is a member of the Optical Society of America, the Institute of Electrical and Electronics Engineers, and Eta Kappa Nu.